Università degli Studi di Pavia

Facoltà di Ingegneria

Dipartimento di Ingegneria Civile e Architettura

Master degree in Bioengineering

Mechanical characterization of 3D printed thermoplastic material: from experimental investigation to design

Caratterizzazione meccanica di materiale termoplastico stampato in 3D: dall'indagine sperimentale alla progettazione

Supervisor: Professor
Ferdinando Auricchio
Co - supervisor:
Gianluca Alaimo

Author:
Luca Costato
UIN **414706**

Academic year 2015/2016

... ai miei nonni Paolo e Lino

Il dubbio è l'inizio della conoscenza.

René Descartes

Abstract

In recent years manufacturing processes have begun to progress from rapid prototyping (RP) techniques towards rapid manufacturing (RM) methods, where the objective is now to produce finished components for potential end use in a product. Fused deposition modeling (FDM), trademarked by Stratasys, is a widely used RP technology that can fabricate prototypes from various materials, including thermoplastics. One of the most crucial aspects to investigate in RM is to know how manufactured parts behave, working under real conditions. From an industrial point of view, processes capable of producing robust parts with high strength and long-term stability are the most relevant, since they allow the direct production of end-user parts. To predict the mechanical response of FDM parts it is essential to comprehend the effects that FDM process parameters have on the printed object.

The absence of approved specific standards that focus on studying the mechanical properties of 3D printed parts has brought to the development of a novel procedure for specimen tuning. A throughout sample preparation has been carried out, with an extensive G-code (i.e. the machine code of the 3D printer) elaboration, to allow an accurate printing of specimens with the desired features. FDM printed parts can be intended as orthotropic composites of thermoplastic material filaments, bonding between filaments, and voids. American standard test method for tensile properties of polymer matrix composite materials (ASTM D3039/D3039M - 00) has been considered as a guideline to find the best experimental setup.

Afterwards, an experimental study of the mechanical behavior of an FDM printed thermoplastic material has been carried out, through tensile testing. The relation between elastic and strength properties and raster orientation of FDM printed parts has been investigated and described.

Classical Lamination Theory (CLT) and Tsai-Hill failure theory have been used to characterize, respectively, the mechanical and strength behavior of FDM printed specimens. These two theories allow the mechanical characterization of the material in its linear elasticity domain, but cannot go further.

Raster orientation has been considered as the main process parameter and it has been shown that the FDM material properties highly depend on it. Experimental data have shown a very good agreement with both CLT and Tsai-Hill theory. Subsequently, a comparison between various cross sections has been carried out: filament cross section influences both elastic modulus and strength of the FDM part. Finally, a comparison between two different types of a thermoplastic material has been performed, showing significant differences between them.

After having obtained the material's mechanical properties, a brief design approach has been carried out: the goal was to minimize the mass of a 3D printed holed thin plate, while maintaining certain safety requirements. Following an optimization procedure, the optimized specimen's features have been found. A finite element analysis (FEA) has been applied to find the admissible stress state of the sample, after which it starts deform plastically, and the more dangerous regions, i.e. the first regions to exhibit yielding. Finally, 3D printed optimized holed specimens have been tested, to validate the finite element simulation. The test results show very good agreement

with the FE simulation, as long as the analysis remains in the linear elasticity domain. Once the specimen starts to exhibit yielding, other constitutive models, which include plastic deformations, must be considered to further characterize the material.

Sommario

Nei recenti anni i processi manifatturieri hanno iniziato ad evolversi, da tecnologie di prototipazione rapida (RP) a metodi di manifattura rapida (RM), in cui l'obiettivo è quello di produrre componenti finiti e completi, per essere potenzialmente utilizzati dal consumatore. La modellazione a deposizione fusa (FDM), marchio registrato da Stratasys, è una tecnologia RP largamente utilizzata per fabbricare prototipi partendo da svariati materiali, compresi i termoplastici. Uno degli aspetti cruciali relativo alle tecnologie RM è quello di conoscere come gli oggetti fabbricati si comportano quando vengono sottoposti a reali condizioni di lavoro. Da un punto di vista prettamente industriale, i processi più rilevanti sono quelli che permettono la produzione di parti robuste e capaci di durare nel tempo, poichè consentono la produzione diretta di oggetti di consumo. Per predire la risposta meccanica di parti prodotte con tecnologia FDM è essenziale comprendere gli effetti che i relativi parametri di processo hanno sull'oggetto stampato.

L'assenza di specifici standard approvati, che si focalizzino sullo studio delle proprietà meccaniche di pezzi stampati in 3D, ha portato allo sviluppo di una nuova procedura di messa a punto dei provini di test. È stata effettuata un'accurata preparazione dei campioni, con una vasta elaborazione del G-code (il codice macchina delle stampanti 3D), per permettere la stampa in 3D di provini con le caratteristiche desiderate. Gli oggetti stampati con tecnologia FDM possono essere considerati come dei compositi ortotropi di filamenti di materiale termoplastico, adesi uno con l'altro. Per trovare il miglior setup sperimentale, lo standard ASTM D3039/D3039M - 00 è stato utilizzato come linea guida.

Successivamente, attraverso dei test meccanici di trazione, è stato effettuato uno studio sperimentale sulle caratteristiche meccaniche di un materiale termoplastico stampato tramite FDM. Sono state studiate e descritte le relazioni tra proprietà elastiche e di resistenza con l'orientamento di stampa dei filamenti.

Per caratterizzare elasticità e resistenza sono state utilizzate, rispettivamente, la Teoria Classica dei Laminati (CLT) e il criterio di rottura di Tsai-Hill. Le teorie utilizzate consentono la caratterizzazione meccanica nel dominio di elasticità lineare del materiale, ma non possono spingersi oltre.

L'orientamento dei filamenti è stato considerato come il parametro di processo principale ed è stato dimostrato che le proprietà di un materiale stampato FDM dipendono ampiamente da esso. I dati sperimentali hanno mostrato un'ottima corrispondenza con entrambi i modelli utilizzati. Successivamente, sono state messi a confronto provini stampati con filamenti aventi sezioni trasversali differenti: è stato mostrato che la sezione trasversale del filamento influisce sia sul modulo elastico che sulla resistenza del pezzo stampato FDM. Infine è stato effettuato un confronto fra due diversi tipi del materiale termoplastico considerato, mostrando significative differenze delle proprietà meccaniche.

Dopo aver caratterizzato meccanicamente il materiale, è stato effettuato un breve approccio alla progettazione: l'obiettivo era minimizzare la massa dell'oggetto, rispettando certi requisiti di sicurezza. Seguendo una procedura di ottimizzazione, sono state trovate le caratteristiche del

campione ottimizzato. Tramite un'analisi agli elementi finiti (FEA), è stato possibile ottenere il massimo stato tensionale ammissibile del provino, dopo il quale inizia il suo snervamento e la sua deformazione plastica. Sono state anche trovare le regioni di maggior rischio, cioè le zone che per prime sono soggette allo snervamento del materiale. Infine, i provini ottimizzati sono stati stampati in 3D e sottoposti a test di trazione, per verificare i risultati della simulazione agli elementi finiti. È stata trovata un'ottima corrispondenza tra dati sperimentali e simulazione, a patto che l'analisi rimanga nel dominio di elasticità lineare. Quando il campione inizia a mostrare snervamento, per caratterizzare ulteriormente il materiale, è necessario utilizzare altri modelli costitutivi, che includano deformazioni plastiche.

Contents

List of Tables

List of Figures

Chapter 1

Introduction to 3D printing

1.1 Additive manufacturing

1.1.1 Overview

The term Additive Manufactutring (AM) is defined by the American Society for Testing and Materials (ASTM) as the "Process of joining materials to make objects from 3D model data, usually layer upon layer, as opposed to subtractive manufacturing methodologies, such as traditional machining. Synonyms: additive fabrication, additive processes, additive techniques, additive layer manufacturing, layer manufacturing and freeform fabrication" [63]. The term additive manufacturing describes technologies which can cover an entire product life cycle, from pre-production, i.e. rapid prototyping (RP), to large scale production, i.e. rapid manufacturing (RM).

Additive manufacturing first emerged in 1984, with Charles (Chuck) Hull as its pioneer, with stereolithography (SL) from 3D Systems, a process that solidifies thin layers of ultraviolet (UV) light-sensitive liquid polymer using a laser. Hull defined the process as a "System for generating three-dimensional objects by creating a cross sectional pattern of the object to be formed" [33].

In the early 2010s, the expressions "3D printing" and "additive manufacturing" took on a similar meaning: they were alternate terms for AM technologies, the first one being mostly used by consumers, maker communities and mass media, while the other used officially by industrial AM end use part producers, AM machine manufacturers and global technical standards organizations. Both terms simply reflect the concept that the technologies all share the common process of layer upon layer material addition/joining in a 3D work environment, under automated control.

Additive manufacturing has always been very useful for rapid prototype development but it is starting to make its impact on the manufacturing world as well. Now numerous manufacturers are producing end-use components and entire products via additive manufacturing. Such new techniques, while still evolving, are projected to exert a profound impact on manufacturing industry. They can give new design flexibility, reduce energy use, and shorten time to market [32]. Interest in AM methods has grown rapidly as applications have progressed from rapid prototyping to rapid manufacturing. AM technologies can now use metals, polymers, composites, or other powders to "print" a range of functional components, layer by layer, including complex structures that cannot be manufactured by other means [29].

1.1.2 Benefits of additive manufacturing

The process that may be most affected by 3D printing is machining, referred to subtractive manufacturing. Subtractive processes involve removal of the material from a blank, which is usually a block of material, whose dimensions are greater than the final product, while additive manufacturing is the process of creating a product by using various methods to bind layers of material together (fig. 1.1).

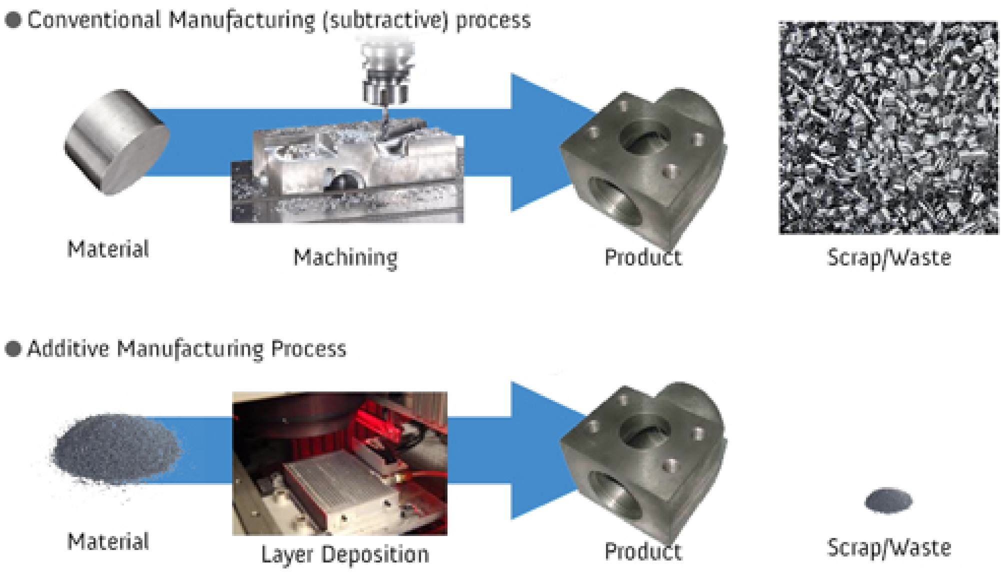

Figure 1.1: Additive manufacturing vs subtractive manufacturing [73]

Additive and traditional manufacturing face different trade-offs: each process is going to play a specific role in the manufacturing industry. Additive manufacturing has the potential to shorten supply chains, minimize material and energy consumption, hence reduce waste production. Some of the most important benefits of additive manufacturing are listed below:

- Reduced time to market: items can be fabricated as soon as the virtual 3D model of the object has been created, eliminating the need for expensive and time-consuming part tooling [4].
- Lower energy consumption: additive manufacturing saves energy usage by removing unnecessary production steps, using less material, allowing the manufacturing of lighter products [4].
- Less waste production: the process of building objects up layer by layer, unlike traditional machining methods, which cut away excess material, can reduce material needs and cost up to 90% [21].
- More complexity: additive manufacturing enables designs with novel and more complex geometries, that would be difficult, if not impossible, to achieve using traditional manufacturing technologies [31].
- Part consolidation: the ability to design products with fewer and more complex parts, rather than a large number of simpler parts, is a very important benefit, because it requires less time and labor for the product's assembly, reducing the overall manufacturing costs [69].

Compared with subtractive manufacturing, additive manufacturing is suitable for producing low volumes of products, especially objects with complex geometry [29]. Nowadays, AM is widely spread within known fields of application 1.2, for example aerospace and defense (A&D), automotive and electronics industry, and the medical sector, including dental applications, prostheses and implants for bone internal fixation [25]. Even consumer industries such as the sports, the furniture, the jewelry, or the food industry are becoming more and more aware of AM technologies' benefits for their business. Nevertheless, additive manufacturing is still not the best solution for all cases, in some cases traditional machining processes still need to be used: for instance, parts dimension could be larger than available additive manufacturing printers.

Additive manufacturing could be viewed as a disruptive technology, since it has successfully disrupted the prototyping industry and given birth to new fields in the areas of design and manufacturing. Moreover, it allows the design and creation of objects of complex geometry with accuracy. This is attainable because 3D printing can control almost exactly how materials are deposited, making it possible to create structures which could not be produced using conventional manufacturing processes. Another advantage is the fact that a single 3D printer can create different products, while traditional manufacturing methods must be tailored in function of the product target, requiring expensive investment in terms of time and money. With the ongoing improvement of 3D printers in terms of accuracy, speed and quality, the potential for future impact is immense [48].

1.1.3 Applications and state of art

AM technologies' expansion into production has been under development in the last decades. Since the start of the 21st century there has been a large growth in the sales of AM machines, and their price has dropped substantially [56].

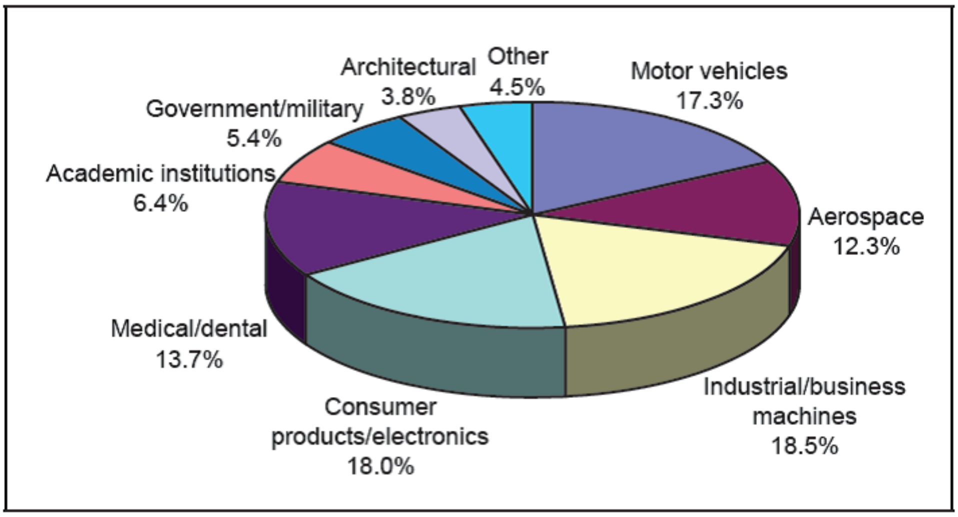

Figure 1.2: Industries served by AM manufacturers and service providers [69]

According to Wohlers Associates, a consultancy, the market for 3D printers and services was worth $2.2 billion worldwide in 2012, up 29% from 2011 [22]. The development of advanced additive manufacturing techniques has swiftly progressed in recent years. The following paragraphs briefly summarize the main application fields of additive manufacturing and the state of art.

Automotive field

Nowadays, automotive industry is a major user of additive manufacturing, especially of RP technologies, for functional prototypes production. For automotive industry, AM technology is an important tool in the design and fabrication of automotive components, because it shortens development time and reduces manufacturing costs [29]. Especially the motorsport sector is an important field for AM technologies, since it requires parts with high performance and low weight. Automotive industry can attain great benefits from the application of AM, as these technologies allow a rapid production of complex parts, including a wide range of material properties (fig. 1.3).

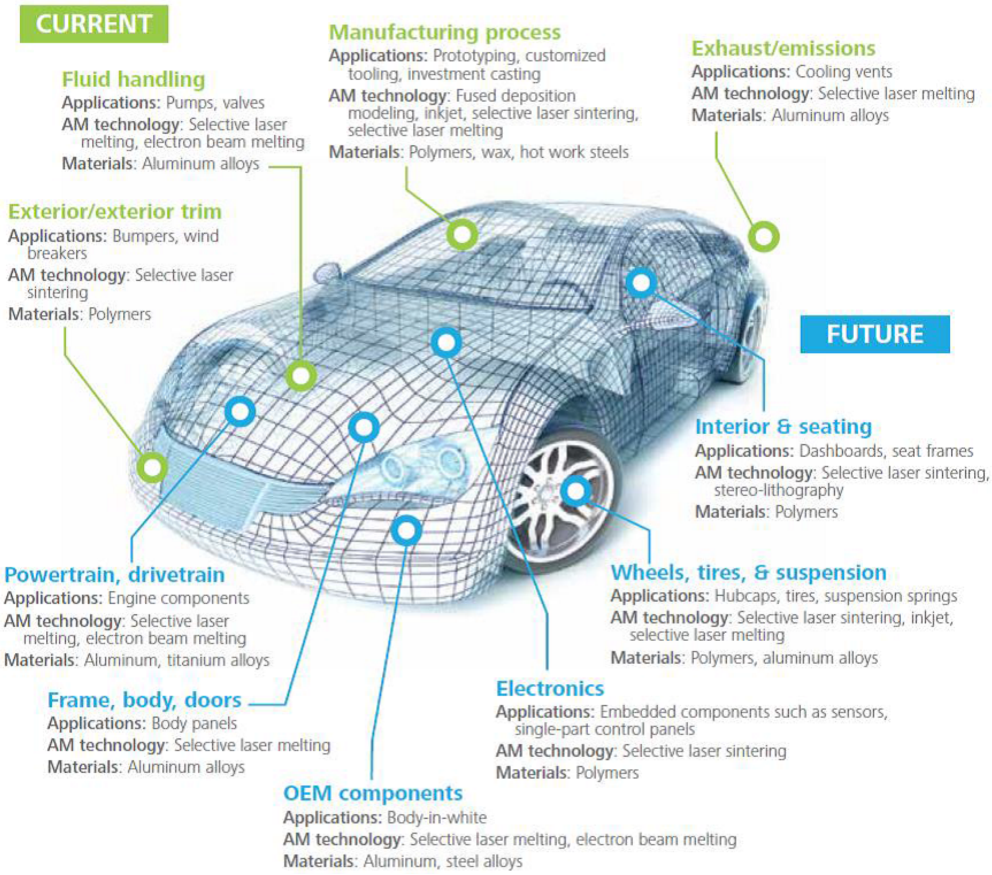

Figure 1.3: Current and future applications of AM in the automotive field [27]

In 2013, the automotive industry contributed 17.3% to the total AM market volume, which corresponds to approximately $531 million US dollars [69]. However, the AM market is still marginal, compared to the world market volume of the automotive industry, which amounted to $2 trillion in 2013 [27].

While AM is already being used for a great variety of applications, such as concept modeling, functional testing and production planning, it is currently only used for prototyping and fabrication of small, complex components, that are non-safety relevant, because process reliability and product consistency are still limited [12]. Furthermore, many parts cannot be fabricated by currently available AM machines because of their excessive size.

In the future, automotive industry is expected to generate a big demand for AM equipment, in particular:

- Higher demand for lightweight structures [67].
- Increasing demand of replacement parts for antique cars [16].

- Increasing emphasis on individual customer needs (more personalization) [14].
- Higher focus on sustainable mobility [14].

Aerospace & Defense (A&D) field

Development and research work in A&D industry aims to constantly improve the aircratf efficiency (including lightweighting) and reduce the air and noise pollution [14]. All these goals need parts that are lightweight, robust and, in some cases, even electrically conductive [70]. In addition, most of these products have a complex geometry and are manufactured in small quantities, with high cost per unit. These features make A&D industry particularly viable for AM technologies. For instance, Boeing and Airbus are intensively using additive manufacturing to build lighter-weight parts and reduce fabrication time and manufacturing costs [12].

The total volume market of AM technologies, in 2013, is around \$3.1 billion US dollars: about 12.3% (\$378 million US dollars) is attributed to aerospace industry [69]. While constantly growing, the AM-market in A&D industry is still marginal (\$378 million US dollars vs \$706 billion US dollars).

Additive manufacturing is already being used for a great variety of applications in aerospace industry, but there are other potential uses (fig. 1.4).

	Current applications	Potential applications
Commercial aerospace and defense	• Concept modeling and prototyping • Printing low-volume complex aerospace parts • Printing replacements parts	• Embedding additively manufactured electronics directly on parts • Printing aircraft wings • Printing complex engine parts • Printing repair parts on the battlefield
Space	• Printing specialized parts for space exploration • Printing structures using lightweight, high-strength materials • Printing parts with minimal waste	• Printing on-demand parts/spares in space • Printing large structures directly in space, thus circumventing launch vehicles' size limitations

Figure 1.4: Current and future applications in A&D industry [60]

Some of the most relevant future trends in A&D industry are listed below:

- Increasing production of lightweight structures.
- Implementation of new features in designs, for adding strength to components.
- Increasing the customization of the interior of aircraft.
- Fabrication of parts with adaptive shapes, especially adaptive wings.
- Embedding additively manufactured electronics directly on parts [60].

Biomedical field

Additive manufacturing has been applied in medicine since the early 2000s, when it was first used to make dental implants and personalized prosthetics. Since then, 3D printing medical applications have greatly developed [28]. The current medical fields involving 3D printing can be organized into several categories: tissue and organ fabrication; prosthesis, implants and anatomical models creation; pharmaceutical design regarding drug delivery and dosage form.

Tissue engeneering and bioprinting Current treatment for organ failure relies mostly on organ transplants from living or deceased donors. However, human organs available for transplant are never enough [55]. As of early 2014, approximately 120.000 people in the U.S. were awaiting an organ transplant [55]. An additional issue consists in the complicated task of finding a donor who is a tissue match. This problem could be limited, if not eliminated, by using cells taken from the organ transplant patient's own body to create a replacement organ: this would minimize the risk of tissue rejection [50]. Although in its early stages, 3D printing offers important advantages over the traditional regenerative method, which only provides scaffold support, such as extremely accurate cell placement and highly precise digital control of extrusion speed, diameter and concentration of printed cells [19].

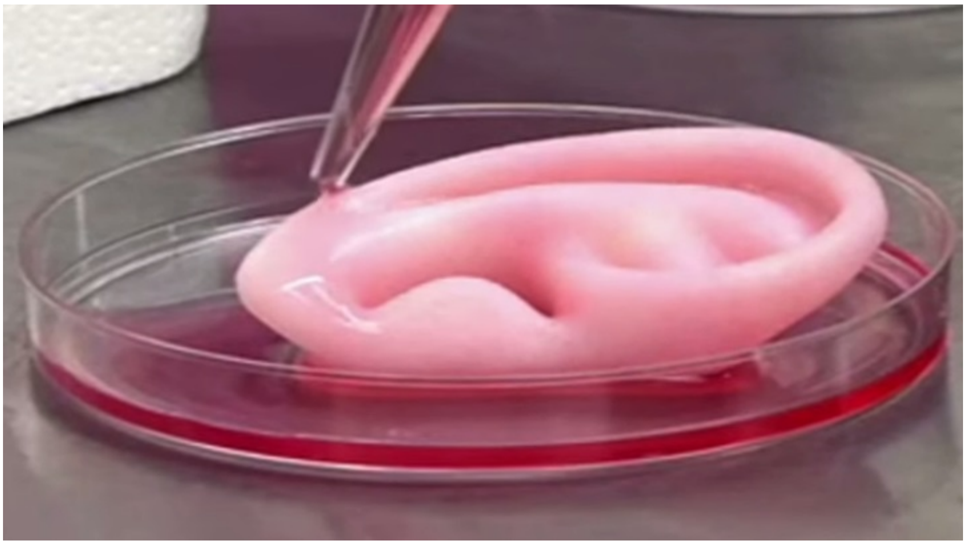

Figure 1.5: Bioprinting of an artificial ear [74]

Scaffolds can be built with various materials, depending on the desired strength, porosity, and type of tissue, with hydrogels usually considered to be most suitable for creating soft tissues. The most common bioprinting method is inkjet-based, which prints a sort of "bioink". Several printheads can be used to print different cell types (bone cells, blood vessel, muscle cells, etc. . .), a mandatory feature for producing whole heterocellular tissues and organs [50]. Researchers have already used 3D printers to create a knee meniscus, heart valve, spinal disk, other types of cartilage and bone, and an artificial ear (fig. 1.5) [28, 45, 10].

3D printing shows great promise in the creation of tissue and organs, especially highly vascularized ones, since it offers precise placement of multiple cell types. A growing number of biotech companies have focused on tissues and organs production for medical research. It may be possible to rapidly screen the effects of new therapeutic drugs on patient tissue, cutting research costs and time. Furthermore an organ created from a patient's own stem cells could be used to determine if a drug will be effective for that individual.

Prostheses and implants Bone implant production for internal fixation has been growing in the last decades (fig. 1.6). Additive manufacturing is already been used to create personalized prosthetic limbs and surgical implants, sometimes even within 24 hours: hip, dental and spinal implants have already been produced through this AM [9]. The possibility to fabricate custom prostheses and implants solves a persistent issue in orthopedics field, where standards implants are not adequate for some patients [9]. This is particularly true in neurosurgery: since skulls have irregular shapes, it is a very complex task to design and fabricate a standardized cranial implant. An increasing number of 3D printed cranial implants has been produced (fig. 1.34), since this technology makes the personalization of the fit and the design much feasible [9].

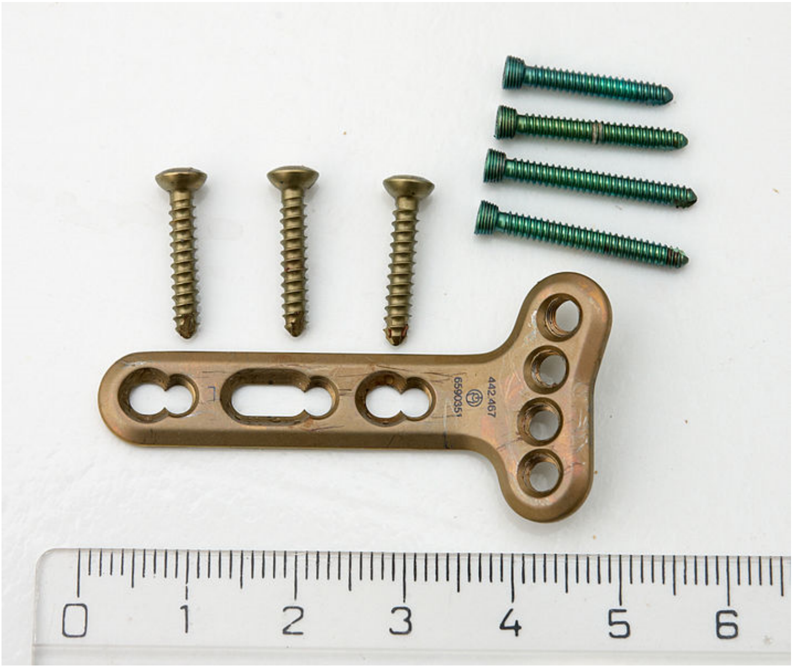

Figure 1.6: Bone implant for fixation of a broken wrist [85]

AM has already had a disruptive effect on hearing aid production: nowadays, 99% of hearing aids that fit into the ear are custom-made using 3D printing [9]. Everyone's ear canal is shaped differently, and 3D printing techniques allow the production custom-shaped devices. An anatomically correct 3D-printed prosthetic ear capable of detecting electromagnetic frequencies has been fabricated using silicon, chondrocytes, and silver nanoparticles [28]. More than 50.000 Invisalign braces are 3D printed every day: they are 3D printed orthodontic braces, which are removable, custom-made and unique to each patient [46].

Anatomical models Since human body is full of complexities and differences, having a tangible 3D printed model of a patient's anatomy, to study or use to simulate surgery, is preferable for physicians and surgeons. CT or MRI scans are not as informative as a physical 3D model, because they are viewed in 2D on a flat screen [9]. Although still in the early stages, 3D printed models have been used in many cases to gain information of the patient's specific anatomy prior to a medical procedure (fig. 1.7).

3D printed neuroanatomical models can be very helpful to neurosurgeons, because cerebral architecture is one of the most complex structures in the human body, where even a small error can potentially lead to devastating consequences. A realistic 3D model reflecting the relationships between damaged and healthy brain structures can be immensely helpful in determining the safest surgical procedure to apply [38]. High-quality 3D anatomical models with the right pathology for training doctors in performing colonoscopies are very important, since colorectal cancer is the second leading cause of cancer-related deaths in the U.S. [9]. Other surgeons have used a 3D printed model of a calcified aorta for surgical planning of plaque removal [9].

3D printed models can be useful beyond surgical planning (fig. 1.8): biomolecular 3D printed models are increasing, since they can help to better understand the various types of biological

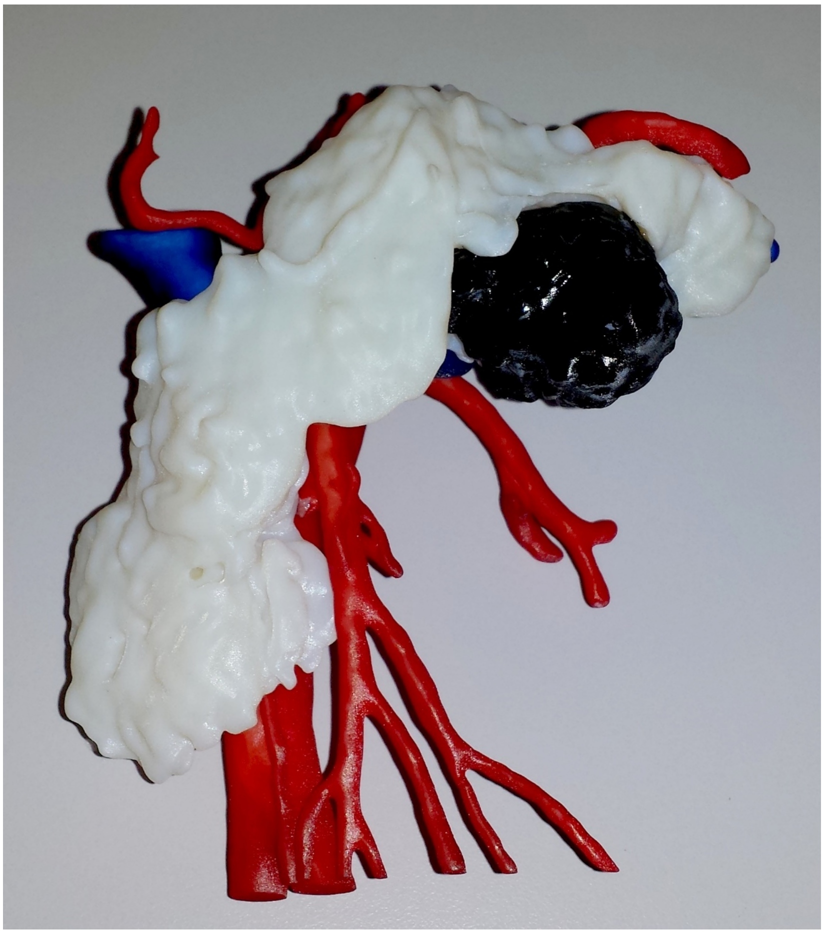

Figure 1.7: Pancreas model with a tumor at the tail: planning of tumor resection (black) [75]

structures.

Custom drug-release profiles AM technologies are also being used in pharmaceutical research: the main advantages include accurate control of droplet size and dose, high reproducibility and the possibility to create complex drug-release profiles [66]. The creation of treatments having complex drug-release profiles is a highly researched field. Traditional compressed dosage forms are often made from a homogeneous mixture of active and inactive ingredients and are limited to a simple drug-release profile [9]. However, 3D printers can print binder onto a matrix powder bed in layers typically 200 micrometers thick, creating a barrier between the active ingredients to allow a more controlled drug release [9]. 3D printed dosage forms can be produced in complex geometries that are porous and loaded with multiple drugs, surrounded by barrier layers that modulate the release [9]. Implantable drug delivery devices with enhanced drug-release profiles can be created through 3D printing: unlike traditional systemic treatments that can affect healthy tissue, these devices can be implanted to provide direct treatment to the area involved [9].

The printing of medications with customized drug release profiles into such bone implant scaffolds has been studied [66]. An example is the printing of a multilayered bone implant with a distinct drug-release profile alternating between rifampicin and isoniazid in a pulse release mechanism [66].

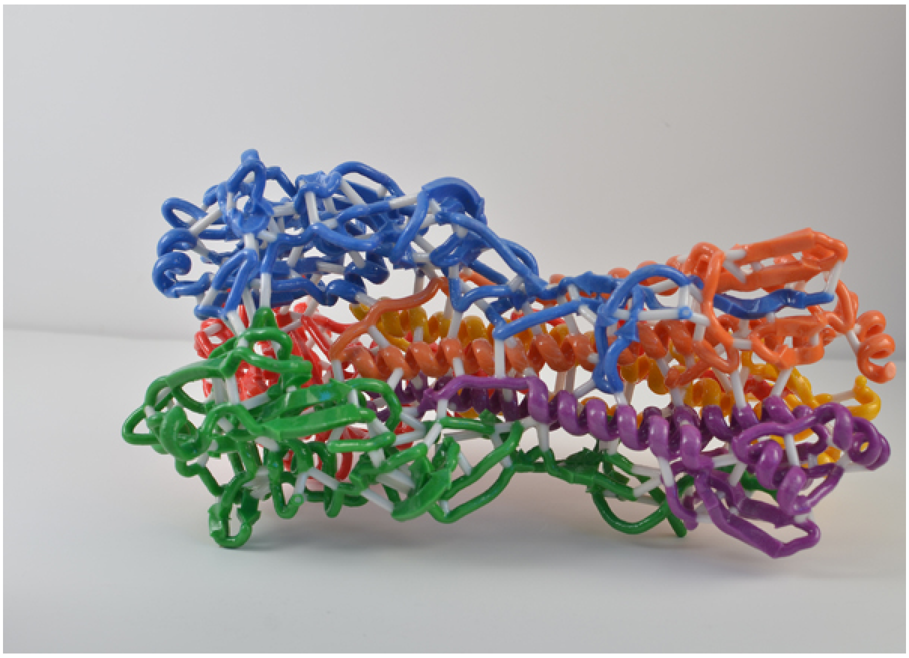

Figure 1.8: A 3D model of influenza hemagglutinin [76]

Systemic administration of the immunosuppressive drug cyclosporin A (CsA) is frequently associated with a number of side effects; therefore, sometimes it cannot be applied in sufficient dosage after allogeneic or xenogeneic cell transplantation. 3D printing has been used to develop a CsA-loaded 3D drug carrier for the purpose of local and sustained delivery of CsA (fig. 1.9) [57]:

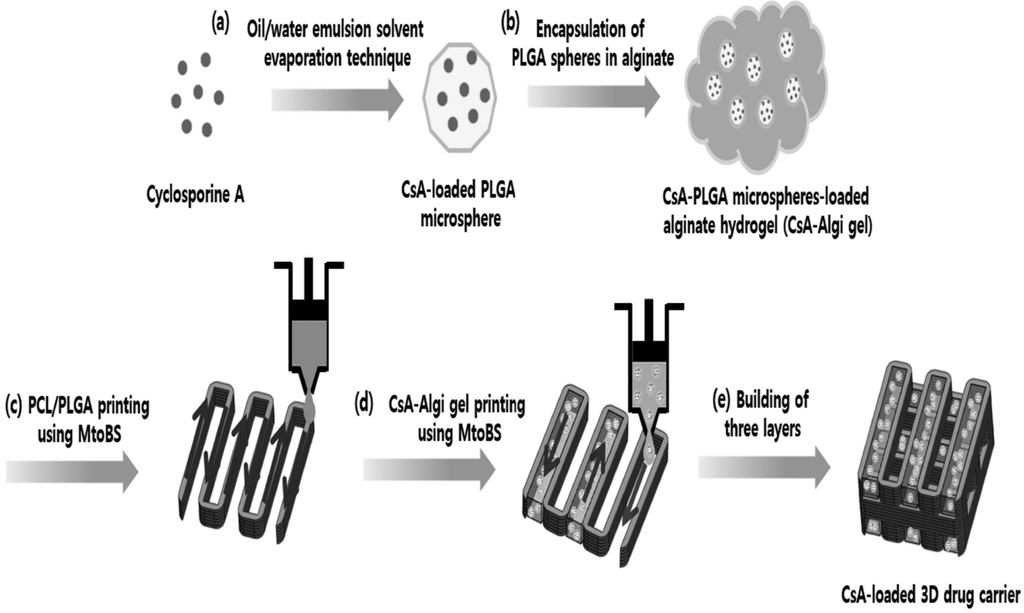

Figure 1.9: Schematic diagram of the preparation of CsA-loaded 3D drug carriers [57]

Customized drugs Oral tablets are the most used drug dosage form because of pain avoidance, ease of manufacture, good patient compliance and accurate dosing. However, a standard procedure to make personalized tablets that could be routinely used is not available yet [36]. Tablets are currently made using traditional methods, such as mixing, milling, and dry and wet granulation of powdered ingredients, which, through compression or molding methods, are made into tablets [36]. These processes are highly unsuitable for creating personalized medicines.

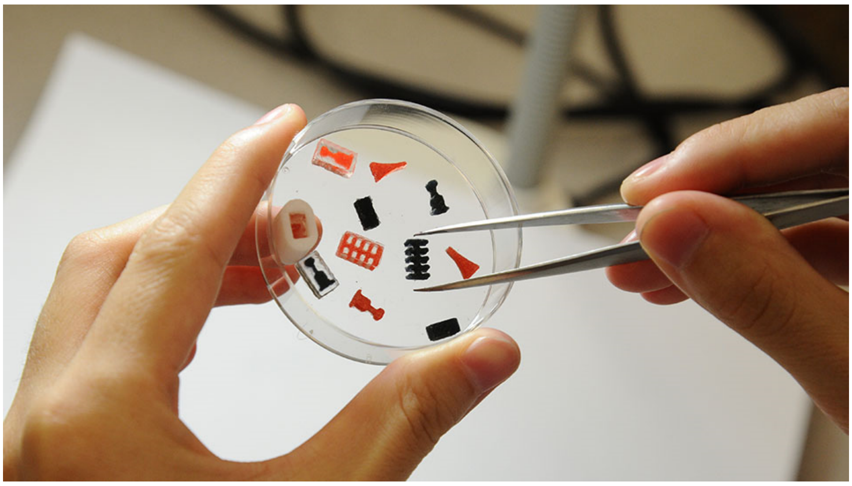

Figure 1.10: 3D printed personalized medical tablets [77]

An optimized customized tablet could be 3D-printed (fig. 1.10) according to a patient's pharmacogenetic profile and other characteristics, such as age, race and gender [66]. Additionally, if necessary, the dosage could be adjusted further, based on the patient's clinical response.

1.1.4 Additive manufacturing technologies

Additive manufacturing covers a vast range of different technologies and methods. The difference between individual processes depends on the material and the technology used. ASTM group "ASTM F42 – Additive Manufacturing" formulated a set of standards that classify the range of additive aanufacturing processes into seven categories [63]:

- Material extrusion
- Vat photopolymerization
- Powder bed fusion
- Material jetting
- Binder jetting
- Sheet lamination
- Direct energy deposition

Material extrusion

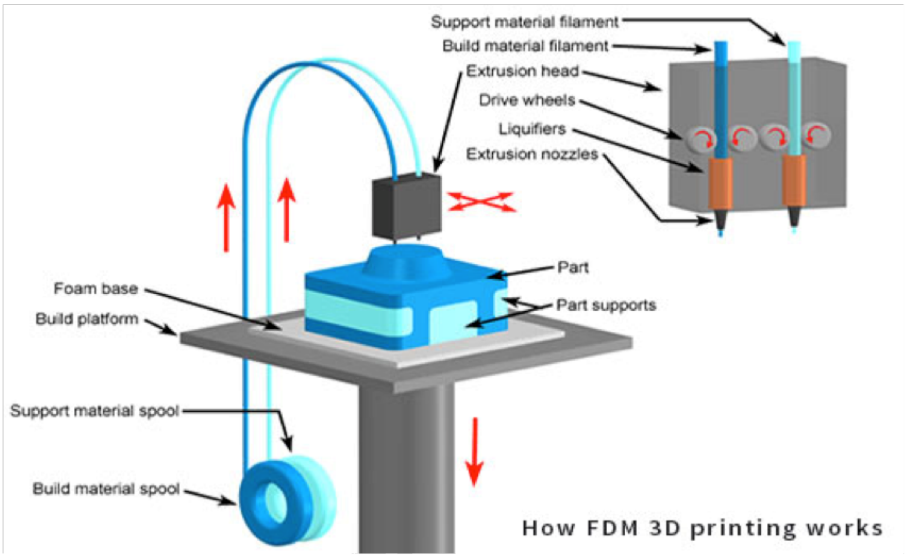

Figure 1.11: Material extrusion process [78]

The most used technology in this process is fused deposition modeling (FDM), which is trademarked by the company Stratasys. The exactly equivalent term, fused filament fabrication (FFF), was coined by the members of the RepRap project, in order to have an expression that could be used without any legal constraints. FDM technology works using a thermoplastic filament or metal wire, which is unwound from a coil and supplying material to an extrusion nozzle, which can turn the flow on and off. The nozzle is heated to melt the material and can be moved in horizontal direction, while the building platform is moved in vertical direction, by a numerically controlled mechanism, directly controlled by a computer-aided manufacturing (CAM) software package. The object is created by extruding the semi-molten material to form layers, while the material hardens immediately after the extrusion from the nozzle (fig. 1.11).

This technology is mostly used with two thermoplastic filaments: acrylonitrile butadiene styrene (ABS) and polylactic acid (PLA) but many other materials are available, such as polycarbonate (PC), polyamide (PA), polystyrene (PS), rubber, etc. FDM was invented by Scott Crump in the late 80s. After patenting this technology, he started the company Stratasys in 1988. The software that comes with this technology automatically generates support structures, if required. The machine extrudes two materials, one for the model and one for the disposable support structure.

It is a commonly used technique used on many inexpensive, domestic and hobby 3D printers. The process has many factors that influence the final model quality but has great potential and viability when these factors are controlled successfully. Whilst FDM is similar to all other 3D printing processes, as it builds layer by layer, it varies in the fact that material is added through a nozzle, under pressure and in a continuous stream. This pressure must be kept steady and at a constant speed to enable accurate results.

Vat photopolymerization

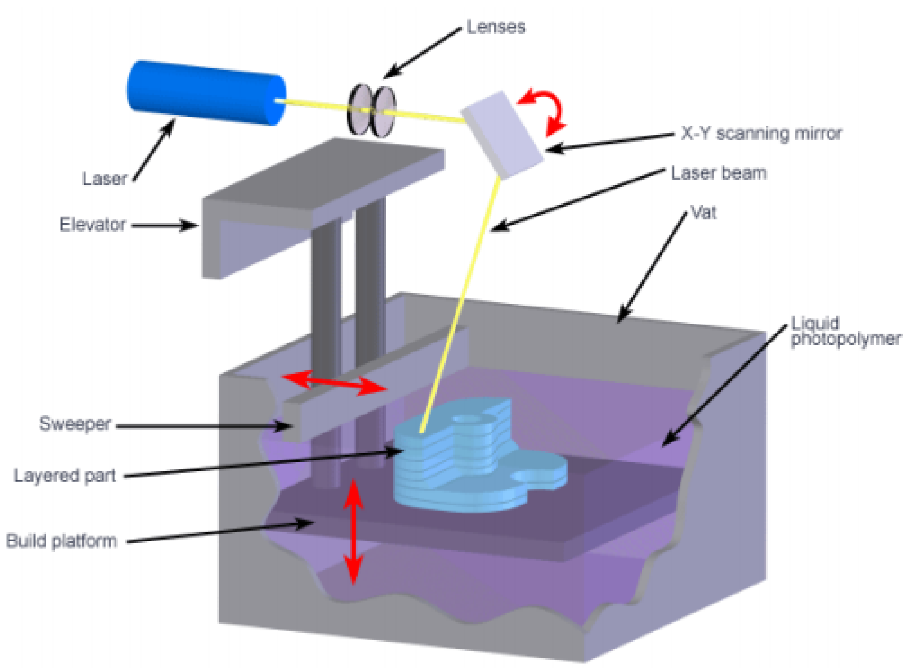

Figure 1.12: Vat photopolymerization process [79]

This technique was invented in 1986 by Charles Hull, who also at the time founded the company, 3D Systems. A 3D printer based on the vat photopolymerisation method has a container filled with photopolymer resin which is then hardened with UV light source. The most commonly used technology in this processes is stereolithography (SLA).

This technology employs a vat of liquid ultraviolet curable photopolymer resin and an ultraviolet laser to build the object's layers one at a time (fig. 1.12). For each layer, the laser beam traces a cross section of the part pattern on the surface of the liquid resin. Exposure to the ultraviolet laser light cures and solidifies the pattern traced on the resin and joins it to the layer below. After the pattern has been traced, the SLA's elevator platform descends by a distance equal to the thickness of a single layer, typically 0.05 mm to 0.15 mm. Then, a resin-filled blade sweeps across the cross section of the part, re-coating it with fresh material. On this new liquid surface, the subsequent layer pattern is traced, joining the previous layer. The complete three dimensional object is formed by this process. Stereolithography requires the use of supporting structures which serve to attach the part to the elevator platform and to hold the object because it floats in the basin filled with liquid resin. These are removed manually after the object is finished.

Powder bed fusion

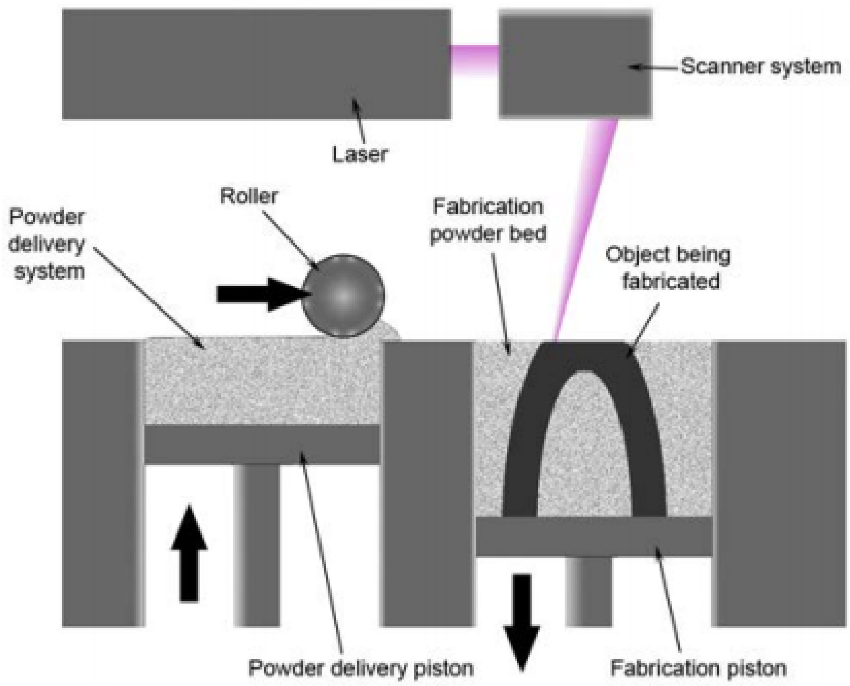

Figure 1.13: Powder bed fusion process [79]

The most commonly used technology in this processes is selective laser sintering (SLS). This technology uses a high power laser to fuse small particles of plastic, metal, ceramic or glass powders into a mass that has the desired 3D shape. The laser selectively fuses the powdered material by scanning the cross sections (or layers) generated by the 3D modeling program on the surface of a powder bed (fig. 1.13). After each cross section is scanned, the powder bed is lowered by one layer thickness. Then a new layer of material is applied on top and the process is repeated until the object is completed. All untouched powder remains as it is and becomes a support structure for the object. All unused powder can be used for the next print.

Besides SLS, other techniques included in powder bed fusion processes are direct metal laser sintering (DMLS), electron beam melting (EBM), selective heat sintering (SHS) and selective laser melting (SLM). Electron beam melting (EBM) methods require a vacuum but can be used with metals and alloys for the creation of functional parts. Direct metal laser sintering (DMLS) is the same as SLS, but with the use of metals and not plastics. The process sinters the powder, layer by layer. Selective Heat Sintering differs from other processes by way of using a heated thermal print head to fuse powder material together. Layers are added with a roller in between fusion of layers. A platform lowers the model accordingly.

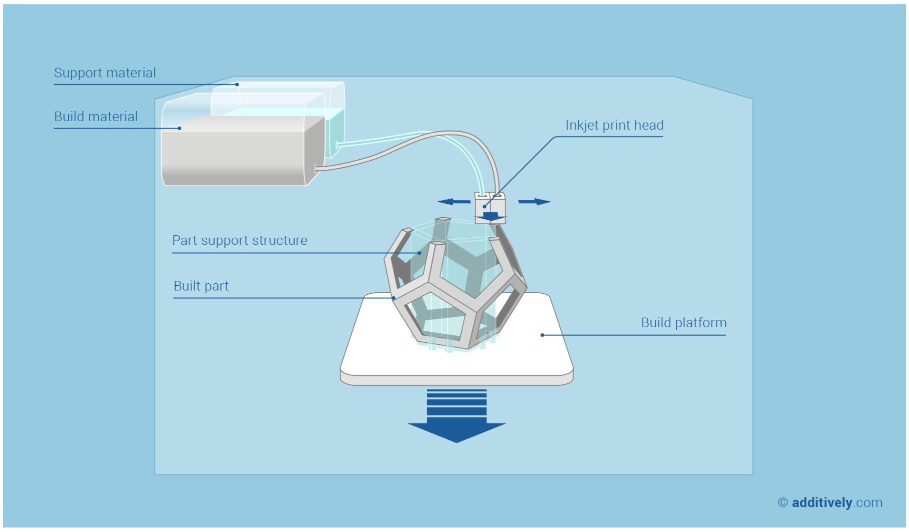

Figure 1.14: Material jetting process [80]

Material jetting

Material jetting creates objects in a similar method to a two dimensional ink jet printer. Material is jetted, using either a continuous or drop on demand (DOD) approach, onto the build surface or platform, where it solidifies and the model is built layer by layer. Material is deposited from a nozzle which moves horizontally across the build platform (fig. 1.14). Machines vary in complexity and in their methods of controlling the deposition of material. The material layers are then cured or hardened using ultraviolet (UV) light. As material must be deposited in drops, the number of materials available to use is limited. Polymers and waxes are suitable and commonly used materials, due to their viscous nature and ability to form drops.

Binder jetting

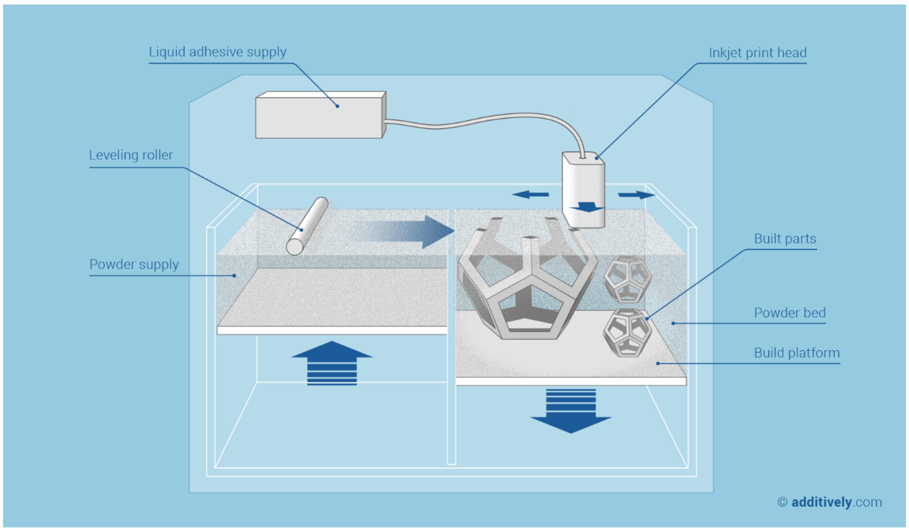

Figure 1.15: Binder jetting process [80]

The binder jetting process uses two materials; a powder based material and a binder. The binder acts as an adhesive between powder layers. The binder is usually in liquid form and the build material in powder form. A print head moves horizontally along the x and y axes of the machine and deposits alternating layers of the build material and the binding material. After each layer, the object being printed is lowered on its build platform (fig. 1.15). After the print is finished, the remaining powder is cleaned off and used for 3D printing the next object. As with other powder based manufacturing methods, the printed object is self-supported within the powder bed and is removed from the unbound powder once completed.

Sheet lamination

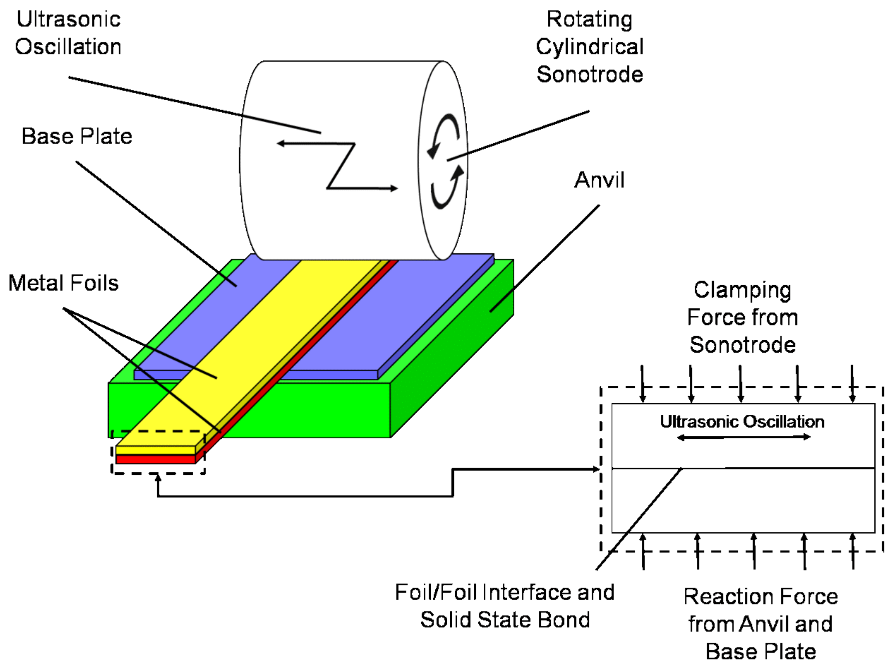

Figure 1.16: Sheet lamination process [81]

Sheet lamination involves material in sheets which is bound together with external force. Sheets can be metal, paper or a form of polymer. Metal sheets are welded together by ultrasonic welding in layers and then CNC milled into a proper shape. Sheet lamination processes include ultrasonic additive manufacturing (UAM) and laminated object manufacturing (LOM).

The ultrasonic additive manufacturing (fig. 1.16) process uses sheets or ribbons of metal, which are bound together using ultrasonic welding. The process does require additional CNC machining and removal of the unbound metal, often during the welding process. Laminated object manufacturing (LOM) uses a similar layer by layer approach but uses paper as material and adhesive instead of welding. The LOM process uses a cross hatching method during the printing process to allow for easy removal post build. Laminated objects are often used for aesthetic and visual models and are not suitable for structural use. UAM uses metals and includes aluminium, copper, stainless steel and titanium. The process is low temperature and allows for internal geometries to be created. The process can bond different materials and requires relatively little energy, as the metal is not melted.

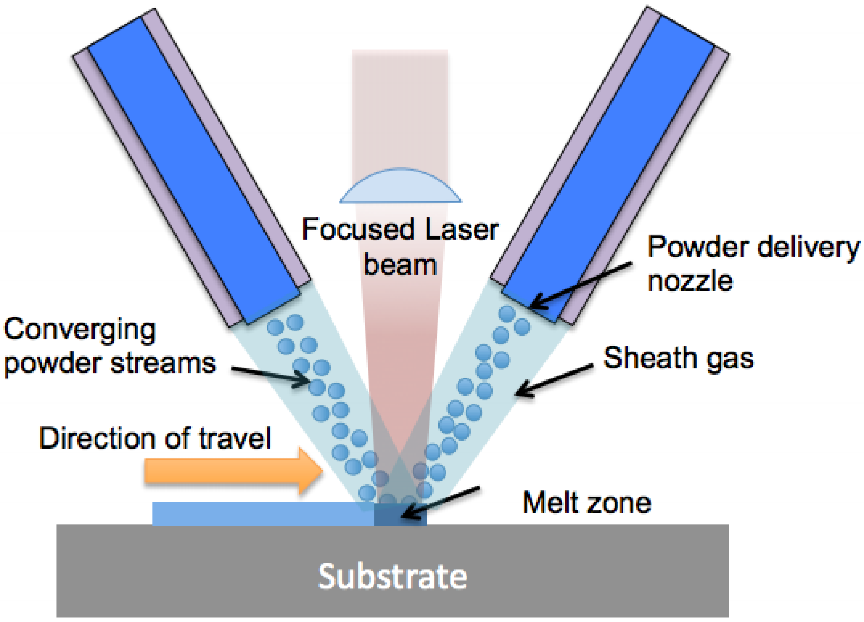

Figure 1.17: Directed energy deposition [79]

Direct energy deposition

This process is mostly used in the high-tech metal industry and in rapid manufacturing applications. It is a more complex printing process commonly used to repair parts, create new ones and add additional material to existing components. A typical DED machine consists of a nozzle mounted on a multi axis arm, which deposits melted material onto the specified surface, where it solidifies (fig. 1.17). The process is similar in principle to material extrusion, but the nozzle can move in multiple directions and is not fixed to a specific axis. The material, which can be deposited from any angle due to 4 and 5 axis machines, is melted upon deposition with a laser or electron beam. The process can be used with polymers, ceramics but is typically used with metals, in the form of either powder or wire.

1.2 FDM - Fused deposition modeling

1.2.1 FDM process

The fused deposition modeling (trademarked by Stratasys) method forms three-dimensional objects from virtual 3D models, which can be obtained from a Computer aided design (CAD) software or from a digital scanning system such as, for example, computer tomography or magnetic resonance imaging. In this process, a thermoplastic is extruded through a nozzle that traces the part's cross sectional geometry layer by layer (fig. 1.18). The build material is usually supplied in filament form, but, rarely, some industrial setups utilize plastic pellets fed from a hopper instead.

The nozzle contains resistive heaters that keep the plastic filament at a temperature just above its glass transition point, bringing it to a semi-molten state, so that it flows easily through the nozzle, which moves horizontally and forms the layer. After flowing from the nozzle, the semi-molten plastic hardens almost immediately and bonds to the layer below. Once an entire layer is completed, the platform shifts down a distance equal of the current layer thickness, and the material laying process repeats as the next layer is deposited. The stacking of these layers eventually results in a solid three-dimensional object. The material deposition path and process parameters for every layer are chosen depending on the material used, the printing conditions, the final purpose of the object and the preferences of the designer [71].

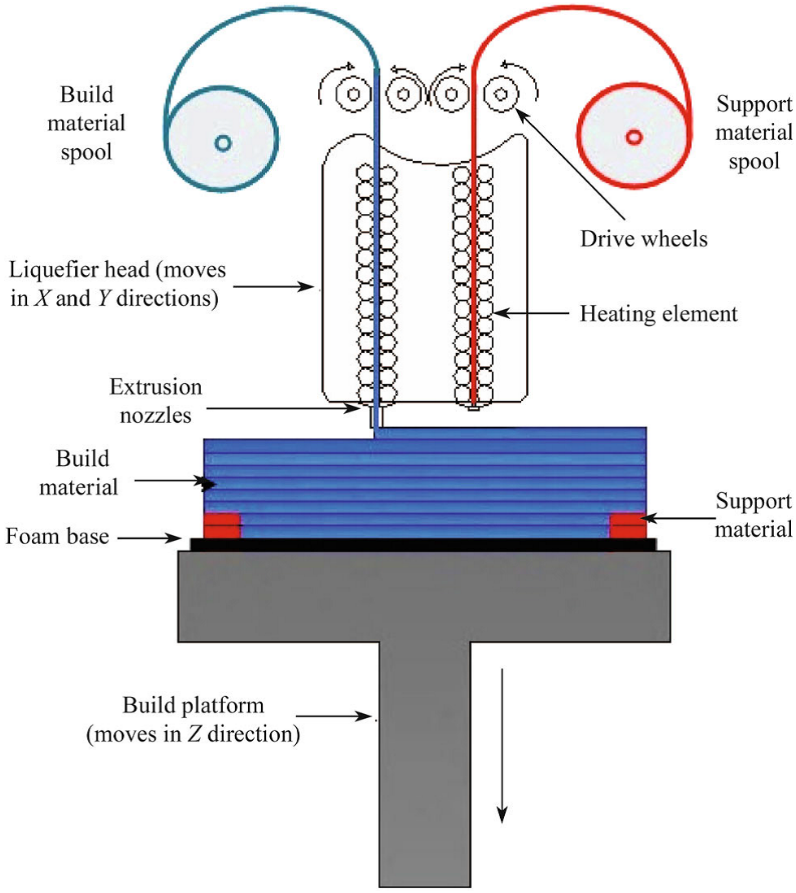

Figure 1.18: Principle of FDM process [47]

In order to be able to print a physical object, i.e. an object in 3 dimensions, a 3D printer needs to be able to move on 3 coordinate axes (namely, x,y and z axes). Nearly every 3D printer is built around the principle that its 3 principal axes are linear. This means that their axes are at right angles to each other and that they move in straight lines (that is: they do not rotate). Machines which use this principle are known as linear robots or cartesian coordinate robots, as opposed to Delta- or Polar-type robots. In order to move along these 3 axes, 3D printers generally make use of fixed rods, timing belts and pulleys, in order to move the print head(s) and or the print platform to the exact position needed. These timing belts and pulleys are connected to small motors, which are generally referred to as "stepper motors". These relatively small motors permit extremely precise movements, often in the vicinity of a fraction of a millimeter. The stepper motors form an important part of any printer, as they are in a great part responsible for the quality of your print, i.e. a cheap stepper motor is not able to realise the same accuracy as more expensive models. Also, when working, they tend to make quite some noise and cheap stepper motors can be especially noisy. However, more recent models have been addressing this particular issue and are far quieter then the older models.

Each printed layer is made of extruded filaments known as “roads” (also called “beads” or “fibers”) deposited in the x and y direction (xy plane) (fig. 1.19). The printed object is composed by two main parts, the internal raster (infill) and its contour (perimeters). The direction of the deposited material is known as raster angle (or fiber angle) and can be set differently for every layer. The ability to create overhanging or hollow features through FDM technology is based on

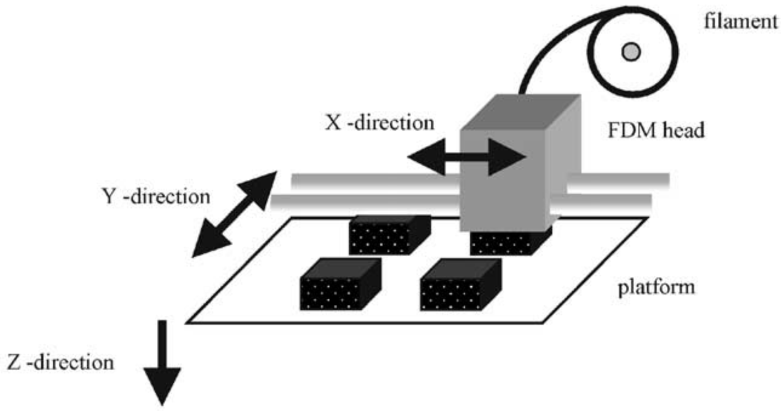

Figure 1.19: Schematic diagram of FDM extrusion directions [71]

Figure 1.20: Chair in transparent PLA with red support material [82]

the application of a support material, which must be deposited directly upon the previous layer (fig. 1.20). The support layers are usually made of chemically-soluble material, to facilitate the removal after the build is complete: the support structures are removed using either a chemical bath (usually with sodium hydroxide and water in an ultrasonic bath) or through mechanical detachment. It is imperative that the printed object must not be soluble by the same chemical solution of the support material, in order not to compromise the printed part. In some hollow features mechanical detachment is not possible, so only the chemical removal is applicable.

The strength of the printed object depends on the deposited material properties and the interface between the filaments, or beads. The interface is important because the neighboring beads are at a lower temperature than the heated bead leaving the nozzle. The temperature between the two materials will melt the existing bead and cause polymers molecule to diffuse across the interface. The strength of this fusion is dependent on many factors such as temperature gradient, glass transition temperature, molecular orientation and bead geometry [3]. It is possible for this fusion to exist under stress prior to any mechanical loading: as the beads start to cool, the polymer contracts which creates a localized residual stress [1]. As the performance of AM materials increases by using semi-crystalline and more rigid polymers, the physics to model interfacial strength and stress are different from amorphous materials. There are additional challenges such as FDM surface roughness, void space between filaments, and various printing defects that can initiate failure modes within the part under loading. The nature of the printing process and the aligned structure of the beads make AM parts highly anisotropic and this anisotropy may exhibit a non-linear dependence on processing parameters.

1.2.2 FDM process parameters

Nowadays, additive manufacturing processes, including FDM process, have to meet specific requirements, such as superior quality of the 3D-printed object, guaranteed safety, high productivity rate, short fabrication time and low production cost. Additive manufacturing process conditions must be determined first, in order to meet the customer needs. The additive manufacturing process outcome highly depends on the proper choice of the process parameters. Reduction of build time and material consumption without compromising the mechanical properties is a major concern in most industrial applications.

There is a multitude of process parameters involved in FDM technology, some of them more impactful than others on the mechanical properties of FDM printed parts. A list of the main process parameters is shown below:

- Raster orientation (raster angle): it is angle θ between the deposition direction of the beads of material and the loading direction (x) (fig. 1.21). Can vary layer by layer. Different raster angle orientations greatly affect the mechanical properties of the part, including helping it to become more isotropic and/or tougher.

- Infill pattern (fig. 1.22): how the internal structure will be printed; there are many geometrical patterns available, such as, rectilinear, linear, concentric, honeycomb, etc.

- Infill density (fig. 1.23): refers to the volume density of material that will be printed inside the object. A sparse infill requires less build time, but the mechanical properties of the printed part decrease, while a dense infill takes much more time to be completed, but the mechanical properties improve [2].

- Road (bead) width: it is the width of each printed bead of material that the FDM nozzle deposits (fig. 1.24).

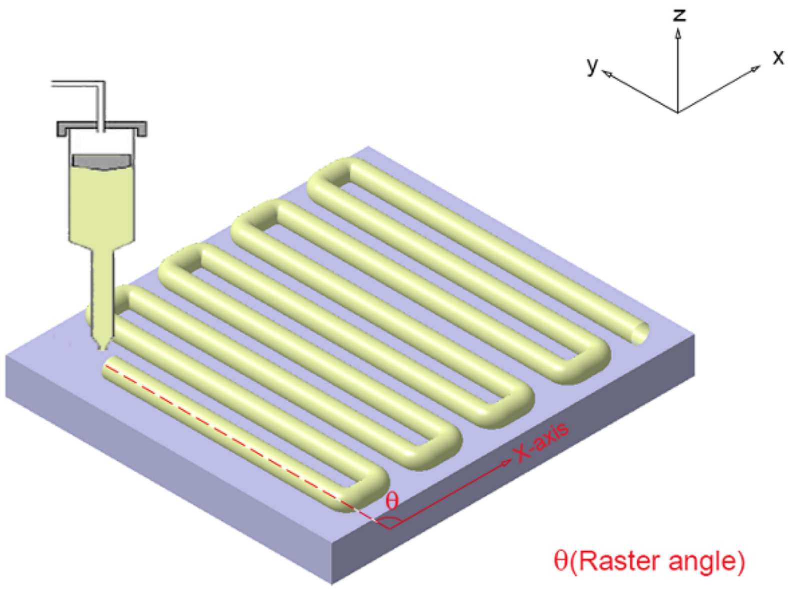

Figure 1.21: Raster orientation [83]

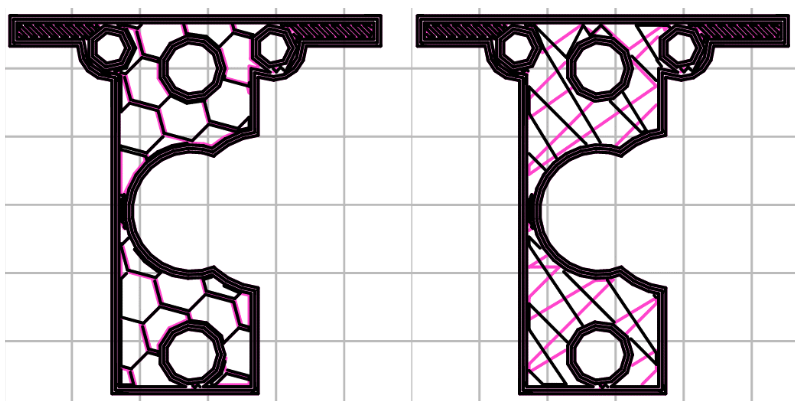

Figure 1.22: Infill pattern comparison: honeycomb pattern to the left, linear pattern to the right [84]

- Layer thickness: it is the thickness of each layer and it is the step along the vertical axis (direction z) taken before extruding a new layer atop the previous one.

- Gap between beads: it is the space between the beads of the FDM material. Ideally, if the infill density is 100%, the gap should be zero, meaning that the beads just touch in a single point (which should be, ideally, at half the current layer thickness). Diminishing fill density, layer thickness or extrusion width can leave a positive gap, which means that adjacent beads of material do not touch one another. A positive gap means less material and less build time required, but the mechanical properties are inferior [2]. A negative gap means that two adjacent beads partially occupy the same space (fig. 1.24). The result will be a denser, tougher structure, even if the build time and material consumption increase [2].

- Print speed: increasing print speed shortens the time required to produce the desired object. An additional benefit is that a faster travel movement, between extrusions, can reduce the effects of oozing. Too much printing speed may compromise the integrity of the structure

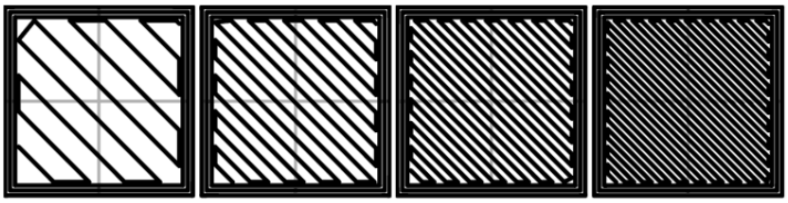

Figure 1.23: Infill pattern at varying densities [84]

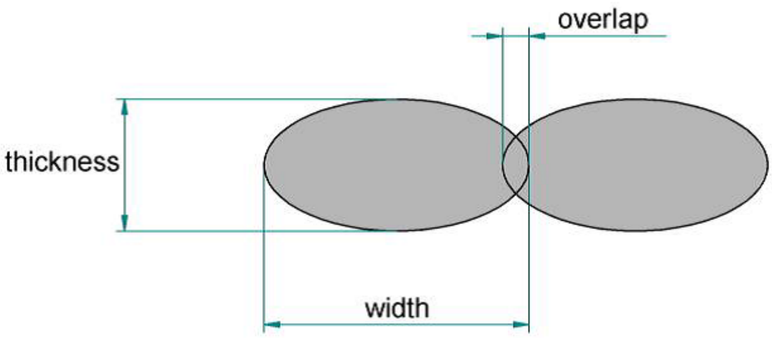

Figure 1.24: Overlapping of two fibers

and faster extrusions decrease the object's strength, thus can break and result in weak spots [17]. Support structures may be printed faster, since later will be removed. On the contrary the first layer must printed at a much slower pace, to avoid the object detachment from the printing bed.

- Extruder, bed and chamber temperature: extruder temperature must be set to the correct value in order to bring the material to a semi-molten state and to allow its extrusion through the nozzle. Bed temperature increases the adhesion of the extruded material to the printing surface and it's crucial for the first layer [84]. Chamber temperature helps discharging eventual residual tensions that may appear in the object during and/or after the printing procedure.

- Air gap: it's the distance, in the z direction, between the object and the support interface. Too much air gap makes the mechanical detachment between object and support much easier, but greatly compromises its structure, considerably weakening it. A lower air gap strengthens the structure, but the detachment may be difficult, with the risk of damaging and even breaking the object.

- Z-offset: it's the distance, in the z direction, between the object and the printing bed. It's very important to correctly set this parameter, since a too much high value involves the risk of the detachment of the object from the printing bed, compromising the entire structure.

- Perimeters: the presence of perimeters can reinforce the integrity of the product. Multiple perimeters can be printed, usually no more than three.

- Nozzle diameter: it plays an important role in the print resolution of your object. The smaller the nozzle, the finer the print, but the longer it will take to complete.

- Flowrate: it's the volume of material that is extruded from the nozzle in a unit of time (usually seconds). It can be calculated using the following equation:

$$f = tws \tag{1.1}$$

where:

- f is the flowrate.
- t is the layer thickness.
- w is the extrusion width.
- s is the printing speed.

1.2.3 FDM printing phases: from the model to the physical object

The process to obtain a physical, tangible, 3D printed object can be summarized in three main, distinct phases:

- Modeling
- Printing
- Finishing

Modeling phase

The first step consists in the creation of the 3D model that will be subsequently printed. The model must describe the external of the object and can be obtained in two ways: through the use of a CAD (Computer Aided Design) software or through reverse engineering equipment (e.g. laser or optical scanning). Some software may provide some hint as to the structural integrity you can expect in the finished product, too, using scientific data about certain materials to create virtual simulations of how the object will behave under certain conditions. After finishing the 3D model, the CAD drawing must be saved/converted to STL file format (e.g. test01.stl).

STL file format The STL extension (STL is an acronym for standard tessellation language) is a file format developed by 3D Systems in 1987 for use by its stereolithography apparatus machine. The STL format describes the external surfaces of the original CAD model and forms the basis for calculation of the slices. STL file, as the de facto standard, has been used as a connection linking CAD model design and prototype fabrication in many systems [18]. The STL file is created from the CAD database via an interface on the CAD system. It consists of a mesh of triangular facets representing the outside shell of the solid object, where each triangular facet shares the sides with adjacent elements and the vertices are ordered by the right-hand rule (fig. 1.25). It also consists of the x, y and z coordinates of the three vertices of each surface triangle, with an index to describe the orientation of the normal surface [43]. Essentially an STL file consists of a list of facet data. Each facet is uniquely identified by a unit normal and three vertices. The normal and each vertex are specified by three coordinates each, so there is a total of 12 numbers stored for each facet. The facets define the surface of a 3-dimensional object. As such, each facet is part of the boundary between the interior and the exterior of the object. The orientation of the facets is specified redundantly in two ways which must be consistent. First, the direction of the normal is outward. Second, the vertices are listed in counterclockwise order when looking at the object from the outside (right-hand rule). Moreover each triangle must share two vertices with each of its adjacent triangles. In other words, a vertex of one triangle cannot lie on the side of another. All vertex coordinates must be positive-define (nonnegative and nonzero) numbers.

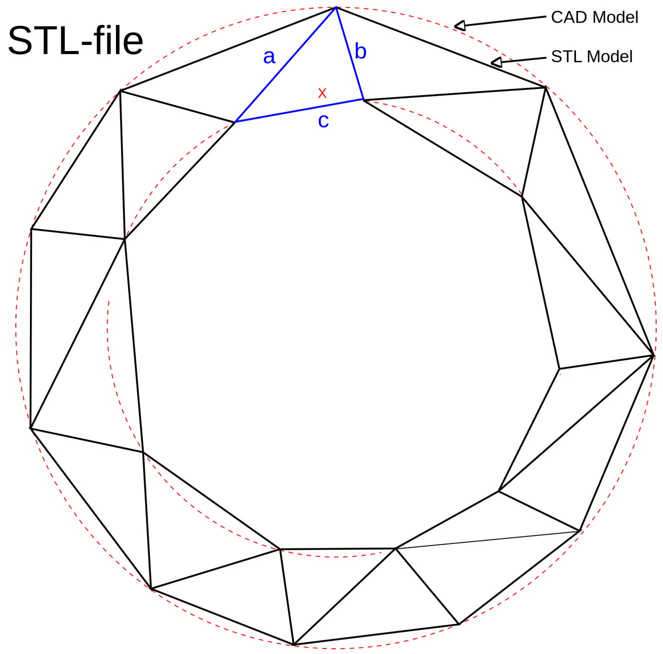

Figure 1.25: Difference between CAD and STL geometries [85]

The representations of color, texture or other common CAD model attributes are not available in the STL files (fig. 1.26). Furthermore, STL files do not contain any scale information, the coordinates are in the arbitrary units. The STL file format specifies in two representations:

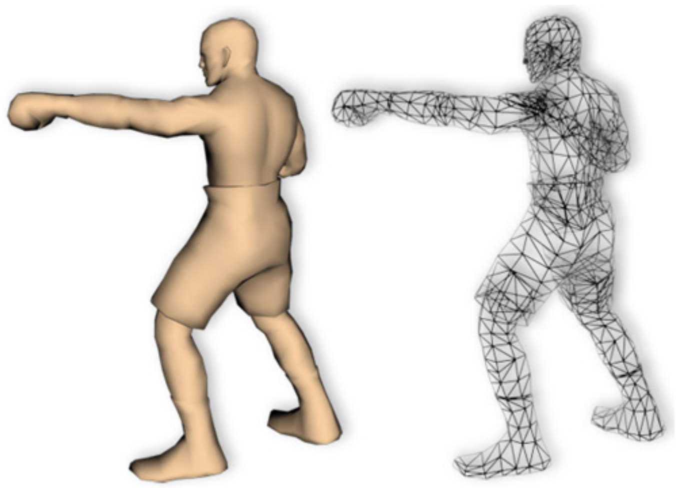

Figure 1.26: CAD model and STL model [86]

ASCII and Binary. Binary files are more common, because they are more compact compared to ASCII files. The ASCII format is primarily intended for testing new CAD interfaces. The syntax for an ASCII STL file is as follows (fig. 1.27): Bold face indicates a keyword. Words in italics are variables which are to be replaced with user-specified values. The numerical data in the facet normal and vertex lines are single precision floats. A facet normal coordinate may have a leading minus sign; a vertex coordinate may not.

```
solid name
    facet normal n_i n_j n_k
        outer loop
            vertex v1 v1 v1
            vertex v2 v2 v2
            vertex v3 v3 v3
        endloop
    endfacet
endsolid name
```

Figure 1.27: STL ASCII file format [87]

The binaryformat uses the IEEE integer and floating point numerical representation. The syntax for a binary file is as follows (fig. 1.28): The header record consists of 84 bytes, the first

Byte	Data type	Description
80	ASCII	Header. No data significance
4	unsigned long integer	Number of facets in file
4	float	*i* for normal
4	float	*j*
4	float	*k*
4	float	*x* for vertex 1
4	float	*y*
4	float	*z*
4	float	*x* for vertex 2
4	float	*y*
4	float	*z*
4	float	*x* for vertex 3
4	float	*y*
4	float	*z*
2	unsigned integer	Attribute byte count

Figure 1.28: STL binary file format [87]

eighty are used for information about the file, author's name and other miscellaneous comments, the last 4 bytes represent the number of triangular facets. Next, for each facet, 50 bytes are used to represent the x, y and z components of the normal to the facets, then the x, y and z coordinates of each vertex of the triangle. 4 bytes are used for each coordinate, resulting is 48 bytes per facet. The last two bytes are not used. The attribute syntax is not documented in the formal specification. It is specified that the attribute byte count should be set to zero.

The main advantage of the STL file lies in its simplicity, since everything is described using triangles, the most basic planar entities. It can also make the process robust and reliable to get the correct result the first time. However, several problems still afflict STL to date, owing to the very nature of STL files as they contain no topological data [18]. Many commercial tessellation algorithms used by CAD vendors today are also not robust, and as a consequence, they tend to create polygonal approximation models which may exhibit many types of errors, such as gaps, degenerate facets, overlapping, non-manifold topology conditions. Additionally, STL files are not compatible for all the RP devices, in terms of solid model construction, programs may vary from business to business. Some systems can accept the STL files directly, whereas others require pre-processing. Although STL format is not perfect for the RP, it is still being widely used around the world.

Once the STL file is obtained, a necessary passage (at least for complex structures) is to check the possible presence of defects, such as holes, boundary edges and invalid triangle orientation, before loading it in the slicer software. A commonly used software that controls and solves these errors is Netfabb, which exists in two main versions, basic and professional (fig. 1.29). After

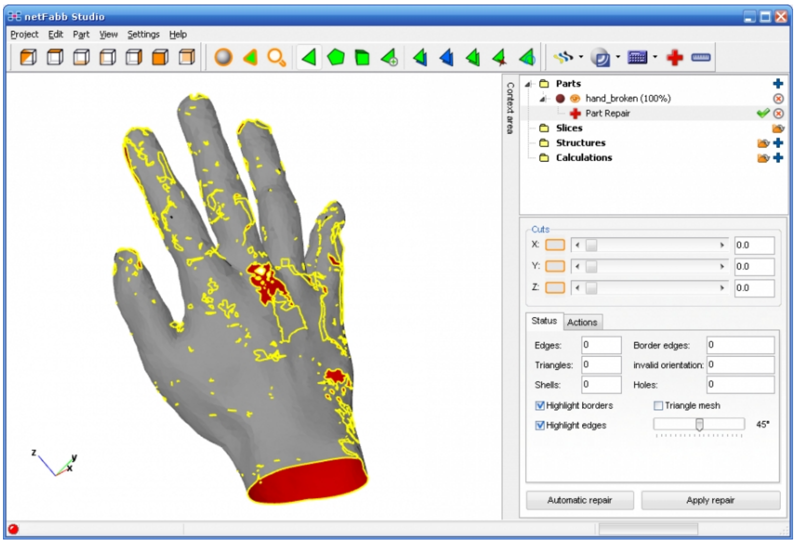

Figure 1.29: Netfabb software: repairing the defects [88]

checking and eventually repairing the STL file, it is ready to be loaded in the slicer software.

Printing phase

Once the STL file is ready, the next step is to load it in a slicing software, which slices it at a particular orientation. The STL model slicing procedure is to generate a series of closely spaced 2D cross sections of a 3D model. The distance between every two cross sections or layers is Z-thickness, which can be specified. The actual thickness varies, and depends on the accuracy requirements and the properties of different materials. The slicing the STL file is an approximate procedure. The main error, which is known as stair-case effect, occurs in this stage and also leads to rough surfaces.

At the beginning of the slicing process, a model in the STL format file is properly oriented and positioned. A series of parallel flat planes are introduced directly to slice the STL file. The distance between every adjacent plane is equal to the thickness of the filament or the curing depth of the photo/heat-sensitive resin or powder layers. As the STL file is a triangular-facet model, contains no extra information about the inner details of the model. The parallel planes cut through the triangulated surfaces of the model, getting the layer contour information. The outcome of the slicing process is a series of contour curves, formed by connecting the intersection points. Since all the facets are planar triangles and all the curves are made of line sections, the slicing process is to get the intersection points. The coordinates of the intersection points are recorded down for the tool path generation. However, it is a time-consuming task, and might waste a great deal of time while dealing with redundant or erroneous information.

Before beginning the slicing operation a great variety of parameters can be set, such as raster orientation, infill density, extrusion width, layer thickness, the temperatures, etc., which greatly affect the final outcome. Thus, to achieve a good printing quality, it is necessary to correctly set the parameter values. Once the parameters are correctly set, the slicing operation can be initiated: its output is a text file, which contains a machine language called G-code (while it is a text file, its extension is ".gcode").

G-code G-code is the common name for the most widely used numerical control (NC) programming language. It is used mainly in computer-aided manufacturing to control automated machine tools. G-code defines instructions on where to move, how fast to move, and what path to move. The most common situation is that, within a machine tool, a cutting tool is moved according to these instructions through a toolpath and cuts away material to leave only the finished workpiece. The same concept also extends to noncutting tools such as forming or burnishing tools, photoplotting, additive methods such as 3D printing, and measuring instruments (fig. 1.30). G-codes are also called preparatory codes and they generally tell the machine tool what type of action to perform, such as:

- Rapid movement (transport the tool as quickly as possible through space to the location where it will cut)
- Controlled feed in a straight line or arc
- Series of controlled feed movements that would result in a hole being bored, a workpiece cut (routed) to a specific dimension, or a profile (contour) shape added to the edge of a workpiece
- Set tool information such as offset
- Switch coordinate systems

Students and hobbyists have pointed out over the years that the term "G-code" is imprecise. It comes from the literal sense of the term, referring to one letter address (G) and to the specific codes that can be formed with it (for example, G00, G01, G28). But every letter of the English alphabet is used somewhere in the language: for example, the letter M indicates miscellaneous functions, such as the temperature values to be set for extruder, print-bed and chamber. Nevertheless, "G-code" is established as the common name of the language. Once the G-code is created from the slicing procedure, the physical printing begins. Printing time depends on a multitude of factors, such as the dimensions and the complexity of the object, the printing speed, the layer thickness, the infill density, the presence of support structures and many others. Once the object is completed, it will be physically removed from the bed.

Finishing phase

The finishing can be considered an optional step, because it involves post-processing operations that are not always required. Supporting features, if used, must be eliminated, through mechanical detachment or through baths in chemical solutions. Furthermore it may be required to smooth the object surface (for example through sanding it), paint it, or other post-processing operations, meant to improve the final quality of the product (fig. 1.31).

```
G1 X272.623 Y95.585 E88.8527 ; infill
G1 X22.874 Y95.585 E93.7723 ; infill
G1 X22.874 Y94.931 E93.7852 ; infill
G1 X272.623 Y94.931 E98.7048 ; infill
G1 X272.623 Y94.278 E98.7177 ; infill
G1 X22.874 Y94.278 E103.6374 ; infill
G1 X22.874 Y93.625 E103.6502 ; infill
G1 X272.623 Y93.625 E108.5699 ; infill
G1 X272.623 Y92.971 E108.5827 ; infill
G1 X22.874 Y92.971 E113.5024 ; infill
G1 X22.874 Y92.318 E113.5152 ; infill
G1 X272.623 Y92.318 E118.4349 ; infill
G1 E113.4349 F2700 ; retract
G92 E0 ; reset extrusion distance
G1 Z2.55 F9000 ; lift Z
G1 X22.874 Y106.69 F9000 ; move to first infill point
G1 Z2.55 F9000 ; restore layer Z
G1 E5 F2700 ; unretract
G1 X272.623 Y106.69 E9.9196 F3000  ; infill
G1 X272.623 Y106.037 E9.9325 ; infill
G1 X22.874 Y106.037 E14.8522 ; infill
G1 X22.874 Y105.383 E14.865 ; infill
G1 X272.623 Y105.383 E19.7847 ; infill
G1 X272.623 Y104.73 E19.7975 ; infill
G1 X22.874 Y104.73 E24.7172 ; infill
G1 X22.874 Y104.077 E24.73 ; infill
G1 X272.623 Y104.077 E29.6497 ; infill
G1 X272.623 Y103.424 E29.6626 ; infill
G1 X22.874 Y103.424 E34.5822 ; infill
G1 X22.874 Y102.77 E34.5951 ; infill
```

Figure 1.30: An example of G-code

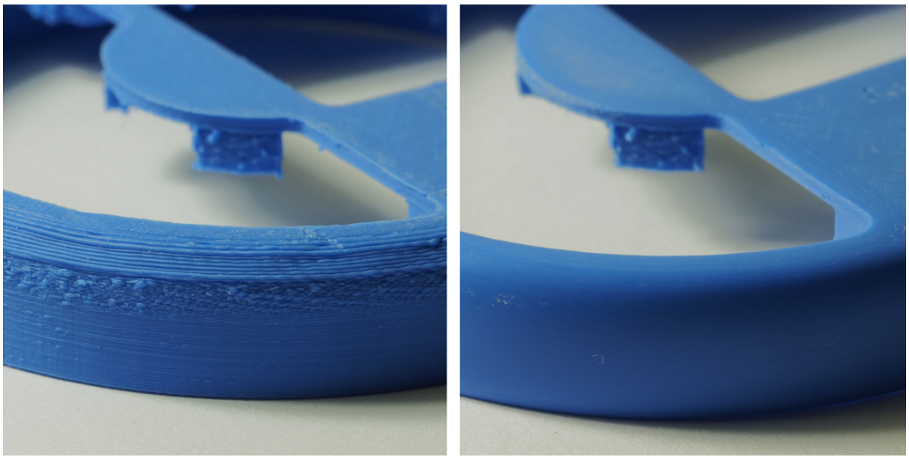

Figure 1.31: Surface smoothing through sanding: before and after [77]

1.3 3D printing materials

In the last decade, the sheer number of materials that can be used for additive manufacturing greatly increased. While at the beginning only polymeric resins and thermoplastics were printed, nowadays many other classes of materials are available, such as ceramics, metals, bio-materials and even food.

1.3.1 Main types of printable materials

A brief summary of the main types of printable materials is shown below:

Plastics Polyamide is commonly used in powder form with the sintering process or in filament form with the FDM process. It is a strong, flexible and durable plastic material that has proved reliable for 3D printing. It is naturally white in colour but it can be coloured — pre- or post printing. This material can also be combined (in powder format) with powdered aluminium to produce another common 3D printing material for sintering — Alumide.

Acrylonitrile Butadiene Styrene (ABS) is another common plastic used for 3D printing, and is widely used on the entry-level FDM 3D printers in filament form. It comes in a wide range of colours and can be bought in filament form from a number of non-propreitary sources, which is another reason why it is so popular (fig. 1.32).

Polylactic Acid (PLA) is a bio-degradable plastic material that has gained traction with 3D printing for this reason. It can be utilized in resin format for DLP/SL processes as well as in filament form for the FDM process. It is offered in a variety of colours. However it is not as durable or as flexible as ABS, but it is stronger. PLA-based filaments can be charged with other materials wood fibers, metallic powders and carbon fibers

Resins are also being used in 3D Printing, although design freedom is limited due to the structure necessary to support the objects during the printing process. Resins are usually in liquid phase and are then hardened through laser or other light sources (fig. 1.33).

Figure 1.32: 3D printed action figure through FDM process: pre-processed (left) and post-processed (right) [89]

Metals A growing number of metals and metal composites are used for industrial grade 3D printing. The most common are aluminium, steel, cobalt derivatives and titanium alloys. One of the strongest and therefore most commonly used metals for 3D printing is stainless steel in powder form for the sintering/melting/EBM processes. It is naturally silver, but can be plated with other materials to give a gold or bronze effect. In the last years gold and silver have been added to the range of metal materials that can be 3D printed directly, with obvious applications across the jewellery sector. These are both very strong materials and are processed in powder form. Titanium is one of the strongest possible metal materials for high temperature applications,

Figure 1.33: Dental arch in polymeric hardened resin [89]

it is biocompatible and has been used for 3D printing industrial applications for some time (fig. 1.34). Supplied in powder form, it can be used for the sintering/melting/EBM processes.

Figure 1.34: Additive manufactured implant made of a biocompatible titanium alloy [89]

Ceramics Ceramics are a relatively new group of materials that can be used for 3D printing with various levels of success (fig. 1.35). The particular thing to note with these materials is that, post printing, the ceramic parts need to undergo the same processes as any ceramic part made using traditional methods of production — namely firing and glazing.

Paper Standard A4 copier paper is a 3D printing material employed by the proprietary SDL process supplied by Mcor Technologies (fig. 1.36). The company operates a notably different business model to other 3D printing vendors, whereby the capital outlay for the machine is in the

Figure 1.35: 3D printed ceramic coffee cup [90]

mid-range, but the emphasis is very much on an easily obtainable, cost-effective material supply, that can be bought locally. 3D printed models made with paper are safe, environmentally friendly, easily recyclable and require no post-processing.

Figure 1.36: Topographical map, 3D printed in full colour by the Mcor paper 3D printer [91]

Bio-materials There is a huge amount of research being conducted into the potential of 3D printing bio materials for a host of medical (and other) applications. Living tissue is being investigated at a number of leading institutions with a view to developing applications that include printing human organs for transplant, as well as external tissues for replacement body parts (fig. 1.37).

Food Experiments with extruders for 3D printing food substances has increased dramatically over the last couple of years. Chocolate is the most common (and desirable) (fig. 1.38). There are also printers that work with sugar and some experiments with pasta and meat. Looking to the

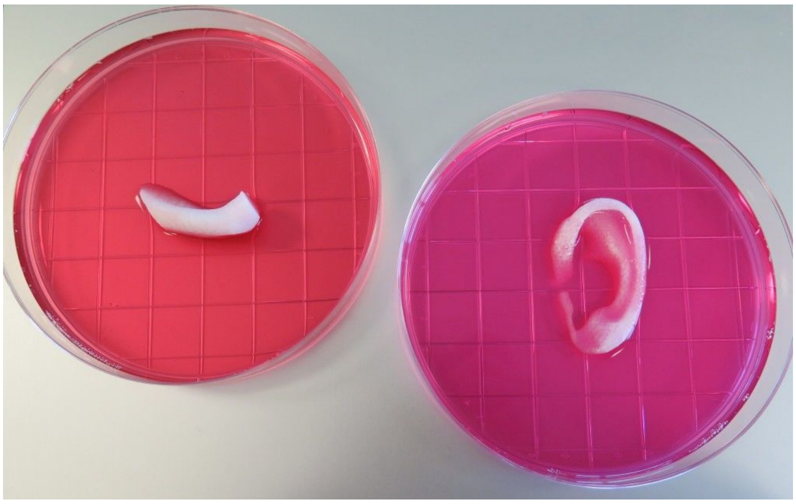

Figure 1.37: Completed ear and jaw bone structures [92]

future, research is being undertaken, to utilize 3D printing technology to produce finely balanced whole meals.

Figure 1.38: 3D printed chocolate roses [93]

Chapter 2

Constitutive modeling

2.1 Theoretical background

To describe the mechanical response of the 3D printed sample, two constitutive models have been considered:

- Classical Lamination Theory (for elastic behavior modeling).
- Tsai-Hill failure criterion (for strength modeling).

When it comes to model the mechanical behavior of a 3D printed material as function of process parameters, the number of studies is fairly low, with a slight increase only in the past few years. Despite this, Classical Lamination and Tsai-Hill theories have already been considered by other researchers, in previous studies. Kulkarni and Dutta [39] adopted the composite laminates theory to extract the elastic moduli of FDM printed parts. Bertoldi *et al.* [11] assumed orthotropic material symmetry of FDM prototypes and determined the material's stiffness and strength values for various raster orientations. Significant differences in the average tensile strength and modulus, depending on the specimen orientation, have been found, as well as differences in the failure mode. Rodriguez *et al.* [54] characterized the mechanical behavior of fused deposited ABS through laminate theory and used Tsai-Hill theory to describe the strength response. Li *et al.* [42] used Classical Lamination Theory to analyze FDM prototypes with locally controlled properties.

2.1.1 Classical Lamination Theory

In this section the elastic behavior of the composite material will be described through stress-strain relations, going from a three dimensional state to a two dimensional state of the composite laminate. The effects of ply (lamina) orientation will be analyzed, with corresponding transformations between generic cartesian and material coordinates. The analysis determines the conditions required, to be satisfied by the plies, in order to constitute a laminate. If the laminate meets the required conditions, classical theory can be appropriately applied. Classical Lamination Theory (CLT) aims to find effective and realistic simplifying assumptions that reduce the three dimensional elastic problem to a two dimensional one. It determines the response of the laminate to forces and moments acting on the laminate by applying the hypotheses of thin laminates, where a number of deformed geometrical occurrences are assumed.

The stiffness matrix

The generalized Hooke's Law relating stresses to strains can be written as the following expression:

$$\sigma_{ij} = C_{ijkl}\varepsilon_{kl}, \tag{2.1}$$

where:

- σ_{ij} are the stress components.
- ε_{kl} are the strain components.
- C_{ijkl} is the 6x6 stiffness matrix relating stresses to strains.

The stress-strain relationship and the corresponding stiffness matrix for the anisotropic, or triclinic (no planes of symmetry for the material properties), linear elastic case are shown, in Voigt notation, in equation (2.2):

$$\begin{bmatrix}\sigma_{11}\\ \sigma_{22}\\ \sigma_{33}\\ \tau_{12}\\ \tau_{13}\\ \tau_{23}\end{bmatrix} = \begin{bmatrix} C_{1111} & C_{1122} & C_{1133} & C_{1112} & C_{1113} & C_{1123}\\ C_{1122} & C_{2222} & C_{2233} & C_{2212} & C_{2213} & C_{2223}\\ C_{1133} & C_{2233} & C_{3333} & C_{3312} & C_{3313} & C_{3323}\\ C_{1112} & C_{2212} & C_{3312} & C_{1212} & C_{1213} & C_{1223}\\ C_{1113} & C_{2213} & C_{3313} & C_{1213} & C_{1313} & C_{1323}\\ C_{1123} & C_{2223} & C_{3323} & C_{1223} & C_{1323} & C_{2323}\end{bmatrix} \begin{bmatrix}\varepsilon_{11}\\ \varepsilon_{22}\\ \varepsilon_{33}\\ 2\gamma_{12}\\ 2\gamma_{13}\\ 2\gamma_{23}\end{bmatrix}. \tag{2.2}$$

The stiffness matrix itself is symmetric [35], thus only 21 of the 36 elastic constants are independent. Depending on the material type, different extents of symmetry of material properties occur and further reductions in the number of elastic constants in the stiffness matrix occur. Written in the material coordinates, the stiffness matrix becomes as shown below (2.3). This matrix defines an orthotropic material, which is essential in the composite laminates analysis.

$$\begin{bmatrix}\sigma_{11}\\ \sigma_{22}\\ \sigma_{33}\\ \tau_{12}\\ \tau_{13}\\ \tau_{23}\end{bmatrix} = \begin{bmatrix} C_{1111} & C_{1122} & C_{1133} & 0 & 0 & 0\\ C_{1122} & C_{2222} & C_{2233} & 0 & 0 & 0\\ C_{1133} & C_{2233} & C_{3333} & 0 & 0 & 0\\ 0 & 0 & 0 & C_{1212} & 0 & 0\\ 0 & 0 & 0 & 0 & C_{1313} & 0\\ 0 & 0 & 0 & 0 & 0 & C_{2323}\end{bmatrix} \begin{bmatrix}\varepsilon_{11}\\ \varepsilon_{22}\\ \varepsilon_{33}\\ 2\gamma_{12}\\ 2\gamma_{13}\\ 2\gamma_{23}\end{bmatrix}. \tag{2.3}$$

The compliance matrix

To resolve the elastic material behavior, the inverse of the previous stress-strain relation (eq. (2.1)) is defined such that:

$$\varepsilon_{ij} = S_{ijkl}\sigma_{kl}, \tag{2.4}$$

where S_{ijkl} is the compliance matrix, which contains more reduced expressions of the elastic constants. The 6x6 symmetric [35] compliance matrix is shown in eq. (2.5):

$$\begin{bmatrix}\varepsilon_{11}\\ \varepsilon_{22}\\ \varepsilon_{33}\\ \gamma_{12}\\ \gamma_{13}\\ \gamma_{23}\end{bmatrix} = \begin{bmatrix} S_{1111} & S_{1122} & S_{1133} & S_{1112} & S_{1113} & S_{1123}\\ S_{1122} & S_{2222} & S_{2233} & S_{2212} & S_{2213} & S_{2223}\\ S_{1133} & S_{2233} & S_{3333} & S_{3312} & S_{3313} & S_{3323}\\ S_{1112} & S_{2212} & S_{3312} & S_{1212} & S_{1213} & S_{1223}\\ S_{1113} & S_{2213} & S_{3313} & S_{1213} & S_{1313} & S_{1323}\\ S_{1123} & S_{2223} & S_{3323} & S_{1223} & S_{1323} & S_{2323}\end{bmatrix} \begin{bmatrix}\sigma_{11}\\ \sigma_{22}\\ \sigma_{33}\\ \tau_{12}\\ \tau_{13}\\ \tau_{23}\end{bmatrix}. \tag{2.5}$$

For an anisotropic material, there exists a significant coupling effect between the applied stress and the resulting deformation. S_{1111}, S_{2222} and S_{3333} represent the coupling due to the individual applied stresses σ_{11}, σ_{22} and σ_{33}, respectively, in the same direction. S_{1212}, S_{1313} and S_{2323} are the shear strain responses caused by the applied shear stress in the same plane. S_{1122}, S_{1133} and S_{2233} represent the extension-extension coupling, i.e. the coupling between distinct normal stresses and normal strains, also known as Poisson effect. S_{1112}, S_{1113}, S_{1123}, S_{2212}, S_{2213}, S_{2223}, S_{3312}, S_{3313} and S_{3323} feature the shear-extension coupling, or a more complex coupling of the normal strain response to applied shear stress. S_{1213}, S_{1223} and S_{1323} represent shear-shear coupling, that is the shear strain response to shear stress applied in another plane. The remaining terms of compliance matrix are a result of symmetry. For an orthotropic material, the compliance matrix becomes as shown in eq. (2.6):

$$\begin{bmatrix} \varepsilon_{11} \\ \varepsilon_{22} \\ \varepsilon_{33} \\ \gamma_{12} \\ \gamma_{13} \\ \gamma_{23} \end{bmatrix} = \begin{bmatrix} S_{1111} & S_{1122} & S_{1133} & 0 & 0 & 0 \\ S_{1122} & S_{2222} & S_{2233} & 0 & 0 & 0 \\ S_{1133} & S_{2233} & S_{3333} & 0 & 0 & 0 \\ 0 & 0 & 0 & S_{1212} & 0 & 0 \\ 0 & 0 & 0 & 0 & S_{1313} & 0 \\ 0 & 0 & 0 & 0 & 0 & S_{2323} \end{bmatrix} \begin{bmatrix} \sigma_{11} \\ \sigma_{22} \\ \sigma_{33} \\ \tau_{12} \\ \tau_{13} \\ \tau_{23} \end{bmatrix}, \tag{2.6}$$

where the number of independent elastic constants is reduced from 21 to 9. If the orthotropic material is also transversely isotropic, then the number of independent elastic constants is further reduced from 9 to 5, as shown in eq (2.7):

$$\begin{bmatrix} \varepsilon_{11} \\ \varepsilon_{22} \\ \varepsilon_{33} \\ \gamma_{12} \\ \gamma_{13} \\ \gamma_{23} \end{bmatrix} = \begin{bmatrix} S_{1111} & S_{1122} & S_{1122} & 0 & 0 & 0 \\ S_{1122} & S_{2222} & S_{2233} & 0 & 0 & 0 \\ S_{1122} & S_{2233} & S_{2222} & 0 & 0 & 0 \\ 0 & 0 & 0 & S_{1212} & 0 & 0 \\ 0 & 0 & 0 & 0 & S_{1212} & 0 \\ 0 & 0 & 0 & 0 & 0 & 2(S_{2222} - S_{2233}) \end{bmatrix} \begin{bmatrix} \sigma_{11} \\ \sigma_{22} \\ \sigma_{33} \\ \tau_{12} \\ \tau_{13} \\ \tau_{23} \end{bmatrix}. \tag{2.7}$$

In relation to more realistic cases of engineering problems of thin plate elements, the 2D case of in-plane stress of the lamina is characterized by the reductions shown in eq. (2.8):

$$\sigma_{33} = \tau_{23} = \tau_{13} = 0. \tag{2.8}$$

In-plane stress state objects are characterized by a significantly lower dimension, usually thickness, than the other two dimensions, namely width and length (fig. 2.1). This simplification reduces the 6x6 stiffness matrix to a 3x3 one (eq. (2.9)). The reduced stress-strain relations are:

$$\begin{bmatrix} \varepsilon_{11} \\ \varepsilon_{22} \\ \gamma_{12} \end{bmatrix} = \begin{bmatrix} S_{1111} & S_{1122} & 0 \\ S_{1122} & S_{2222} & 0 \\ 0 & 0 & S_{1212} \end{bmatrix} \begin{bmatrix} \sigma_{11} \\ \sigma_{22} \\ \tau_{12} \end{bmatrix}. \tag{2.9}$$

Simplifying the tensorial notation, eq. (2.9) becomes:

$$\begin{bmatrix} \varepsilon_{1} \\ \varepsilon_{2} \\ \gamma_{12} \end{bmatrix} = \begin{bmatrix} S_{11} & S_{12} & 0 \\ S_{12} & S_{22} & 0 \\ 0 & 0 & S_{33} \end{bmatrix} \begin{bmatrix} \sigma_{1} \\ \sigma_{2} \\ \tau_{12} \end{bmatrix}. \tag{2.10}$$

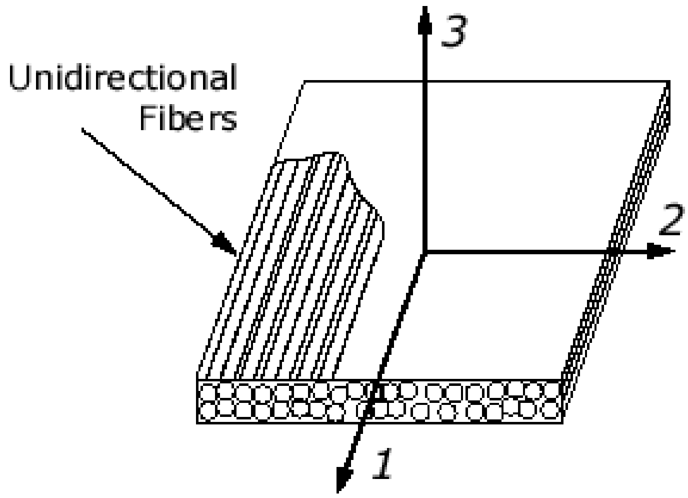

Figure 2.1: Coordinates of an unidirectional reinforced lamina [94]

There are only 5 elastic constants, of which only 4 are independent. The orthotropic compliance matrix components, in terms of elastic constants, are:

$$S_{11} = \frac{1}{E_1}, \qquad S_{22} = \frac{1}{E_2}, \qquad S_{12} = S_{21} = -\frac{\nu_{21}}{E_2} = -\frac{\nu_{12}}{E_1}, \qquad S_{33} = \frac{1}{G_{12}}, \tag{2.11}$$

where:

- E_1 is longitudinal Young's modulus.
- E_2 is transverse Young's modulus.
- ν_{12} is major Poisson's ratio.
- ν_{21} is minor Poisson's ratio.
- G_{12} is shear modulus.

The resulting stiffness matrix will be:

$$\begin{bmatrix} \sigma_1 \\ \sigma_2 \\ \tau_{12} \end{bmatrix} = \begin{bmatrix} Q_{11} & Q_{12} & 0 \\ Q_{12} & Q_{22} & 0 \\ 0 & 0 & Q_{33} \end{bmatrix} \begin{bmatrix} \varepsilon_1 \\ \varepsilon_2 \\ 2\gamma_{12} \end{bmatrix}, \tag{2.12}$$

where Q_{ij} are the reduced stiffnesses of the lamina that are related to the compliance matrix components and elastic constants by the following equations:

$$Q_{11} = \frac{S_{22}}{S_{11}S_{22} - S_{12}^2} = \frac{E_1}{1 - \nu_{12}\nu_{21}}, \tag{2.13a}$$

$$Q_{22} = \frac{S_{11}}{S_{11}S_{22} - S_{12}^2} = \frac{E_2}{1 - \nu_{12}\nu_{21}}, \tag{2.13b}$$

$$Q_{12} = Q_{21} = \frac{S_{12}}{S_{11}S_{22} - S_{12}^2} = \frac{\nu_{12}E_2}{1 - \nu_{12}\nu_{21}}, \tag{2.13c}$$

$$Q_{33} = \frac{1}{S_{33}} = G_{12}. \tag{2.13d}$$

Lamina orientation

It is useful to move between the generic cartesian coordinates (x,y) and the material coordinates (1,2) of the lamina and vice-versa. To do that a rotation matrix must be applied, to shift from the generic to the material coordinates; the same, inverted, matrix allows to go from the material coordinates to the generic ones. The transformation equations to go from material coordinates to

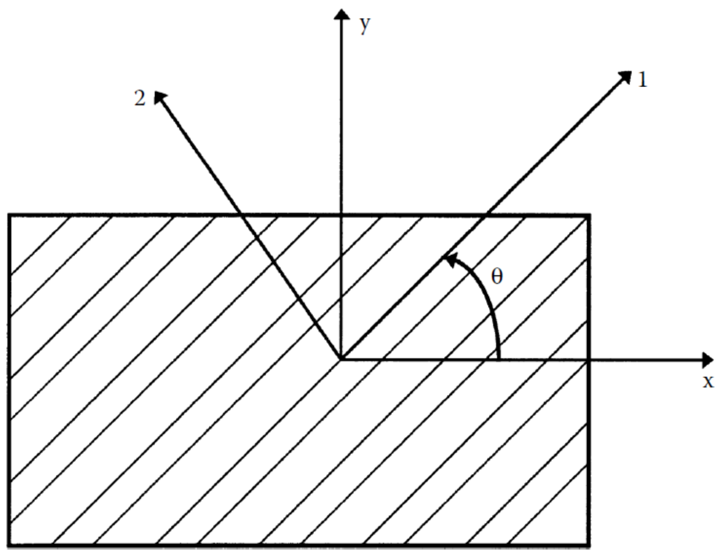

Figure 2.2: Rotation to material coordinates from generic coordinates [35]

generic coordinates for the stress tensor are given by the expression below, where θ is the angle from the x-axis to the 1-axis (fig. 2.2):

$$\begin{bmatrix}\sigma_x\\ \sigma_y\\ \tau_{xy}\end{bmatrix} = \begin{bmatrix} cos^2\theta & sin^2\theta & -2cos\theta sin\theta \\ sin^2\theta & cos^2\theta & 2cos\theta sin\theta \\ cos\theta sin\theta & -cos\theta sin\theta & cos^2\theta - sin^2\theta \end{bmatrix} \begin{bmatrix}\sigma_1\\ \sigma_2\\ \tau_{12}\end{bmatrix}. \tag{2.14}$$

The 3x3 transformation matrix is written as:

$$[T]^{-1} = \begin{bmatrix} c^2 & s^2 & -2cs \\ s^2 & c^2 & 2cs \\ cs & -cs & c^2 - s^2 \end{bmatrix}, \tag{2.15}$$

where:

- $c = cos^2\theta$.
- $s = sin^2\theta$.

The same transformation matrix can be applied to the strain tensor. The expressions, both for stress and strain tensor, in short are written as:

$$\begin{bmatrix}\sigma_x\\ \sigma_y\\ \tau_{xy}\end{bmatrix} = [T]^{-1}\begin{bmatrix}\sigma_1\\ \sigma_2\\ \tau_{12}\end{bmatrix}, \qquad \begin{bmatrix}\varepsilon_x\\ \varepsilon_y\\ \gamma_{xy}\end{bmatrix} = [T]^{-1}\begin{bmatrix}\varepsilon_1\\ \varepsilon_2\\ \gamma_{12}\end{bmatrix}. \tag{2.16}$$

The transformation equations to go from the generic coordinates to the material coordinates are given from the expression below:

$$\begin{bmatrix} \sigma_1 \\ \sigma_2 \\ \tau_{12} \end{bmatrix} = \begin{bmatrix} cos^2\theta & sin^2\theta & 2cos\theta sin\theta \\ sin^2\theta & cos^2\theta & -2cos\theta sin\theta \\ -cos\theta sin\theta & cos\theta sin\theta & cos^2\theta - sin^2\theta \end{bmatrix} \begin{bmatrix} \sigma_x \\ \sigma_y \\ \tau_{xy} \end{bmatrix}. \tag{2.17}$$

The transformation matrix is written as:

$$[T] = \begin{bmatrix} c^2 & s^2 & 2cs \\ s^2 & c^2 & -2cs \\ -cs & cs & c^2 - s^2 \end{bmatrix}. \tag{2.18}$$

As before the same transformation matrix can be applied to both the strain tensor and the stress tensor, in a more compact form:

$$\begin{bmatrix} \sigma_1 \\ \sigma_2 \\ \tau_{12} \end{bmatrix} = [T] \begin{bmatrix} \sigma_x \\ \sigma_y \\ \tau_{xy} \end{bmatrix}, \qquad \begin{bmatrix} \varepsilon_1 \\ \varepsilon_2 \\ \gamma_{12} \end{bmatrix} = [T] \begin{bmatrix} \varepsilon_x \\ \varepsilon_y \\ \gamma_{xy} \end{bmatrix}. \tag{2.19}$$

Resolving equation (2.17), stresses in material coordinates can be obtained:

$$\sigma_1 = \sigma_x cos^2\theta + \sigma_y sin^2\theta + 2\tau_{xy} cos\theta sin\theta, \tag{2.20a}$$

$$\sigma_2 = \sigma_x sin^2\theta + \sigma_y cos^2\theta - 2\tau_{xy} cos\theta sin\theta, \tag{2.20b}$$

$$\tau_{12} = -\sigma_x cos\theta sin\theta + \sigma_y cos\theta sin\theta + \tau_{xy}(cos^2\theta - sin^2\theta). \tag{2.20c}$$

The same procedure can be applied for strains:

$$\varepsilon_1 = \varepsilon_x cos^2\theta + \varepsilon_y sin^2\theta + 2\gamma_{xy} cos\theta sin\theta, \tag{2.21a}$$

$$\varepsilon_2 = \varepsilon_x sin^2\theta + \varepsilon_y cos^2\theta - 2\gamma_{xy} cos\theta sin\theta, \tag{2.21b}$$

$$\gamma_{12} = -\varepsilon_x cos\theta sin\theta + \varepsilon_y cos\theta sin\theta + \gamma_{xy}(cos^2\theta - sin^2\theta). \tag{2.21c}$$

Transformed stiffness and compliance matrices

Starting from stress-strain relations in the material coordinates (2.12), it is possible to obtain stress-strain relations in generic coordinates using $[T]^{-1}$ and $[T]$, through the following relation:

$$\begin{bmatrix} \sigma_x \\ \sigma_y \\ \tau_{xy} \end{bmatrix} = [T]^{-1} \begin{bmatrix} Q_{11} & Q_{12} & 0 \\ Q_{12} & Q_{22} & 0 \\ 0 & 0 & Q_{33} \end{bmatrix} [T] \begin{bmatrix} \varepsilon_x \\ \varepsilon_y \\ 2\gamma_{xy} \end{bmatrix}. \tag{2.22}$$

Following equation (2.22), the stress-strain relation in xy coordinates becomes:

$$\begin{bmatrix} \sigma_x \\ \sigma_y \\ \tau_{xy} \end{bmatrix} = \begin{bmatrix} \bar{Q}_{11} & \bar{Q}_{12} & \bar{Q}_{13} \\ \bar{Q}_{12} & \bar{Q}_{22} & \bar{Q}_{23} \\ \bar{Q}_{13} & \bar{Q}_{23} & \bar{Q}_{33} \end{bmatrix} \begin{bmatrix} \varepsilon_x \\ \varepsilon_y \\ \gamma_{xy} \end{bmatrix}, \tag{2.23}$$

where $[\bar{Q}] = [T]^{-1}[Q][T]$ and its components are:

$$\bar{Q}_{11} = Q_{11} cos^4\theta + Q_{22} sin^4\theta + 2(Q_{12} + 2Q_{33}) cos^2\theta sin^2\theta, \tag{2.24a}$$

$$\bar{Q}_{12} = \bar{Q}_{21} = (Q_{11} + Q_{22} - 4Q_{33})cos^2\theta sin^2\theta + Q_{12}(cos^4\theta + sin^4\theta), \tag{2.24b}$$

$$\bar{Q}_{22} = Q_{11}sin^4\theta + Q_{22}cos^4\theta + 2(Q_{12} + 2Q_{33})cos^2\theta sin^2\theta, \tag{2.24c}$$

$$\bar{Q}_{13} = \bar{Q}_{31} = (Q_{11} - Q_{12} - 2Q_{33})cos^3\theta sin\theta - (Q_{22} - Q_{12} - 2Q_{33})cos\theta sin^3\theta, \tag{2.24d}$$

$$\bar{Q}_{23} = \bar{Q}_{32} = (Q_{11} - Q_{12} - 2Q_{33})cos\theta sin^3\theta - (Q_{22} - Q_{12} - 2Q_{33})cos^3\theta sin\theta, \tag{2.24e}$$

$$\bar{Q}_{33} = (Q_{11} + Q_{22} - 2Q_{12} - 2Q_{33})cos^2\theta sin^2\theta + Q_{33}(cos^4\theta + sin^4\theta). \tag{2.24f}$$

The $\bar{Q}_{ij}$ matrix represents the transformed reduced stiffness matrix and contains terms in all the nine positions, conversely to the reduced stiffness matrix. The compliance matrix, in generic coordinates, is:

$$\begin{bmatrix} \varepsilon_x \\ \varepsilon_y \\ \gamma_{xy} \end{bmatrix} = \begin{bmatrix} \bar{S}_{11} & \bar{S}_{12} & \bar{S}_{13} \\ \bar{S}_{12} & \bar{S}_{22} & \bar{S}_{23} \\ \bar{S}_{13} & \bar{S}_{23} & \bar{S}_{33} \end{bmatrix} \begin{bmatrix} \sigma_x \\ \sigma_y \\ \tau_{xy} \end{bmatrix}, \tag{2.25}$$

where the transformed orthotropic compliances are $\bar{S}_{ij}$:

$$\bar{S}_{11} = S_{11}cos^4\theta + S_{22}sin^4\theta + (2S_{12} + S_{33})cos^2\theta sin^2\theta, \tag{2.26a}$$

$$\bar{S}_{12} = \bar{S}_{21} = (S_{11} + S_{22} - S_{33})cos^2\theta sin^2\theta + S_{12}(cos^4\theta + sin^4\theta), \tag{2.26b}$$

$$\bar{S}_{22} = S_{11}sin^4\theta + S_{22}cos^4\theta + (2S_{12} + S_{33})cos^2\theta sin^2\theta, \tag{2.26c}$$

$$\bar{S}_{13} = \bar{S}_{31} = (2S_{11} - 2S_{12} - S_{33})cos^3\theta sin\theta - (2S_{22} - 2S_{12} - S_{33})cos\theta sin^3\theta, \tag{2.26d}$$

$$\bar{S}_{23} = \bar{S}_{32} = (2S_{11} - 2S_{12} - S_{33})cos\theta sin^3\theta - (2S_{22} - 2S_{12} - S_{33})cos^3\theta sin\theta, \tag{2.26e}$$

$$\bar{S}_{33} = 2(2S_{11} + 2S_{22} - 4S_{12} - S_{33})cos^2\theta sin^2\theta + S_{33}(cos^4\theta + sin^4\theta). \tag{2.26f}$$

Mechanical behavior of the laminate

A laminate is constituted by two or more laminas stacked together to act as a unique structural element. The mechanical behavior of the laminate is analyzed on a macro-mechanical scale, in which the individual components of the lamina such as fibers and matrix are not considered individually, but the entire lamina is taken into account. The mechanical behavior of a composite laminate can be described through Classical Lamination Theory, if these hypotheses, here summarized, are satisfied:

- Every lamina in the laminate is perfectly bonded, so that, under applied loading, no mutual slip between laminas occurs.
- The generic straight line, orthogonal to the laminate mid-plane 2.3, remains rectilinear and perpendicular to the mid-plane even after a deformation occurred, i.e.

$$\gamma_{xz} = \gamma_{yz} = 0. \tag{2.27}$$

- Deformation ε_z is much smaller and negligible than deformations ε_x and ε_y.
- The laminate thickness is much smaller than the other dimensions.

If the 3D printed part satisfies these conditions, then its mechanical behavior can be studied through CLT. While FDM printed prototypes do not possess the identical features of a laminate, they can be viewed as orthotropic composites of material filaments, bonding between filaments and voids [42], thus CLT can be used to describe their mechanical behavior.

Constitutive equations of the laminate

The first part of the CLT approach includes the stress-strain behavior of an individual lamina of an orthotropic material under plane stress in material coordinates, expressed by equation (2.12) previously described. Similarly, stress-strain relations and the transformed reduced stiffness matrix (Eq. (2.23)) are required. Generally, for a lamina that occupies the k^{th} position in the laminate, the previous expression can be written as:

$$\{\sigma\}^k = [\bar{Q}]^k \{\varepsilon\}^k. \tag{2.28}$$

The CLT approach assumes that the complete laminate acts as a single layer where there is perfect bonding between laminas, enabling continuous displacement between laminas, so that no lamina can slip relative to the other. The hypothesis of Kirchhoff assumes that, if the laminate is thin, a line that is originally straight and perpendicular to the middle surface of the laminate before deformation is assumed to remain straight and perpendicular to the middle surface after the deformation (fig. 2.3). This assumption ignores the shear strains in planes perpendicular to

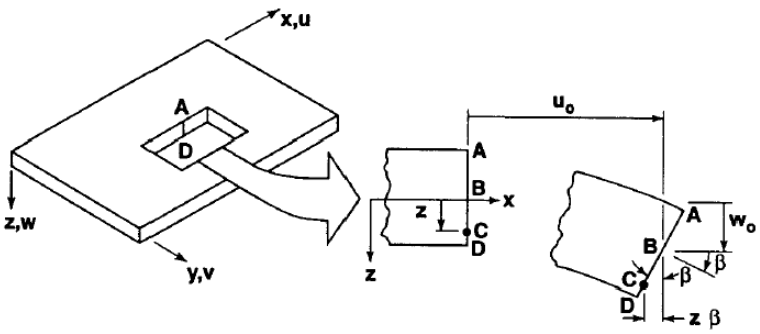

Figure 2.3: Laminate axis orientation, laminate section before and after deformation [34]

the middle surface, that is:

$$\gamma_{xz} = \gamma_{yz} = 0. \tag{2.29}$$

Additionally, the lines perpendicular to the middle surface are assumed to have a constant length, so that the strain perpendicular to the middle surface is ignored:

$$\varepsilon_z = 0. \tag{2.30}$$

The laminate cross section derives the hypothesis of Kirchhoff, where the displacement of the point B (middle surface) from the undeformed to the deformed state is u_0. Because the ABCD line remains straight after deformation, the displacement of point C in the x-direction is:

$$u = u_0 - z\beta. \tag{2.31}$$

From the hypothesis of Kirchhoff-Love for shells, the line ABCD remains perpendicular to the middle surface, β is the slope of the middle laminate surface in the x-direction and is:

$$\beta = \frac{\partial w_0}{\partial x}, \tag{2.32}$$

then, the displacement at any point is:

$$u = u_0 - z\frac{\partial w_0}{\partial x}. \tag{2.33}$$

Similarly, displacement in the y-direction is:

$$v = v_0 - z\frac{\partial w_0}{\partial y}. \tag{2.34}$$

As a consequence of the hypothesis of Kirchhoff, the remaining laminate strains are defined in terms of displacements as:

$$\varepsilon_x = \frac{\partial u}{\partial x} = \frac{\partial u_0}{\partial x} - z\frac{\partial^2 w_0}{\partial x^2}, \tag{2.35a}$$

$$\varepsilon_y = \frac{\partial v}{\partial y} = \frac{\partial v_0}{\partial y} - z\frac{\partial^2 w_0}{\partial y^2}, \tag{2.35b}$$

$$\gamma_{xy} = \frac{\partial u}{\partial y} + \frac{\partial v}{\partial x} = \frac{\partial u_0}{\partial y} + \frac{\partial v_0}{\partial x} - z\frac{\partial^2 w_0}{\partial x \partial y}. \tag{2.35c}$$

In vector form:

$$\begin{bmatrix} \varepsilon_x \\ \varepsilon_y \\ \gamma_{xy} \end{bmatrix} = \begin{bmatrix} \dfrac{\partial u_0}{\partial x} \\ \dfrac{\partial v_0}{\partial y} \\ \dfrac{\partial u_0}{\partial y} + \dfrac{\partial v_0}{\partial x} \end{bmatrix} + z \begin{bmatrix} -\dfrac{\partial^2 w_0}{\partial x^2} \\ -\dfrac{\partial^2 w_0}{\partial y^2} \\ -\dfrac{\partial^2 w_0}{\partial x \partial y} \end{bmatrix} = \begin{bmatrix} \varepsilon_x^0 \\ \varepsilon_y^0 \\ \gamma_{xy}^0 \end{bmatrix} + z \begin{bmatrix} k_x^0 \\ k_y^0 \\ k_{xy}^0 \end{bmatrix}, \tag{2.36}$$

where ε_x^0, ε_y^0 and γ_{xy}^0 are the mid-plane strains (elongations and distortions) and k_x^0, k_x^0 and k_x^0 are the three middle-surface curvatures (bending curvatures and torsions). The stresses for the k^{th} layer are expressed in terms of the laminate strains and curvatures as:

$$\begin{bmatrix} \sigma_x \\ \sigma_y \\ \tau_{xy} \end{bmatrix}^k = \begin{bmatrix} \bar{Q}_{11} & \bar{Q}_{12} & \bar{Q}_{13} \\ \bar{Q}_{12} & \bar{Q}_{22} & \bar{Q}_{23} \\ \bar{Q}_{13} & \bar{Q}_{23} & \bar{Q}_{33} \end{bmatrix}^k \left[\begin{bmatrix} \varepsilon_x^0 \\ \varepsilon_y^0 \\ \gamma_{xy}^0 \end{bmatrix} + z \begin{bmatrix} k_x^0 \\ k_y^0 \\ k_{xy}^0 \end{bmatrix} \right], \tag{2.37}$$

where z corresponds with the coordinates of the k^{th} lamina. The component of the stiffness matrix $\bar{Q}_{ij}$ is generally different for each layer of the laminate. This implies that the stresses at the interface are discontinuous, even though the strain variation is continuous through the lamina interface (fig. 2.4). Even though the stress variation is discontinuous at the interface, it does vary

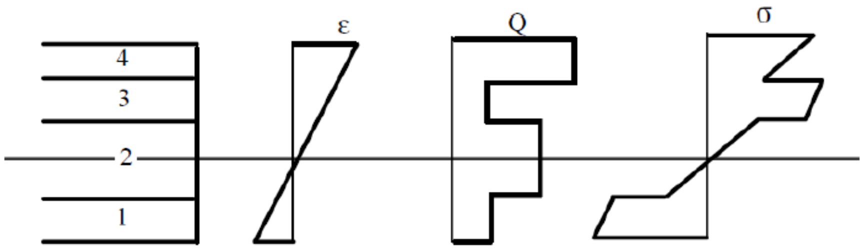

Figure 2.4: Schematic distribution of strains, characteristic moduli and stresses in the laminate [51]

linearly within each of the laminas.

The final stage of the CLT approach includes the characterization of the relation of the laminate forces and moments to the strains and the curvatures. The resultant forces and moments acting on

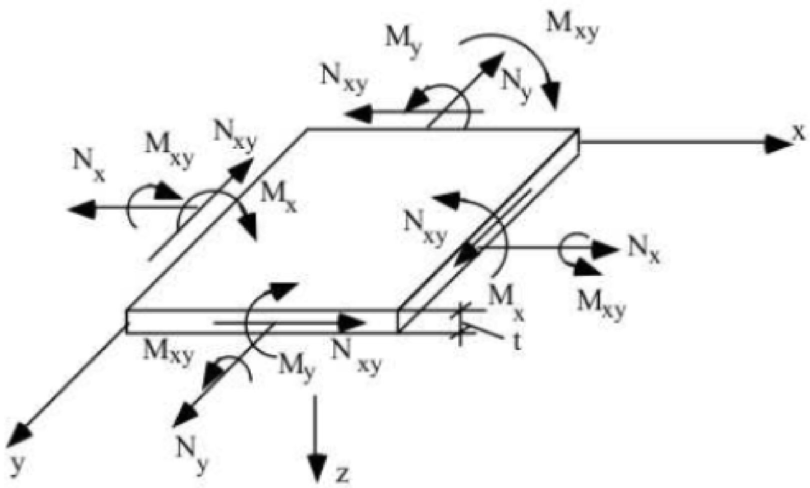

Figure 2.5: In-plane forces and moments on a laminate [51]

a laminate (fig. 2.5) are obtained by integration of the stresses in each layer through the laminate thickness and are defined as:

$$\begin{bmatrix} N_x \\ N_y \\ N_{xy} \end{bmatrix} = \int_{-t/2}^{t/2} \begin{bmatrix} \sigma_x \\ \sigma_y \\ \tau_{xy} \end{bmatrix} dz = \sum_{k=1}^{N} \int_{z_{k-1}}^{z_k} \begin{bmatrix} \sigma_x \\ \sigma_y \\ \tau_{xy} \end{bmatrix}^k dz, \tag{2.38}$$

$$\begin{bmatrix} M_x \\ M_y \\ M_{xy} \end{bmatrix} = \int_{-t/2}^{t/2} \begin{bmatrix} \sigma_x \\ \sigma_y \\ \tau_{xy} \end{bmatrix} zdz = \sum_{k=1}^{N} \int_{z_{k-1}}^{z_k} \begin{bmatrix} \sigma_x \\ \sigma_y \\ \tau_{xy} \end{bmatrix}^k zdz, \tag{2.39}$$

where z_k and z_{k-1} are the laminate geometry and the configurations of the laminas are shown in fig. 2.6, in which z is positive downwards. The stress-strain relations in (2.37) can be substituted

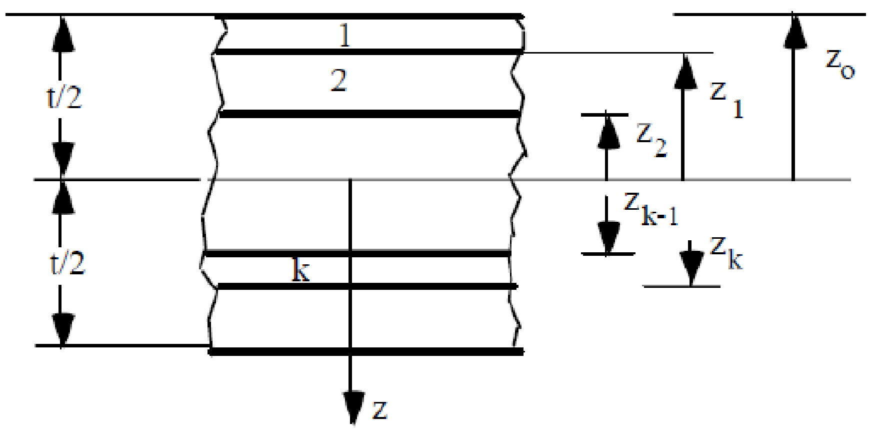

Figure 2.6: Lamina configurations [51]

into the forces and moments equations in (2.38) and (2.39), respectively. The results of the substitutions are shown in (2.40) and (2.41):

$$\begin{bmatrix} N_x \\ N_y \\ N_{xy} \end{bmatrix} = \sum_{k=1}^{N} \begin{bmatrix} \bar{Q}_{11} & \bar{Q}_{12} & \bar{Q}_{13} \\ \bar{Q}_{12} & \bar{Q}_{22} & \bar{Q}_{23} \\ \bar{Q}_{13} & \bar{Q}_{23} & \bar{Q}_{33} \end{bmatrix}^k \left[\int_{z_{k-1}}^{z_k} \begin{bmatrix} \varepsilon_x^0 \\ \varepsilon_y^0 \\ \gamma_{xy}^0 \end{bmatrix} dz + \int_{z_{k-1}}^{z_k} \begin{bmatrix} k_x^0 \\ k_y^0 \\ k_{xy}^0 \end{bmatrix} zdz \right], \tag{2.40}$$

$$\begin{bmatrix} M_x \\ M_y \\ M_{xy} \end{bmatrix} = \sum_{k=1}^{N} \begin{bmatrix} \bar{Q}_{11} & \bar{Q}_{12} & \bar{Q}_{13} \\ \bar{Q}_{12} & \bar{Q}_{22} & \bar{Q}_{23} \\ \bar{Q}_{13} & \bar{Q}_{23} & \bar{Q}_{33} \end{bmatrix}^k \left[\int_{z_{k-1}}^{z_k} \begin{bmatrix} \varepsilon_x^0 \\ \varepsilon_y^0 \\ \gamma_{xy}^0 \end{bmatrix} zdz + \int_{z_{k-1}}^{z_k} \begin{bmatrix} k_x^0 \\ k_y^0 \\ k_{xy}^0 \end{bmatrix} z^2dz \right]. \tag{2.41}$$

Since middle-plane strains (ε_x^0,ε_y^0,γ_{xy}^0) and curvatures (k_x^0,k_y^0,k_{xy}^0) are independent of z and are middle surface values, they can be removed from within the summation signs. The resultant equations are shown below:

$$\begin{bmatrix} N_x \\ N_y \\ N_{xy} \end{bmatrix} = \begin{bmatrix} A_{11} & A_{12} & A_{13} \\ A_{12} & A_{22} & A_{23} \\ A_{13} & A_{23} & A_{33} \end{bmatrix} \begin{bmatrix} \varepsilon_x^0 \\ \varepsilon_y^0 \\ \gamma_{xy}^0 \end{bmatrix} + \begin{bmatrix} B_{11} & B_{12} & B_{13} \\ B_{12} & B_{22} & B_{23} \\ B_{13} & B_{23} & B_{33} \end{bmatrix} \begin{bmatrix} k_x^0 \\ k_y^0 \\ k_{xy}^0 \end{bmatrix}, \tag{2.42}$$

$$\begin{bmatrix} M_x \\ M_y \\ M_{xy} \end{bmatrix} = \begin{bmatrix} B_{11} & B_{12} & B_{13} \\ B_{12} & B_{22} & B_{23} \\ B_{13} & B_{23} & B_{33} \end{bmatrix} \begin{bmatrix} \varepsilon_x^0 \\ \varepsilon_y^0 \\ \gamma_{xy}^0 \end{bmatrix} + \begin{bmatrix} D_{11} & D_{12} & D_{13} \\ D_{12} & D_{22} & D_{23} \\ D_{13} & D_{23} & D_{33} \end{bmatrix} \begin{bmatrix} k_x^0 \\ k_y^0 \\ k_{xy}^0 \end{bmatrix}, \tag{2.43}$$

where:

$$A_{ij} = \sum_{k=1}^{N} \bar{Q}_{ij}^k (z_k - z_{k-1}), \tag{2.44a}$$

$$B_{ij} = \frac{1}{2} \sum_{k=1}^{N} \bar{Q}_{ij}^k (z_k^2 - z_{k-1}^2), \tag{2.44b}$$

$$D_{ij} = \frac{1}{3} \sum_{k=1}^{N} \bar{Q}_{ij}^k (z_k^3 - z_{k-1}^3). \tag{2.44c}$$

A_{ij}, B_{ij} and D_{ij} are symmetric matrices. A_{ij} represent the extensional stiffnesses matrix, with A_{13} and A_{23} the shear-extension coupling, B_{ij} is the bending-extension coupling matrix and the D_{ij} is the bending stiffnesses matrix, with D_{13} and D_{23} representing bend-twist coupling. The presence of B_{ij} implies coupling between:

- Forces and curvatures.
- Moments and middle plane deformations.

Equations (2.42) and (2.43) can be written in a more compact form:

$$\begin{bmatrix} N_x \\ N_y \\ N_{xy} \end{bmatrix} = [A] \begin{bmatrix} \varepsilon_x^0 \\ \varepsilon_y^0 \\ \gamma_{xy}^0 \end{bmatrix} + [B] \begin{bmatrix} k_x^0 \\ k_y^0 \\ k_{xy}^0 \end{bmatrix}, \tag{2.45}$$

$$\begin{bmatrix} M_x \\ M_y \\ M_{xy} \end{bmatrix} = [B] \begin{bmatrix} \varepsilon_x^0 \\ \varepsilon_y^0 \\ \gamma_{xy}^0 \end{bmatrix} + [D] \begin{bmatrix} k_x^0 \\ k_y^0 \\ k_{xy}^0 \end{bmatrix}. \tag{2.46}$$

Finally, equations (2.45) and (2.46) can be assembled in a single expression:

$$\begin{bmatrix} \tilde{N} \\ \tilde{M} \end{bmatrix} = \begin{bmatrix} \bar{A} & \bar{B} \\ \bar{B} & \bar{D} \end{bmatrix} \begin{bmatrix} \tilde{\varepsilon}^0 \\ \tilde{k}^0 \end{bmatrix}, \tag{2.47}$$

where:

$$[\tilde{N}] = \begin{bmatrix} N_x \\ N_y \\ N_{xy} \end{bmatrix}, \qquad [\tilde{M}] = \begin{bmatrix} M_x \\ M_y \\ M_{xy} \end{bmatrix}, \qquad [\tilde{\varepsilon}^0] = \begin{bmatrix} \varepsilon_x^0 \\ \varepsilon_y^0 \\ \gamma_{xy}^0 \end{bmatrix}, \qquad [\tilde{k}^0] = \begin{bmatrix} k_x^0 \\ k_y^0 \\ k_{xy}^0 \end{bmatrix}. \tag{2.48}$$

Equation (2.47) can be inverted, in order to find deformations and curvatures, given forces and moments. This can be achieved by considering (2.45) and (2.46) as a system of six scalar equations. Expliciting the middle plane deformations in (2.45) and the curvatures in (2.46), we have:

$$\begin{bmatrix} \varepsilon_x^0 \\ \varepsilon_y^0 \\ \gamma_{xy}^0 \end{bmatrix} = [A]^{-1} \begin{bmatrix} N_x \\ N_y \\ N_{xy} \end{bmatrix} - [A]^{-1}[B] \begin{bmatrix} k_x^0 \\ k_y^0 \\ k_{xy}^0 \end{bmatrix}, \tag{2.49}$$

$$\begin{bmatrix} k_x^0 \\ k_y^0 \\ k_{xy}^0 \end{bmatrix} = [D]^{-1} \begin{bmatrix} M_x \\ M_y \\ M_{xy} \end{bmatrix} - [D]^{-1}[B] \begin{bmatrix} \varepsilon_x^0 \\ \varepsilon_y^0 \\ \gamma_{xy}^0 \end{bmatrix}. \tag{2.50}$$

Solving the system by substitution, we have:

$$\begin{bmatrix} \varepsilon_x^0 \\ \varepsilon_y^0 \\ \gamma_{xy}^0 \end{bmatrix} = ([A] - [B][D]^{-1}[B])^{-1} \begin{bmatrix} N_x \\ N_y \\ N_{xy} \end{bmatrix} - ([A] - [B][D]^{-1}[B])^{-1}[B][D]^{-1} \begin{bmatrix} M_x \\ M_y \\ M_{xy} \end{bmatrix}, \tag{2.51}$$

$$\begin{bmatrix} k_x^0 \\ k_y^0 \\ k_{xy}^0 \end{bmatrix} = -([D] - [B][A]^{-1}[B])^{-1}[B][A]^{-1} \begin{bmatrix} N_x \\ N_y \\ N_{xy} \end{bmatrix} + ([D] - [B][A]^{-1}[B])^{-1} \begin{bmatrix} M_x \\ M_y \\ M_{xy} \end{bmatrix}, \tag{2.52}$$

with:

$$[a] = ([A] - [B][D]^{-1}[B])^{-1}, \tag{2.53a}$$

$$[b_1] = -([A] - [B][D]^{-1}[B])^{-1}[B][D]^{-1} = -[a][B][D]^{-1}, \tag{2.53b}$$

$$[d] = ([D] - [B][A]^{-1}[B])^{-1}, \tag{2.53c}$$

$$[b_2] = -([D] - [B][A]^{-1}[B])^{-1}[B][A]^{-1} = -[d][B][A]^{-1} = [b]^T. \tag{2.53d}$$

Finally, the inverse laminate constitutive law is shown below:

$$\begin{bmatrix} \tilde{\varepsilon}^0 \\ \tilde{k}^0 \end{bmatrix} = \begin{bmatrix} \bar{a} & \bar{b} \\ \bar{b}^T & \bar{d} \end{bmatrix} \begin{bmatrix} \tilde{N} \\ \tilde{M} \end{bmatrix}. \tag{2.54}$$

Special types of laminates

A particular class of laminates is characterized by the absence of coupling between normal forces and curvatures and between moments and middle plane deformations. These laminates are called symmetric and they have $[B] = 0$. In symmetric laminates the disposition of laminas must respect symmetry between the laminate mid-plane (fig. 2.7). Another characteristic class is constituted by balanced laminates, in which $A_{13} = A_{23} = 0$, such that coupling between normal forces and shear strain and between shear forces and lineic deformations is nullified. In these types of laminates the laminas are orientated in such a way that, for every lamina with orientation θ there is a

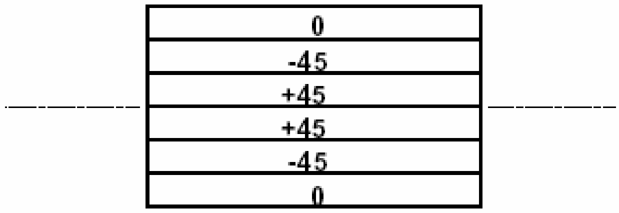

Figure 2.7: Example of a symmetric and balanced laminate [95]

corresponding lamina with orientation $-\theta$ and with the same thickness, as shown in fig. 2.8. Note

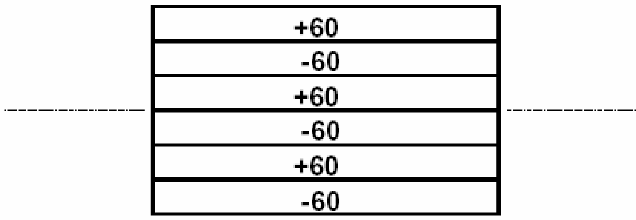

Figure 2.8: Example of an antisymmetric and balanced laminate [95]

that, in fig. 2.7, the laminate is both symmetric and balanced.

2.1.2 Tsai-Hill failure criterion

Strength of specimens has been modeled using the Tsai-Hill failure criterion for composite materials under multiaxial loading [7]. This theory is based on the distortion energy failure theory of Von Mises distortional energy yield criterion for isotropic materials. Distortion energy is actually a part of the total strain energy in a body [35]. The strain energy in a body consists of two parts; one due to a change in volume and is called dilation energy and the second is due to a change in shape and is called distortion energy [35]. It is assumed that failure in the material takes place only when the distortion energy is greater than the failure distortion energy of the material [35]. Hill [30] adopted Von Mises distortional energy yield criterion to anisotropic materials. Then Tsai adapted it to a unidirectional lamina [64]. Tsai-Hill failure criterion can be considered as a particular case, in which tensile and compressive strength are equal, of the more general criterion proposed by Tsai and Wu [65]. Based on the distortion energy theory, he proposed that a lamina has failed if the condition below is violated:

$$(G+H)\sigma_1^2+(F+H)\sigma_2^2+(G+F)\sigma_3^2-2H\sigma_1\sigma_2-2G\sigma_1\sigma_3-2F\sigma_2\sigma_3+2L\tau_{23}^2+2M\tau_{13}^2+2N\tau_{12}^2 \leq 1, \tag{2.55}$$

where F, G, H, L, M, and N coefficients are Hill's strength parameters and are considered as ultimate values, after which the material is subjected to failure. The type of failure depends on the material: for brittle ones failure coincides with breaking, while for ductile ones failure coincides with the deviation from the linear elastic behavior [72]. In the present study these parameters have been intended as peak stress values, after which the material starts yielding (ductile behavior) or breaks (brittle behavior). Tsai adapted these parameters to the orthotropic lamina case, considering simple loading situations. If:

$$\tau_{12} \neq 0, \qquad \sigma_1 = \sigma_2 = \sigma_3 = 0, \qquad \tau_{13} = \tau_{23} = 0, \tag{2.56}$$

then:

$$2N\tau_{12}^2 = 1 \qquad \rightarrow \qquad N = \frac{1}{2\tau_{12}^2}. \tag{2.57}$$

In an ultimate strength situation, it means that τ_{12} corresponds to its limit value, that is S_{12}^2, thus:

$$N = \frac{1}{2S_{12}^2}. \tag{2.58}$$

Similarly, if $\sigma_{23} \neq 0$ and $\sigma_{13} \neq 0$, with other tensile components null, L and M values are obtained:

$$L = \frac{1}{2S_{23}^2}, \tag{2.59}$$

$$M = \frac{1}{2S_{13}^2}. \tag{2.60}$$

If:

$$\sigma_1 \neq 0, \qquad \sigma_2 = \sigma_3 = 0, \qquad \tau_{12} = \tau_{13} = \tau_{23} = 0, \tag{2.61}$$

then:

$$(G + H)\sigma_1^2 = 1 \qquad \rightarrow \qquad G + H = \frac{1}{\sigma_1^2}. \tag{2.62}$$

In an ultimate strength situation, it means that σ_1 corresponds to its limit value, that is S_1^2, thus:

$$G + H = \frac{1}{S_1^2}. \tag{2.63}$$

Similarly, if $\sigma_2 \neq 0$ and $\sigma_3 \neq 0$, with other tensile components null, we obtain:

$$F + H = \frac{1}{S_2^2}, \tag{2.64}$$

$$G + F = \frac{1}{S_3^2}. \tag{2.65}$$

From equations (2.63), (2.64), (2.65), we obtain:

$$F = \frac{1}{2}\left[\tfrac{1}{S_2^2} + \tfrac{1}{S_3^2} - \tfrac{1}{S_1^2}\right], \qquad G = \frac{1}{2}\left[\tfrac{1}{S_1^2} + \tfrac{1}{S_3^2} - \tfrac{1}{S_2^2}\right], \qquad H = \frac{1}{2}\left[\tfrac{1}{S_1^2} + \tfrac{1}{S_2^2} - \tfrac{1}{S_3^2}\right]. \tag{2.66}$$

Substituting F, G, H, L, M and N parameters obtained in an ultimate strength situation in equation (2.55), Tsai-Hill criterion is obtained. In the case of a lamina under plane stress, $\sigma_3 = \tau_{23} = \tau_{13} = 0$ and the expression (2.55) is reduced as shown below:

$$\frac{\sigma_1^2}{S_1^2} + \frac{\sigma_2^2}{S_2^2} - \left[\tfrac{1}{S_1^2} + \tfrac{1}{S_2^2} - \tfrac{1}{S_3^2}\right]\sigma_1\sigma_2 + \frac{\tau_{12}^2}{S_{12}^2} \leq 1. \tag{2.67}$$

From the transversal isotropy of the lamina, $z = y$, i.e. $S_3 = S_2$ hence:

$$\frac{\sigma_1^2}{S_1^2} + \frac{\sigma_2^2}{S_2^2} - \frac{\sigma_1\sigma_2}{S_1^2} + \frac{\tau_{12}^2}{S_{12}^2} \leq 1. \tag{2.68}$$

Equation (2.68) shows Tsai-Hill failure criterion for an orthotropic plane stress lamina, which is the case of interest in composite material study.

Equation (2.68) determines the limit condition: an admissible stress state is achieved when the first member of the equation assumes a lower value than 1. The main drawback of Tsai-Hill criterion is that there is no difference between tensile and compressive strength, while generally they are different.

Through the rotation matrix, the expression of Tsai-Hill criterion for a general reference system can be calculated. For an uniaxial stress state that varies with orientation, the following expression is obtained:

$$\sigma_x^2 \left[\frac{cos^4\theta}{S_1^2} + \frac{sin^4\theta}{S_2^2} - \frac{cos^2\theta sin^2\theta}{S_1^2} + \frac{cos^2\theta sin^2\theta}{S_{12}^2} \right] = 1. \tag{2.69}$$

Equation (2.69) can be used to calculate the in-plane shear strength, S_{12}, from an off-axis test. In fact, one advantage of the off-axis specimens is that their measured tensile strength can be used to estimate their shear strength [34]. In fig. 2.9, an example of Tsai-Hill curve in function of orientation θ, for uniaxial tensile loading, is shown:

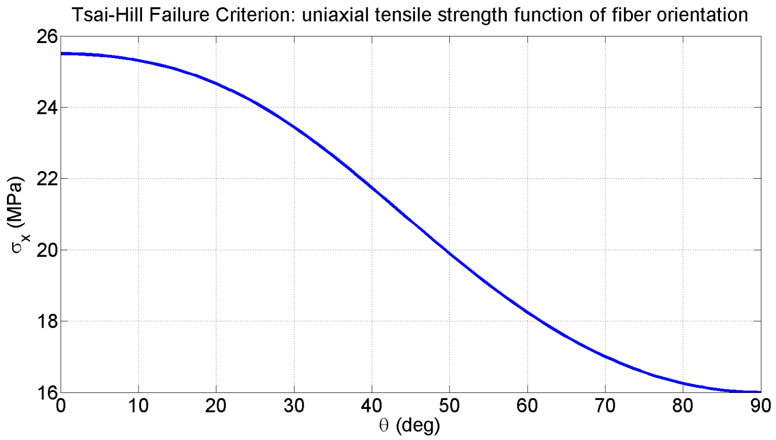

Figure 2.9: Tsai-Hill failure criterion for an uniaxial stress state

Chapter 3

Experimental setup

3.1 From rapid prototyping to rapid manufacturing

In recent years, layered manufacturing processes have begun to evolve from RP techniques towards RM ones, where the objective is now the production of finished components for potential end use in a product [15]. One of the most impending issues to resolve in rapid manufacturing is to know how manufactured parts behave, working under real conditions. Additive manufacturing technologies are mature for industrial production and due to a rising competition between service providers, AM is becoming economically sustainable for a growing number of industrial and end-user applications [8]. From a design perspective the challenge of additive manufacturing is to understand limitations and opportunities of these new processes and right fields to applicate them [37]. Lately, new AM technologies are able to process more than one material e.g. thermoplastics of different color [26]. In the last decade the development of these technologies was largely increased thanks to extensive researches on new materials and creation of better hardware and software, which further improved AM processes [68].

This strong migration from rapid prototyping to rapid manufacturing comes with many market expectations, such as:

- How to achieve mass production without compromise on quality, detail and accuracy.
- Verifying if the process is stable enough to have consistent quality within the build job and between build jobs.
- Verifying if production results are repeatable over time.
- Checking if the single fabricated parts, with permanent quality, are stable over a long period of time (long aging).
- Using a large range of materials.

From an industrial perspective, processes capable of producing robust parts with high strength and long-term stability are most relevant, because they allow the direct production of end-user parts. The objective behind product improvements or optimizations may vary. Typical examples are an increase of performance, a better efficiency or the reduction of costs. This is only possible if mechanical properties are well known in the design stage, depending on the process parameters.

The goal of this work are:

- Carry out a preliminary evaluation of printing parameters, in order to identify suitable printing profiles.

- Understand the relation between mechanical and strength properties and raster orientation of FDM printed parts.
- Analyze the behavior of FDM printed parts while under tensile loading.
- Establish a solid and reliable basis for designing optimized rapid manufacturing parts, in terms of mechanical response and strength.

Two different types (here called Type A and Type B) of thermoplastic material have been analyzed and tested. High impact polystyrene (HIPS) has been used for the present study as support material.

3.2 Printing parameters preliminary assessment

Before attempting to analyze the mechanical behavior, of each material, a preliminary evaluation of printing characteristics has been carried out, in order to find suitable printing profiles. The 3D printer used for the present study is the 3NTR A4V3 (http://www.3ntr.eu). The machine is equipped with three extruders, which can be heated up to 410°C, through a ceramic heating component. The bed temperature can reach 120°C, while the heated chamber can reach 75°C. For the present study, a nozzle of 0,4 mm of diameter has been used. The aim of the preliminary evaluation is to identify a suitable:

- Printing temperature range.
- Heated chamber temperature.
- Printing maximum flow of material.
- Bed temperature.
- Compatibility with support material.

A sample geometry is used for the test. A cylinder of 34 mm of inner diameter and 1 mm of wall thickness is printed (fig. 3.1). This geometry is useful to highlight printing defects due to:

- Incorrect adhesion between layers, resulting from low printing temperature.
- Bad surface finishing, due to a high printing temperature.
- Drawbacks in material extrusion, due to incorrect velocity settings.

The preliminary assessment results in the printing main parameters (tab. 3.1) for the two materials under investigation. The maximum flowrate guides the choice of admissible printing speeds that can be used in relation to the following parameters:

- Layer thickness.
- Extrusion width.
- Nozzle diameter.

For example, using a layer height of 0,2 mm and an extrusion width of 0,4 mm, a velocity of 40 mm/s should be set (resulting in a flowrate of 0,2 mm x 0,4 mm x 40 mm/s = 3,2 mm^3/s). A layer height of 0,3 mm and an extrusion width of 0,6 mm, will result in a velocity of 20 mm/s (flowrate of 3,6 mm^3/s).

Figure 3.1: Sample cylinder to assess main printing parameters in (tab. 3.1)

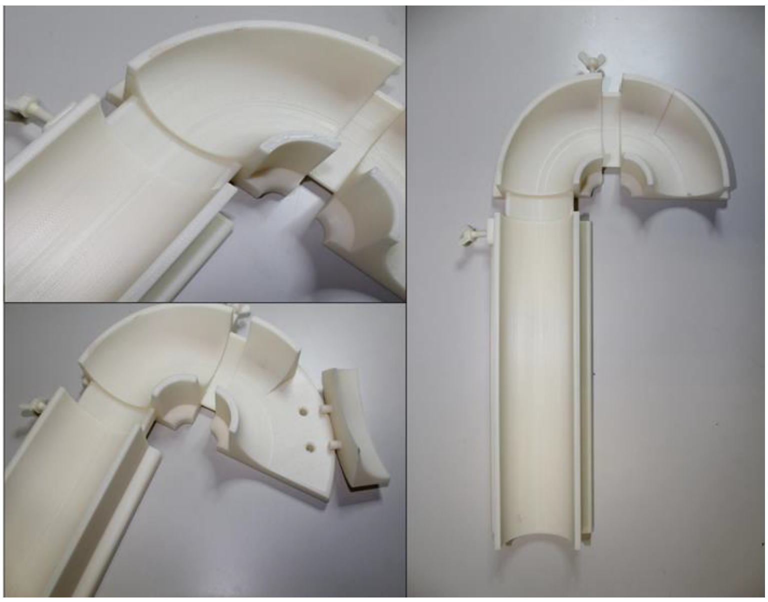

Figure 3.2: Three views of the 3D printed inter-locking guide

Table 3.1: Main printing parameters identified during preliminary assessment

Parameters	Type A material	Type B material	Unit
Extrusion Temperature	250-260	250-260	°C
Bed Temperature	100	100	°C
Heated Chamber Temperature	70	70	°C
Maximum Flowrate	6	5	mm^3/s

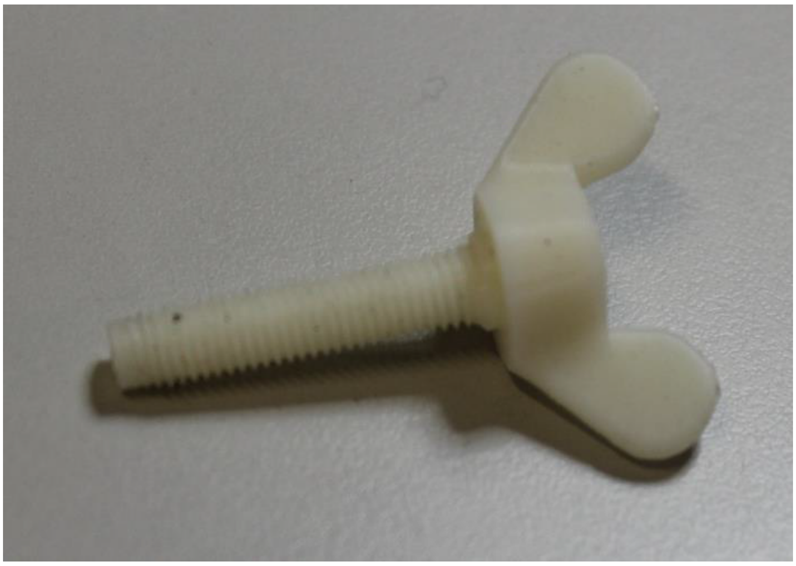

Figure 3.3: 3D printed screw, using a cutting threader machine

Thermal distortion and compatibility with support materials are tested through the printing of objects with a large base in contact with the bed (fig. 3.2). Type A material shows an optimal compatibility with HIPS, one of the most performing materials to be used as printing support. HIPS can be detached from the final object using a mechanical or chemical approach, the latter thanks to the use of limonene. Type A material stitches well on a HIPS base during the printing and the support structure is extremely easy to remove after the final object has cooled down for some minutes. The distance between the last layer of support material and the first layer of the printed part (commonly called air gap) can be set to 0,1-0,2 mm. Type A shows also a low thermal shrinkage when printed in heated environment (about 70 °C), even for large objects. After good preliminary results, the material has been tested for the printing of large functional objects, as a case study. An example is the prototype shown in fig. 3.2, which is a guide composed by interlocking parts, to be used for *ex-vivo* experiments. The object has a large base and requires a huge amount of support material: it is printed in 4 separated parts to be assembled and blocked by two screws. The longest part of the model requires about 10 hours of printing. The model shows a good finishing, also for surfaces in contact with the support material.

The material can also undergo to post-processing operation with good results: the two small screws, of 7 mm of diameter, are printed without the thread, realized through a thread cutting machine (fig. 3.3, fig. 3.4).

Type B material shows a lower compatibility with HIPS: better results can be retrieved lowering the air gap to 0. This solution allowed us to perform the printing of all the required samples, but the printing of large objects could not be carried out. It is not recommended to use the material itself to build its support structures, since it shows strong adhesion properties and thus it would

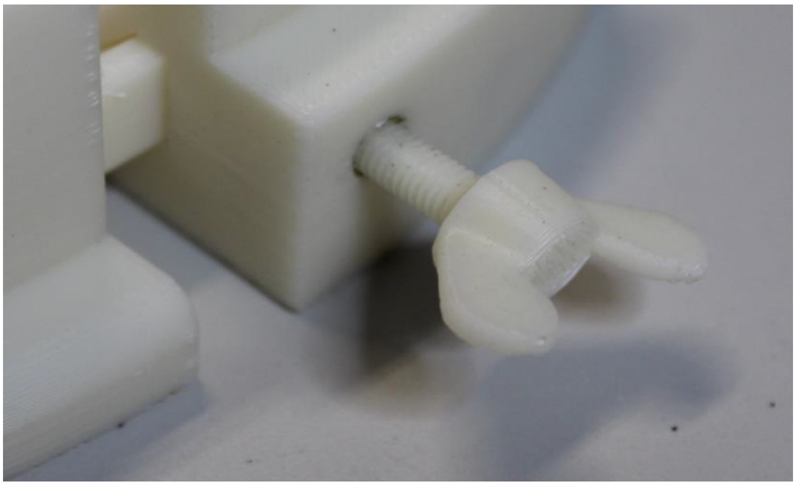

Figure 3.4: Good material post-processing: the 3D printed screw works without problems

be impossible to remove the support without damaging the print or compromising the surface quality.

3.3 Investigating the mechanical behavior of 3D printed parts: development of a novel standard procedure

At the moment there are no approved specific standards that primarily focus on studying the mechanical behavior of 3D printed parts; the two most used standards are:

- Standard Test Method for Tensile Properties of Plastics (ASTM D638).
- Standard Test Method for Tensile Properties of Polymer Matrix Composite Materials (ASTM D3039/D3039M).

ASTM D638 test method covers the determination of the tensile properties of unreinforced and reinforced plastics in the form of standard dumbbell-shaped test specimens when tested under defined conditions of pretreatment, temperature, humidity, and testing machine speed [62]. ASTM D3039 test method determines the in-plane tensile properties of polymer matrix composite materials reinforced by high-modulus fibers. The composite material forms are limited to continuous fiber or discontinuous fiber-reinforced composites in which the laminate is balanced and symmetric with respect to the test direction [61].

ASTM D3039 has been chosen to analyze the mechanical behavior of the 3D printed material, because, while ASTM D638 is a fitting test method for plastic material objects, it is more appropriate for isotropic materials and for injection molding technology. Moreover the geometry of the ASTM D638 specimen reveals problems (fig. 3.5) (fig. 3.6). A previous study of Ahn *et al.* [2] shows that ASTM D638 shape gives rise to complications to the loading of the FDM parts, which causes them to fail prematurely. These complications involve big stress concentrations, which are produced by the termination of the longitudinal roads used to approximate the large radii [2]. These specimens fail prematurely by shearing at the stress concentrations, while the rest of the sample remains intact (fig. 3.7). Ahn *et al.* [2] attempted to solve the issue by using offset contours that followed the perimeter of the sample, in order to relieve the stress concentrations. However, this approach gives rise to ulterior problems:

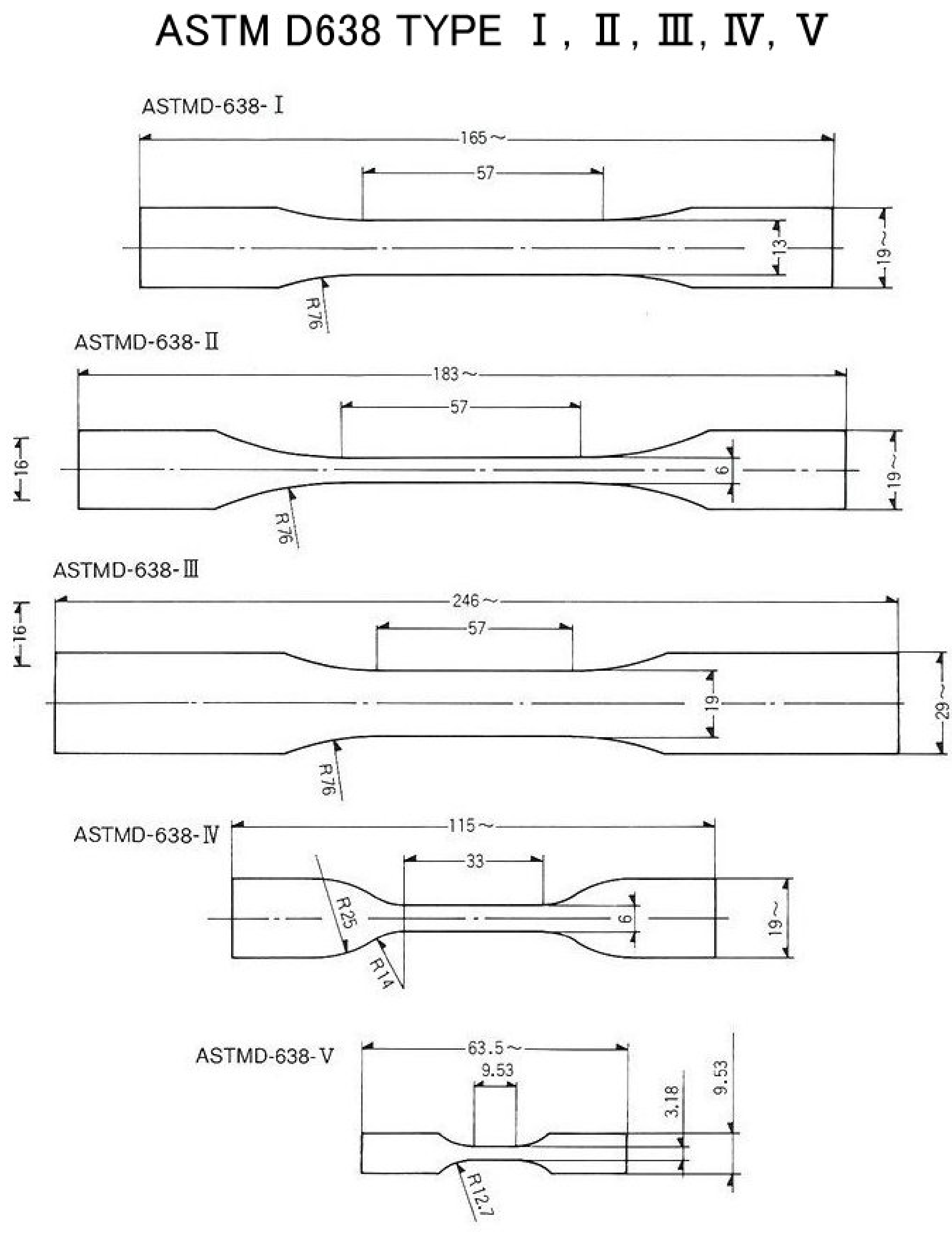

Figure 3.5: Dog bone shapes of ASTM D638 types - 1 to 5 - [96]

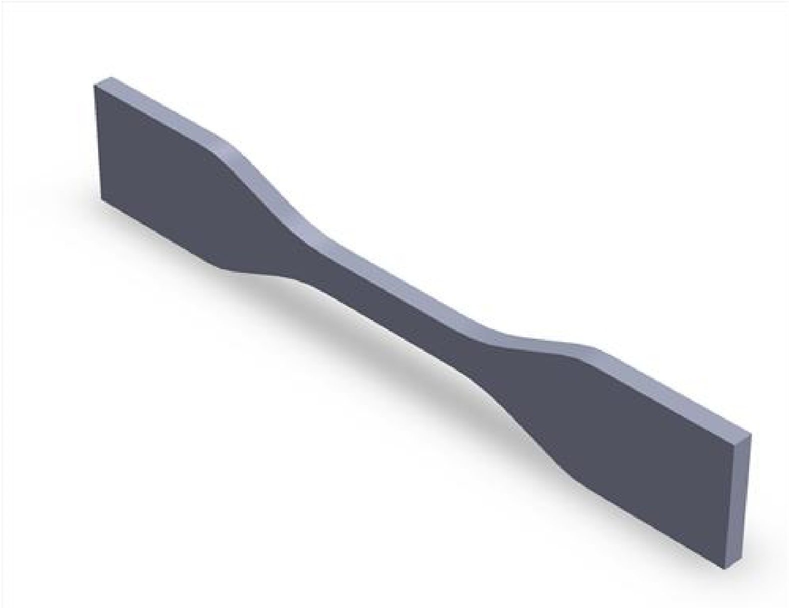

Figure 3.6: 3D model of ASTM D638 Type IV [97]

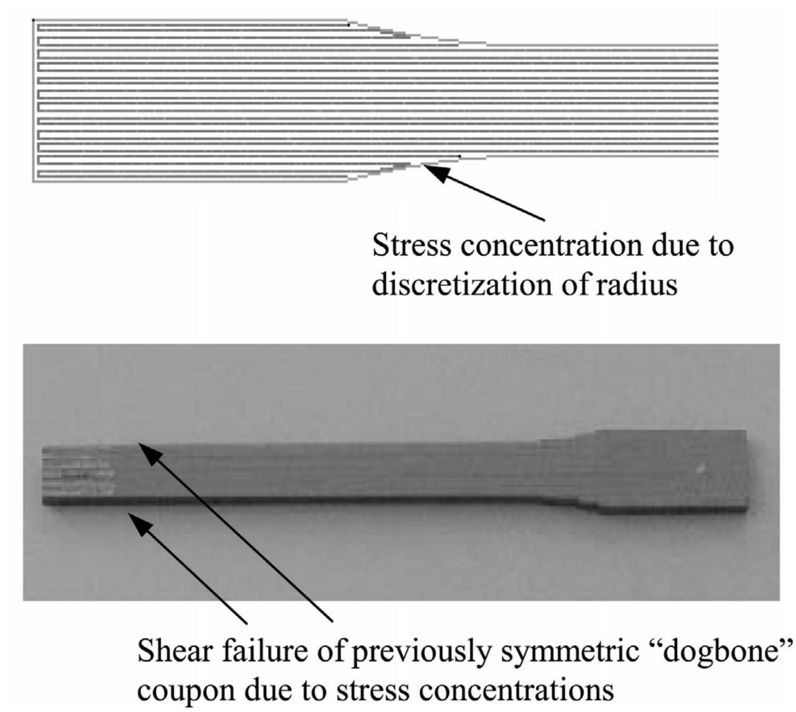

Figure 3.7: Premature shear failure of ASTM D638 standard test specimens with longitudinal roads [2]

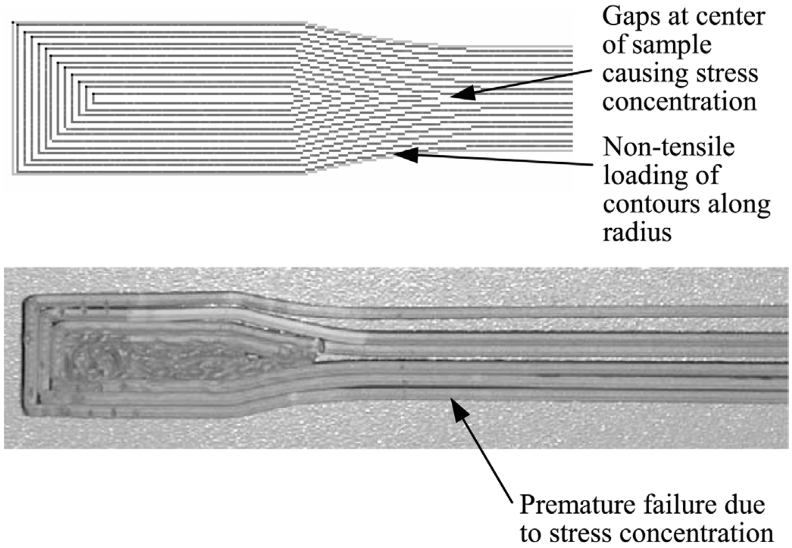

Figure 3.8: Premature shear failure of ASTM D638 standard test specimens with offset contours [2]

- Stress-concentrating gaps in the center of the sample
- Areas where the roads are no longer in pure tension (nullifying the intent of the ASTM D638 standard)

The specimens tend to fail prematurely at these areas of multi-state stress (fig. 3.8). Thus, the choice fell on ASTM D3039, since the shape is rectangular and it is more suited for anisotropic materials. As a matter of fact FDM printed parts can be considered as objects characterized by highly anisotropic material properties [2, 58].

Several researchers have specifically considered the anisotropic characteristics of FDM parts in recent years. Rodriguez *et al.* [52] investigated elastic modulus and tensile strength of FDM printed samples with different mesostructures in comparison with the properties of the ABS monofilament feedstock. They concluded that parts with fibers aligned with the loading direction have the greatest tensile strength. Afterwards, Rodriguez *et al.* [54] continued their research on constitutive and strength modeling of FDM parts, considering for both an anisotropic approach. Effective elastic moduli were obtained using the strength of materials approach and an elasticity approach based on the asymptotic theory of homogenization. For moduli predictions, the difference between experimental and theoretical values were less than 10% in most cases. Ahn *et al.* [2] designed an experiment to determine the effects temperature, filament width, raster orientation, gap between filaments, and ABS color on both tensile and compressive strengths of FDM parts. They concluded that both gap between beads and raster orientation had significant effects on the resulting tensile strength, while compressive strength was less affected. A similar study was carried out by Sood *et al.* [58], with varying parameters such as layer thickness, raster angle, filament width, and gap between filaments. They analyzed the functional relationship between process parameters and specimen strength using response surface methodology (RSM). The results show that the considered parameters influence the mesostructural configuration of the built part as well as the bonding and distortion within the part. Subsequently, Sood *et al.* [59] further examined the effect of the same five process parameters on the compressive strength of test specimens. They determined that fiber-to-fiber bond strength and control of distortion during the printing process play an important role on the compressive strength of FDM parts. Li *et al.* [42] studied the materials, the fabrication process and the mechanical properties of FDM specimens. Theoretical and experimental analyses of mechanical properties of FDM processes and samples were carried out to establish the constitutive models. Classical Lamination Theory was proposed to determine the elastic constants, function of raster angle, of FDM prototypes. Experimental data were in good agreement with the results of the laminate modeling. A study conducted by Es Said *et al.* [23] analyzed the effect of raster orientation and the subsequent alignment of polymer molecules along the direction of deposition during the printing process. The researchers studied the influence of volumetric shrinkage and raster orientation on tensile, flexural and impact strengths. Lee *et al.* [40] has shown that layer thickness, raster angle, and gap between beads affect the elastic performance of ABS FDM printed samples. Lee *et al.* [41] focused their research on compressive strength of layered parts as a function of build direction. They determined that the compressive strength is greater for the axial FDM specimens than for the transverse.

The previous studies revealed the anisotropy of FDM printed parts as a result of the dependence of the mechanical and strength properties on the raster orientation.

3.3.1 ASTM D3039/D3039M - 00 standard test method

ASTM D3039 test method consists in a thin flat strip of material having a constant rectangular cross section, which is mounted in the grips of a mechanical testing machine and then monotonically loaded in tension. The load is recorded during the testing phase. The ultimate tensile strength can be determined from the maximum load recorded before failure of the specimen. If the sample strain is recorded with extensometers, then the stress-strain response of the material can be determined. After having measured the strain, tensile modulus of elasticity and Poisson's ratio can be obtained, through the chord method.

The rectangular sample should follow some general geometry recommendations. Width and thickness of the specimen should be selected to promote failure in the gage section. The coupon length should normally be substantially longer than the minimum requirement, to minimize bending stresses caused by minor grip eccentricities. The minimum length required is determined in this way:

$$l_m = 2l_r + 2w + l_g, \tag{3.1}$$

where:

- l_m is the minimum specimen length required.
- l_r is the length of the specimen gripping area.
- w is the specimen width.
- l_g is the specimen gage length.

Tabs are not required , but are strongly recommended when testing unidirectional materials (or strongly unidirectionally dominated laminates), to failure in the fiber direction. Tabs are also recommended when there is the risk of damaging the specimen in the gripping areas: in this work they are used specially for the latter purpose, due to the high pressure applied by the gripping jaws of the testing machine.

For this study, five different fiber orientations (0°, 90°, 45°, 20°, 70°) have been considered, with θ being the angle between fiber (printing) direction and loading direction (fig. 3.9).

Three fiber angles (0°, 90°, 45°) are used to extract the mechanical properties of the specimen, while the other two orientations (20°, 70°) serve the purpose to validate the experimental data obtained. For every fiber angle, a precise geometric configuration has been adopted, with specific sample and tabs dimensions (fig. 3.10), reported in (tab. 3.2).

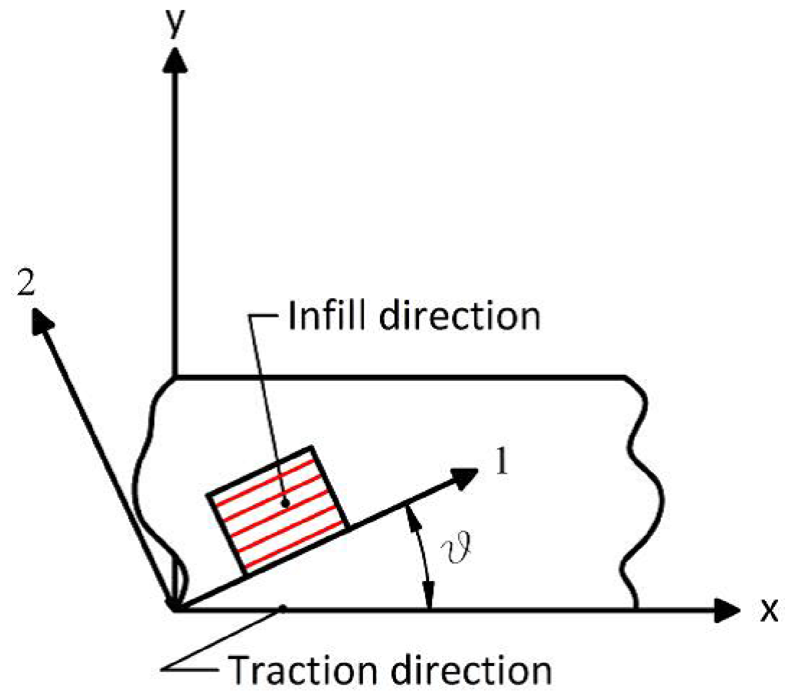

Figure 3.9: Fiber direction, loading direction and raster angle (θ)

Table 3.2: Specimen dimensions used following ASTM D3039/D3039M – 00 standard geometry recommendations

Fiber orientation (°)	Specimen length (mm) l_1	Specimen width (mm) w	Specimen thickness (mm) t_1	Tabs length (mm) l_2	Tabs width (mm) w	Tabs thickness (mm) t_2
0°	250	15	1,2	36	15	1,6
90°	175	25	2	25	25	1,6
45°	250	15	2,4	36	15	1,6
20°	250	15	2,4	36	15	1,6
70°	250	15	2,4	36	15	1,6

The three fiber orientations (0°, 90°, 45°) allow to calculate the main parameters that serve to characterize the material in terms of stiffness and strength. Classical Lamination Theory and Tsai-Hill failure criterion have been considered to describe the mechanical behavior of the material in function of the fiber angle, thus seven parameters are necessary, which can be extracted through tensile tests; each angle is used to find some of the required parameters:

- 0° orientation allows to obtain longitudinal Young's modulus, major Poisson's ratio and ultimate longitudinal strength.
- 90° orientation allows to obtain transverse Young's modulus and ultimate transverse strength.
- 45° orientation allows to obtain shear modulus and ultimate shear strength.

The shape and geometry of the specimen, with tabs, is shown in fig. 3.10:

Since this study focuses on fiber orientation, the infill density has been maintained the same (100%) for every specimen. The extensometer gage length has been set to be two times the sample width, starting from the center of the specimen, one unit width to the left and one to the right. ASTM D3039 requires that at least five specimens must be tested per test condition. Following

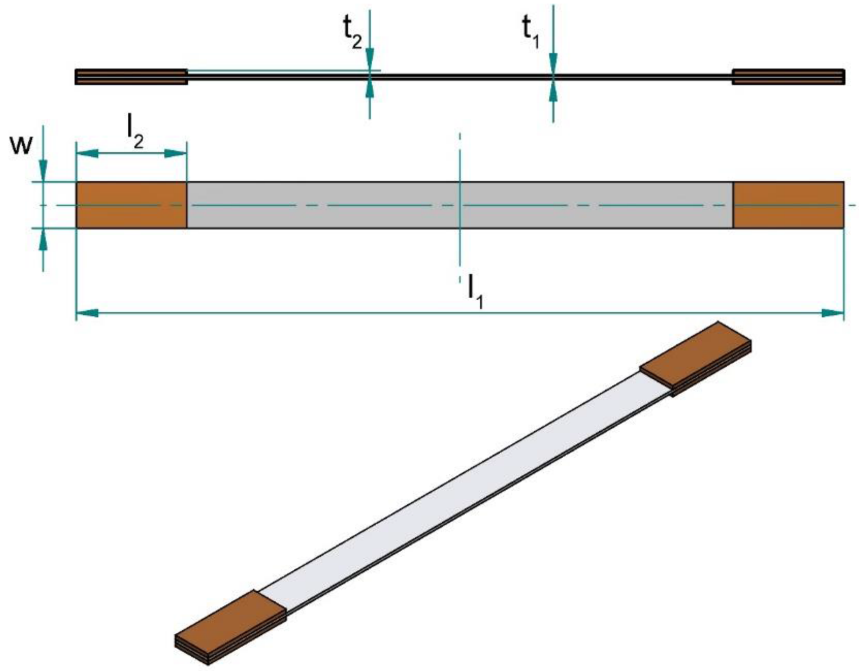

Figure 3.10: Specimen and tab dimensions according to tab. 3.2

final specimen machining and any conditioning, but before the tension testing, the real specimen area must be determined, at three places in the gage section, at least one measure per place, as:

$$A = wh, \tag{3.2}$$

where:

- A is the specimen cross section area.
- w is the specimen width.
- h is the specimen thickness.

The real cross section area is reported as the average of the measurements carried out. The strain rate should be selected so as to produce failure within 1 to 10 min. The standard head displacement must be a constant value of 2 mm/min. Following ASTM D3039 standard's directions, tensile moduli of elasticity and major Poisson's ratio will be extracted using the chord method.

In this study three mesostructures (fig. 1.24, fig. 3.11) differing in the single fiber cross section have been considered, for Type A material. For Type B material only one mesostructure has been considered. Four different printing configurations have been carried out, as shown in tab. 3.3:

Table 3.3: Different printing configurations

Configuration	Material type	Layer Height	Extrusion Width
1	A	0,2	0,4
2	A	0,25	0,5
3	A	0,3	0,6
4	B	0,2	0,4

For each mesostructure the total number of layer changes, as reported in tab. 3.4:

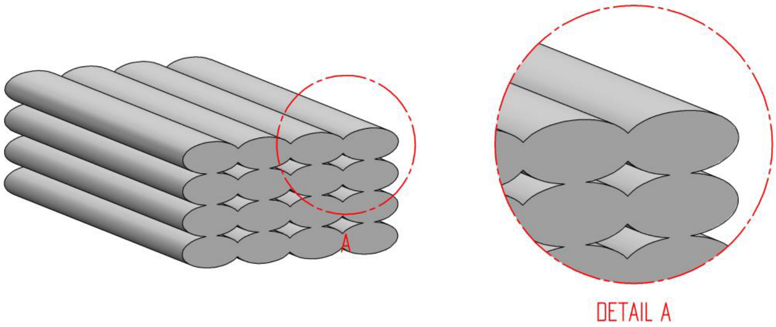

Figure 3.11: Scheme of the extruded fiber section

Table 3.4: Total number of layers varies in function of the mesostructure

Single layer height	Extrusion width	Fiber orientation	Total number of layers
0,2	0,4	0°	6
0,2	0,4	90°	10
0,2	0,4	45°-20°-70°	12
0,25	0,5	0°	6
0,25	0,5	90°	8
0,25	0,5	45°-20°-70°	8
0,3	0,6	0°	4
0,3	0,6	90°	6
0,3	0,6	45°-20°-70°	8

The samples have been printed without perimeters. Although the absence of perimeters may result in a lower mechanical performance of the specimen, this choice has been made to isolate and emphasize the raster angle contribution to the mechanical properties. In fact, the perimeter may disturb the effective measurements carried out, as the long sides (aligned to the loading direction) always contribute only to the longitudinal mechanical properties, while the short sides (perpendicular to the loading direction) always contribute only to the transverse mechanical properties. Therefore, for example, in a 90° specimen (where the fibers are perpendicular to the loading di-

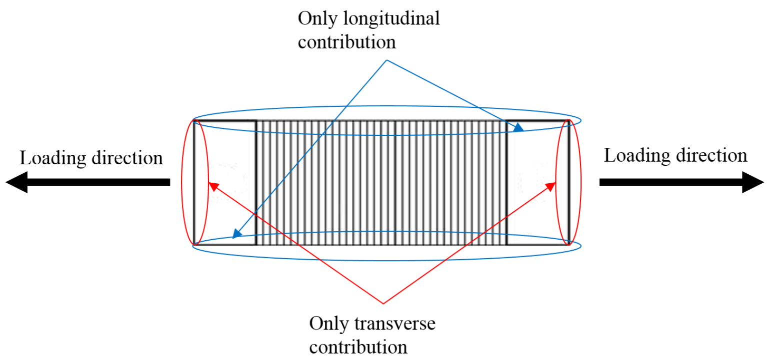

Figure 3.12: Contribution of the perimeter

rection), the long sides of the perimeter contribute to the longitudinal properties, disturbing the effective measure (fig. 3.12). Thus, the issue has been simply resolved by printing the samples without perimeters.

The specimens have been printed in an aligned configuration, as shown in fig. 3.13. A skewed configuration was also available, but in the end, only the aligned mesostructure was chosen, mainly because there were already three different mesostructure configurations to analyze (for Type A, plus the single mesostructure for Type B), with a varying cross section, thus it has been decided to not over-complicate the work.

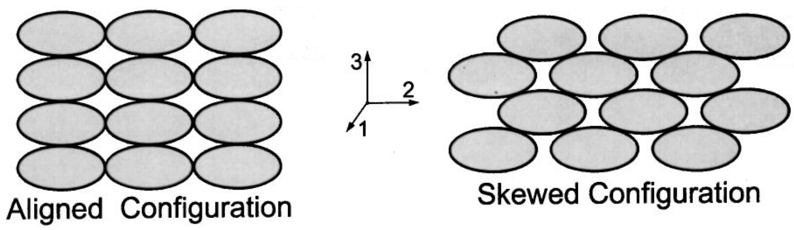

Figure 3.13: Aligned and skewed mesostructures [53]

As stated before, this study focuses on fiber orientation, therefore infill density (which is the other parameter that greatly affects the material mechanical properties [2]), has been maintained constant, with a value of 100%. Theoretically this means that the inner part of the object should be completely filled with material, but in reality this is not true. In fact, observing the cross section of the specimen, one could notice that the beads of extruded material take an elliptic shape (fig. 3.14): this causes the formation of void spaces between filaments, which obviously weaken the structure. The extruded material takes an elliptic form for a simple reason. If the material is extruded in free air, its cross section shape will always be round and its diameter equal to the nozzle diameter. The printed filament will have an elliptic cross section if it is printed above a solid surface and if the layer height is lower than the nozzle diameter: in this way, the extruded material is pressed on the surface, thus forming an elliptic shape.

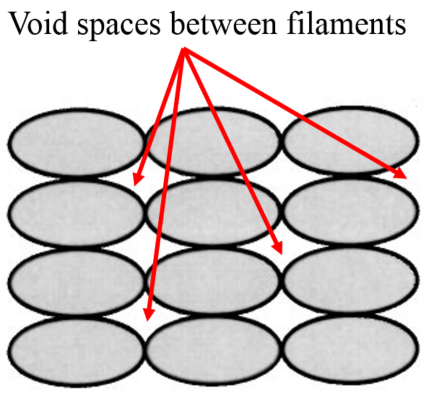

Figure 3.14: Presence of void spaces between extruded filaments in an aligned mesostructure

In an aligned mesostructure, the printed beads are vertically aligned, thus, if they have an elliptic geometry, it is notable that void spaces between filaments will be created (fig. 3.14).

The 100% infill density causes a 10% horizontal overlap, compared to the extrusion width, between adjacent filaments: this means that 10% of the volume of two adjacent beads partially occupy the same horizontal space. More overlapping can be obtaining by selecting the "solid infill" option in the slicing software, which, by extruding more material, will print a denser and tougher structure.

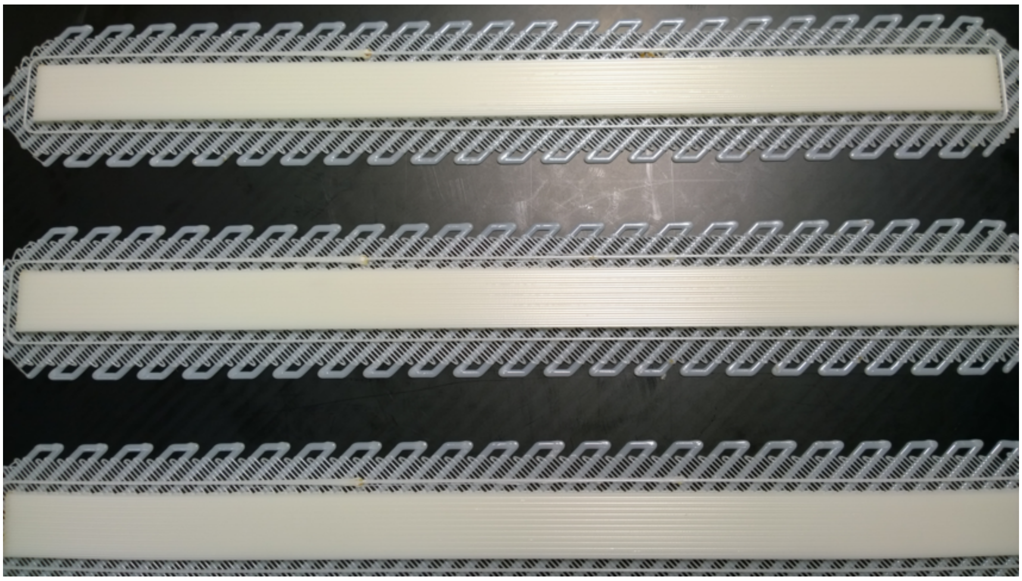

Figure 3.15: Printed samples above the raft support

The specimens have been printed with unidirectional fibers: every layer of a sample has the same geometric disposition. Furthermore, all the layers, except for the first one, retain the same printing features (i.e. they have been printed with the same process parameters). It is a very different layout than the much used criss-cross configuration, where one layer's fibers are rotated by 90° compared to the previous one. An unidirectional disposition allows a thorough characterization of the material, since it isolates the individual contribution of the fibers, both longitudinal and transverse.

The specimen could not be printed directly on the build surface, because the thermoplastic gave rise to adhesion problems, causing distortions and warping of the sample. To solve this issue it has been decided to print the samples on a raft structure with a support interface (fig. 3.15), which is a horizontal latticework of filament that is located underneath the printed part.

In fact, raft supports are primarily used to help with bed adhesion. The raft support used for this work is a five-layer structure, in which the first two bottom layers are made of a thermoplastic material (raft structure) and the three upper layers are made of HIPS (support interface). The only drawback is that printing a raft support, with the HIPS interface, significantly increases build time. Once the entire structure has been printed and has cooled down for some minutes, the support structure is easily removed by mechanical detachment. Tabs have also been printed on the support structure (fig. 3.16).

Figure 3.16: HIPS interface (up) and thermoplastic raft support (down)

3.3.2 G-Code elaboration

Once the specimens design have been elaborated, the next step consists in printing them. First of all, 3D models have been created for both samples and tabs, through Solidworks computer aided design (CAD) software. They have been then exported as STereoLithography (STL) files, which will be subsequently loaded in the slicing software. Currently, there are not slicing programs that directly create the G-Code necessary to print the samples with all the features previously described. Therefore, an extensive elaboration has been made mandatory, to obtain the desired specimen characteristics.

The software used for this purpose are:

- Repetier-Host
- Slic3r
- KISSlicer
- MATLAB software environment

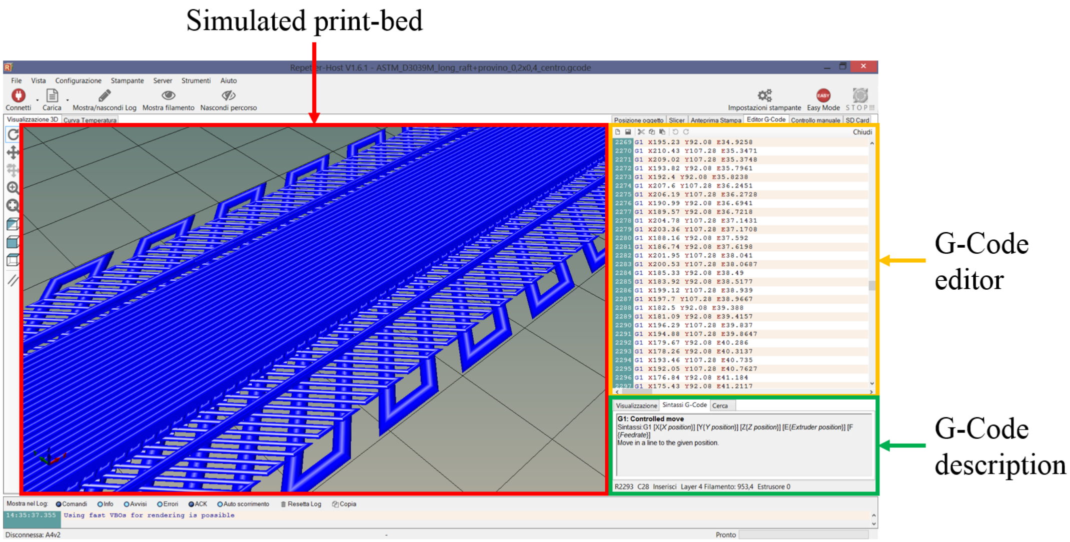

Figure 3.17: Repetier-Host G-Code editor

Repetier-Host is a simple to use host software, which is compatible with most firmwares around. Multiple STL files can be added and positioned on the simulated print-bed and sliced all together. For the slicing procedure, the built-in Slic3r and Skeinforge slicers are available. In the G-Code editor the code can be viewed and changed. A short description of the current code is shown below the editor, to help the user (fig. 3.17). Through USB connection, with Repetier-Host it is possible to manually control various parameters of the 3d printer (fig. 3.18), such as temperatures, speed, flowrate, etc.

Slic3r (fig. 3.19) and KISSlicer (fig. 3.20) are tools that convert a digital 3D model into printing instructions (namely G-Code) for the 3D printer. They cut the model into horizontal slices (layers), generate toolpaths to fill them and calculate the amount of material to be extruded. Slic3r has been used for the generation of the specimens G-Code, while KISSlicer has been used to generate the G-Code for the raft support.

MATLAB software environment has been used to modify a part of the G-Codes, with the purpose of executing a shifting operation of the object, to fix it in the center of the build surface.

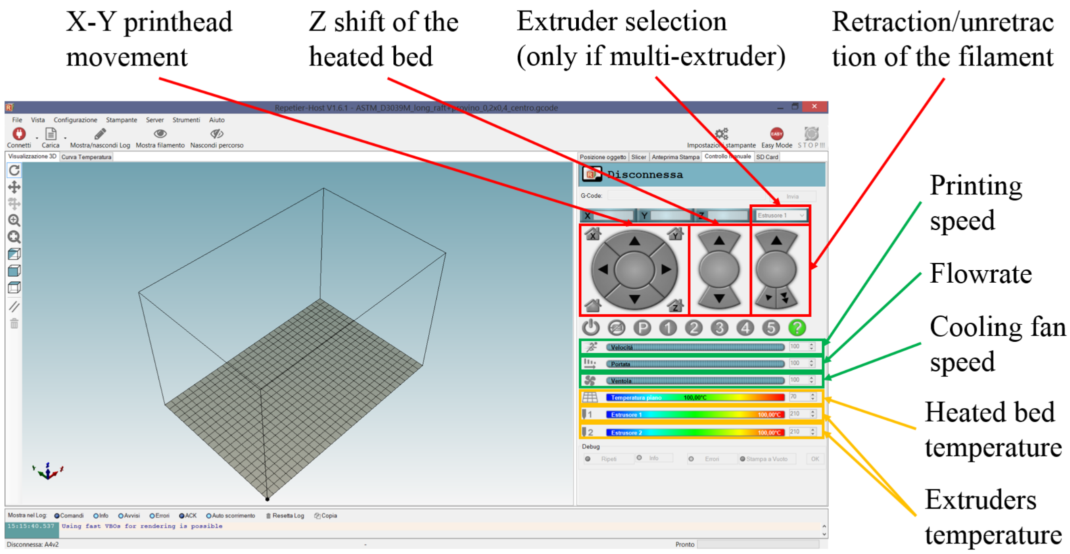

Figure 3.18: Repetier-Host 3d printer monitoring interface

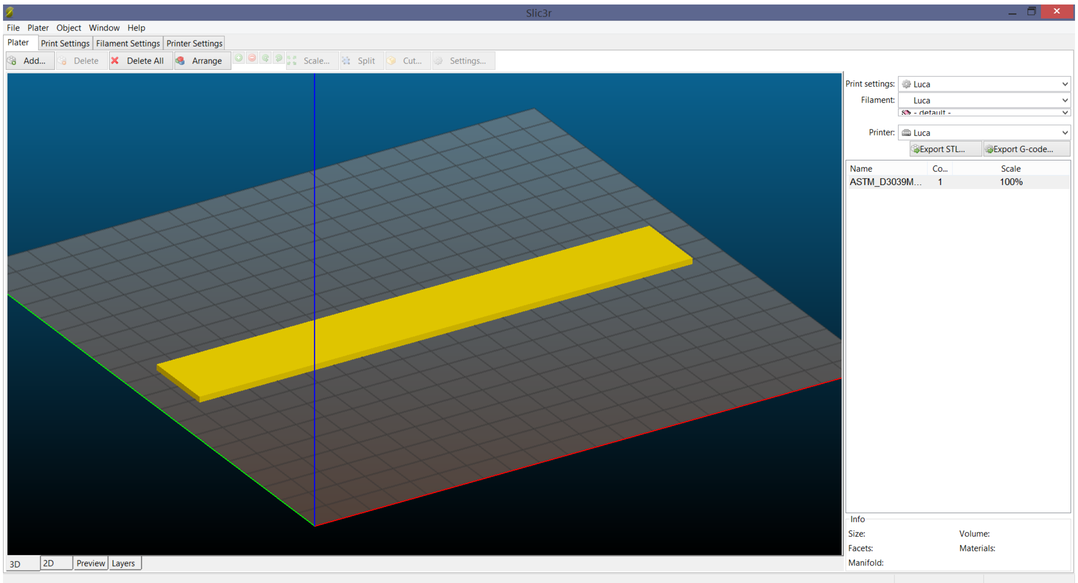

Figure 3.19: An example of Slic3r working interface

In addition to MATLAB modifications, some G-Code part has been changed manually, through a simple text editor, namely Notepad++, mainly because there were too many complications (especially the "hybridization" of the G-Code) to try to automate the entire procedure.

G-Code hybridization

The first step consists in importing the STL file of the specimen in Slic3r and setting the chosen printing parameters. The slicing output will be the G-Code of the specimen, without the raft support underneath, which will be created with KISSlicer. The G-Code produced by Slic3r has two problems:

- The specimen configuration is cross-ply (also called criss-cross), rather than unidirectional,

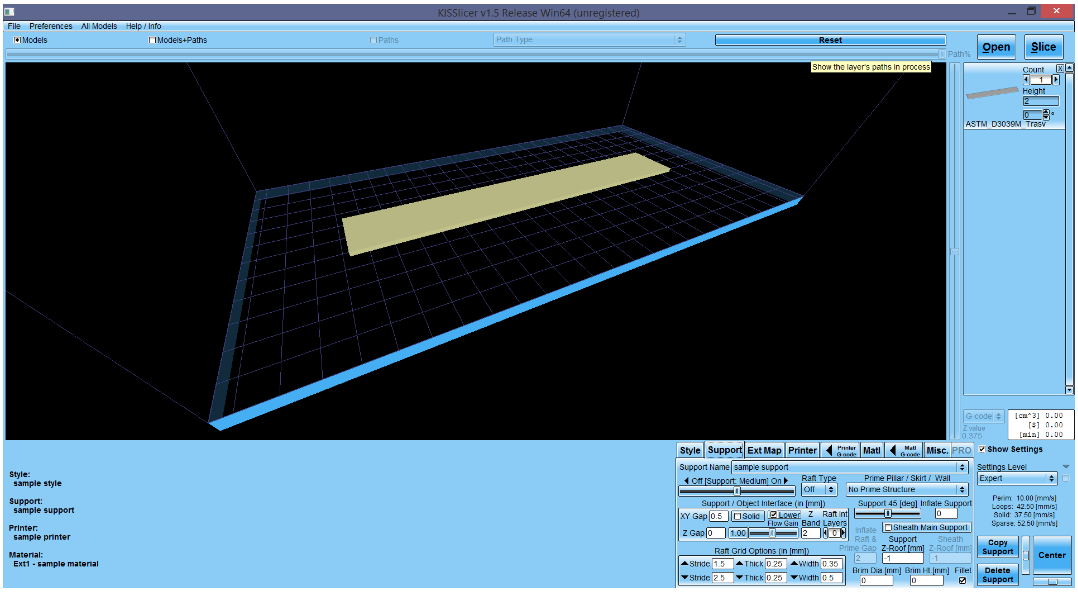

Figure 3.20: An example of KISSlicer working interface

i.e. there is an alternation between layers with perpendicular fibers, in the xy plane (e.g. the first layer has fibers oriented at 0°, the second one fibers oriented at 90°, the third one at 0°, the fourth one at 90°, and so on) (fig. 3.21). This study requires unidirectional fiber configuration: every layer must have the same fiber orientation.

- The sample is not positioned in the center of the build surface. While this issue has not caused any major problem, it has been decided to translate the object to the center of the bed, since it could be convenient to have a centered specimen, to be used as a reference of some sort.

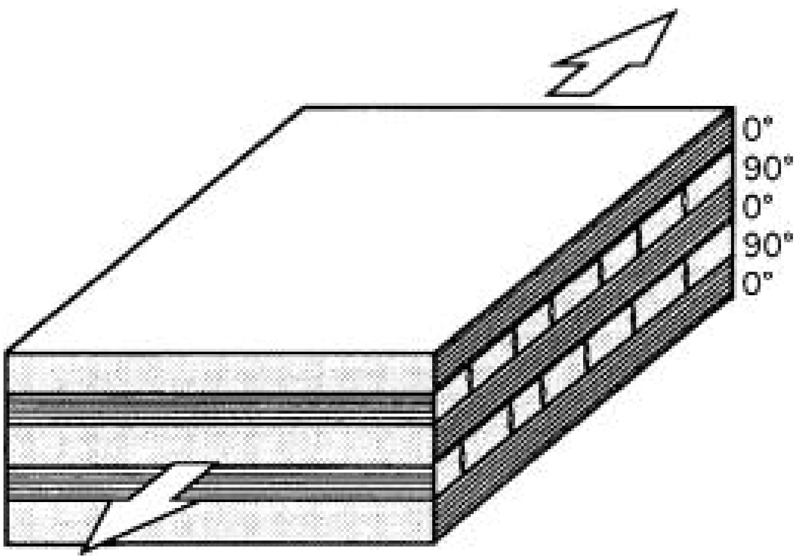

Figure 3.21: Example of cross-ply configuration [98]

The following steps have been carried out, to solve the cross-ply issue:

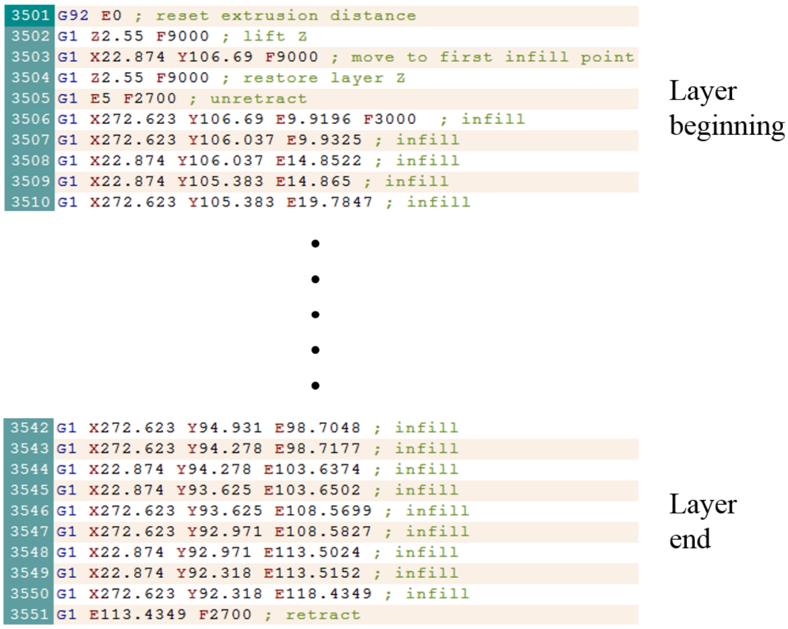

Figure 3.22: Portion of G-Code: beginning and ending of a single layer

1. It is noticeable that, enumerating the layers, starting from the bottom one and then following up, the odd-numbered layers have the correct fiber orientation, while the even-numbered layers have the wrong one. The first step consists in the removal of the G-Code portions that refer to the even layers. The beginning and the ending of a single layer, in a G-Code portion, are shown in fig. 3.22.

2. After the first operation, the same number of layers must be replaced in place of the previous one. These new layers will obviously have the correct fiber orientation, that is the same of the odd-numbered layers. In the second step, the G-Code portion regarding the third layer must be copied and pasted instead of the previously deleted layers. It is important that it is not the first layer to be chosen, but subsequent odd-numbered ones (third, fifth, seventh, etc., it makes no difference), because the first layer usually retains unique properties and features, different from the other ones (e.g. the reduced printing speed, to improve the adhesion).

3. In the final step the heights of the copied layers must be edited to match the values of the deleted ones. To achieve this purpose, the z-coordinate values (fig. 3.23) must be corrected.

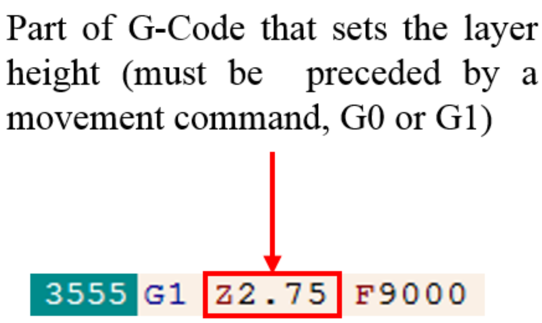

Figure 3.23: Height value of the single layer

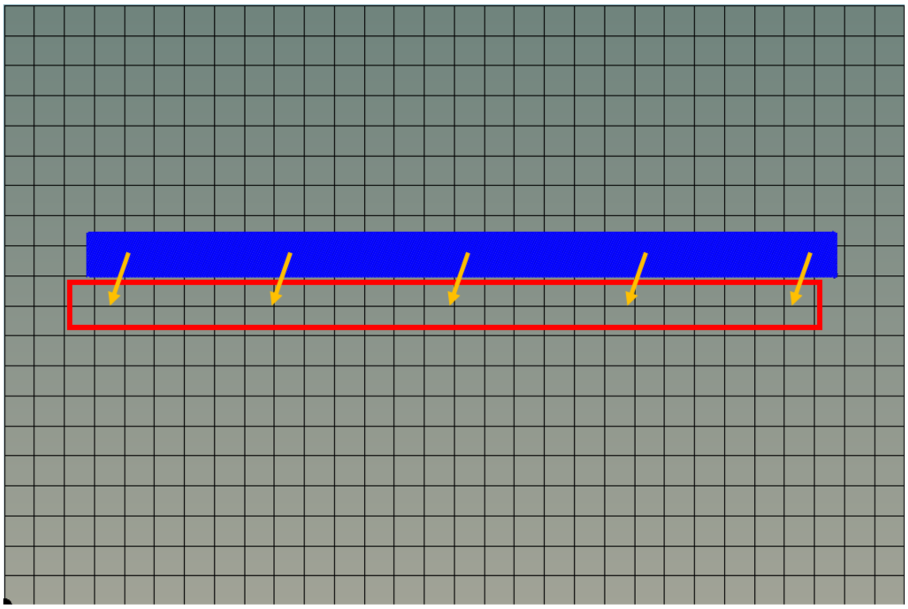

Figure 3.24: Centering the sample

To position the sample in the center of the printing bed, MATLAB software environment has been used:

1. A MATLAB function has been created, to allow the customization of the xyz coordinates of the specimen. The coupon has been centered on the build surface. The shifting procedure only affects the body of the G-Code, excluding pre-printing and post-printing settings (e.g. printhead homing after finishing the printing of the object). When needed, some manual correction of the G-Code has been executed.

2. After shifting the sample (fig. 3.24), the raft support has been centered (fig. 3.25).

3. The final step consists in raising the specimen height, in such a way that it will be positioned directly above the raft support, adding an air gap of 0,1-0,2 mm for Type A material (0 for Type B material) between specimen and support interface, to enable a safe detachment after the printing is finished. Finally, the specimen will be centered above the raft support, as shown in fig. 3.26.

Thanks to the shifting procedure, more specimens could be placed on the printing bed. The process is simple: the G-Code portion including both the raft support and the sample must be copied and pasted in the text file. The initial and final settings portions of the G-Code must not be copied, otherwise many critical issues will arise. This procedure cuts approximately the 10% of the total production time, where total production time includes printing phase, time necessary for build surface and chamber to reach the desired temperature and time necessary to extract the samples from the machine, let them cool down a bit and detach the support interface from them. The results of the procedure is shown both on the simulated printing bed (fig. 3.27) and in a real situation (fig. 3.28).

Taking into account the three different configuration considered (the Type B configuration is almost identical to a Type A one) and the five fiber orientations, a total of 15 "hybridized" G-Codes (because the final G-Code contains code portions generated from Slic3r and KISSlicer) have been created. In addition, every hybrid G-Code has a version in which multiple samples are printed on the same bed surface, thus the overall number of hybrid G-Codes produced is 30.

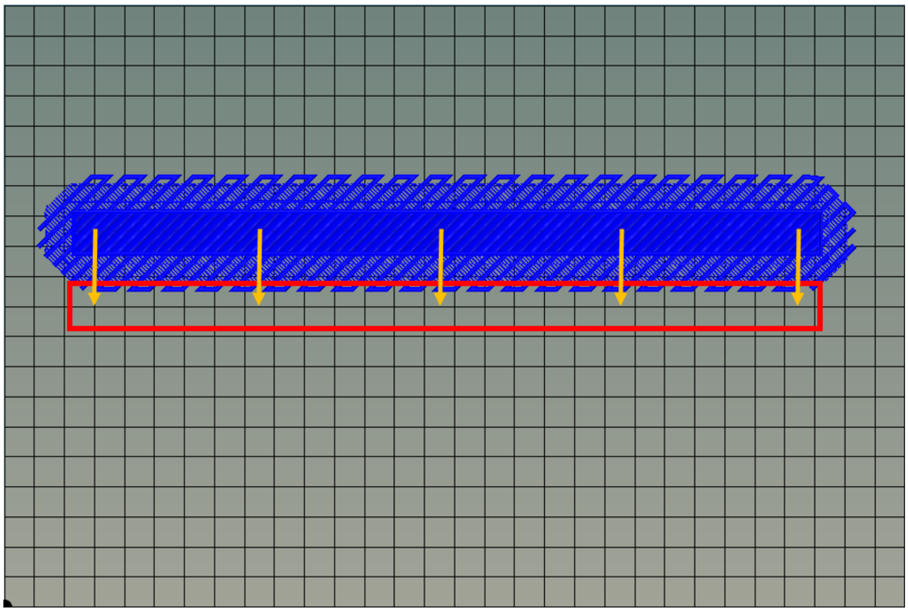

Figure 3.25: Centering the raft support

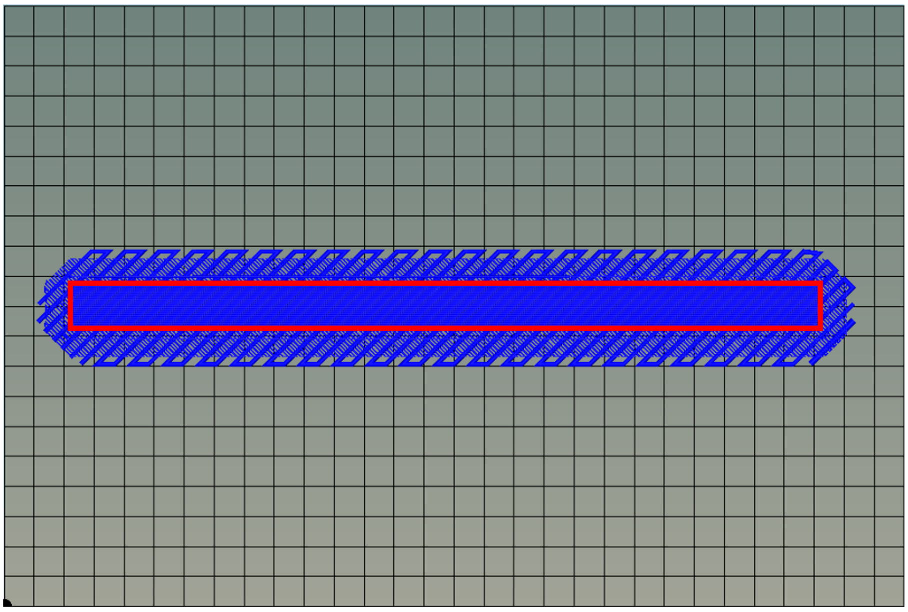

Figure 3.26: The sample is centered above the support interface

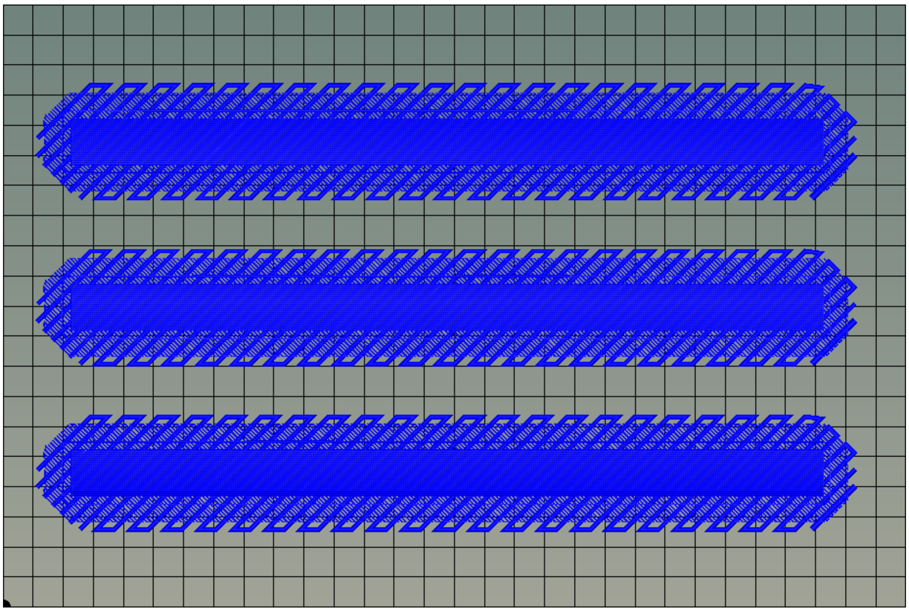

Figure 3.27: More samples can be printed consecutively on the same build surface

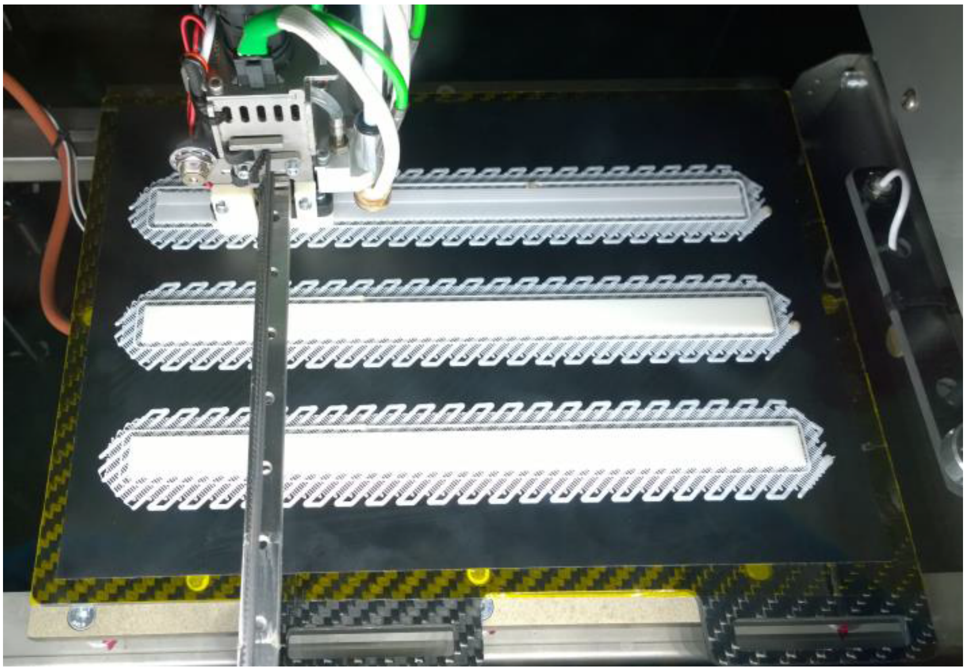

Figure 3.28: Printing of three longitudinal specimens

Tabs did not undergo the same customization of the specimens, so they have been printed with a criss-cross configuration. Furthermore, since tabs did not require a modification of their G-Code, more of them could be printed simply by adding more of the same STL files on the simulated printing bed of the slicing software.

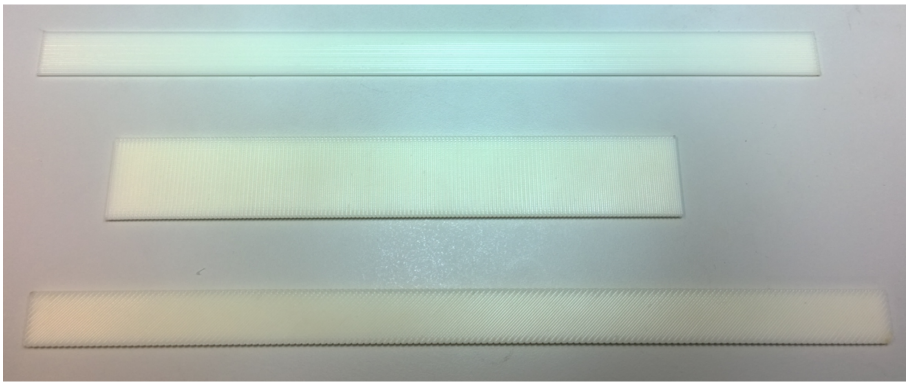

Figure 3.29: Thermoplastic samples after the printing and the support removal

3.3.3 Preparation of the specimens

After producing the necessary G-Codes, the thermoplastic samples have been printed. The 0° and 45° coupons printing went smoothly, without any issue. The 90° specimens gave some problems, mainly because, during the printing, the second extruder attached to the printhead slightly touched the upper side of the specimen, sometimes damaging the structure. The 20° and 70° generally gave printing issues, such as poorly optimized infill path and not so good adhesion to the support interface (partially solved by lowering the air gap). Support interface detachment did not give notable problems in any case.

Table 3.5: Number of valid printed samples

Fiber orientation	Number of specimens
0°	27
90°	28
45°	27
20°	12
70°	12

An extensive number of samples have been printed and tested, as shown in tab. 3.5. The total amount of valid samples is 106, with more than 250 hours of printing time, comprehensive of:

- Initial trials
- Parameter assessment
- Failed prints
- Prototype printing

After the printing phase (fig. 3.29), it is necessary to prepare the specimens for the tensile test. Following the ASTM D3039 standard test method, the real cross section area of every specimen has been measured, applying this procedure:

1. The gage section length of the specimens must be determined as:

$$l_g = \frac{l}{2} \pm w, \tag{3.3}$$

where:

- l_g is the gage section length.
- l is the specimen length.
- w is the specimen width.

The gage section and length for every sample are shown in tab. 3.6:

Table 3.6: Gage sections and gage section lengths for every fiber orientation

Fiber orientation (°)	Sample length (mm)	Sample width (mm)	Gage section (mm)	Gage section length (mm)
0	250	15	125 ± 15	30
90	175	25	87,5 ± 25	50
45	250	15	125 ± 15	30
20	250	15	125 ± 15	30
70	250	15	125 ± 15	30

2. Using a digital caliper, width and height of the sample have been measured at three places in the gage section; the measurements are repeated three times, for a total of nine measures, for both width and thickness. The real cross section area is an essential parameter, so the need for repeated measurements is mandatory, to minimize the error component.

3. The average width and thickness have been calculated.

4. The specimen cross section area has been determined as:

$$\bar{A} = \bar{w}\bar{h}, \tag{3.4}$$

where:

- $\bar{A}$ is the average cross section area.
- $\bar{w}$ is the average width.
- $\bar{h}$ is the average thickness.

A pair of black and white paper markers have been used to measure axial (longitudinal) strain (strain along the loading direction) and have been bonded to the specimens through polyvinyl acetate (PVA) adhesive. They have been positioned directly above the two gage section delimiters. In addition, a second pair of black and white markers have been attached to the specimens, in order to measure the transverse strain (strain perpendicular to the loading direction) and, thus, calculate major Poisson's ratio (with 0° samples). This second set of markers did not need precise positioning: they only needed to have a minimum distance from each other. Axial and transverse strain are measured through a video extensometer, the axial strain in the gage section of the specimen. Before using PVA adhesive, cyanoacrylate glue had been tried, with poor results: this type of glue has the major drawback of wetting the paper marker, darkening its white part. This caused many issues with the video extensometer, since the camera was unable to detect the contrast between black and white. Therefore the choice fell on PVA adhesive, which provides an optimal bonding and does not wet the paper marker, so that black and white contrast is easily detectable.

Once the markers have been manually placed, the real, effective, distance between each pair of markers have been measured, using a digital caliper, at three different places (top, center and bottom). For each place the measure has been executed two times, for a total of six effective measures. The effective distance between each pair of markers is the average of the six measures. This procedure has been applied for both longitudinal and transverse markers.

Afterwards, tabs have been attached to the specimen ends, through cyanoacrylate adhesive, which ensures a strong bonding. Four tabs per sample have been glued, to prevent possible damage from the strong pressure of the tensile machine gripping jaws. Following ASTM D3039 standard test method recommendations, the tabs have been designed in such a way that they do not extend beyond the machine grips, otherwise the coupon is prone to failure at the tab ends, because of excessive interlaminar stresses [61].

Figure 3.30: The specimens are ready to be tested

3.3.4 Tensile test

After the preliminary preparation, the samples are ready to be tested (fig. 3.30). The tensile tests have been conducted in displacement control, using MTS Insight machine. The strain is measured through ME-46 video extensometer. The speed of testing must be set to effect a nearly constant strain rate in the gage section. The strain rate has been selected to produce failure within 1 to 10 minutes, consequently the head displacement rate has been set equal to 2 mm/min, following ASTM D3039 standard test method recommendations. A video extensometer has been used to measure the strain in the gage section: the extensometer gage length was in the range of 30 to 50 mm, depending on the sample configuration (tab. 3.7).

Table 3.7: Main tensile tests parameters, to be used in all the configurations

Parameter	Value
Test running time	1-10 min
Head displacement rate	2 mm/min
Gage length	30-50 mm

The specimen must be placed in the grips of the testing machine, taking care to align the long axis of the gripped specimen with the loading direction; then the grips must be tighten, to securely block the sample (fig. 3.31).

The video extensometer camera detects the black and white contrast of the paper markers, both longitudinal and transverse, to measure the strain during the testing phase. The machine reads the variation of the distance between markers caused by the mechanical deformation of

Figure 3.31: Tensile machine gripping jaws

the specimen. Both the initial gage length and its elongation are measured through the same dimensional factor associated to the single pixel. The software will compute the strain directly measuring the distance between targets as a percentage of the original length, recorded at the beginning of the test. Strain will be therefore calculated as:

$$\varepsilon = \frac{\Delta l}{l_0}, \tag{3.5}$$

where:

- ε is the strain.
- Δl is the difference between actual length and initial length.
- l_0 is the initial length.

It is extremely important that the distance between the camera and the specimen does not change during the entire testing procedure, because a variation will cause an alteration of the image field, distorting the measure. It is also essential that during this phase the room is not lighted by any light source aside from those used for that specific purpose, to avoid interferences (therefore noise) with the video camera.

The real distances (which have been previously measured) between markers have to be inserted in the video extensometer software (fig. 3.32). Once the markers have been defined, an area around them will be created, so that only the data belonging to this area will be processed in the frame buffer. The markers collimation points are selected where the contrast line intersects the average value between the maximum and the minimum gray level given by the target. This collimation

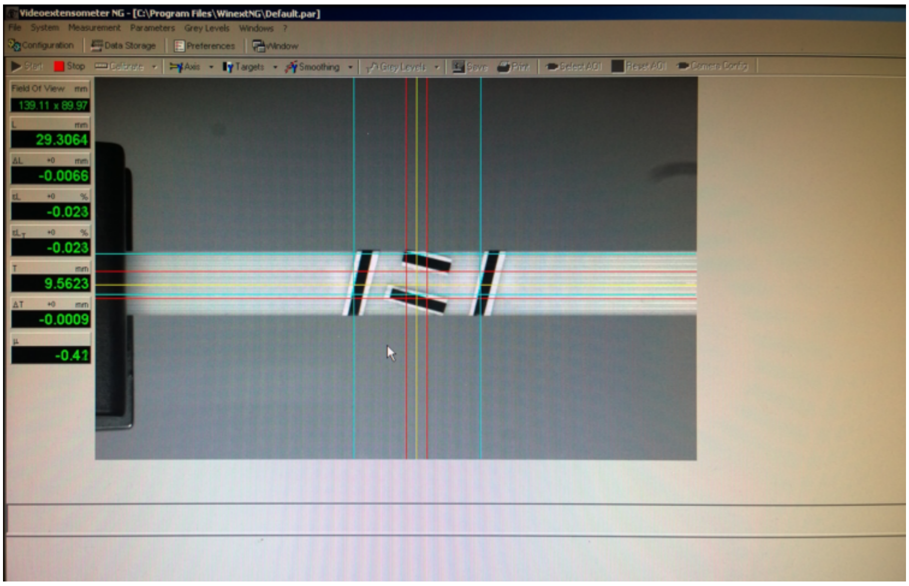

Figure 3.32: Video extensometer

point is dynamically followed and compensated (if its gray level changes), during the elongation of the specimen. Acoustic noise and vibrations must also be avoided, to prevent distortion of measurements.

While the video extensometer records the strain values, it transfers them to Textworks, the tensile machine software, which monitors the state of the tensile test in real time: various parameters can be viewed, such as the load and the stress applied, the deformation of the gage section, the crosshead displacement from its original position, the time elapsed from the test beginning and many others. A stress-strain curve is drawn in real time together with the continuous advancing of the test.

Textworks software (fig. 3.33) allows the user to control the machine crosshead, in such a way that the specimen can be placed in the correct position, so that the gripping jaws extend approximately 10 mm past the beginning of the tabbed portion of the sample. Data acquisition frequency and head displacement speed can be set (following ASTM D3039 standard test method, it has been set to 2 mm/min). Before starting the tensile test, the real cross section area of the specimen (previously measured) must be inserted. Through the software, the test can be started and ended at the user's discretion.

Once the specimen has failed, the testing machine must be stopped and the sample removed from the gripping jaws. The results of the tensile test are saved in a text file: the user decides the parameters of interest that will be reported. For this study, the following parameters have been recorded:

- Load applied (N)
- Time elapsed (s)
- Gage section axial elongation (mm)
- Stress applied (MPa)
- Gage section axial strain (mm/mm)
- Specimen deformation (tabbed portions are excluded, they do not undergo a significant deformation, because of the strong pressure applied by the grip jaws) (mm/mm)

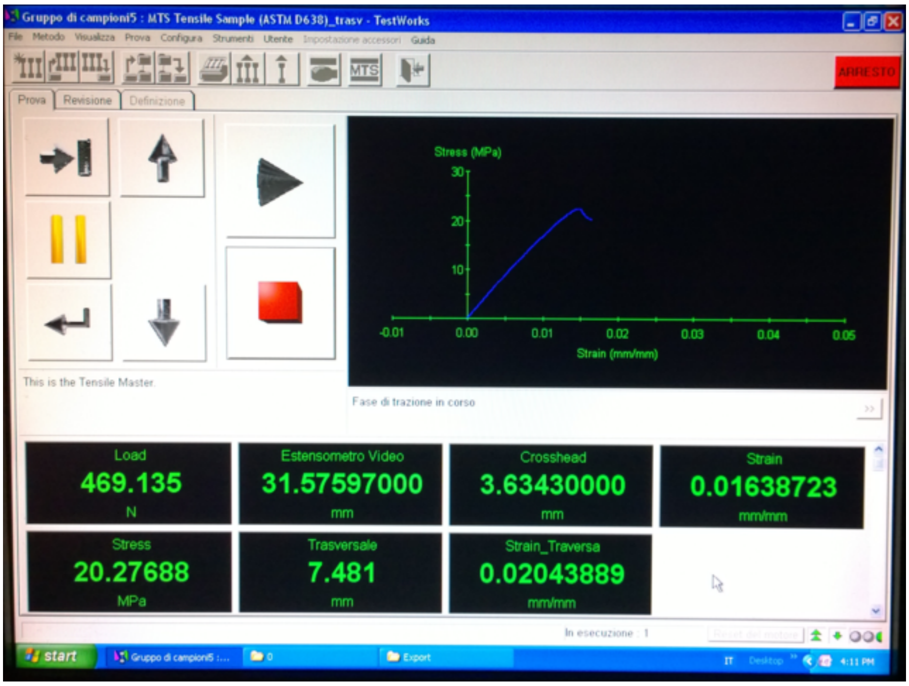

Figure 3.33: Textworks software interface

- Gage section transverse shrinkage (mm)

3.3.5 Data elaboration

The data obtained is not ready to be used yet, an elaboration is necessary for minimizing the eventual noise in the measurements. The data processing consists in the following steps:

- Minimize the noise in the signal through a moving average window.
- Apply the toe compensation to the stress-strain curve.
- Removing possible outliers.

The moving average window serves the purpose of minimizing the noise coming from the strain measurement extracted from the tensile machine results (fig. 3.34). The period of the moving window is 9 (i.e. the average is executed over nine values, the current one, four backward and four forward). The mean is not weighted.

The toe compensation has the purpose of correcting an artifact, called toe region (AC section in fig. 3.35), which does not represent a property of the material. It is an artifact caused by a take-up of slack and alignment or seating of the specimen. In order to obtain correct values of such parameters as tensile modulus, strain, and offset yield point, this artifact must be compensated for, to give the corrected zero point on the strain or extension axis [62].

In the case of a material exhibiting a region of Hookean (linear) behavior (fig. 3.35), a continuation of the linear (CD) region of the curve is constructed through the zero-stress axis. This intersection (B) is the corrected zero-strain point from which all extensions or strains must be measured, including the yield offset (BE), if applicable [62].

To perform the toe compensation, linear regression has been used: the straight line that approximate to the best the linear region of the stress-strain curve must be found. Using Microsoft Excel functions, the three following parameters has been found:

	A	B	C	D	E	F	G	H
1	Load (N)	Time (s)	Extension (mm)	Stress (MPa)	Strain (mm/mm)	Strain_Traversa (mm/mm)	Trasversale (mm)	media centrata
2								
3	0,158	0,5	30,05818	0,0074	****	-0,00000168	7,458	
4	0,201	0,6	30,05826	0,00938	****	-0,00000168	7,458	
5	0,21	0,7	30,05795	0,00983	****	-0,00000168	7,458	
6	0,163	0,8	30,05803	0,00762	****	-0,00000168	7,458	
7	0,156	0,9	30,05784091	0,00728	****	-0,00000168	7,458	
8	0,155	1	30,05822	0,00723	****	-0,00000168	7,458	
9	0,291	2,3	30,05734	0,01361	-0,00002928	-0,00000168	7,458	-0,00002928
10	0,204	2,4	30,05731375	0,00954	-0,00003015	-0,00000168	7,458	-3,05667E-05
11	0,351	2,5	30,05725	0,0164	-0,00003227	-0,00000168	7,458	-0,000025126
12	0,475	2,6	30,05713	0,02219	-0,00003626	0,00000955	7,458	-1,17686E-05
13	0,972	2,7	30,05829	0,04539	0,00000233	0,00002752	7,458	2,04189E-05
14	1,513	2,8	30,05866	0,07069	0,00001464	0,00004493	7,458	5,03978E-05
15	2,134	2,9	30,05908	0,09971	0,00002861	0,00006234	7,458	8,94933E-05
16	2,802	3	30,06131	0,13092	0,0001028	0,00008031	7,459	0,000134752
17	3,279	3,1	30,06313	0,15317	0,00016335	0,00009885	7,459	0,000190828
18	4,063	3,2	30,06545	0,18983	0,00024053	0,00011738	7,459	0,000250416
19	4,606	3,3	30,06789	0,21518	0,00032171	0,00013536	7,459	0,000314366
20	5,205	3,4	30,06949364	0,24315	0,00037506	0,00015277	7,459	0,000380792
21	5,736	3,5	30,0723	0,26797	0,00046842	0,0001713	7,46	0,000443781
22	6,565	3,6	30,07441	0,30671	0,00053862	0,00019096	7,46	0,000503776
23	7,28	3,7	30,07596	0,34013	0,00059019	0,00021061	[illegible]	0,000559223
24	8,008	3,8	30,07705	0,37414	0,00062645	0,00022859	7,461	0,000607093
25	8,606	3,9	30,07835	0,40208	0,0006697	0,00024656	7,461	0,000652696
26	9,372	4	30,07936	0,43783	0,0007033	0,00026509	7,46	0,000689107
27	10,038	4,1	30,08045	0,46897	0,00073956	0,00028419	7,461	0,000722598
28	10,779	4,2	30,08084	0,50358	0,00075254	0,00030329	7,461	0,000750359
29	11,51	4,3	30,08183	0,53774	0,00078548	0,00032182	7,461	0,000778083

Average of nine strain values

Figure 3.34: Simple centered moving average window of period 9.

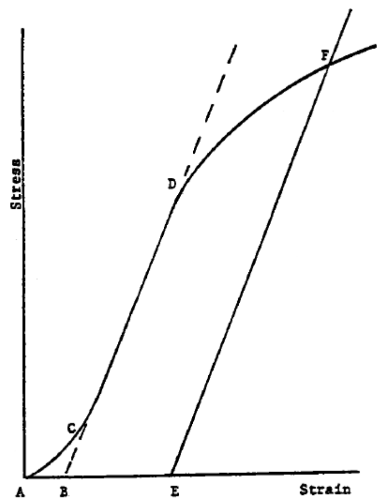

Figure 3.35: Toe region (AC) for material with a Hookean behavior [62]

- The slope of the linear regression line between the known coordinates.
- The intercept of the linear regression line between the known coordinates (i.e. the line interception point with the y-axis, drawing a linear regression between the known coordinates).
- The square root of Pearson moment correlation coefficient between the known coordinates, which is the correlation coefficient between the linear regression line and the linear region.

Once a satisfying correlation has been found (at least above 99%), a shifting value has been calculated, through the following formula:

$$s = -\frac{b}{a}, \tag{3.6}$$

where:

- s is the shifting value.

- b is the intercept value.
- a is the slope value.

Adding the shift to the average strain values previously calculated through the mobile mean window, the corrected strain values are obtained. Finally, the corrected stress-strain curve can be plotted (fig. 3.36).

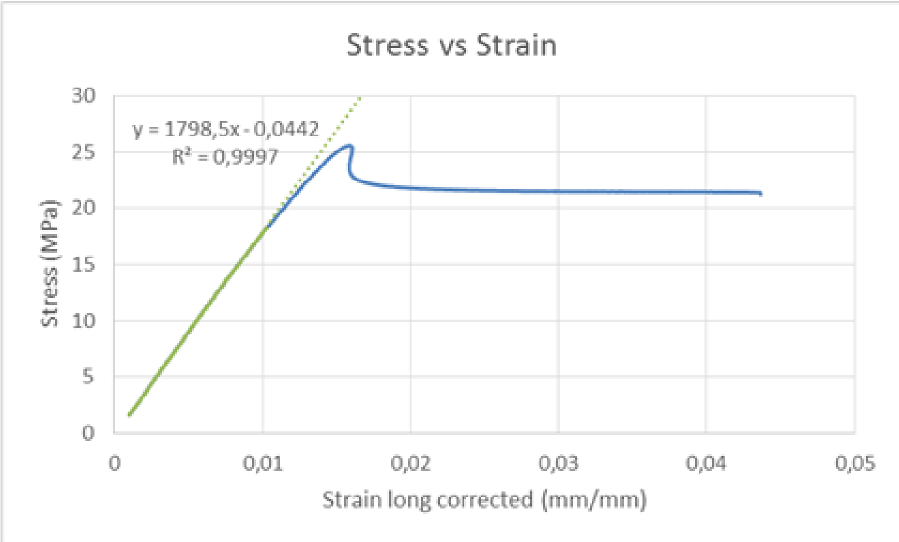

Figure 3.36: Example of corrected stress-strain curve, with the linear regression line

After the preliminary data elaboration, the following parameters of interest have been calculated:

- Tensile chord modulus of elasticity.
- Major Poisson's ratio by chord method (for 0° samples).
- Yield stress.
- Yield strain.
- Failure stress.
- Failure strain.
- Shear modulus.
- Shear strength.

Tensile chord modulus of elasticity is the slope of the chord drawn between any two specified points on the stress-strain curve [5]. To calculate the tensile chord modulus of elasticity, after selecting a strain range between 0,001 and 0,003 (absolute strain), the following equation (3.7) has been used:

$$E = \frac{\Delta\sigma}{\Delta\varepsilon}, \tag{3.7}$$

where:

- E is tensile chord modulus of elasticity.

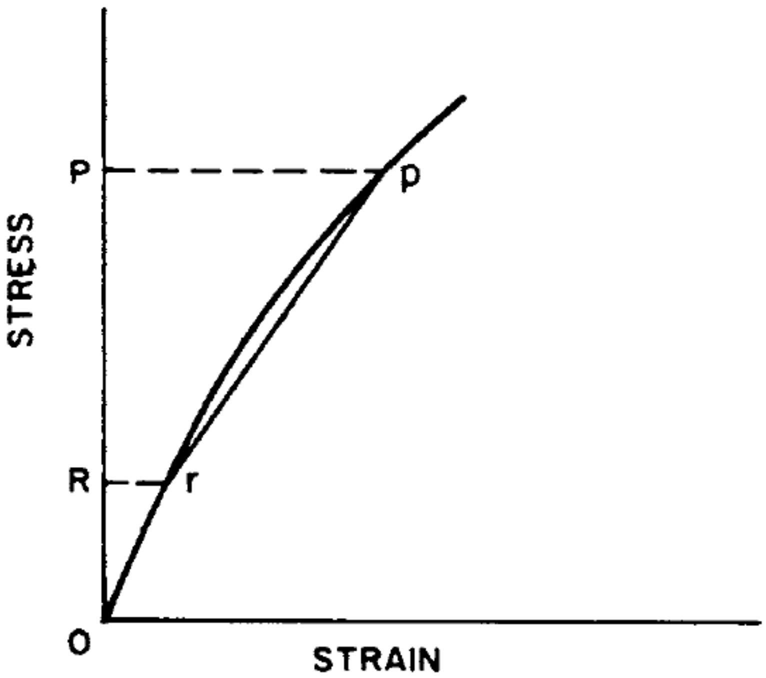

Figure 3.37: Chord modulus between two stress points [5]

- $\Delta\sigma$ is the difference in applied tensile stress between the two strain points previously chosen.
- $\Delta\varepsilon$ is the difference between the two strain points (nominally 0,002).

Since data was not available at the exact strain range end points (as often occurs with digital data), the closest available data points have been used.

The same procedure must be followed to calculate Poisson's ratio by chord method, using the following equation (3.8):

$$\nu = -\frac{\Delta\varepsilon_t}{\Delta\varepsilon_l}, \tag{3.8}$$

where:

- ν is major Poisson's ratio calculated by chord method.
- $\Delta\varepsilon_t$ is the difference in transverse strain between two longitudinal strain points.
- $\Delta\varepsilon_l$ is the difference between two longitudinal strain points (nominally 0,002).

Yield stress and strain have been calculated as:

$$\sigma_p = \max(\sigma_i), \qquad \varepsilon_p = \varepsilon(\sigma_p), \qquad i = 1, ..., n, \tag{3.9}$$

where:

- σ_p is yield stress (peak stress).
- ε_p is yield strain.
- n is the total number of recorded stress values.

Failure stress and strain have been calculated as:

$$\sigma_f = \sigma_i|_{i=k}, \qquad \varepsilon_f = \varepsilon(\sigma_f), \qquad i = 1, ..., n, \tag{3.10}$$

where:

- σ_f is failure stress.
- ε_f is failure strain.
- n is the total number of recorded stress values.
- k is the first failure point.

Since a torsion testing machine was not available, shear modulus has been calculated through the following equation (3.11) [44]:

$$G_{12} = \frac{1}{\frac{4}{E_{xx}^{45}} - \frac{1}{E_{11}} - \frac{1}{E_{22}} + \frac{2\nu_{12}}{E_{11}}}, \tag{3.11}$$

where:

- G_{12} is shear modulus.
- E_{xx}^{45} is axial tensile modulus of 45° specimens.
- E_{11} is axial tensile modulus of 0° specimens.
- E_{22} is axial tensile modulus of 90° specimens.
- ν_{12} is major Poisson's ratio.

Finally, for shear strength, Tsai-Hill failure criterion has been considered:

$$\left(\frac{\sigma_1}{S_1}\right)^2 + \left(\frac{\sigma_2}{S_2}\right)^2 + \left(\frac{\tau_{12}}{S_{12}}\right)^2 - \left(\frac{\sigma_1\sigma_2}{S_1^2}\right) \leq 1, \tag{3.12}$$

where:

- σ_1 is the applied axial tensile stress.
- σ_2 is the applied transverse tensile stress.
- τ_{12} is the applied shear stress.
- S_1 is the ultimate axial tensile stress.
- S_2 is the ultimate transverse tensile stress.
- S_{12} is the ultimate shear stress.

In the case of an uniaxial state of tension, equation (3.12) becomes:

$$\sigma_x^2 \left[\frac{cos^4\theta}{S_1^2} + \frac{sin^4\theta}{S_2^2} + \frac{cos^2\theta sin^2\theta}{S_{12}^2} - \frac{cos^2\theta sin^2\theta}{S_1^2}\right] = 1, \tag{3.13}$$

where:

- θ is the angle between loading direction x and fiber direction.

- σ_x is the applied tensile stress in the traction direction x.

For $\theta = 45$ you have $cos\theta = sin\theta$, therefore (3.13) is reduced to:

$$\sigma_x^2 \left[\frac{sin^4\theta}{S_2^2} + \frac{cos^2\theta sin^2\theta}{S_{12}^2} \right] = 1. \tag{3.14}$$

Expliciting the ultimate shear strength, equation (3.14) becomes:

$$S_{12} = \left(\frac{1}{\frac{1}{\sigma_x^2 sin^4\theta} - \frac{1}{S_2}} \right)^{\frac{1}{2}}. \tag{3.15}$$

Knowing both σ_x and θ, S_{12} is easily calculated.

Once these parameters have been determined, arithmetic average, standard deviation, sample variance and standard uncertainty have been calculated for every specimen configuration. Through a Tukey boxplot, eventual outliers have been removed: the data must be included within 1,5 interquartile range (IQR) of the lower quartile and 1,5 IQR of the upper quartile [24].

Chapter 4

Results and discussion

4.1 Tensile tests results

For every configuration, average values and the respective standard deviations, for elastic constants, yield strengths and failure strains, are shown in Table 4.1, 4.2 and 4.3, respectively.

Table 4.1: Elastic constants

Configuration	E_1 [MPa]	E_2 [MPa]	ν_{12} [1]	G_{12} [MPa]
Configuration 1	1810 ± 63	1695 ± 112	0,32 ± 0,1	617 ± 43
Configuration 2	2010 ± 153	1671 ± 57	0,32 ± 0,1	641 ± 47
Configuration 3	1953 ± 83	1752 ± 63	0,35 ± 0,05	772 ± 47
Configuration 4	1606 ± 152	1842 ± 154	0,3 ± 0,2	643 ± 109

Table 4.2: Yield strengths

Configuration	σ_1 [MPa]	σ_2 [MPa]	σ_{12} [MPa]
Configuration 1	25,5 ± 0,2	16 ± 1	13,7 ± 0,6
Configuration 2	26,3 ± 0,2	14,6 ± 0,4	12 ± 0,7
Configuration 3	23,7 ± 0,7	17 ± 0,4	13,2 ± 0,3
Configuration 4	28,6 ± 0,6	22,3 ± 0,7	13,4 ± 0,3

Table 4.3: Failure strains

Configuration	ε_1 [mm/mm]	ε_2 [mm/mm]
Configuration 1	0,04 ± 0,02	0,012 ± 0,002
Configuration 2	0,021 ± 0,007	0,014 ± 0,002
Configuration 3	0,016 ± 0,002	0,017 ± 0,002
Configuration 4	0,31 ± 0,07	0,028 ± 0,004

Below, tensile tests results are shown in detail, for every configuration. Stress-strain curves and tables containing test data are displayed. Elastic modulus and yield strength trends, both function of fiber orientation θ, are plotted in graphics, with experimental data (0°, 90°, 45° orientation) and validation data (20°, 70° orientation). Two comparisons have been carried out:

- Comparison between three different cross sections, with the same material.

- Comparison between two different materials, with the same cross section.

Stress-strain curves and data tables have been made with Microsoft Excel package, while elastic modulus and uniaxial strength function of fiber orientation have been made with Wolfram Mathematica environment.

The following data tables contain Young's modulus, yield stress and strain, failure stress and strain and Poisson's ratio (for 0° orientation), with the respective average, standard deviation and uncertainty. Uncertainty measure has been obtained by calculating the square root of the sample variance.

Screenshots of every tested specimen are displayed at the end of the section.

Note: numbers marked by * are considered outliers and are not included in the calculation of mean, standard deviation and uncertainty.

4.1.1 Configuration 1: Type A material, cross section 0,2 x 0,4

Fiber orientation: 0°

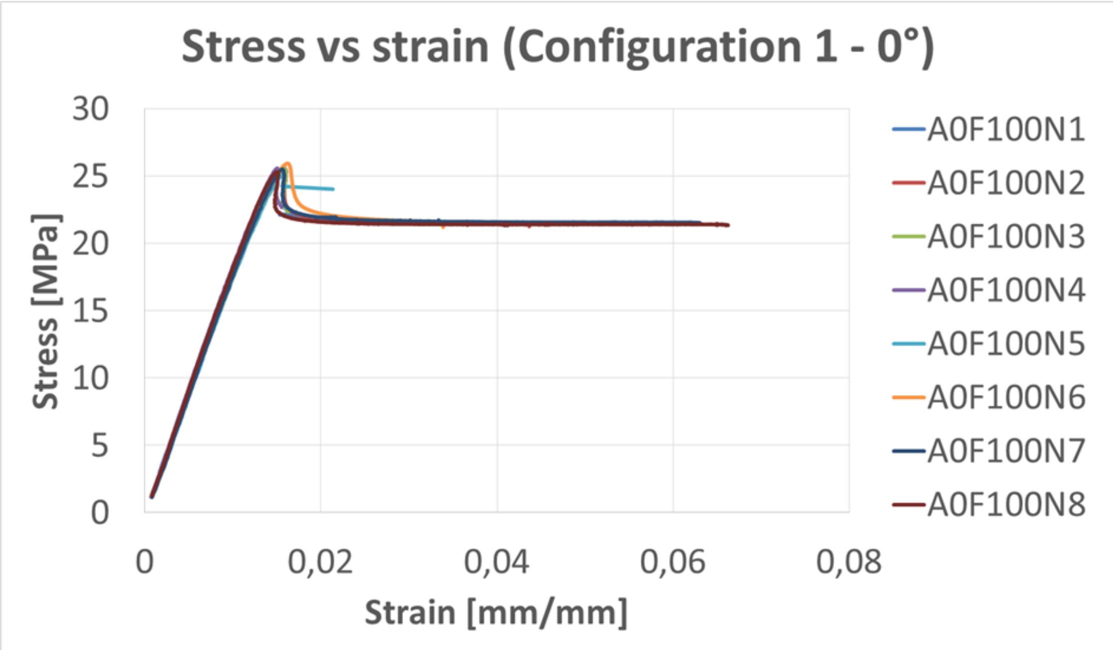

Figure 4.1: Stress-strain curves, configuration 1, 0° orientation

Table 4.4: Tensile test data, configuration 1, 0° orientation

Sample	Young modulus [MPa]	Poisson ratio	Yield stress [MPa]	Yield strain [mm/mm]	Failure stress [MPa]	Failure strain [mm/mm]
A0F100N1	1820	0,22	25,6	0,0157	21,4	0,0281
A0F100N2	1821	1,80*	25,6	0,0159	21,3	0,0437
A0F100N3	1782	-0,53*	25,5	0,0159	22,4	0,0163
A0F100N4	1921	0,30	25,6	0,0150	22,7	0,0155
A0F100N5	1758	0,38	25,1	0,0157	24,0	0,0214
A0F100N6	1770	0,24	25,9	0,0162	21,2	0,0339
A0F100N7	1734	0,29	25,5	0,0157	21,5	0,0631
A0F100N8	1875	0,49	25,3	0,0151	21,3	0,0659
Mean	**1810**	**0,32**	**25,5**	**0,0156**	**22,0**	**0,04**
St. dev.	**63**	**0,10**	**0,2**	**0,0004**	**1,0**	**0,02**
Uncertainty	**24**	**0,04**	**0,1**	**0,0001**	**0,4**	**0,01**

Fiber orientation: 90°

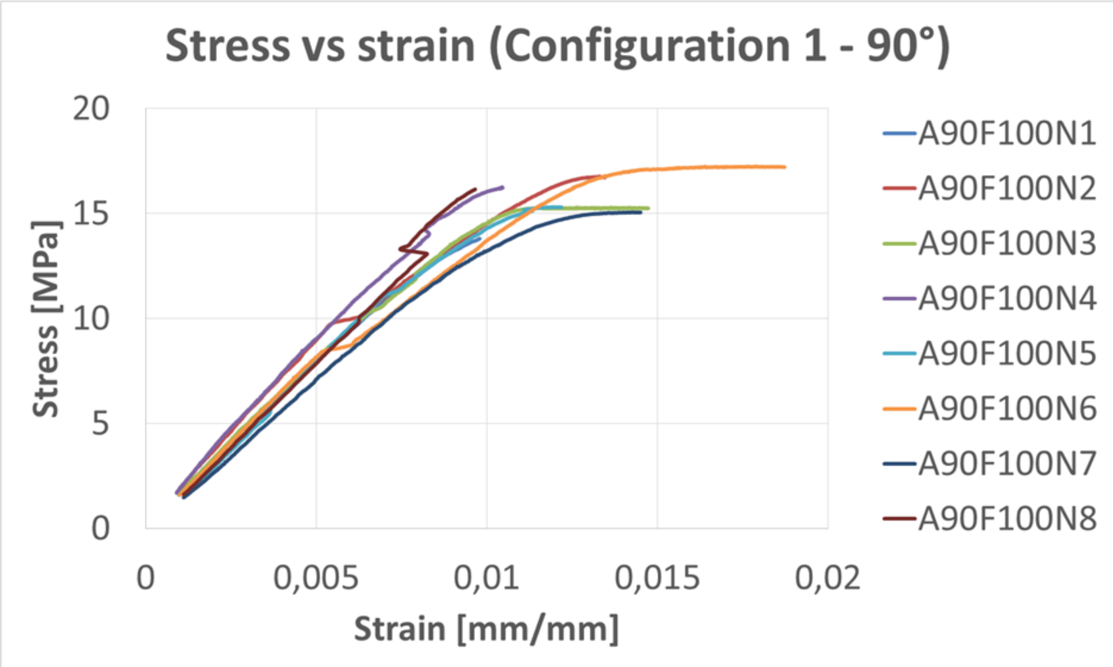

Figure 4.2: Stress-strain curves, configuration 1, 90° orientation

Table 4.5: Tensile test data, configuration 1, 90° orientation

Sample	Young modulus [MPa]	Yield stress [MPa]	Yield strain [mm/mm]	Failure stress [MPa]	Failure strain [mm/mm]
A90F100N1	1620	13,8	0,0098	13,8	0,0098
A90F100N2	1853	16,8	0,0133	16,7	0,0133
A90F100N3	1678	15,3	0,0120	15,2	0,0120
A90F100N4	1855	16,3	0,0104	16,2	0,0104
A90F100N5	1589	15,3	0,0119	15,3	0,0119
A90F100N6	1653	17,2	0,0179	17,2	0,0220*
A90F100N7	1411*	15,0	0,0143	15,0	0,0143
A90F100N8	1619	16,1	0,0097	16,1	0,0097
Mean	**1695**	**16**	**0,012**	**16**	**0,012**
St.dev.	**112**	**1**	**0,003**	**1**	**0,002**
Uncertainty	**46**	**0,4**	**0,001**	**0,4**	**0,001**

Fiber orientation: 45°

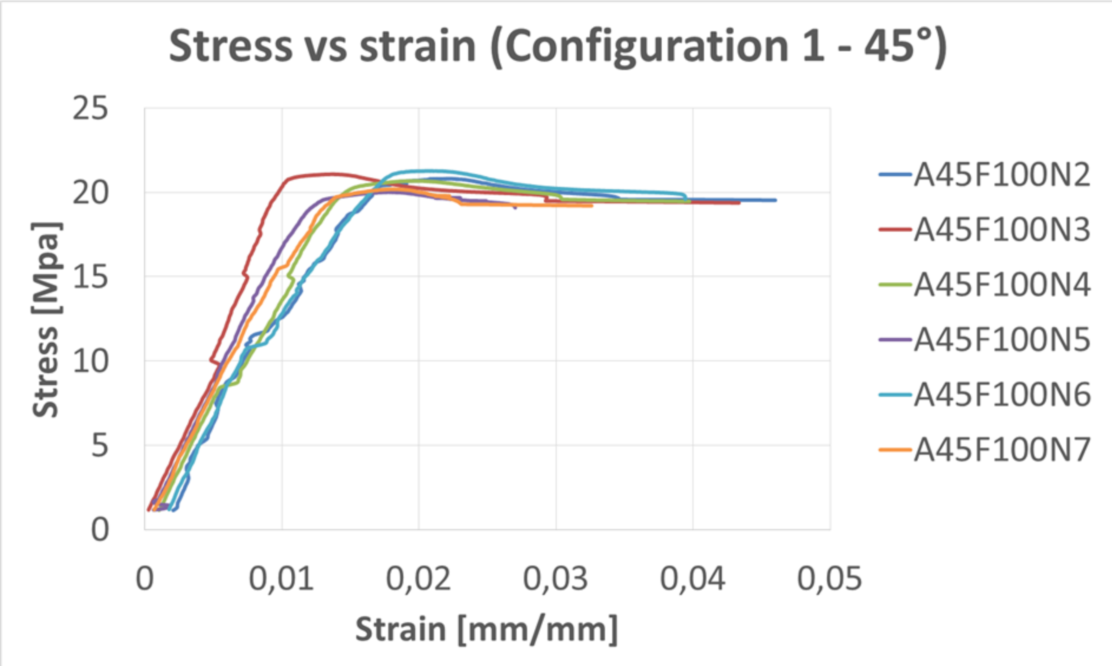

Figure 4.3: Stress-strain curve, configuration 1, 45° orientation

Table 4.6: Tensile test data, configuration 1, 45° orientation

Sample	Young modulus [MPa]	Yield stress [MPa]	Yield strain [mm/mm]	Failure stress [MPa]	Failure strain [mm/mm]
A45F100N1*	NV*	NV*	NV*	NV*	NV*
A45F100N2	1999*	20,8	0,0221	19,5	0,0460
A45F100N3	1689	21,1	0,0137*	19,4	0,0433
A45F100N4	1648	20,7	0,0197	19,5	0,0397
A45F100N5	1684	20,0	0,0180	19,0	0,0245
A45F100N6	1595	21,3	0,0205	19,6	0,0394
A45F100N7	1685	20,2	0,0182	19,2	0,0326
A45F100N8	1653	NV*	NV*	NV*	NV*
Mean	**1659**	**20,7**	**0,020**	**19,4**	**0,038**
St. dev.	**36**	**0,5**	**0,002**	**0,2**	**0,008**
Uncertainty	**16**	**0,2**	**0,001**	**0,1**	**0,004**

Fiber orientation: 20° - 70°

Table 4.7: Tensile test data, configuration 1, 20° orientation

Sample	Young modulus [MPa]	Yield stress [MPa]	Yield strain [mm/mm]	Failure stress [MPa]	Failure strain [mm/mm]
A20F100NV4	1959	25,4	0,0152	25,1	0,0153
A20F100NV5	2022	24,6	0,0143	24,6	0,0143
A20F100NV6	1853	23,6	0,0144	23,6	0,0144
Mean	**1944**	**24,5**	**0,0146**	**24,4**	**0,015**
St. dev.	**85**	**0,9**	**0,0005**	**0,8**	**0,001**
Uncertainty	**60**	**0,6**	**0,0003**	**0,5**	**0,000**

Table 4.8: Tensile test data, configuration 1, 70° orientation

Sample	Young modulus [MPa]	Yield stress [MPa]	Yield strain [mm/mm]	Failure stress [MPa]	Failure strain [mm/mm]
A70F100NV4	1851	20,8	0,0133	20,5	0,0154
A70F100NV5	1749	19,2	0,0131	18,9	0,0221
A70F100NV6	1654	19,5	0,0134	19,3	0,0302
Mean	**1751**	**19,8**	**0,0133**	**19,6**	**0,023**
St. dev.	**98**	**0,8**	**0,0002**	**0,9**	**0,007**
Uncertainty	**70**	**0,6**	**0,0001**	**0,6**	**0,005**

Elastic modulus and uniaxial strength in function of the fiber angle θ

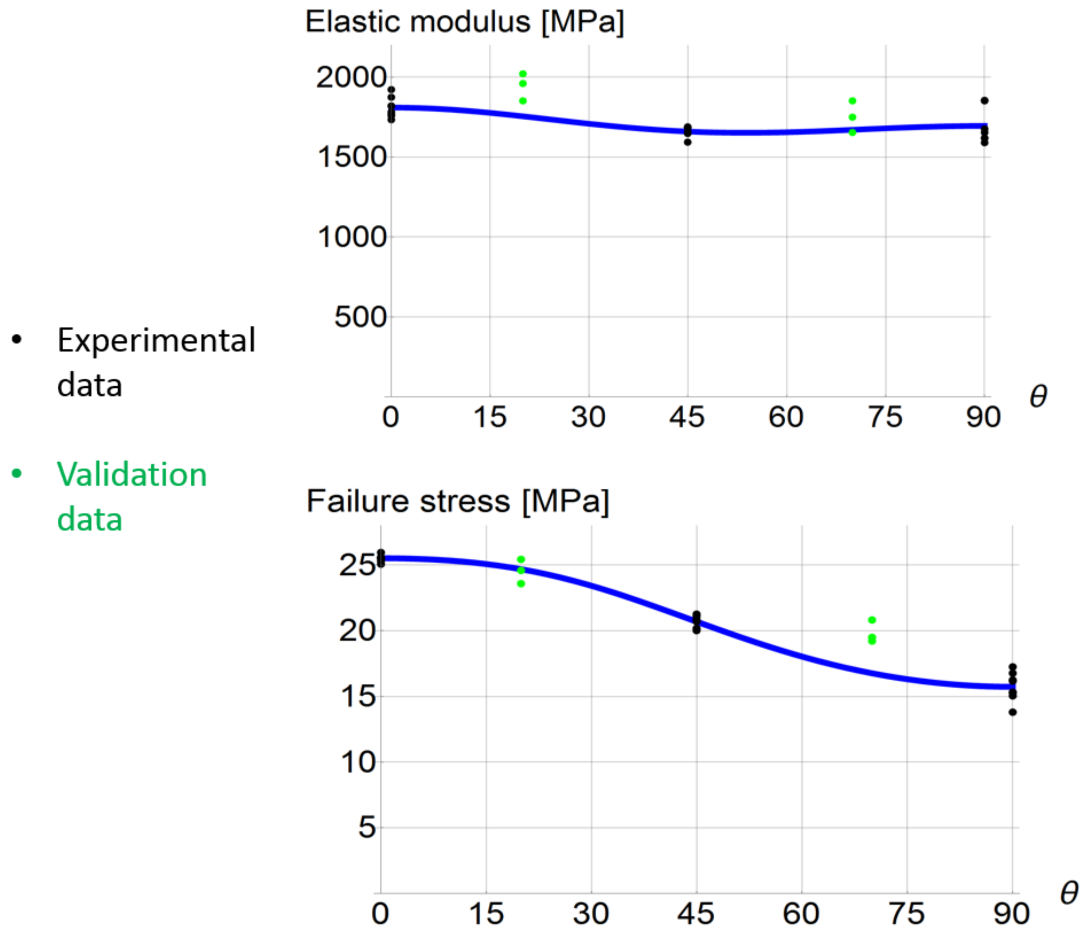

Figure 4.4: Stiffness and strength in function of the fiber angle θ, configuration 1

Configuration 1 tests results discussion

0° specimens show a ductile behavior, with an initial region of linear elasticity, followed by a yielding zone and finally a region of plasticity. Conversely, 90° samples show a brittle behavior, with no plasticity region. 45° coupons' mechanical response is approximately a middle way between 0° behavior and 90° behavior. Elastic modulus is greater at 0°, while for 45° and 90° there is no big difference. Strength at 90° is approximately 60% of strength at 0°, while specimens at 45° lie in the middle: this means that fiber orientation plays a significant role regarding strength of 3D-printed objects. 20° and 70° samples show good fitting with the theoretical curve. Excellent fitting is exhibited by 20° specimens for strength, while 70° specimens have been slightly underestimated.

4.1.2 Configuration 2: Type A material, cross section 0,25 x 0,5

Fiber orientation: 0°

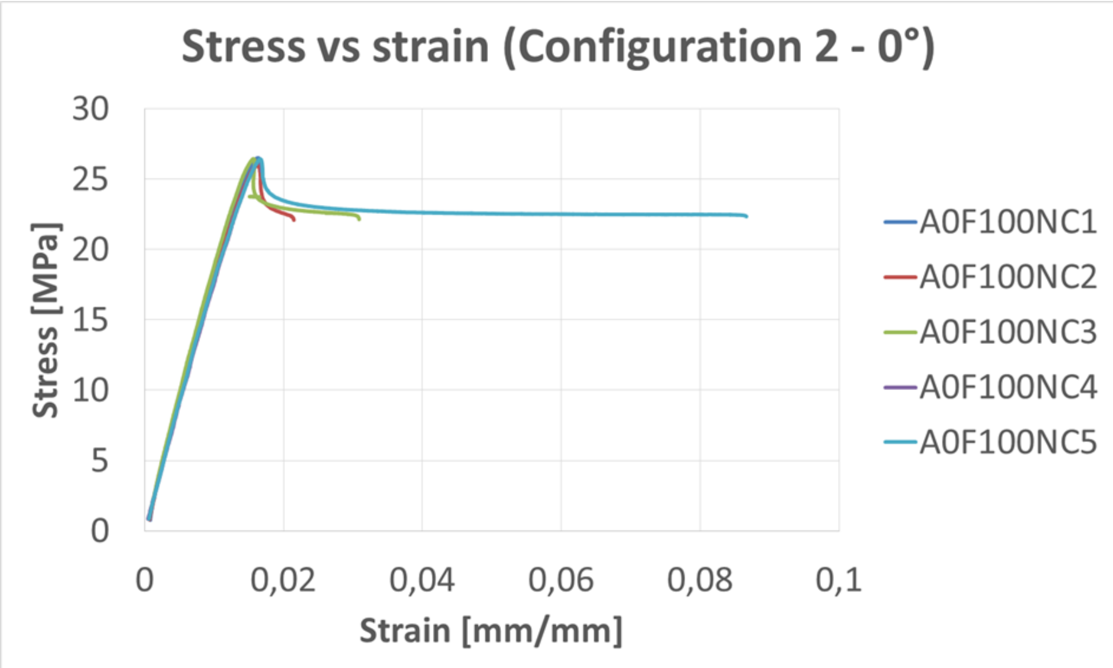

Figure 4.5: Stress-strain curve, configuration 2, 0° orientation

Table 4.9: Tensile test data, configuration 2, 0° orientation

Sample	Young modulus [MPa]	Yield stress [MPa]	Yield strain [mm/mm]	Failure stress [MPa]	Failure strain [mm/mm]
A0F100NC1	2188	26,5	0,0163	25,9	0,0166
A0F100NC2	2039	25,9	0,0162	22,1	0,0215
A0F100NC3	2118	26,4	0,0156	22,1	0,0309
A0F100NC4	1836	26,3	0,0165	25,5	0,0168
A0F100NC5	1870	26,4	0,0166	22,3	0,0866*
Mean	**2010**	**26,3**	**0,0163**	**24**	**0,0214**
St. dev.	**153**	**0,2**	**0,0004**	**2**	**0,0067**
Uncertainty	**77**	**0,1**	**0,0002**	**1**	**0,0039**

Fiber orientation: 90°

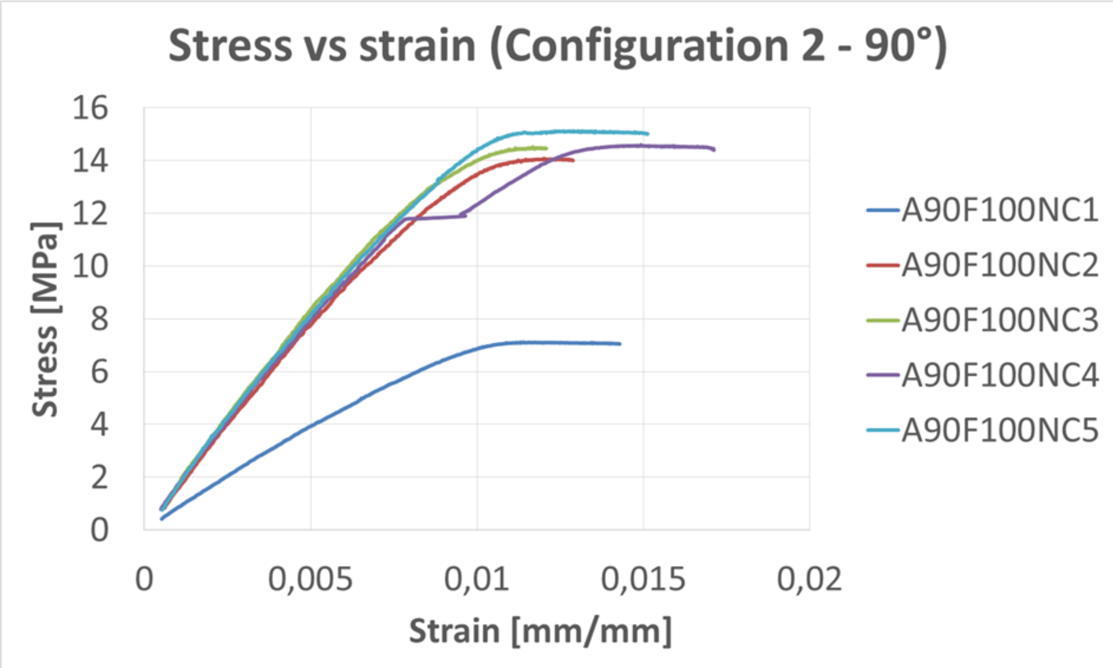

Figure 4.6: Stress-strain curve, configuration 2, 90° orientation

Table 4.10: Tensile test data, configuration 2, 90° orientation

Sample	Young modulus [MPa]	Yield stress [MPa]	Yield strain [MPa]	Failure stress [MPa]	Failure strain [MPa]
A90F100NC1	797*	7,1*	0,0114	7,0*	0,0143
A90F100NC2	1603	14,1	0,0120	14,0	0,0129
A90F100NC3	1719	14,5	0,0117	14,5	0,0121
A90F100NC4	1644	14,6	0,0149	14,4	0,0171
A90F100NC5	1718	15,1	0,0130	15,0	0,0151
Mean	**1671**	**14,6**	**0,013**	**14,5**	**0,014**
St. dev.	**57**	**0,4**	**0,001**	**0,4**	**0,002**
Uncertainty	**33**	**0,2**	**0,001**	**0,2**	**0,001**

Fiber orientation: 45°

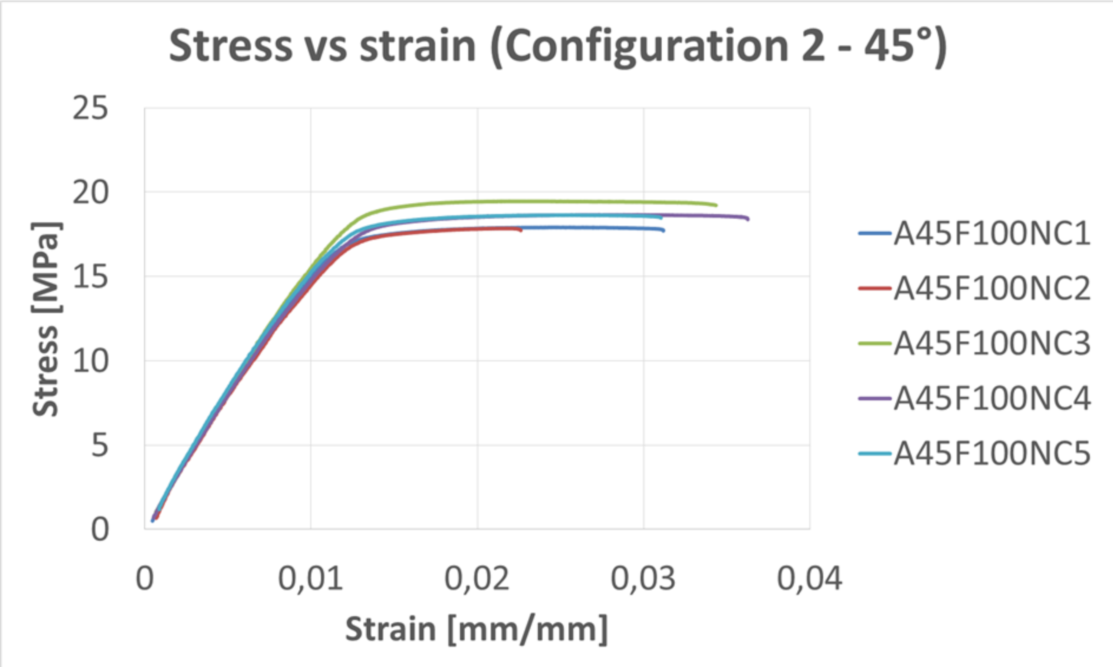

Figure 4.7: Stress-strain curve, configuration 2, 45° orientation

Table 4.11: Tensile test data, configuration 2, 45° orientation

Sample	Young modulus [MPa]	Yield stress [MPa]	Yield strain [MPa]	Failure stress [MPa]	Failure strain [MPa]
A45F100NC1	1720	17,9	0,0227	17,7	0,0312
A45F100NC2	1709	17,9	0,0217	17,7	0,0226
A45F100NC3	1705	19,5	0,0220	19,2	0,0343
A45F100NC4	1651	18,6	0,0245	18,4	0,0363
A45F100NC5	1768	18,6	0,0238	18,5	0,0310
Mean	**1711**	**18,5**	**0,023**	**18,3**	**0,031**
St. dev.	**42**	**0,7**	**0,001**	**0,6**	**0,005**
Uncertainty	**21**	**0,3**	**0,001**	**0,3**	**0,003**

Fiber orientation: 20° - 70°

Table 4.12: Tensile test data, configuration 2, 20° orientation

Sample	Young modulus [MPa]	Yield stress [MPa]	Yield strain [MPa]	Failure stress [MPa]	Failure strain [MPa]
A20F100NCV1	1777	21,8	0,0146	21,6	0,0146
A20F100NCV2	1571	22,7	0,0157	19,2	0,0245
A20F100NCV3	1772	21,5	0,0147	20,2	0,0166
Mean	**1707**	**22,0**	**0,0150**	**20,3**	**0,019**
St. dev.	**1671**	**0,7**	**0,0006**	**1,2**	**0,005**
Uncertainty	**1739**	**0,5**	**0,0004**	**0,9**	**0,004**

Table 4.13: Tensile test data, configuration 2, 70° orientation

Sample	Young modulus [MPa]	Yield stress [MPa]	Yield strain [MPa]	Failure stress [MPa]	Failure strain [MPa]
A70F100NCV1	1582	15,2	0,0213	15,2	0,0217
A70F100NCV2	1242*	14,9	0,0248	14,9	0,0250
A70F100NCV3	1411	14,5	0,0294	14,5	0,0297
Mean	**1496**	**14,9**	**0,025**	**14,9**	**0,025**
St. dev.	**121**	**0,3**	**0,004**	**0,3**	**0,004**
Uncertainty	**121**	**0,2**	**0,003**	**0,2**	**0,003**

Elastic modulus and uniaxial strength in function of the fiber angle θ

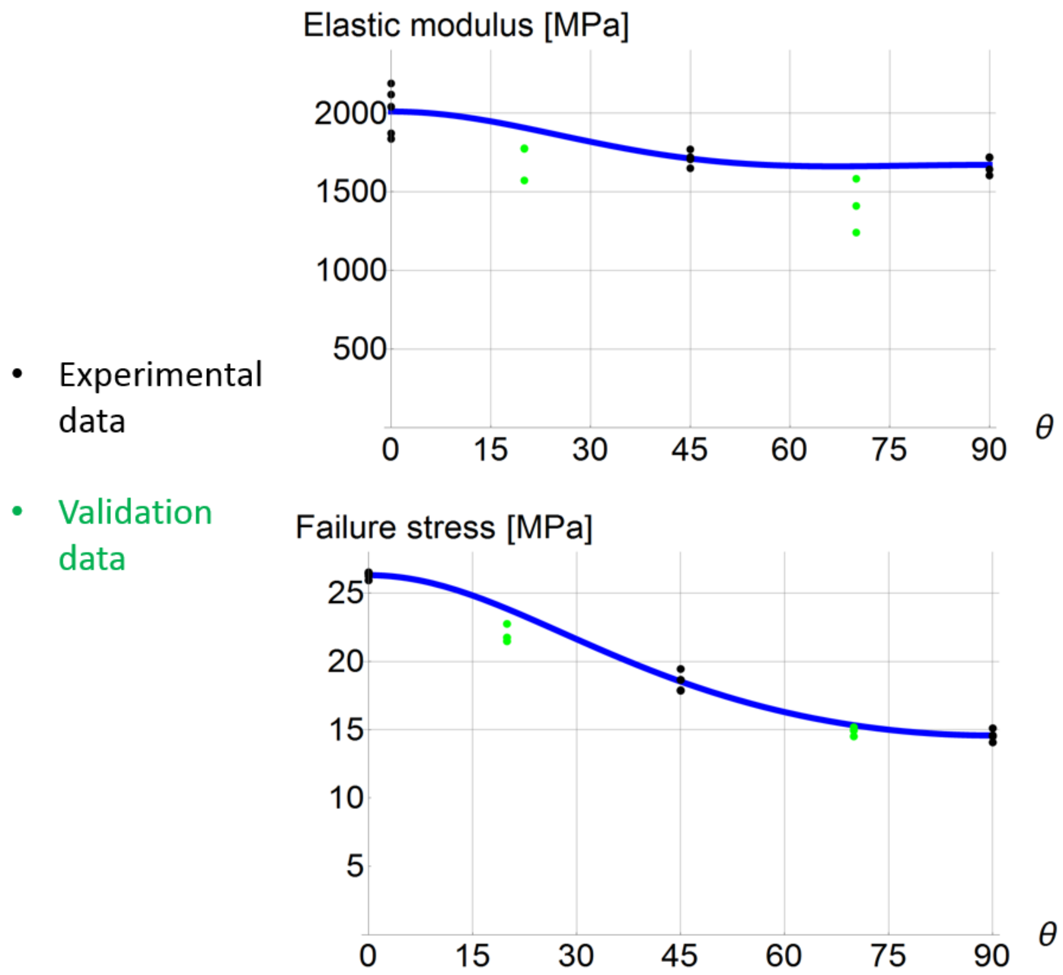

Figure 4.8: Stiffness and strength in function of the fiber angle θ, configuration 2

Configuration 2 tests results discussion

Specimens' behavior is nearly identical to configuration 1 samples. Since this configuration initially meant to be only a trial, tabs used for 0° and 45° were slightly longer than others: this could be one of the causes of the 0° specimens have a failure zone next to the tabbed portion. Elastic modulus and uniaxial strength have a similar trend to configuration 1. Theoretical elastic modulus overestimates both 20° and 70° samples' moduli. Optimal fitting is exhibited both by 20° and 70° specimens for strength.

4.1.3 Configuration 3: Type A material, cross section 0,3 x 0,6

Fiber orientation: 0°

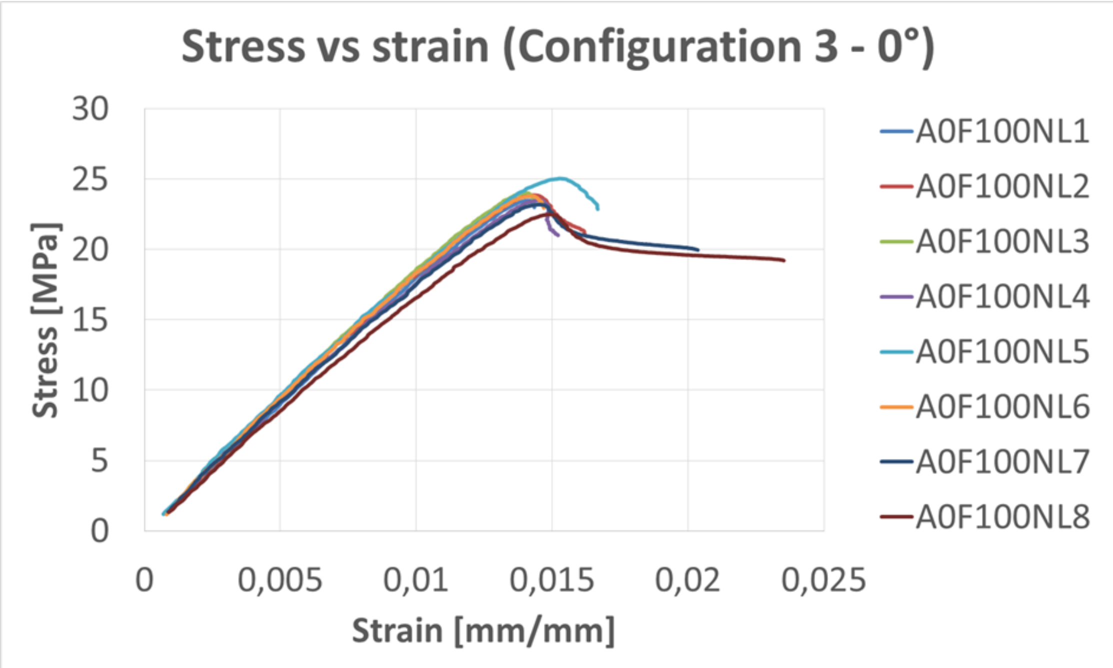

Figure 4.9: Stress-strain curves, configuration 3, 0° orientation

Table 4.14: Tensile test data, configuration 3, 0° orientation

Sample	Young modulus [MPa]	Poisson ratio	Yield stress [MPa]	Yield strain [mm/mm]	Failure stress [MPa]	Failure strain [MPa]
A0F100NL1	1834	0,37	23,5	0,0142	23,0	0,0143
A0F100NL2	1935	0,39	23,9	0,0142	21,0	0,0162
A0F100NL3	1999	0,30	24,0	0,0141	23,4	0,0143
A0F100NL4	1987	0,55*	23,5	0,0145	21,0	0,0152
A0F100NL5	2086	0,36	25,0	0,0153	22,9	0,0167
A0F100NL6	1972	0,41	23,8	0,0143	23,0	0,0147
A0F100NL7	1968	0,29	23,2	0,0145	20,0	0,0204
A0F100NL8	1843	-0,14*	22,5	0,0149	19,2	0,0235*
Mean	**1953**	**0,35**	**23,7**	**0,0145**	**21,7**	**0,016**
St. dev.	**83**	**0,05**	**0,7**	**0,0004**	**1,6**	**0,002**
Uncertainty	**31**	**0,02**	**0,3**	**0,0002**	**0,6**	**0,001**

Fiber orientation: 90°

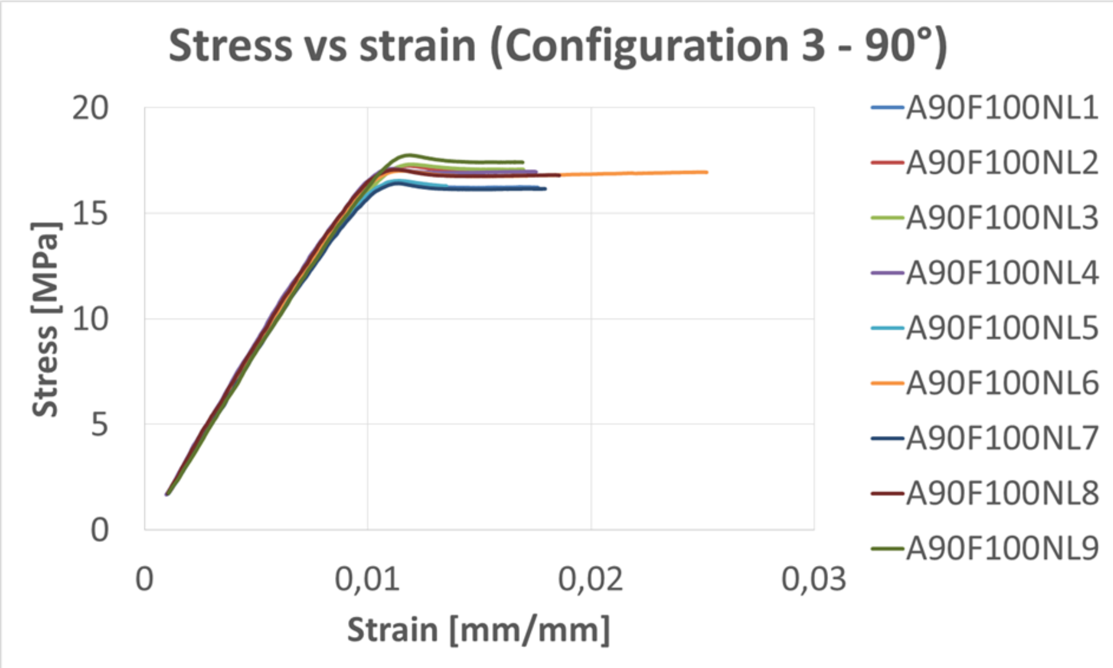

Figure 4.10: Stress-strain curves, configuration 3, 90° orientation

Table 4.15: Tensile test data, configuration 3, 90° orientation

Sample	Young modulus [MPa]	Yield stress [MPa]	Yield strain [mm/mm]	Failure stress [MPa]	Failure strain [MPa]
A90F100NL1	1745	16,5	0,0112	16,2	0,0176
A90F100NL2	1745	17,3	0,0119	16,9	0,0147
A90F100NL3	1714	17,3	0,0120	17,1	0,0170
A90F100NL4	1825	17,1	0,0111	17,0	0,0175
A90F100NL5	1729	16,5	0,0114	16,3	0,0135
A90F100NL6	1779	17,0	0,0115	16,9	0,0252*
A90F100NL7	1676	16,4	0,0114	16,2	0,0174
A90F100NL8	1871	17,1	0,0113	16,8	0,0186
A90F100NL9	1688	17,8	0,0119	17,4	0,0169
Mean	**1752**	**17,0**	**0,0115**	**16,8**	**0,017**
St. dev.	**63**	**0,4**	**0,0003**	**0,4**	**0,002**
Uncertainty	**22**	**0,2**	**0,0001**	**0,2**	**0,001**

Fiber orientation: 45°

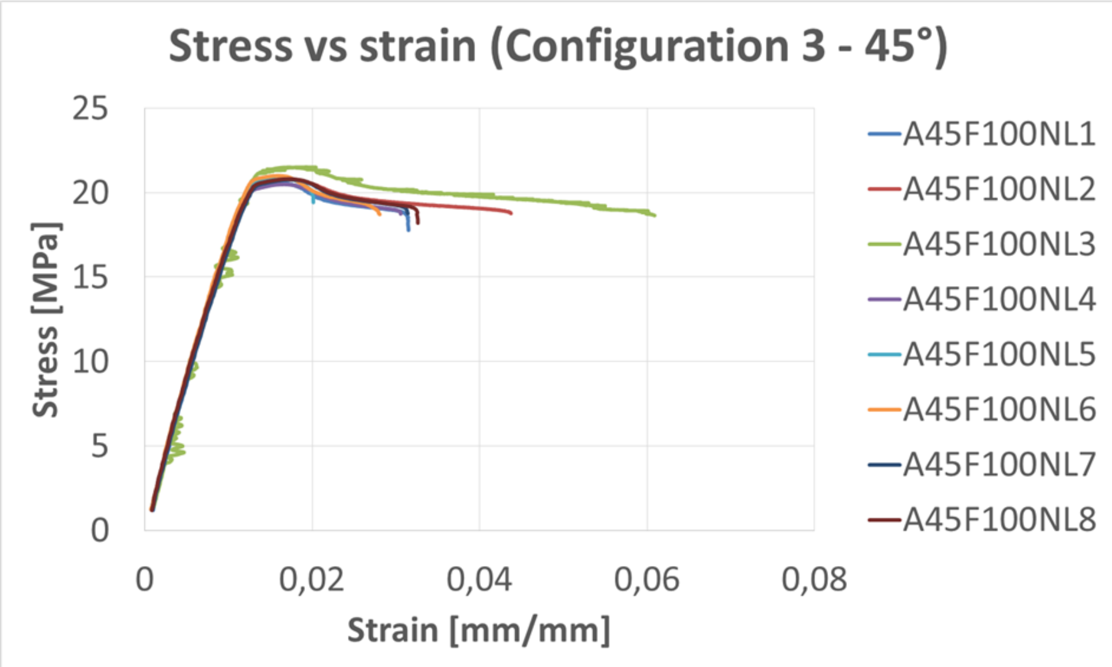

Figure 4.11: Stress-strain curves, configuration 3, 45° orientation

Table 4.16: Tensile test data, configuration 3, 45° orientation

Sample	Young modulus [MPa]	Yield stress [MPa]	Yield strain [mm/mm]	Failure stress [MPa]	Failure strain [MPa]
A45F100NL1	1945	20,6	0,0164	17,8	0,0315
A45F100NL2	1981	20,8	0,0168	18,8	0,0437
A45F100NL3	1385*	21,5	0,0193*	18,6	0,0609*
A45F100NL4	2002	20,5	0,0168	18,7	0,0306
A45F100NL5	1912	20,9	0,0164	19,4	0,0201
A45F100NL6	1992	21,0	0,0160	18,7	0,0281*
A45F100NL7	1976	20,8	0,0173	18,8	0,0314
A45F100NL8	2076	20,8	0,0174	18,2	0,0326
Mean	**1983**	**20,9**	**0,0167**	**18,6**	**0,031**
St. dev.	**51**	**0,3**	**0,0005**	**0,5**	**0,007**
Uncertainty	**21**	**0,1**	**0,0002**	**0,2**	**0,003**

Fiber orientation: 20° - 70°

Table 4.17: Tensile test data, configuration 3, 20° orientation

Sample	Young modulus [MPa]	Yield stress [MPa]	Yield strain [MPa]	Failure stress [MPa]	Failure strain [MPa]
A20F100NLV1	1959	25,4	0,0152	25,1	0,0153
A20F100NLV2	2022	24,6	0,0143	24,6	0,0143
A20F100NLV3	1853	23,6	0,0144	23,6	0,0144
Mean	**1944**	**24,5**	**0,0146**	**24,4**	**0,0147**
St. dev.	**85**	**0,9**	**0,0005**	**0,8**	**0,0006**
Uncertainty	**60**	**0,6**	**0,0003**	**0,5**	**0,0004**

Table 4.18: Tensile test data, configuration 3, 70° orientation

Sample	Young modulus [MPa]	Yield stress [MPa]	Yield strain [MPa]	Failure stress [MPa]	Failure strain [MPa]
A70F100NLV1	1851	20,8	0,0133	20,5	0,0154
A70F100NLV2	1749	19,2	0,0131	18,9	0,0221
A70F100NLV3	1654	19,5	0,0134	19,3	0,0302
Mean	**1751**	**19,8**	**0,0133**	**19,6**	**0,023**
St. dev.	**98**	**0,8**	**0,0002**	**0,9**	**0,007**
Uncertainty	**70**	**0,6**	**0,0001**	**0,6**	**0,005**

Elastic modulus and uniaxial strength in function of the fiber angle θ

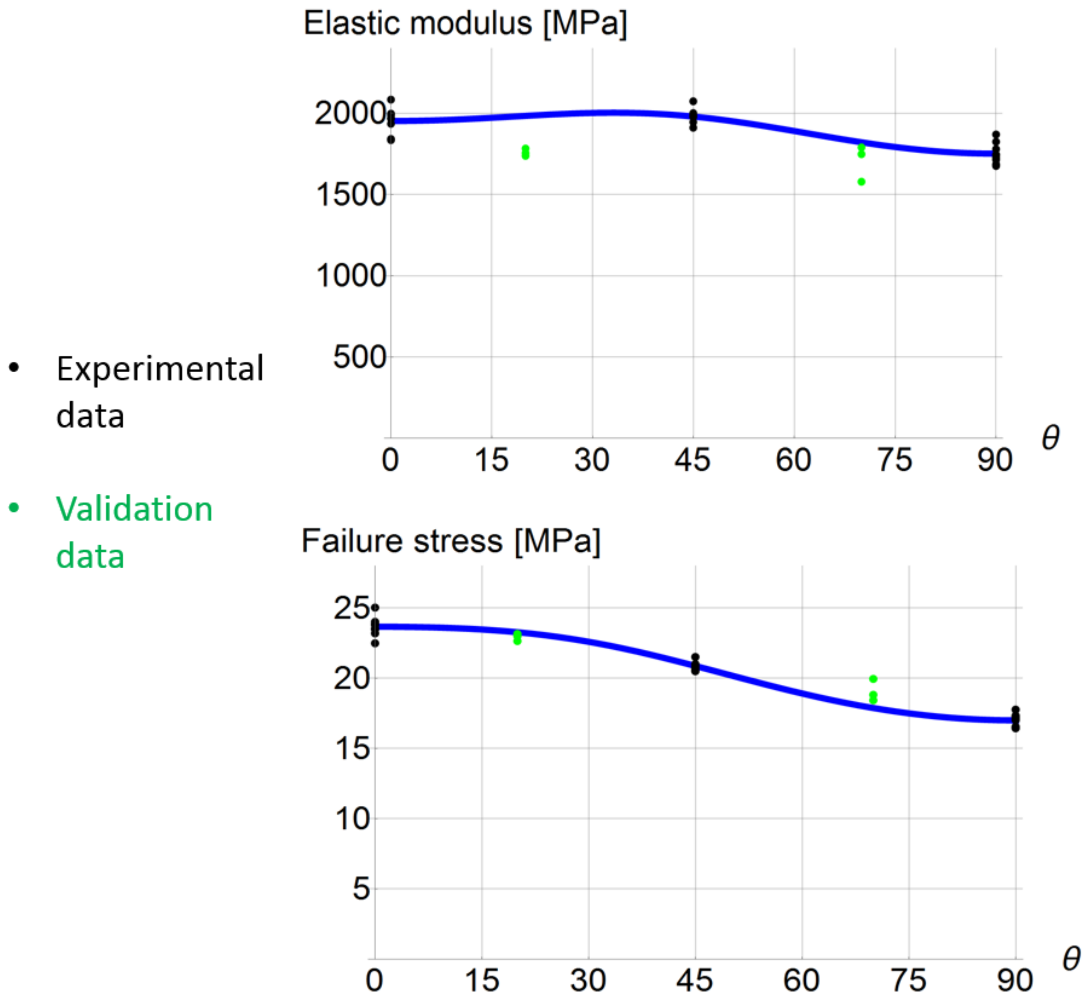

Figure 4.12: Stiffness and strength in function of the fiber angle θ, configuration 3

Configuration 3 tests results discussion

0° samples show less ductility than both the previous configurations, with an average failure strain similar to 90° samples failure strain. Elastic modulus is similar between 0° and 45° specimens, lowering at 90°. Uniaxial strength trend is identical to configuration 1 and 2, with 0° specimens having the highest strength and 90° the lowest. Theoretical elastic modulus overestimates validation data, while an optimal fitting has been found for uniaxial strength.

4.1.4 Configuration 4: Type B material, cross section 0,2 x 0,4

Fiber orientation: 0°

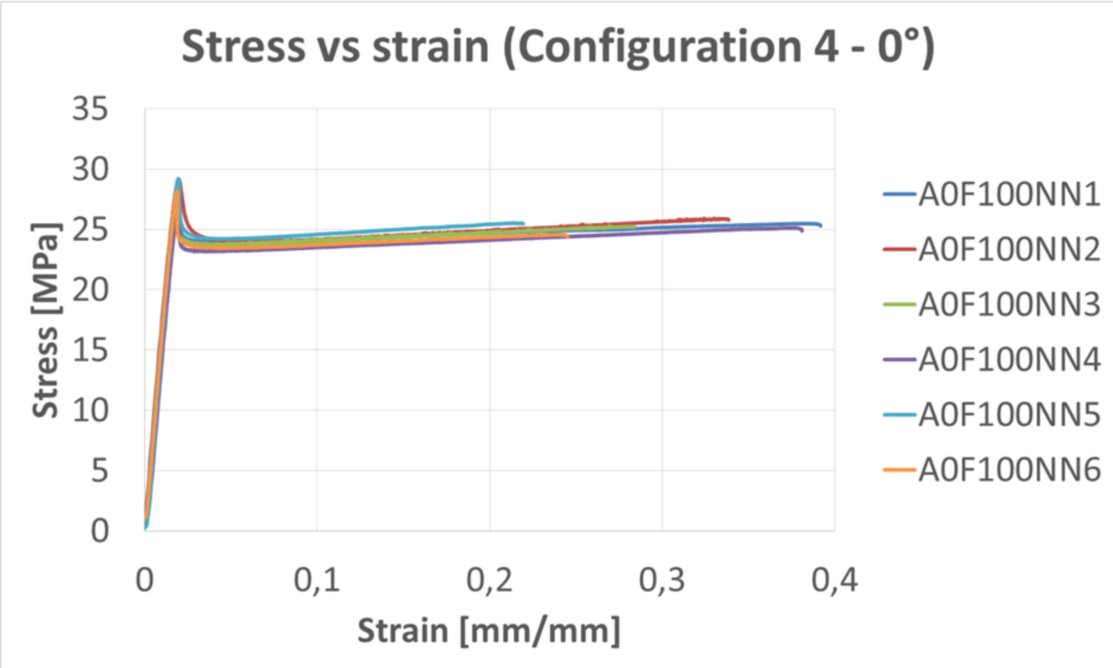

Figure 4.13: Stress-strain curves, configuration 4, 0° orientation

Table 4.19: Tensile test data, configuration 4, 0° orientation

Sample	Young modulus [MPa]	Poisson ratio	Yield stress [MPa]	Yield strain [mm/mm]	Failure stress [MPa]	Failure strain [mm/mm]
A0F100NN1	1833	0,54	28,8	0,0195	25,3	0,3917
A0F100NN2	1660	0,16	29,1	0,0197	25,8	0,3384
A0F100NN3	1522	0,23	28,4	0,0187	25,2	0,2837
A0F100NN4	953*	3,96*	27,8	0,0202	24,9	0,3809
A0F100NN5	1433	0,13	29,2	0,0195	25,5	0,2193
A0F100NN6	1583	-0,02*	28,2	0,0189	24,4	0,2451
Mean	**1606**	**0,3**	**28,6**	**0,0194**	**25,2**	**0,31**
St. dev	**152**	**0,2**	**0,6**	**0,0005**	**0,5**	**0,07**
Uncertainty	**76**	**0,1**	**0,3**	**0,0002**	**0,2**	**0,03**

Fiber orientation: 90°

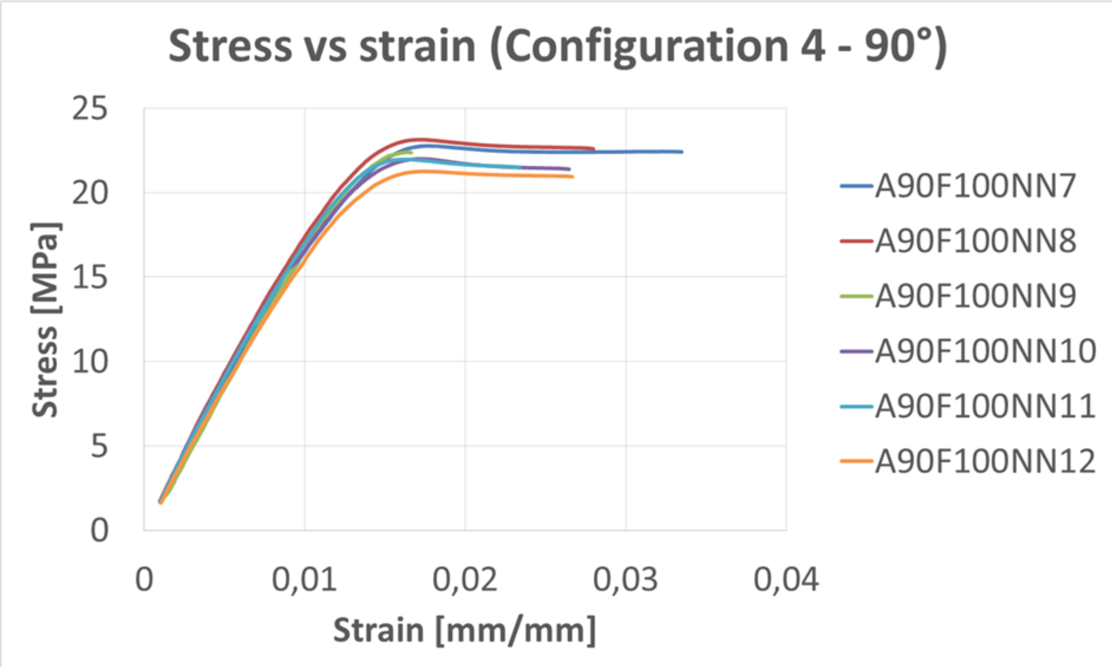

Figure 4.14: Stress-strain curves, configuration 4, 90° orientation

Table 4.20: Tensile test data, configuration 4, 90° orientation

Sample	Young modulus [MPa]	Yield stress [MPa]	Yield strain [mm/mm]	Failure stress [MPa]	Failure strain [mm/mm]
A90F100NN7	1737	22,8	0,0178	22,4	0,0335
A90F100NN8	1964	23,1	0,0172	22,6	0,0280
A90F100NN9	1598	22,4	0,0164	22,4	0,0166*
A90F100NN10	2006	22,0	0,0172	21,4	0,0264
A90F100NN11	1923	22,0	0,0164	21,5	0,0234
A90F100NN12	1823	21,3	0,0175	20,9	0,0266
Mean	**1842**	**22,3**	**0,0171**	**21,9**	**0,028**
St. dev	**154**	**0,7**	**0,0006**	**0,7**	**0,004**
Uncertainty	**69**	**0,3**	**0,0003**	**0,3**	**0,002**

Fiber orientation: 45°

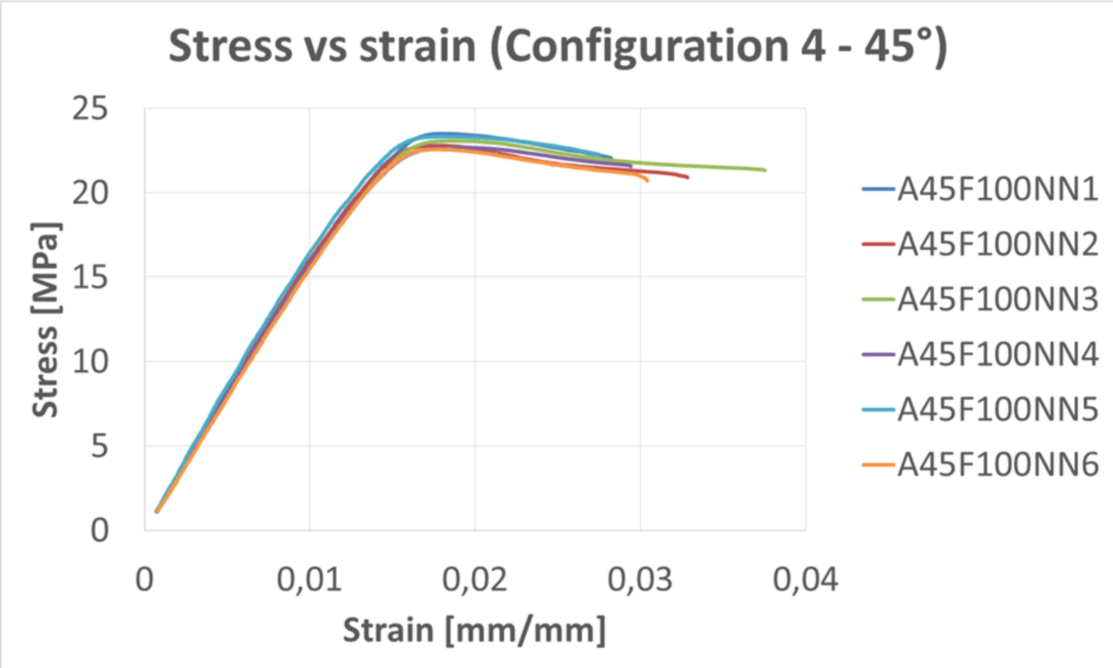

Figure 4.15: Stress-strain curves, configuration 4, 45° orientation

Table 4.21: Tensile test data, configuration 4, 45° orientation

Sample	Young modulus [MPa]	Yield stress [MPa]	Yield strain [mm/mm]	Failure stress [MPa]	Failure strain [mm/mm]
A45F100NN1	1680	23,5	0,0181	22,0	0,0282
A45F100NN2	1743	22,8	0,0177	20,9	0,0328
A45F100NN3	1616	23,1	0,0184	21,3	0,0375
A45F100NN4	1687	22,7	0,0190	21,6	0,0294
A45F100NN5	1762	23,3	0,0184	22,2	0,0275
A45F100NN6	1579	22,6	0,0183	20,7	0,0304
Mean	**1678**	**23,0**	**0,0183**	**21,5**	**0,031**
St. dev	**71**	**0,4**	**0,0004**	**0,6**	**0,004**
Uncertainty	**32**	**0,2**	**0,0002**	**0,3**	**0,002**

Fiber orientation: 20° - 70°

Table 4.22: Tensile test data, configuration 4, 20° orientation

Sample	Young modulus [MPa]	Yield stress [MPa]	Yield strain [mm/mm]	Failure stress [MPa]	Failure strain [mm/mm]
A20F100NNV4	1775	28,0	0,01786	25,1	0,02092
A20F100NNV5	1725	26,0	0,01667	26,0	0,01669
A20F100NNV6	1844	26,8	0,01778	23,7	0,02601
Mean	**1781**	**26,9**	**0,0174**	**24,9**	**0,021**
St. dev	**60**	**1,0**	**0,0007**	**1,2**	**0,005**
Uncertainty	**42**	**0,7**	**0,0005**	**0,8**	**0,003**

Table 4.23: Tensile test data, configuration 4, 70° orientation

Sample	Young modulus [MPa]	Yield stress [MPa]	Yield strain [mm/mm]	Failure stress [MPa]	Failure strain [mm/mm]
A70F100NNV4	1799	25,8	0,01601	23,9	0,01969
A70F100NNV5	1764	25,1	0,01515	23,5	0,02277
A70F100NNV6	1643	25,4	0,01607	23,4	0,02687
Mean	**1735**	**25,4**	**0,0157**	**23,6**	**0,023**
St. dev	**82**	**0,3**	**0,0005**	**0,3**	**0,004**
Uncertainty	**58**	**0,2**	**0,0004**	**0,2**	**0,003**

Elastic modulus and uniaxial strength in function of the fiber angle θ

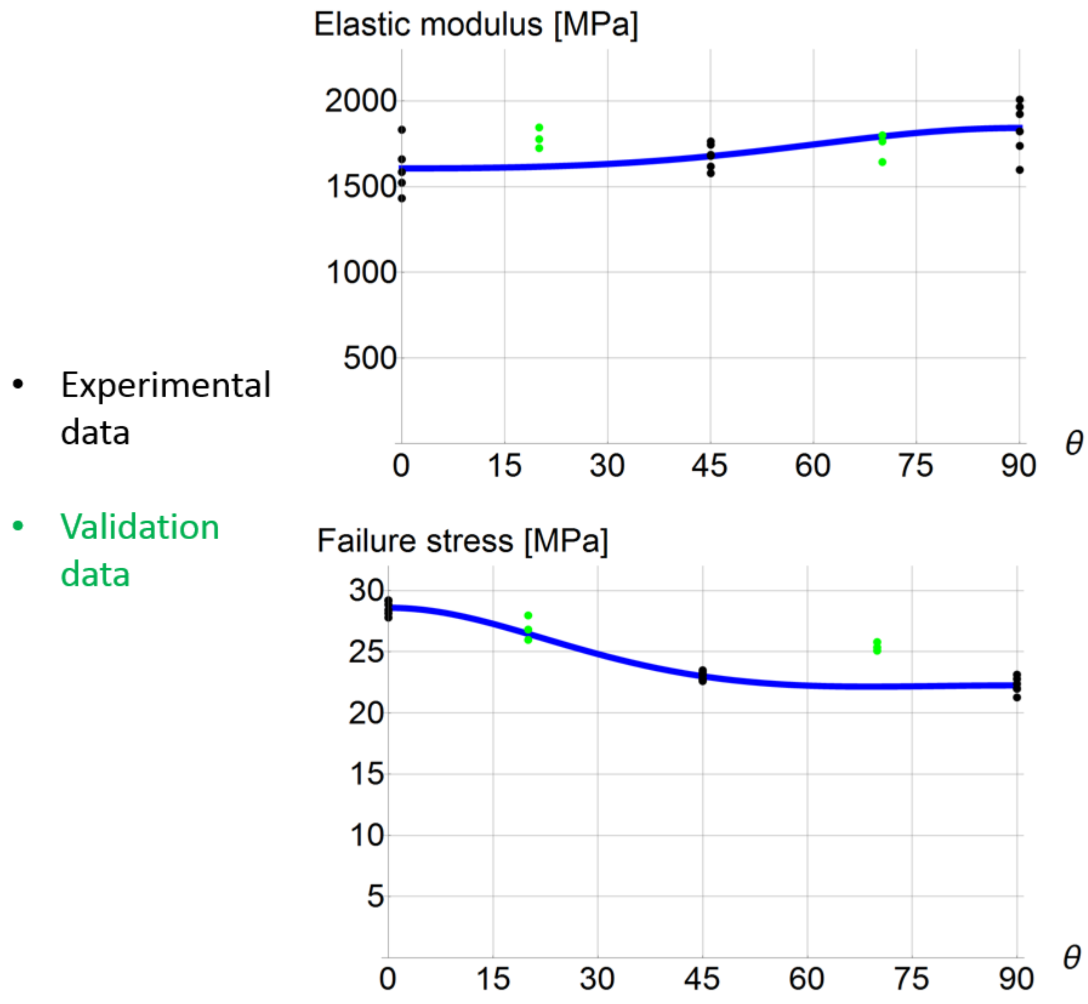

Figure 4.16: Stiffness and strength in function of the fiber angle θ, configuration 4

Configuration 4 tests results discussion

0° samples show an extremely more ductile behavior than the previous configurations, with over 30% average failure strain. After the yielding section, the plasticity region is characterized by a slight hardening behavior. 45° and 90° samples show a similar behavior to the previous configurations. Elastic modulus show an anomalous behavior, since 90° samples show a higher modulus than 0° ones. Uniaxial strength trend is nearly identical to previous ones, where 0° samples are stronger than 90° ones. Good fitting is found between theoretical elastic modulus and validation data. 20° specimens exhibit an excellent fitting to theoretical strength, while 70° ones are underestimated.

4.1.5 General discussion

The results show that fiber orientation plays a significant role on the mechanical properties of the 3D printed material, which is clearly displayed in the stress-strain curves. Longitudinal (0°) specimens show a more ductile behavior, that can also observed in their failure mode, in which the debonding of the sample occurs: a linear elastic deformation is followed by an overstep region in which the maximum stress value is reached, then the final region is characterized by plastic deformation at constant stress. Transverse (90°) specimens show a more brittle behavior, while 45° coupons' mechanical response lies approximately in the middle between 0° and 90° samples. 0° specimens, especially for configuration 1 and 4, exhibit debonding in their failure mode (e.g. fig. 4.25 and fig. 4.26), while other orientations show a brittle failure mode (e.g. fig. 4.27 and fig. 4.28), with the fracture direction aligned to the fiber orientation (failure modes can be seen in detail in the specimens screenshots section, at the end of the chapter).

During the test it has been observed that printed specimens, especially 0° ones, exhibited whitening regions, in which crazing nucleation developed. Failure occurred in proximity of these whitened zones, where localized fiber debonding has been observed. Conversely, 90° specimens did not show considerable crazing and failure always occurred at the interface between adjacent fibers.

Generally speaking, tensile tests on specimen at 0° are able to capture mechanical response of the 3D printed part that mainly depends on the mechanical behavior of the fiber i.e. on intra-fiber properties. Conversely, tensile tests at 90° are suitable for retrieving mechanical characteristics of the 3D printed parts that primarily depend on the bonding process, i.e. on inter-fibers properties.

Classical Lamination Theory and Tsai-Hill failure criterion have been used to describe the mechanical properties of 3D printed specimens. Experimental data necessary to plot elastic modulus and failure stress in function of the fiber angle θ has been obtained through 0°, 90° and 45° samples. 20° and 70° specimens have been used to validate experimental data.

Elastic response analysis shows that Young's modulus at 0° is generally higher than Young's modulus at 90°. Configuration 3 elastic response shows similar values at 0° and 45°. Validation data for elastic modulus shows a good fitting with theoretical estimation for configuration 1 and 4, while for configurations 2 and 3 it has been observed some overestimation. An unusual behavior is observed in configuration 4 elastic response, where 90° elastic modulus is higher than 0° one. This could be caused by the different material used for configuration 4.

Strength modeling shows that fiber orientation significantly affects tensile yield strength: longitudinal specimens have a much higher yield strength than transverse specimens (from 25% to 45% higher). Higher data scatter in strength can be observed in 45° and 90° specimen, while it is significantly lower for 0° specimens. This can be attributed to a transition in the failure mode, from 0° samples ductile fracture to 90° samples brittle fracture, dominated by fiber to fiber interface [54]. The transition from ductile to brittle fracture is suggested to happen very quickly, even after a slight change in the fiber angle from 0° [54]. Validation data show a very good fitting with theoretical estimation, with some slight underestimation for 70° specimens of configurations 1 and 4. 20° samples all show an optimal fitting.

The reason for the 70° specimen underestimation probably lies in the air gap parameter. For configuration 1 and 4, 70° samples could not be printed with the same air gap than the experimental data samples (namely 0,2 mm air gap), because the print always failed. Lowering the air gap to 0,15, the samples could be printed. Too much air gap enables an easy detachment of the specimen from the support, but diminishes its strength, because it reduces the adhesion between layers, especially the first 2-3 layers, weakening the whole specimen. It has been empirically estimated that a reduction of 0,05 mm air gap increases its uniaxial strength by 10%. Decreasing by 10% the values of these 70° specimens, a better fitting is found.

The results from strength modeling shows that Tsai-Hill failure theory can be used to describe the strength behavior of specimens fabricated through FDM method under plane stress.

4.2 Comparison between different cross section of the same material (configurations 1, 2, 3)

In this section a mechanical properties assessment between three different cross sections of the same material has been carried out. Boxplots have been used to carry out the comparisons. Test conditions are almost the same, with some slight changes:

- Configurations 1 and 2 samples have been printed with the same air gap of 0,2 mm, while configuration 3 ones, for printability motives, have been printed with a 0,1 mm air gap.
- Configuration 3 specimens have been printed at a lower speed, in order to maintain a similar flow rate between the three configurations. For printability motives, configuration 2 specimens have been printed at the same speed of configuration 1 specimens.

The following parameters have been compared:

- Elastic modulus at 0°
- Elastic modulus at 90°
- Uniaxial tensile strength at 0°
- Uniaxial tensile strength at 90°
- Strain at failure at 0°
- Strain at failure at 90°
- Shear modulus
- Shear strength

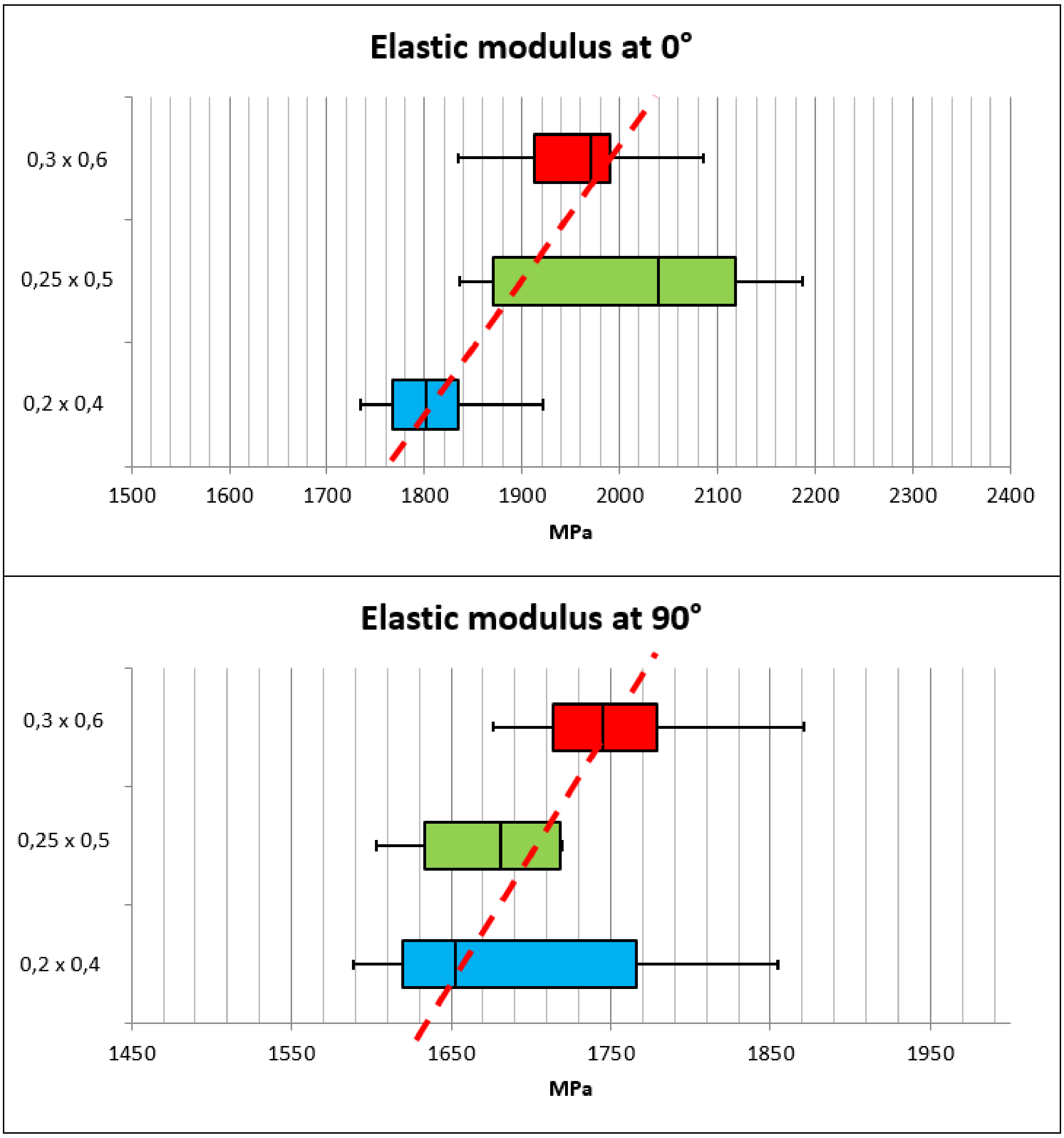

Figure 4.17: Elastic modulus at 0° and 90°

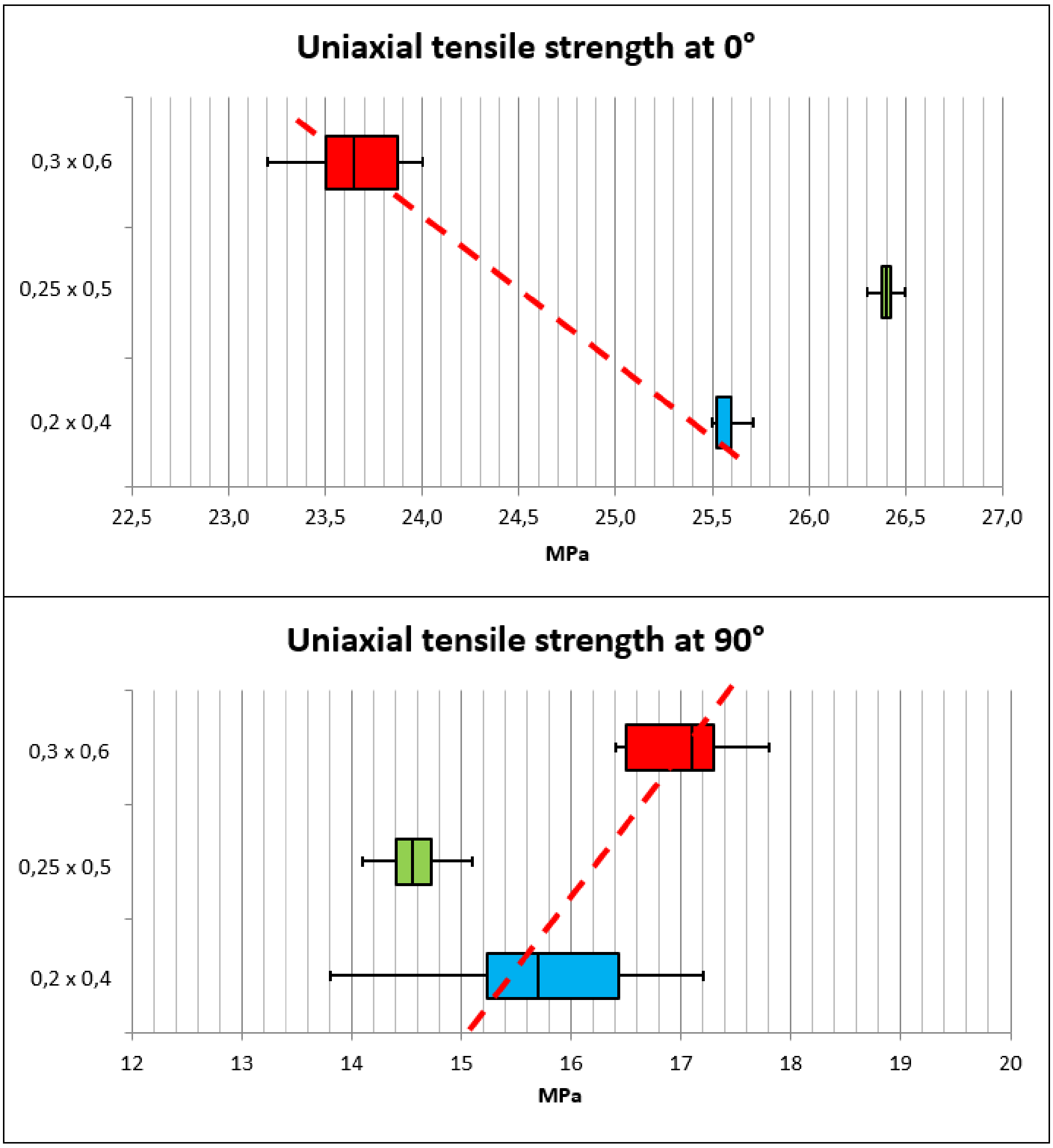

Figure 4.18: Uniaxial tensile strangth at 0° and 90°

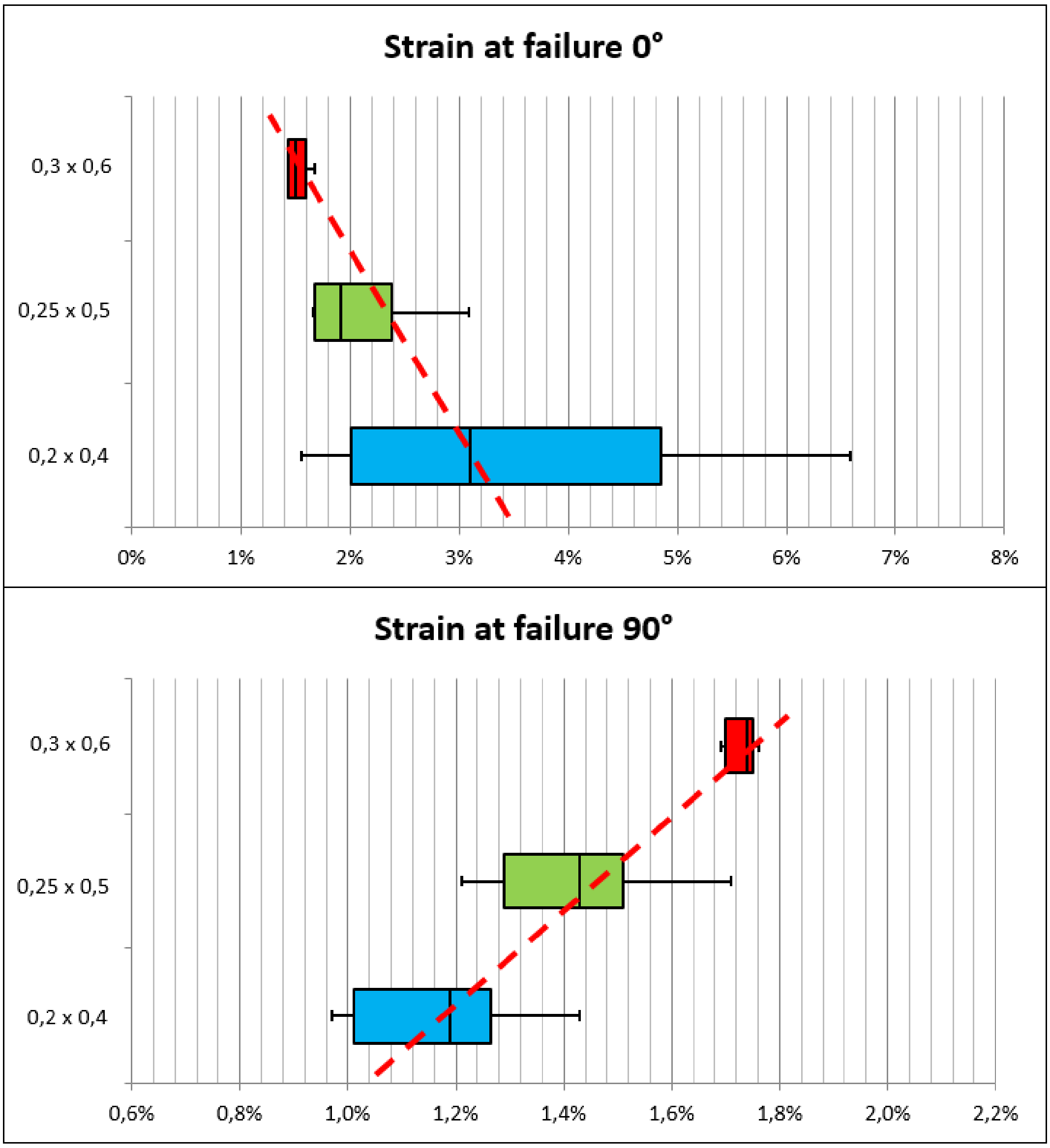

Figure 4.19: Strain at failute at 0° and 90°

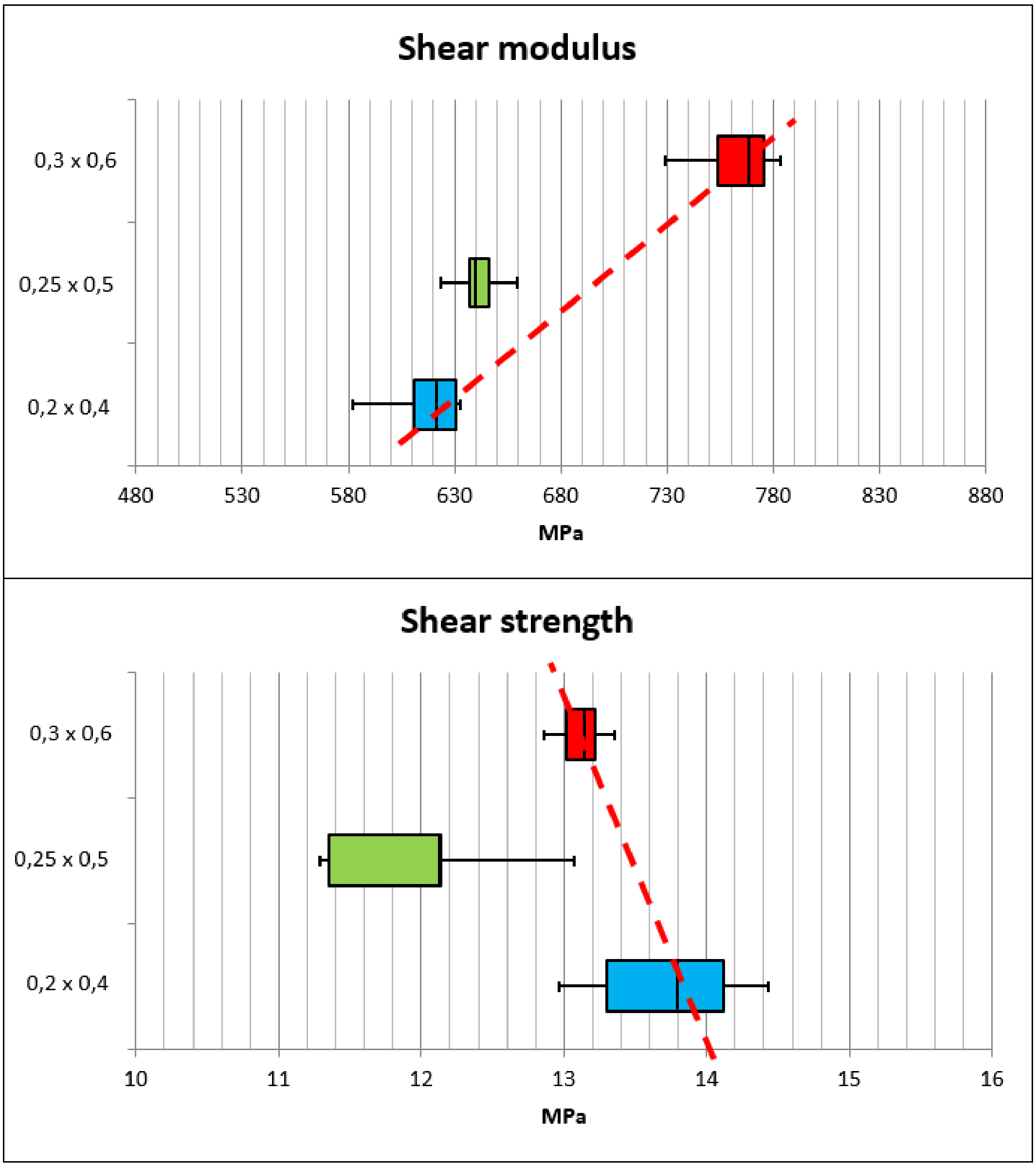

Figure 4.20: Shear modulus and shear strength

4.2.1 Cross section comparison results discussion

The comparison between the various cross section filaments has given the following results:

- Tensile elastic moduli, both at 0° and 90°, raise while increasing filament section. This means that stiffness tends to be higher with bigger filaments, thus with a minor number of filaments in the layer (given a fixed geometry).
- Uniaxial tensile strength at 0° decreases increasing filament section, meaning that more, smaller filaments, in the layer, exhibit an overall higher strength. Values obtained for 0,25 x 0,5 mm seem to be anomalous.
- Uniaxial tensile strength at 90° decreases increasing filament section. Values obtained for 0,25 x 0,5 mm seem to be anomalous.
- Ultimate strain at 0° decreases increasing filament section, conversely strain at failure at 90° increases with filament section.
- Shear modulus raises increasing filament section.
- Shear strength shows a trend similar to uniaxial tensile strength.

Tensile tests for 0,25x0,5 mm configuration have been repeated to assess the anomalous results regarding both tensile strength at 0° and 90°, previously checking g-code instructions, modality of specimen measurement and tensile test conditions. New results, not reported here, are perfectly according to the previous one, presented in this study.

A possible explanation for the anomalous results obtained for 0,25x0,5 mm filaments section comes from the resolution of the motor stepper unit of the z-axis (0,015 mm), responsible for the bed movement and thus for the layer height. The resolution may not allow a precise movement on the z-axis of 0,254 mm, that is the nominal value so far approximated at 0,25 mm. Since the error is systematic, the resulting height of each layer may significantly vary from its nominal value. The error cannot be estimated from specimen thickness measurement, because all the specimens present a significant deviation from the nominal value, independently from filament section (+16%, +13% and +18% for 0,2x0,4, 0,25x0,5 and 0,3x0,6 respectively).

Thus, the anomalous values regarding 0,25 x 0,5 mm filament section may come from a different bonding between subsequent layers due to an incorrect layer height.

4.3 Comparison between different materials with the same cross section (configurations 1, 4)

In this section a comparison of the mechanical properties of Type A and Type B material, maintaining the cross section constant, is presented. The procedure is identical to the previous cross section comparison.

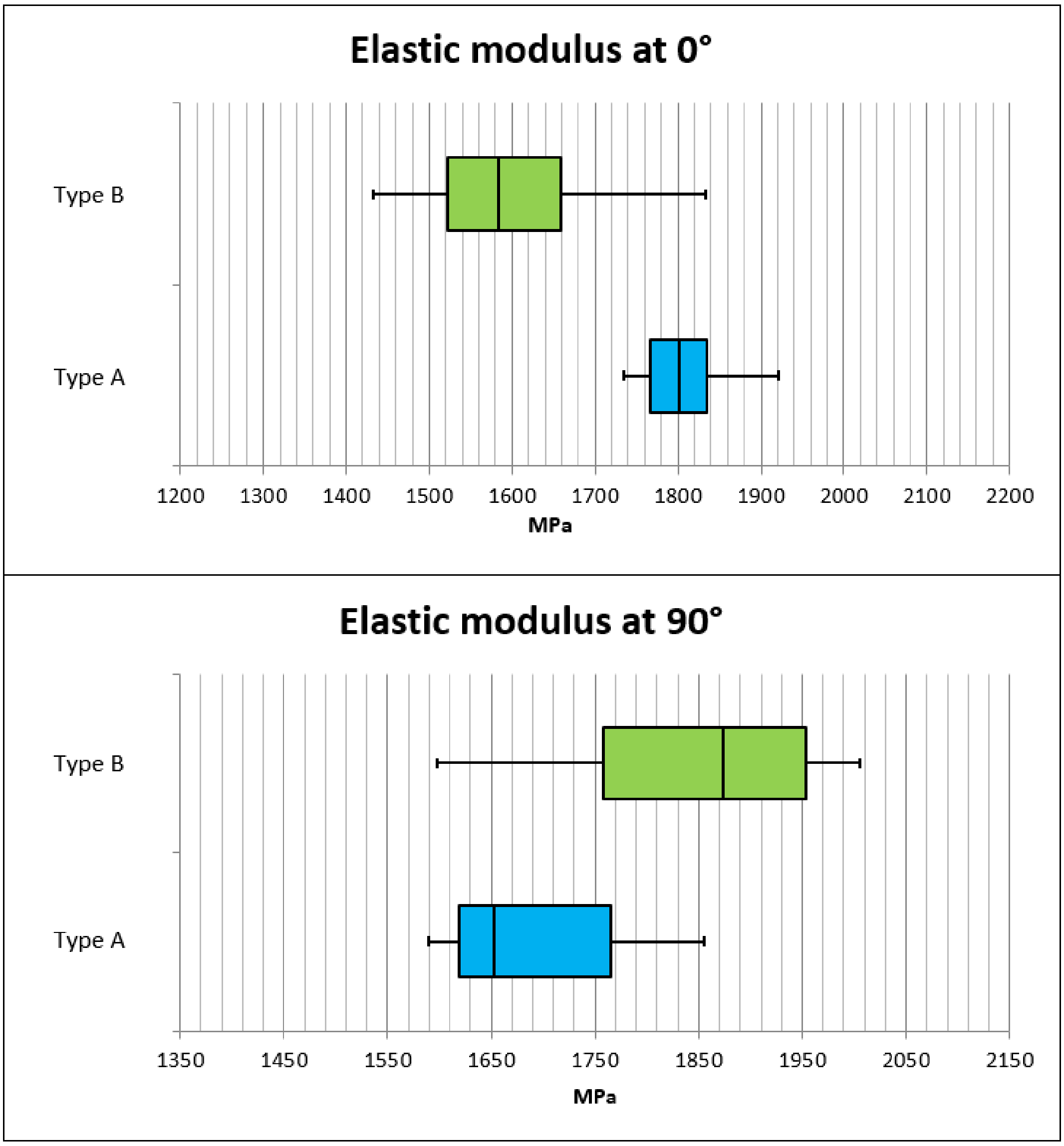

Figure 4.21: Elastic modulus at 0° and 90°

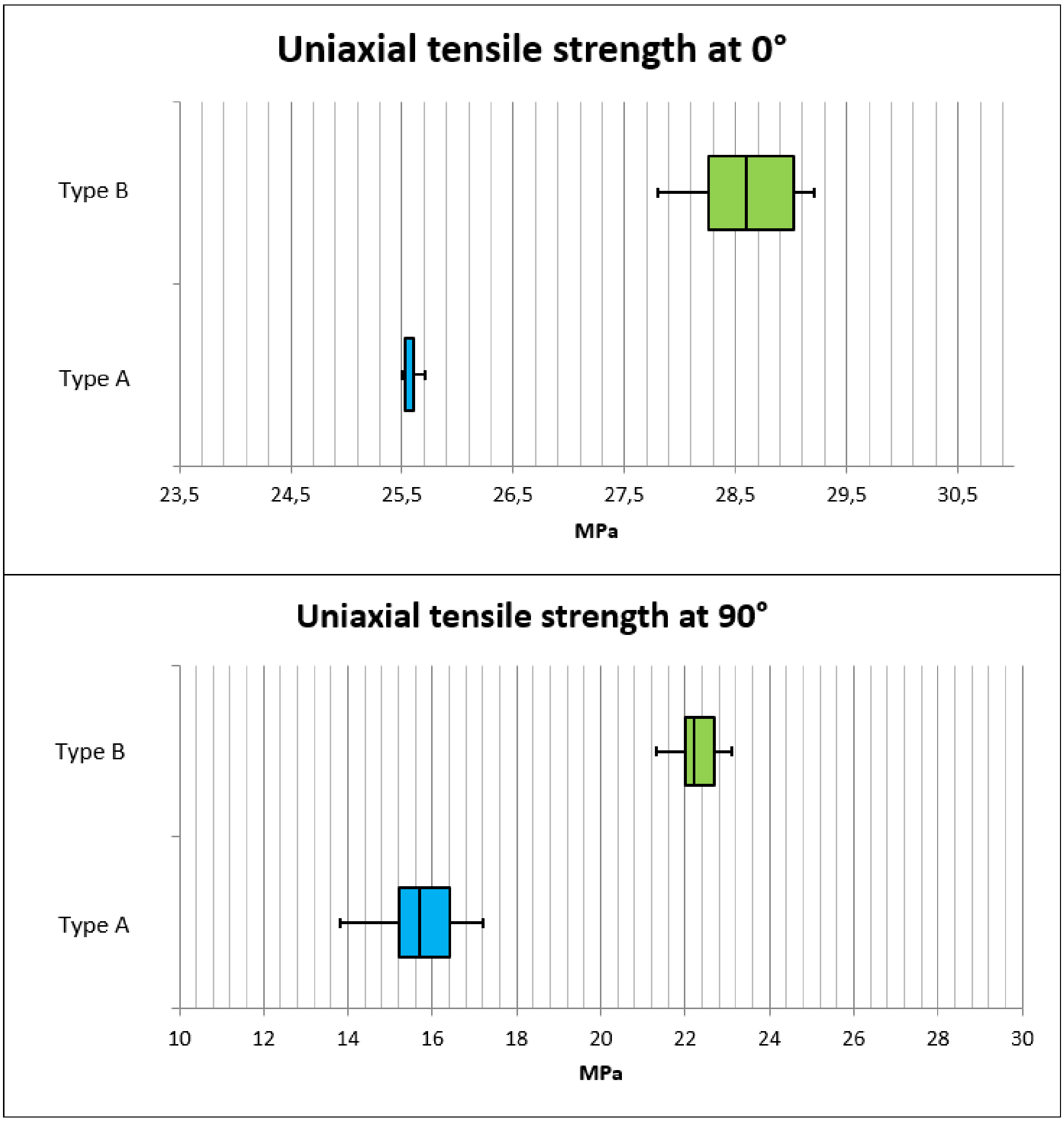

Figure 4.22: Uniaxial tensile strength at 0° and 90°

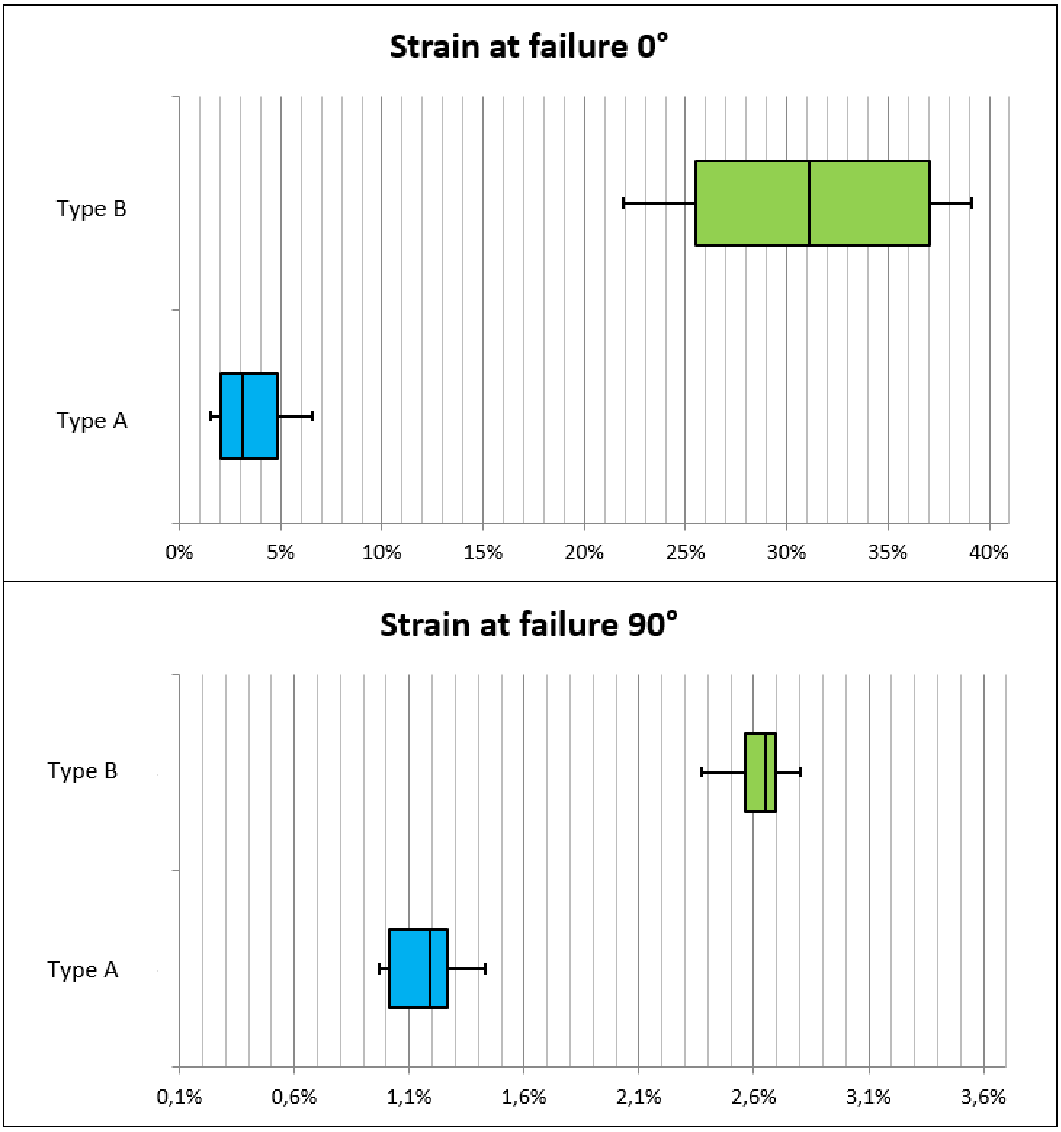

Figure 4.23: Strain at failure at 0° and 90°

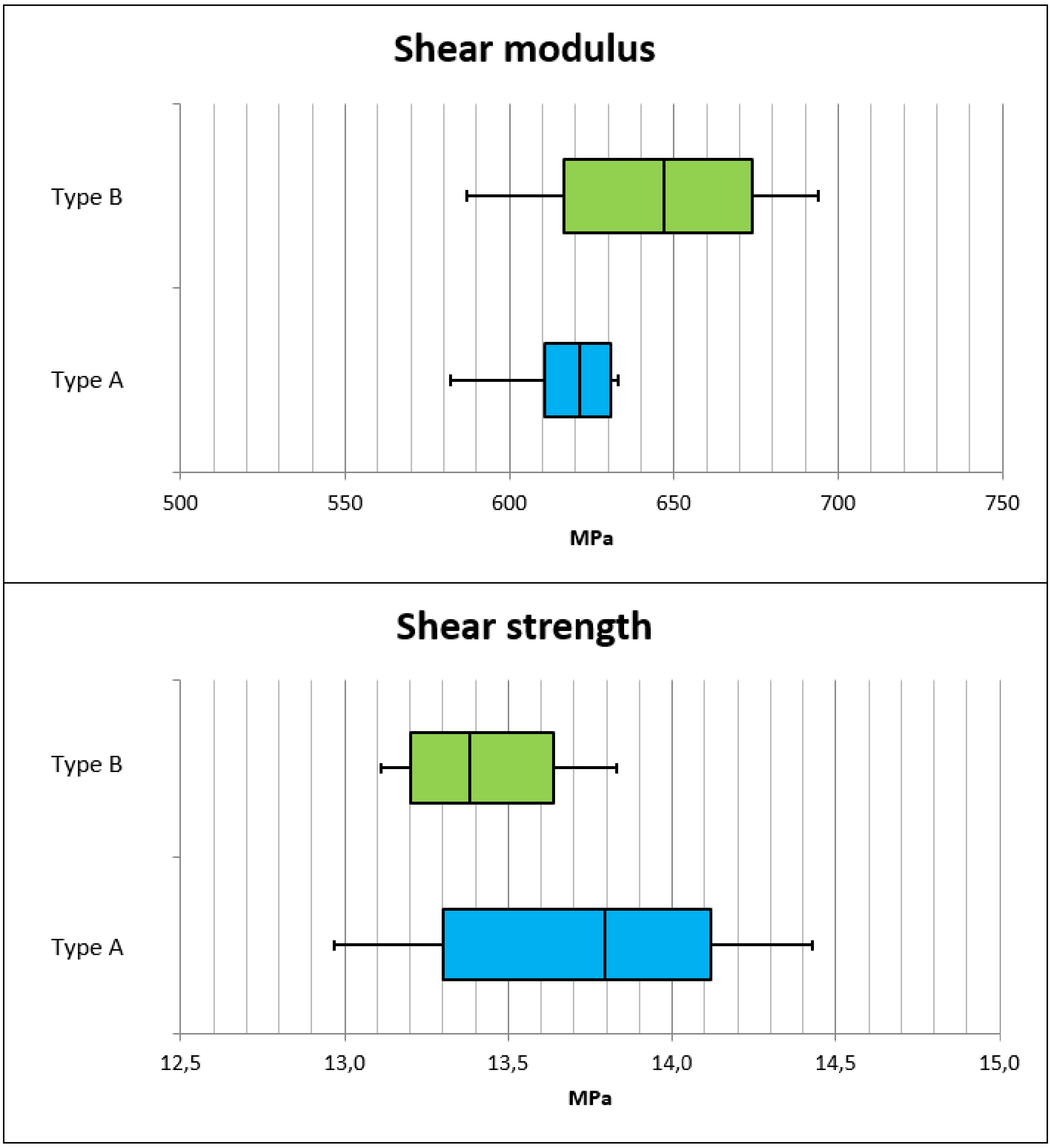

Figure 4.24: Shear modulus and shear strength

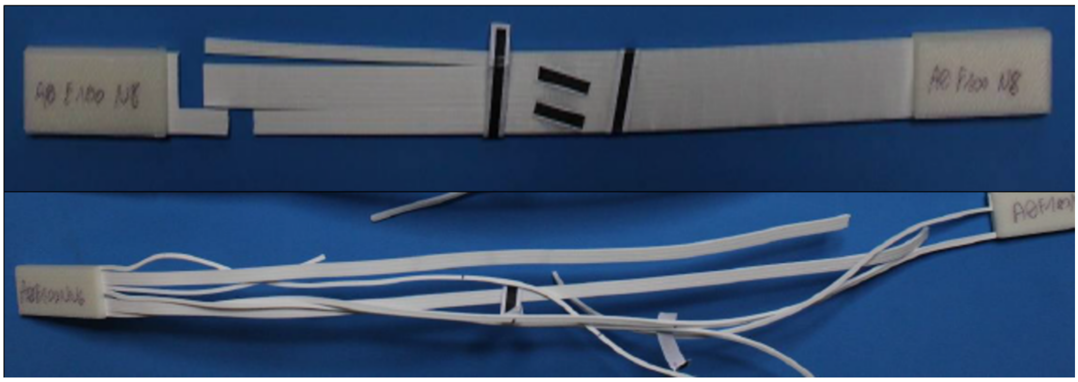

Figure 4.25: Different failure modes for two different materials (longitudinal specimens)

4.3.1 Material comparison results discussion

Type B material has a higher elastic modulus at 90° and higher tensile strength both for 0° and 90° orientations compared to Type A material. Only the elastic modulus at 0° is better for Type A. Strain at failure is higher for Type B, for both 0° and 90° orientations. Starting from the data analysis, it is possible to formulate the following conclusions:

- Intra-fibers bonding properties are better for Type B material. Indeed, tensile strength and stiffness at 90° are higher compared to the Type A material.
- For Type B, elastic modulus at 90° is higher than the elastic modulus at 0°. This behavior may depend on the optimal bonding properties of Type B.
- Intra-fiber stiffness is higher for Type A.
- Generally speaking, Type B shows a more ductile failure mode compared to Type A 4.25. The ultimate strain at 0° is ten times higher than the corresponding Type A failure strain.
- A brittle failure mode is found on 90° specimens, both Type A and Type B.
- Shear modulus and strength do not show significant differences between Type A and Type B.

4.4 Specimen screenshots

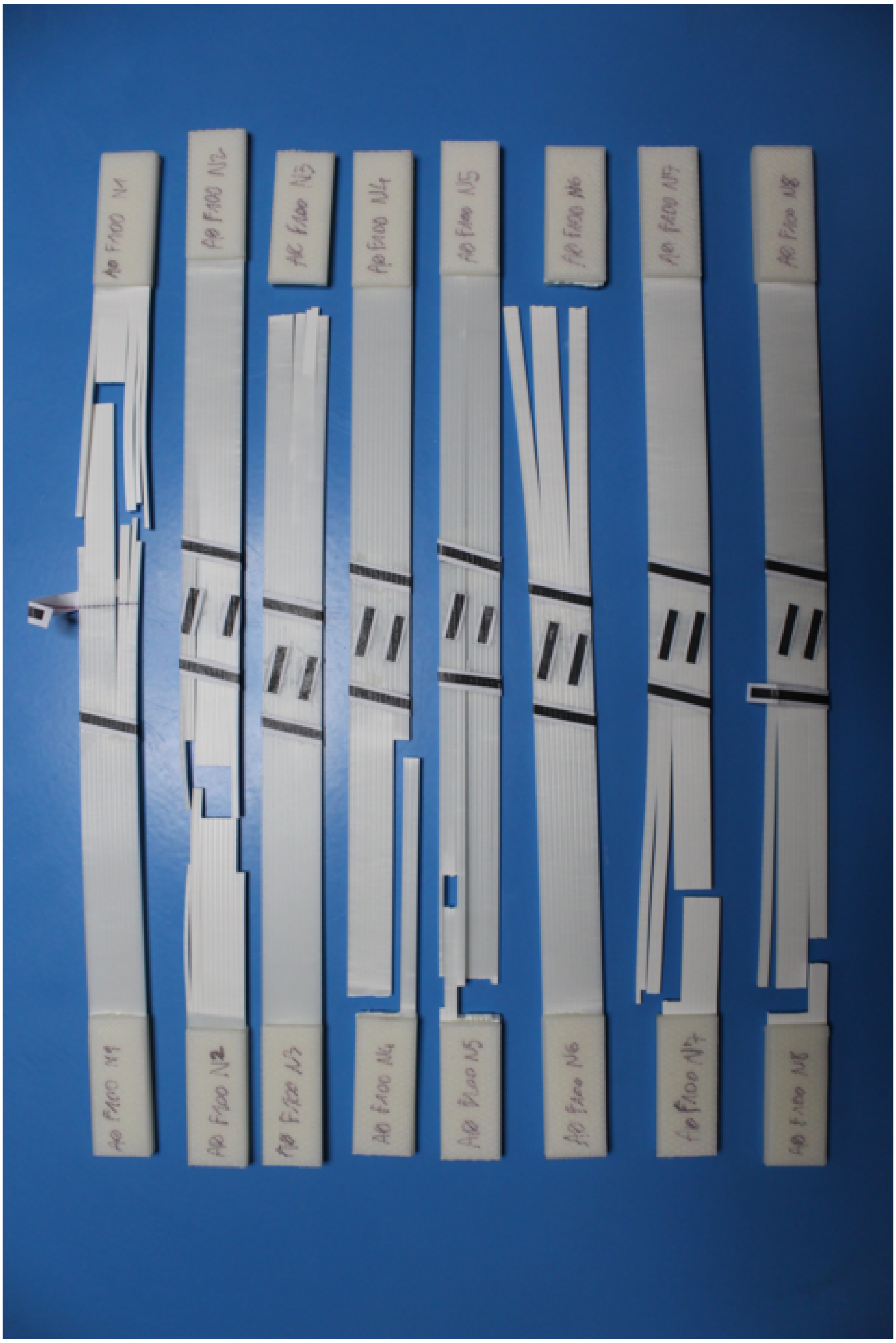

Figure 4.26: Specimen screenshot, configuration 1, 0° orientation

Figure 4.27: Specimen screenshot, configuration 1, 90° orientation

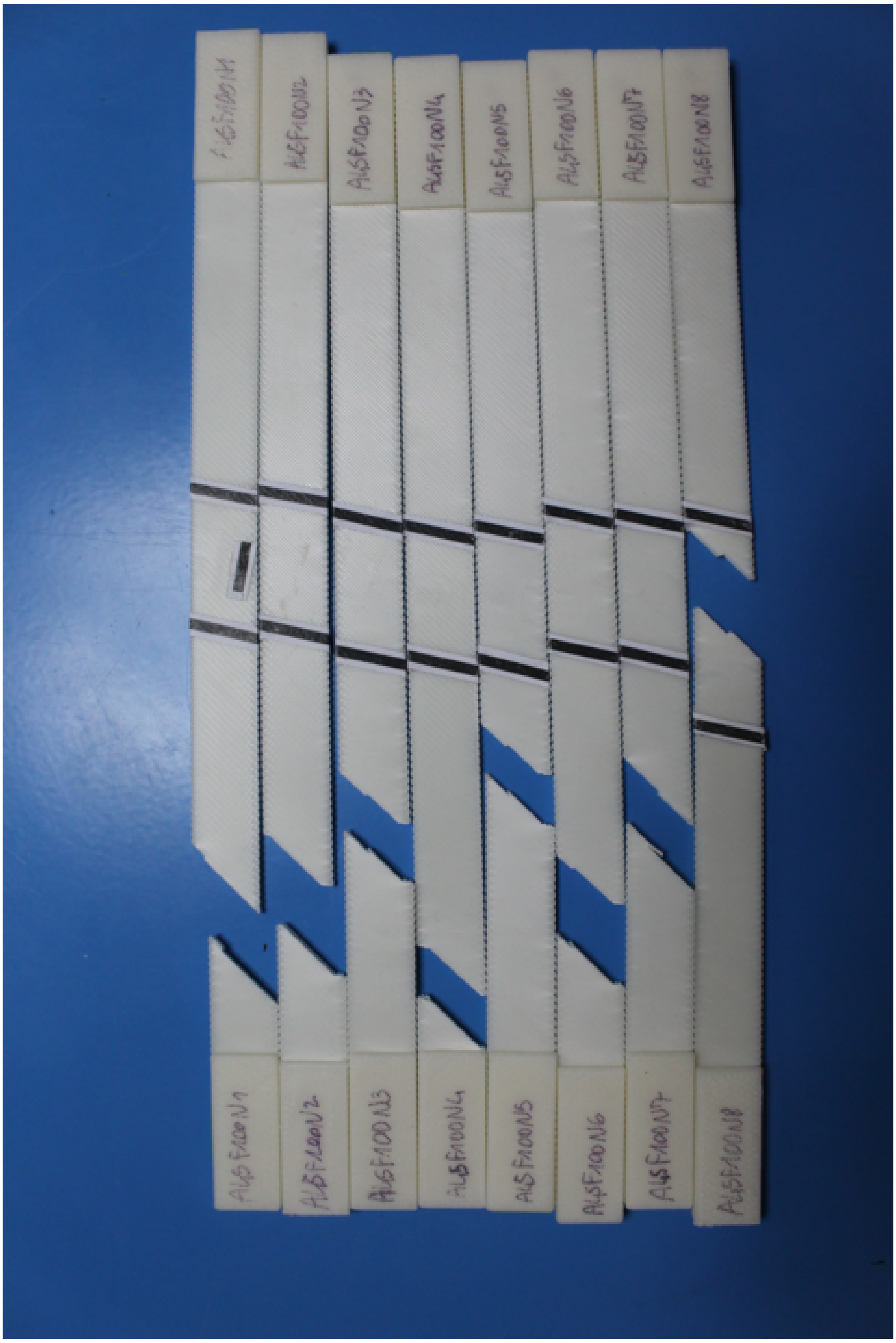

Figure 4.28: Specimen screenshot, configuration 1, 45° orientation

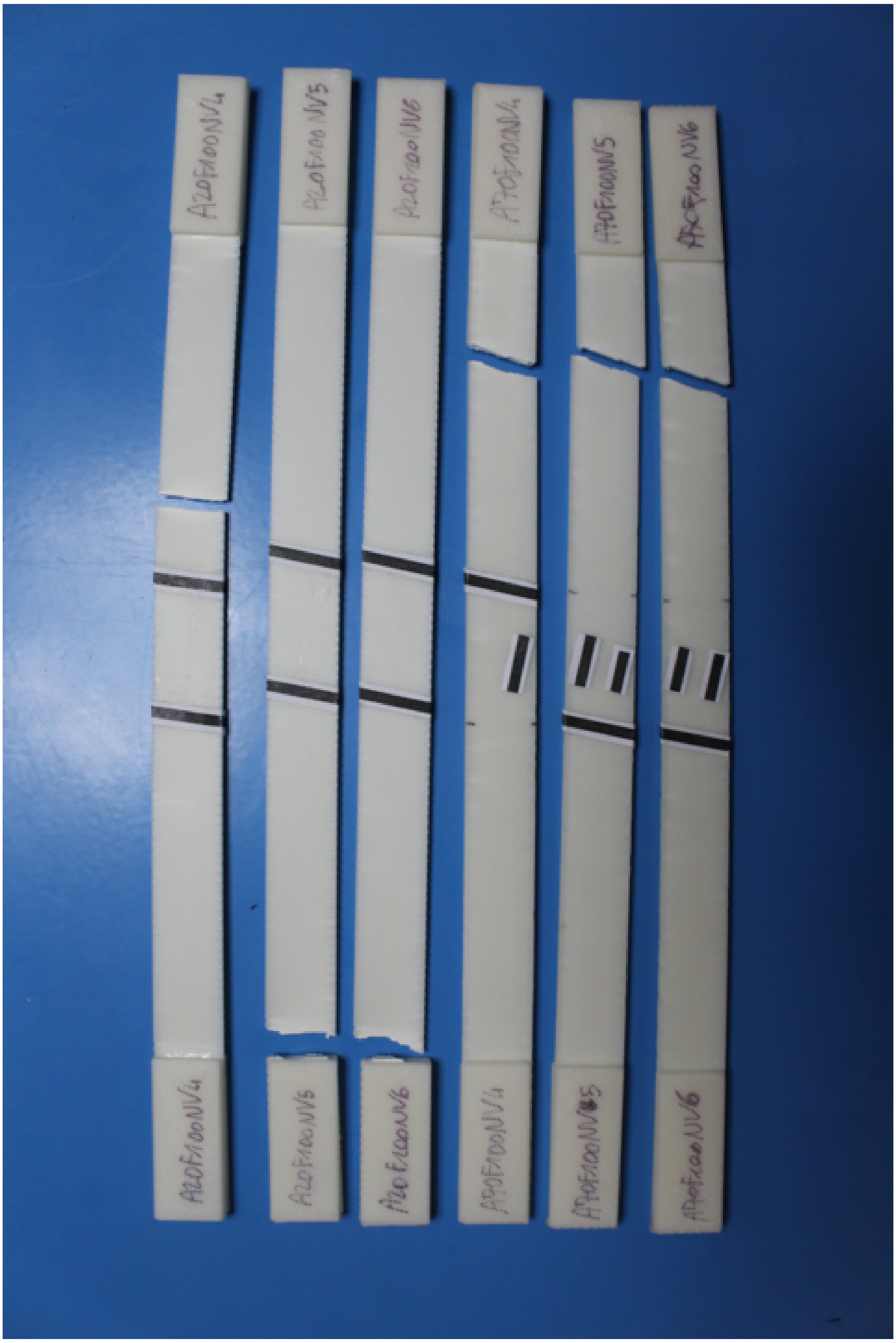

Figure 4.29: Specimen screenshot, configuration 1, 20° and 70° orientation

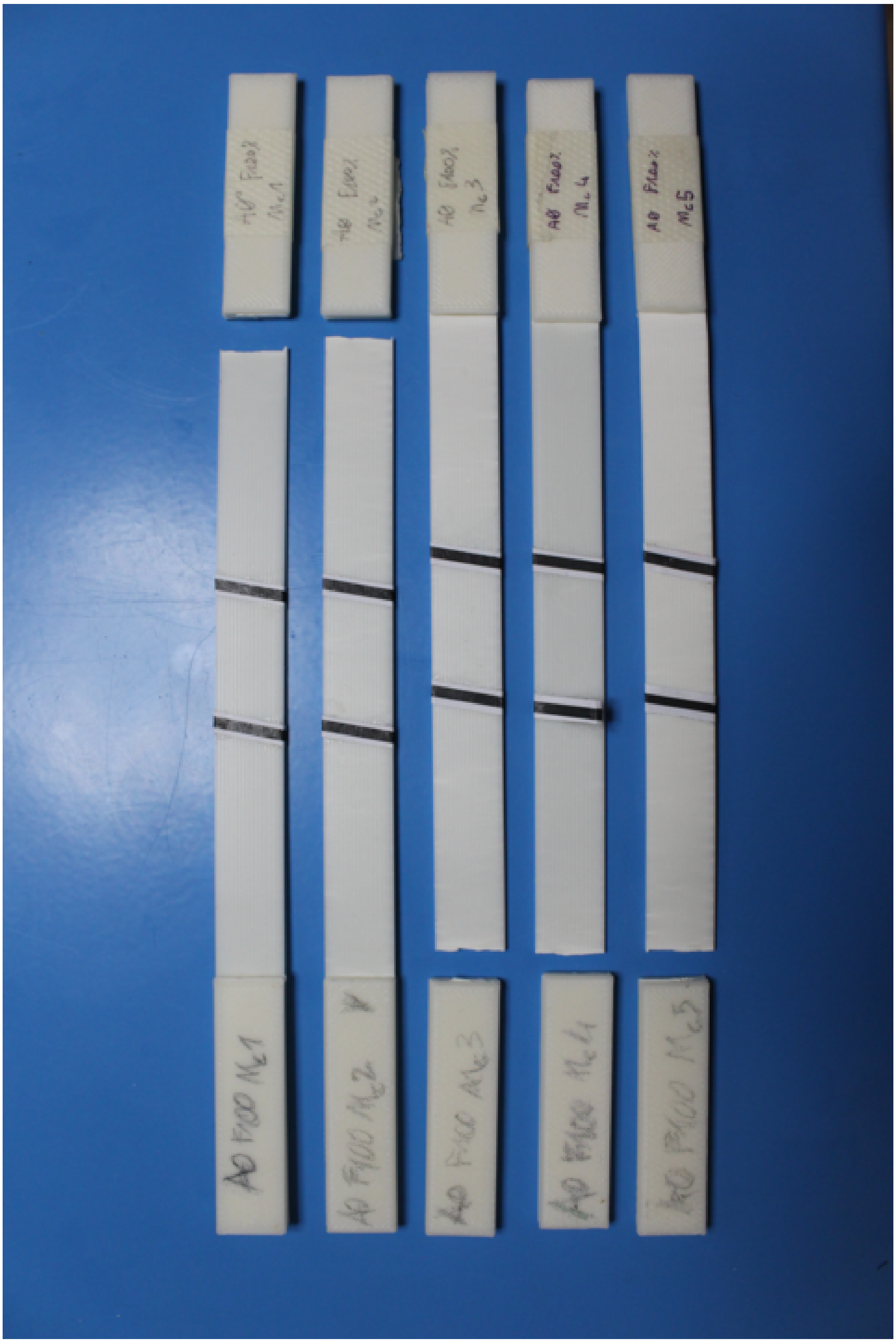

Figure 4.30: Specimen screenshot, configuration 2, 0° orientation

Figure 4.31: Specimen screenshot, configuration 2, 90° orientation

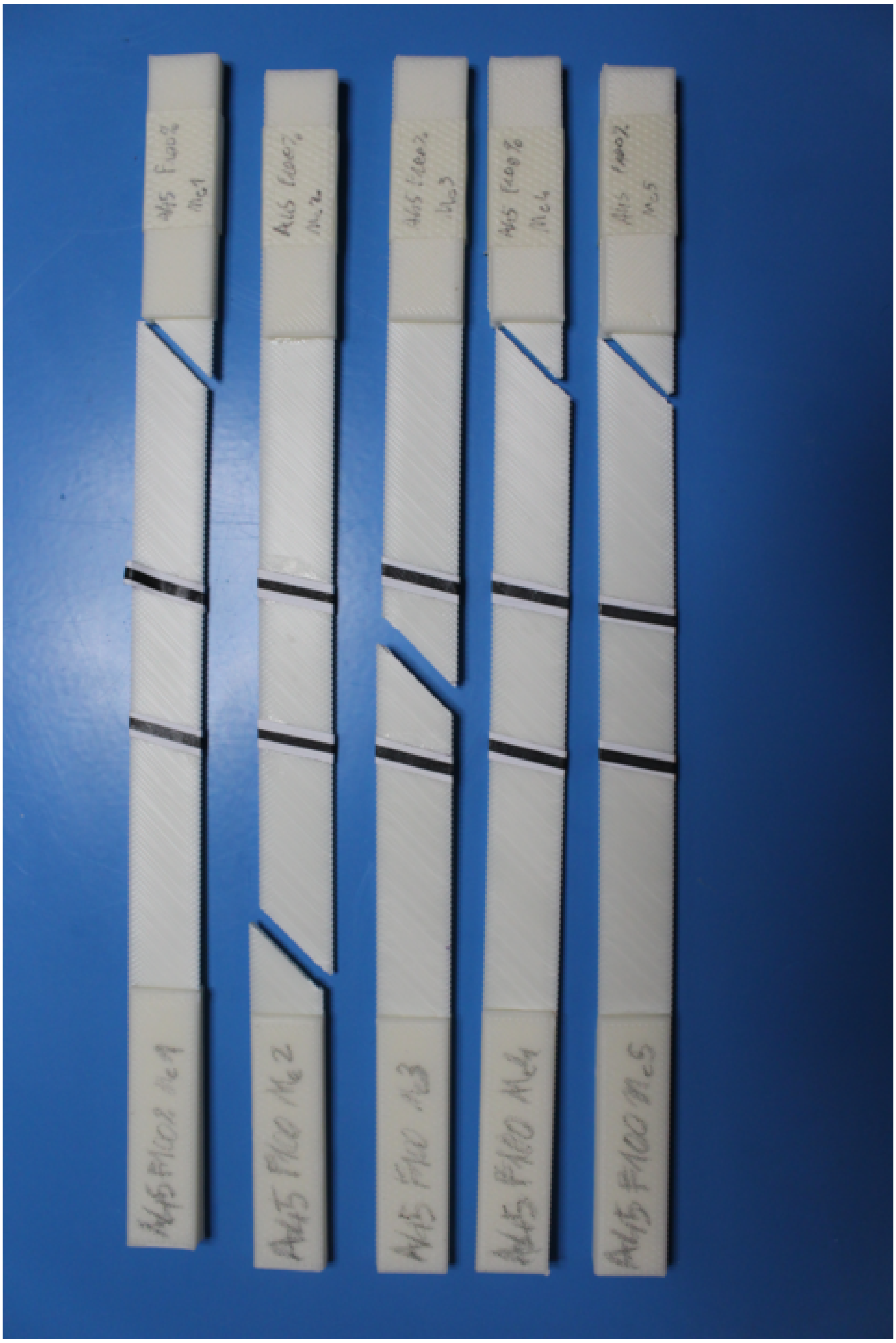

Figure 4.32: Specimen screenshot, configuration 2, 45° orientation

Figure 4.33: Specimen screenshot, configuration 2, 20° and 70° orientation

Figure 4.34: Specimen screenshot, configuration 3, 0° orientation

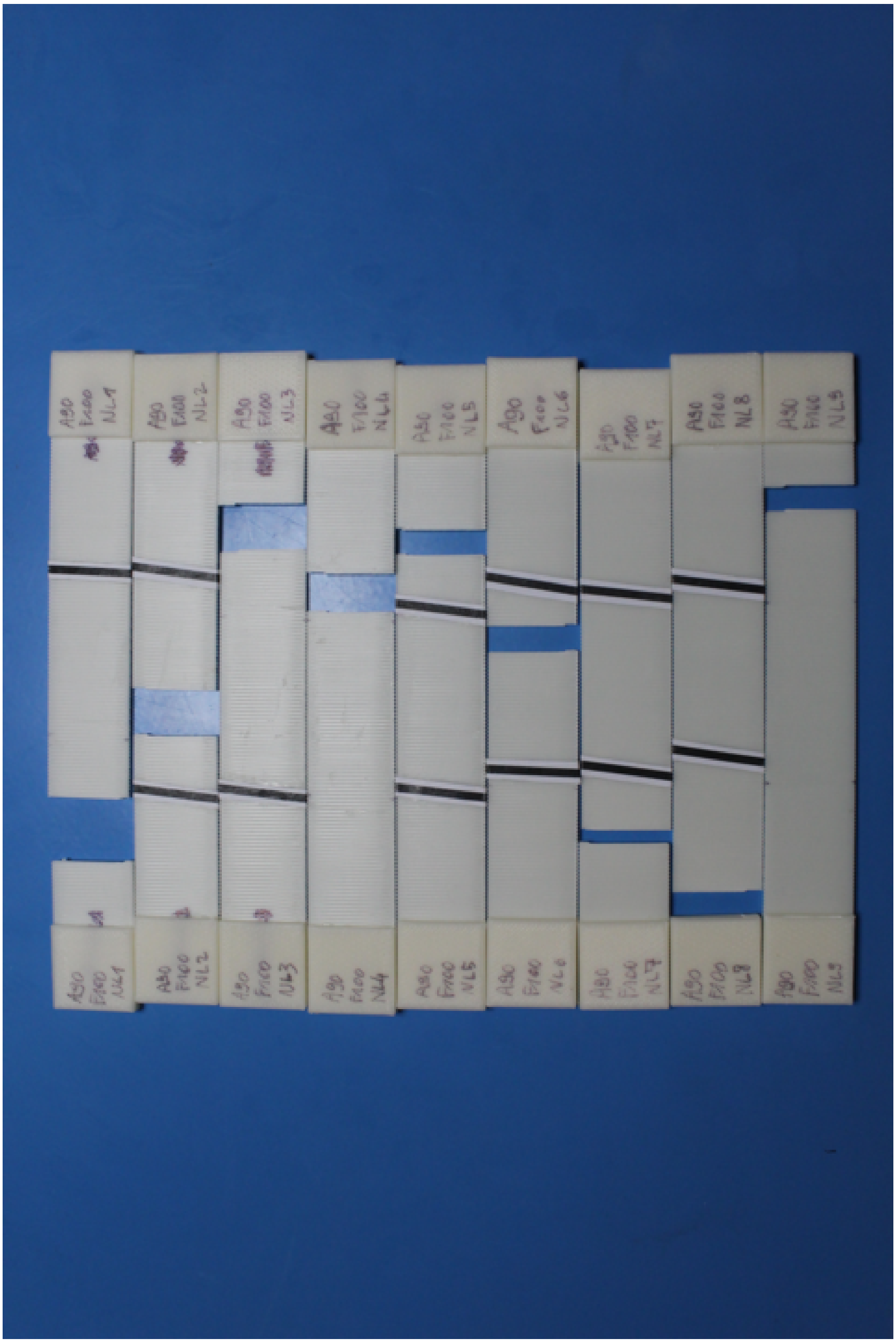

Figure 4.35: Specimen screenshot, configuration 3, 90° orientation

Figure 4.36: Specimen screenshot, configuration 3, 45° orientation

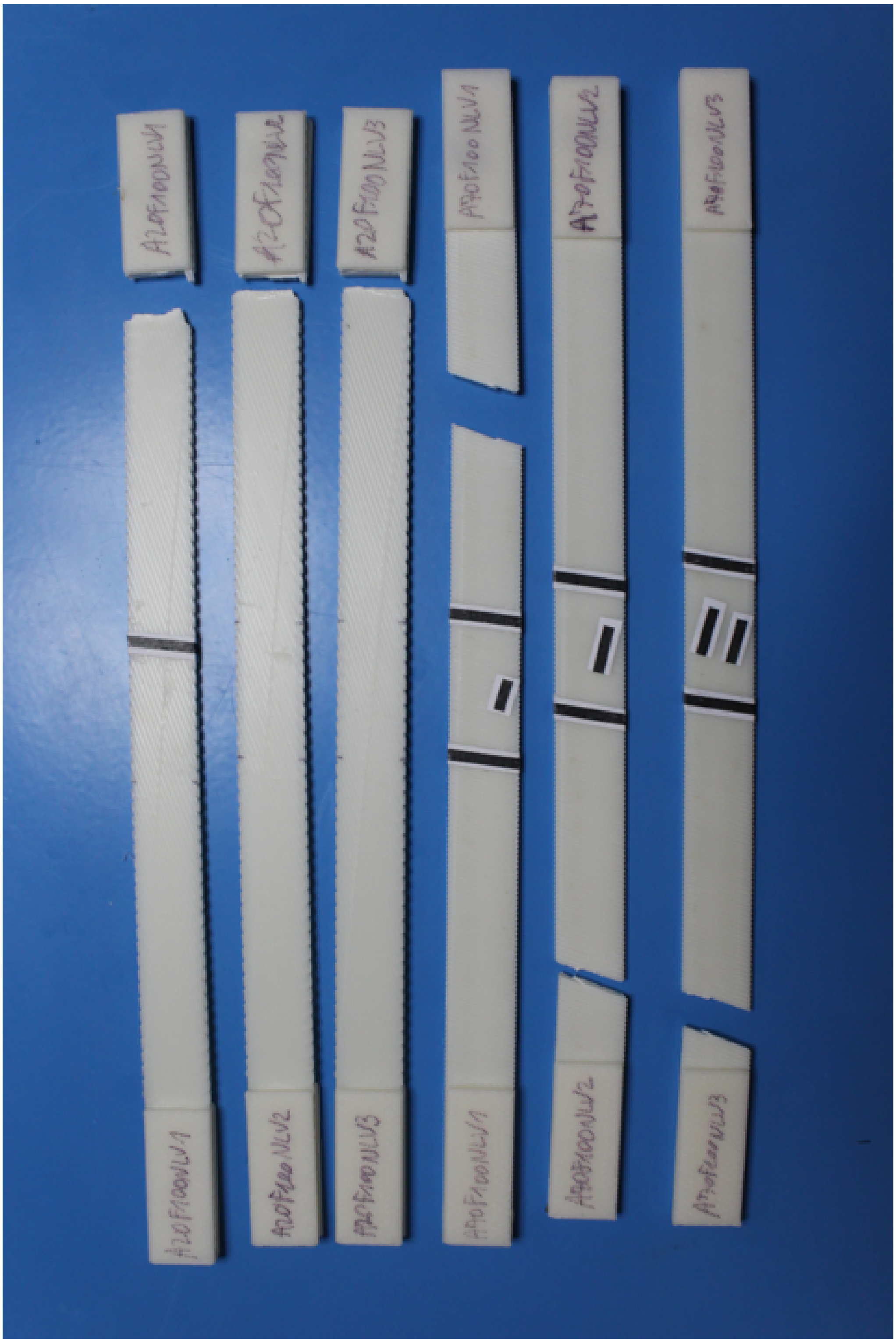

Figure 4.37: Specimen screenshot, configuration 3, 20° and 70° orientation

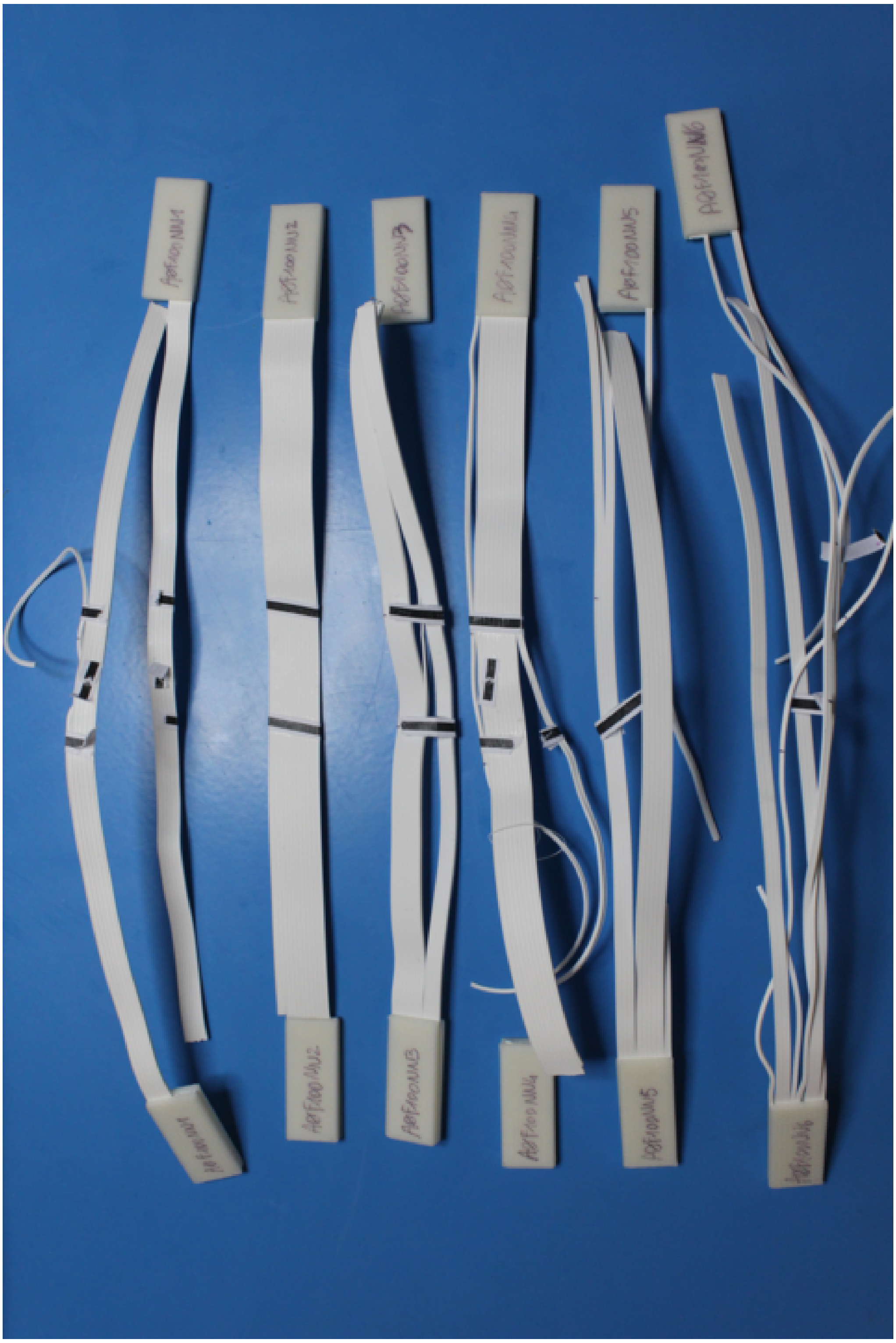

Figure 4.38: Specimen screenshot, configuration 4, 0° orientation

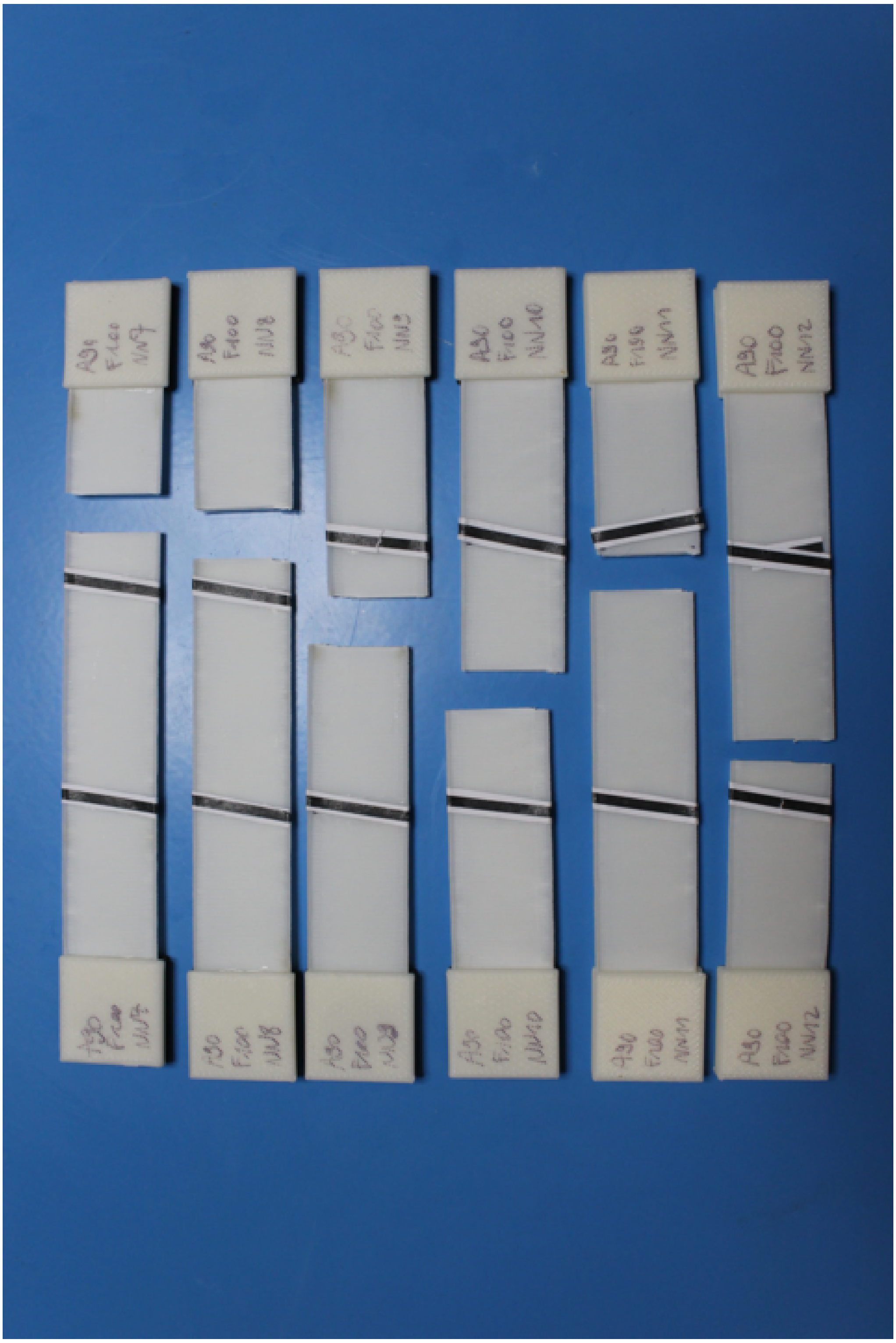

Figure 4.39: Specimen screenshot, configuration 4, 90° orientation

Figure 4.40: Specimen screenshot, configuration 4, 45° orientation

Figure 4.41: Specimen screenshot, configuration 4, 20° and 70° orientation

Chapter 5

Design approach

Knowing the yielding stress state of a structure and its most dangerous regions is essential to design an optimized part. A fitting example can be found in biomedical field: as previously stated, bone implant production for internal fixation has been growing in the last decades. Through 3D printing, complex geometries, strong and light implants and less waste of material are all feasible goals. Using the material's mechanical properties previously obtained, in this section, an extremely simplified geometry of an implant, i.e. a rectangular holed thin plate, has been simulated and optimized using finite element method (FEM), then 3D printed and finally tested. The goals of this procedure are the following:

- Minimize the object's mass, while satisfying certain safety requirements.
- Identify the yielding stress state of the 3D printed part.
- Identify the regions of maximum stress concentration, i.e. the "risk zones", where the part starts to yield.

5.1 Optimization problems: a brief overview

In optimization problems the main goal is to find the best solution among all the feasible solutions, either to minimize effort or to maximize benefit, which can be usually expressed as a function of design parameters. An optimization problem is then the process of finding the conditions that give the maximum or the minimum value of a function, called objective function. Optimization problems are divided in two categories depending on the type of variables considered:

- Discrete variables (combinatorial optimization problems).
- Continuous variables (constrained optimization problems and multimodal optimization problems).

The canonical form of an optimization problem is stated as follows [6]:

find

$$x = (x_1, x_2, ..., x_n) \tag{5.1}$$

which minimizes

$$f(x) \tag{5.2}$$

subject to the constraints

$$g_i(x) \leq 0, \qquad i = 1, .., m \tag{5.3}$$

and

$$h_j(x) = 0, \qquad j = 1, ..., p \tag{5.4}$$

where:

- $x \in \mathbb{R}^n$ is the optimization variable (also called design vector).
- $f(x) : \mathbb{R}^n \longrightarrow \mathbb{R}$ is the objective (or cost) function to be minimized over the variable x.
- $g_i(x) \leq 0$, with $g_i(x) : \mathbb{R}^n \longrightarrow \mathbb{R}$, are called inequality constraints.
- $h_j(x) = 0$, with $h_j(x) : \mathbb{R}^n \longrightarrow \mathbb{R}$, are called equality constraints.

If $m + p = 0$ then the optimization problem is called unconstrained. By convention, the standard form of the optimization problem is defined by minimization, but a maximization problem can be obtained simply by negating the objective function [13]. The variable x can be scalar or a vector of n design parameters. Assignments of specific values to x represents a solution of the optimization problem. Together, all the solutions form a set of solutions X, called search space (or design space), where $x \in X$. Design constraints define the feasible region Ω, in which the solutions are acceptable, from the space where they are unfeasible (fig. 5.1).

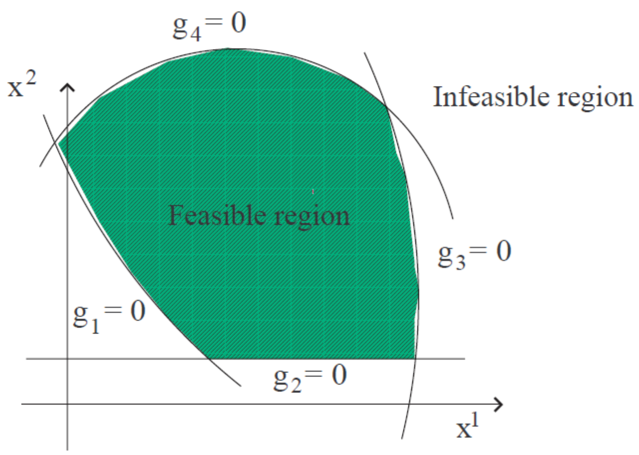

Figure 5.1: Schematic example of a feasible region in a two-dimensional search space, with inequality constraints [6]

The goal is to find the solution x^* in the feasible region Ω that minimize (or maximize) the objective function ($f(x^*)$). Choosing an appropriate objective function is essential, because what is the optimal design with respect to a certain criterion may be unacceptable with respect to another one [6]. Given an objective function $f(x)$, the region of all the values x such that $f(x) = k$ forms a hypersurface, called objective function surface; different values of k give a different hypersurface. Similarly, the set of design values that satisfy the equations $g_i(x) = 0$ forms a hypersurface in the search space, called constraint surface. Once the objective function and constraint surfaces are defined, the optimization problem can be solved. If the objective function is a vector, the optimization problem is called multi-objective.

5.2 Optimization of a holed 3D printed thin plate

After having extracted the material mechanical properties, the next step consisted to optimize a 3D printed rectangular thin plate, with a hole of fixed diameter in its center. Finite element analysis (FEA) has been used to approach the optimization problem, since the constraint function could not be analitically calculated. In the FEA software the specimen has been defined as a shell element of 8 layers. Each layer is characterized with a proper thickness, a proper fiber orientation and a proper safety factor, for a total of 16 design parameters and 8 constraints.

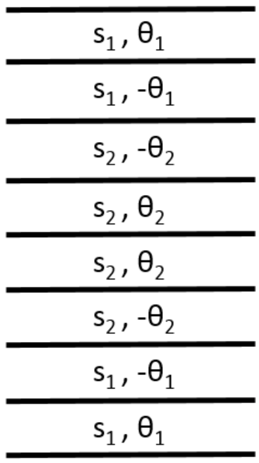

Figure 5.2: Layer sequence of the designed sample

To remove the coupling between normal forces and curvatures and the coupling between normal forces and shear strains, the sample layer sequence has been designed in order to obtain a symmetric and balanced laminate 5.2. The design parameters have been thus reduced from 16 to 4, s_1, s_2, θ_1 and θ_2, while the constraints have been reduced to 2, η_1 and η_2. The last design parameter taken into account is the sample width w.

The objective function $f(x)$ is the printed part's mass and it is calculated as:

$$f(x) = \rho t(lw - \pi \frac{d^2}{4}) \tag{5.5}$$

where (fig. 5.3):

- ρ is the material density.
- l is the specimen length.
- w is the specimen width.
- t is the specimen thickness.
- d is the specimen hole diameter.

The constraint function is represented the safety factor $\eta(x)$. A safety factor of 1,5 means that every point of the specimen must be able to bear at least 1,5 times the applied load, without starting to yield. In this study the following safety factor conditions are required:

$$\eta_1(x) \geq 1,5 \qquad \eta_2(x) \geq 1,5 \tag{5.6}$$

Two optimization procedures have been carried out:

- A first optimization, to identify the optimum region, in a wide, more general, search space.
- A second optimization, with a narrower, more accurate search space, obtained with the first optimization.

In both cases the optimization problem is the following:

$$\begin{cases} \min\limits_{x \in X} & f(x) \\ \text{subject to} & \eta_1(x) \geq 1,5 \\ & \eta_2(x) \geq 1,5 \end{cases} \tag{5.7}$$

5.2.1 General optimization

The first optimization can be considered as an initial screening, which aims to find the region where the global optimum resides. The resulting narrower search space will be later used in the second optimization. The preassigned parameters are shown in tab. 5.1

Table 5.1: Preassigned parameters

Preassigned parameters	Values
Material density - ρ	1,08 g/cm^3
Specimen gage length - l	80 mm
Hole diameter - d	5 mm
Longitudinal Young's modulus - E_1	1810 MPa
Transversal Young's modulus - E_2	1695 MPa
Major Poisson's ratio - ν_{12}	0,32
Minor Poisson's ratio - ν_{21}	0,3
Shear modulus - G_{12}	617 MPa
Longitudinal tensile strength - σ_1^t	25,5 MPa
Transversal tensile strength - σ_2^t	15,7 MPa
Shear strength - τ_{12}	13,7
Longitudinal compressive strength - σ_1^c	-25,5 MPa
Transversal compressive strength - σ_2^c	-15,7 MPa

Compressive strengths have been considered equal to tensile strengths, in order to use Tsai-Hill failure criterion.

The design parameters can vary between the following ranges (tab. 5.2):

Table 5.2: Design parameters ranging values

Design parameters	Minimum value	Maximum value
θ_1	0°	90°
θ_2	0°	90°
s_1	0,2 mm	0,6 mm
s_2	0,2 mm	0,6 mm
w	12 mm	15 mm

A force of 100 N, directed along the sample length, has been applied, as shown in fig. 5.3:

Response surface methodology (RSM), a collection of statistical and mathematical techniques useful for developing, improving, and optimizing processes [49], has been used to deal with the optimization problem. The most extensive applications of RSM are found in the industry field, especially in situations where several input variables potentially influence performance, or quality,

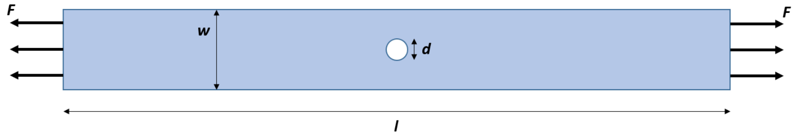

Figure 5.3: Applied load and fixed end constraint

measures (called response) of the product or process[49]. A Kriging response surface model has been considered to determine the optimum region in the search space. Non-dominated sorting genetic algorithm-II (NSGA-II) [20], which is a multi-objective evolutionary algorithm, acts on the response surfaces, in order to find the region where resides the global optimum. While the rate of convergence is low, the algorithm is very robust and does not remain trapped in local minimum values, thus it is useful for searching optimum regions.

The objective function, constraints and design parameters values at which the algorithm converges are shown in 5.4:

After a set number of iterations (13000), the optimum region found by the algorithm has been the following (tab. 5.3):

Table 5.3: Optimum region found with the first optimization

Design parameters	Minimum value	Maximum value
θ_1	0°	15°
θ_2	0°	15°
s_1	0,2 mm	0,22 mm
s_2	0,2 mm	0,22 mm
w	13 mm	14 mm

5.2.2 Focused optimization

From the values obtained through the first optimization process, another, more accurate optimization has been carried out. Relying on the previous solution, a narrower search space has been designed, in order to delve deeper into the optimum region and find the global minimum of the problem. Furthermore, the layers thickness values s_1 and s_2 have been set to 0,2 mm, since it is an easily printable thickness value. The new search space is shown in (tab. 5.4):

Table 5.4: Design parameters ranging values

Design parameters	Minimum value	Maximum value
θ_1	0°	15°
θ_2	0°	15°
w	13 mm	14 mm

This time a gradient descent algorithm (also known as method of steepest descent), which is a first order iterative optimization algorithm, has been applied on the convex response surface. To find the minimum of a function using gradient descent, one takes steps proportional to the negative of the gradient (or of the approximate gradient) of the function at the current point. The rate of convergence of the gradient descent algorithm is very high, so few iterations (65 steps, in this case) are needed to converge to the optimum. In fig. 5.5 the gradient algorithm results are shown:

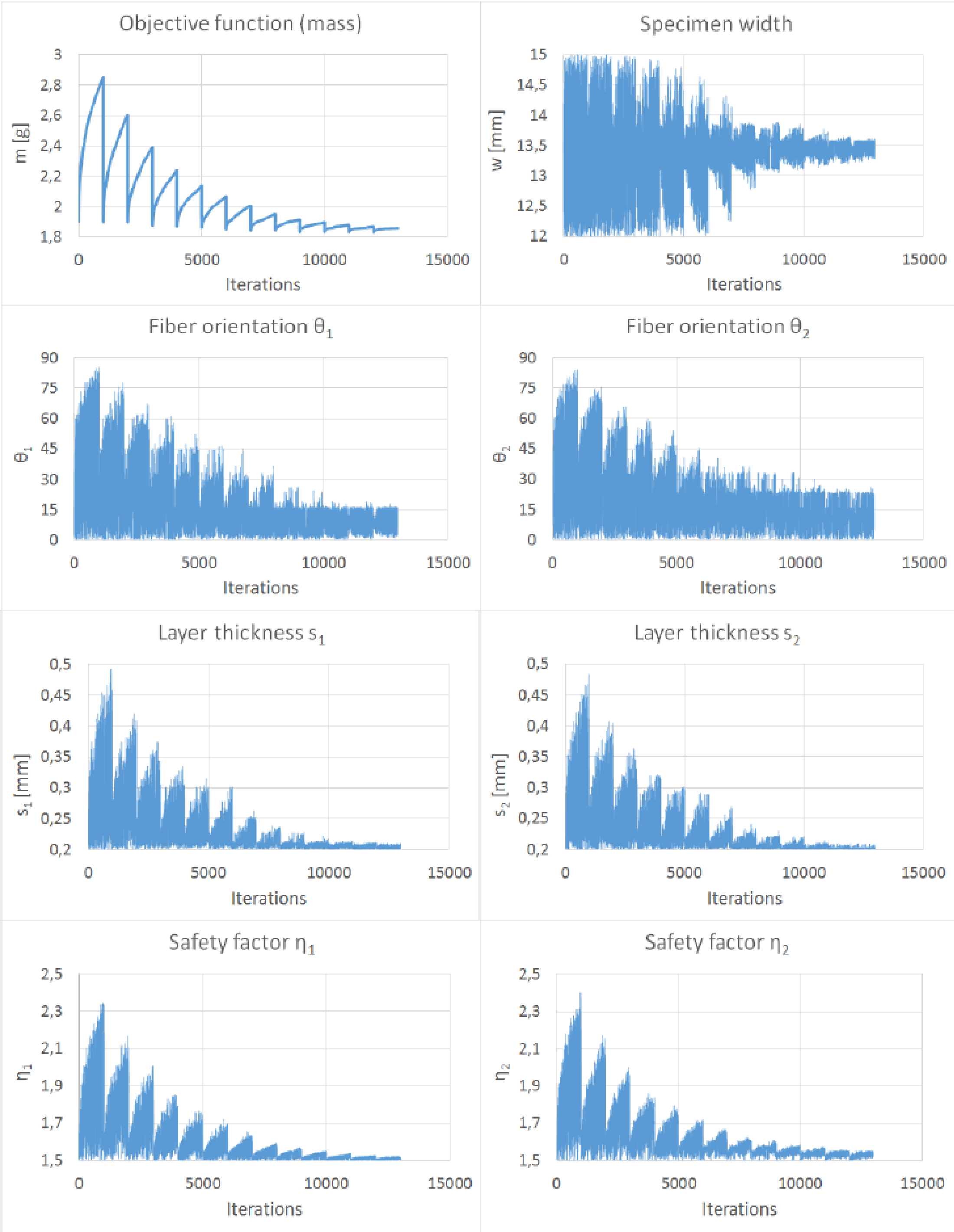

Figure 5.4: Optimization 1 convergence

The results of the second optimization have been approximated to the values shown in tab. 5.5, to insert them in the slicing software. Subsequently, sample printing and tensile tests have been carried out.

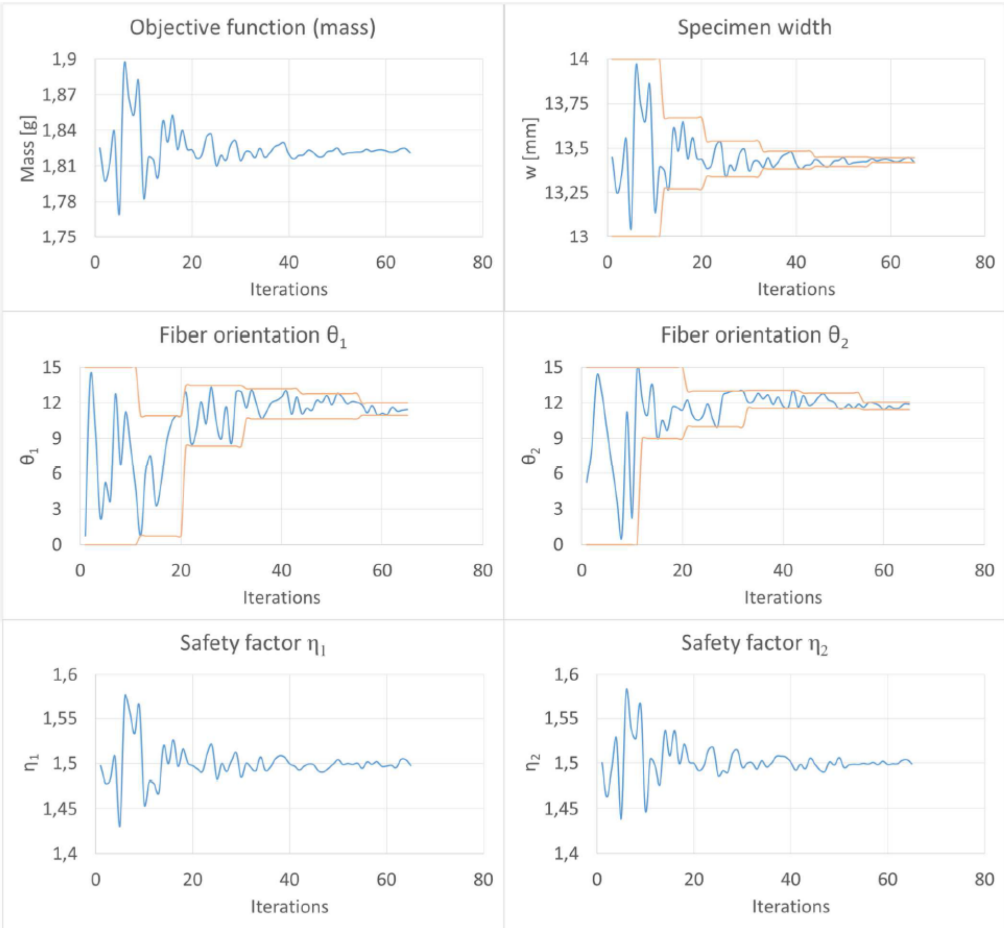

Figure 5.5: Optimization 2 convergence

Table 5.5: Optimum solution found with the second optimization (approximated values)

Design parameters	Optimum values
θ_1	11°
θ_2	11°
w	13,5 mm

5.3 Tensile test results and discussion

The design parameters obtained from the optimization process have been used to 3D print optimized holed thin plates, shown in fig. 5.6. To correctly print these samples, the same experimental procedure described in chapter 3 has been applied, including extensive G-code elaboration, specimen preparation and tensile test.

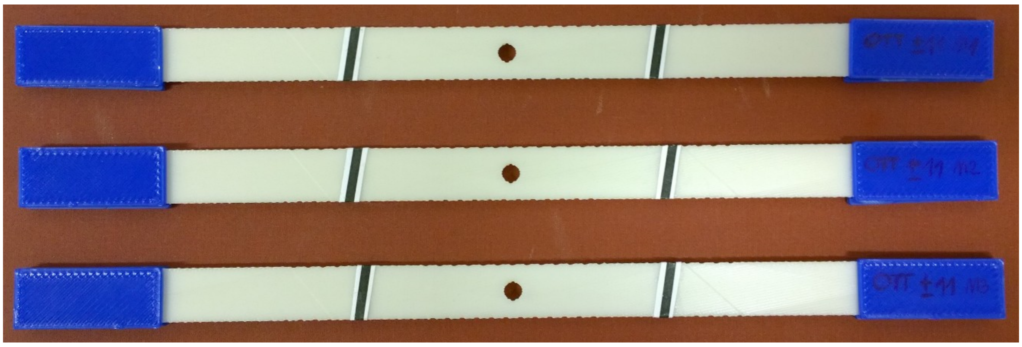

Figure 5.6: 3D printed holed specimens

To find the yielding load, F_y, after which the part starts to yield in at least one point (following Tsai-Hill failure criterion), the real width, thickness and hole diameter dimensions of a holed specimen have been measured and these values have been inserted in the FEA software. For a specific test specimen the actual yielding load found by the FEA is $F_y = 177$ N, and the most dangerous regions are shown in fig. 5.7.

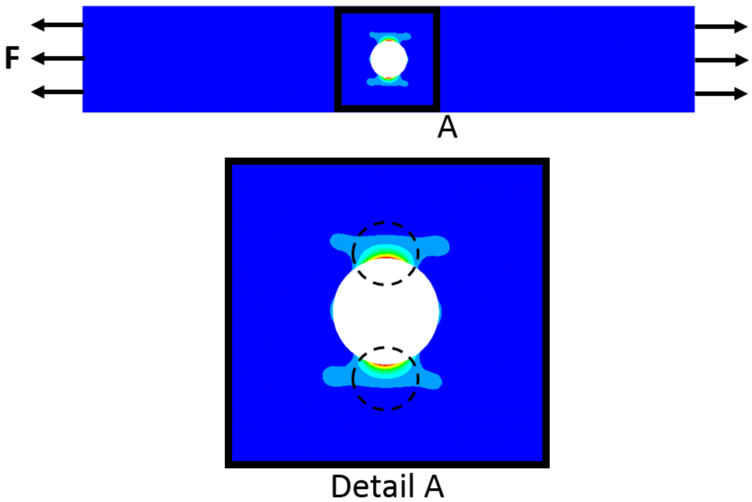

Figure 5.7: Specimen's risk regions identified by the FEA

Afterwards the specimen has been tested. The load-displacement graphic is shown in fig. 5.8. The sample failed at a loading value of $F_u = 380$ N. As it is well known, once a material region reaches its yield point, it begins to deform plastically and its yielded points cannot bear further loading. In this case the yielding phenomenon starts in proximity of the hole (fig. 5.10) and gradually propagates perpendicularly to the loading direction towards the edges of the specimen.

To explain this fact, plastic collapse and stress concentration around the specimen's hole hypotheses have been considered. In a holed thin plate subject to uniaxial loading, the stress around

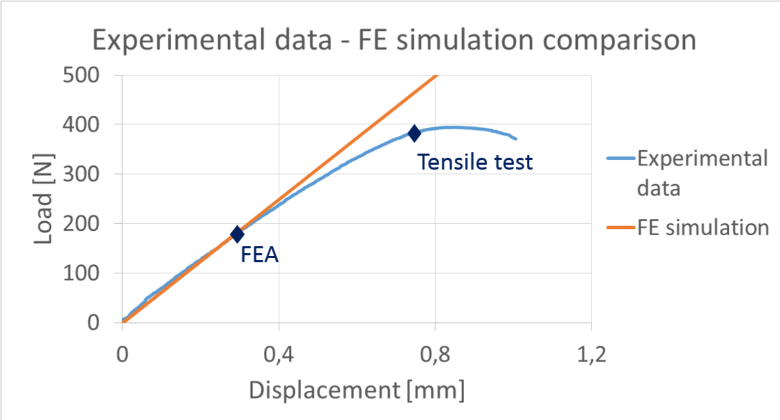

Figure 5.8: Load-displacement curves of the specimen: experimental data and FE simulation results

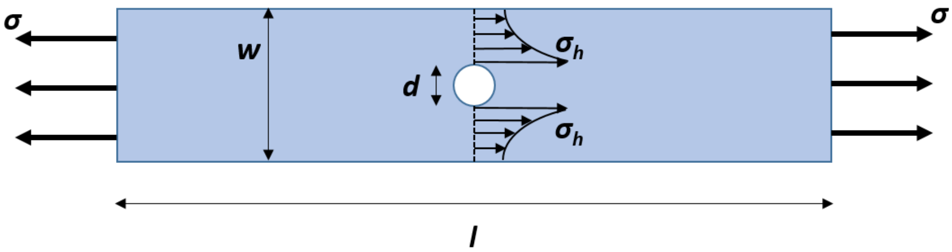

Figure 5.9: Schematic example of a stress gradient around a hole in the case of uniaxial stress state

the hole is not uniformly distributed, but presents a gradient perpendicular to the loading direction, as shown in fig. 5.9. The stress σ_h is at its maximum value at the hole, and decreases as we move away from it in the cross section direction. This means that the first regions that reach the yield point are those near the hole. Once they yielded, they cannot sustain any more loading increment, but the neighboring regions, being still in their elastic domain, can be further loaded. Then, once they reached their yielding point, ulterior loading increment can be sustained only by their neighboring regions. The specimen will sustain further loading increment till the entire cross section at the hole is fully plasticized.

Then the FE analysis is consistent with experimental data, since it actually predicts the first yielding point, which occurs in proximity of the hole. So those regions have actually reached their yielding limit, but, for the presence of a stress gradient, the neighboring regions can bear further loading increment, because they are still in their linear elasticity domain. Hence, in this case, the entire structure's yielding load is 177 N and linear elastic analysis stops here. To further model the behavior till the ultimate failure load of 380 N, constitutive models that include plasticity must be used. Fig. 5.10 shows the gradual yielding (whitening regions) around the specimen hole as the applied load increases, with the relative force values.

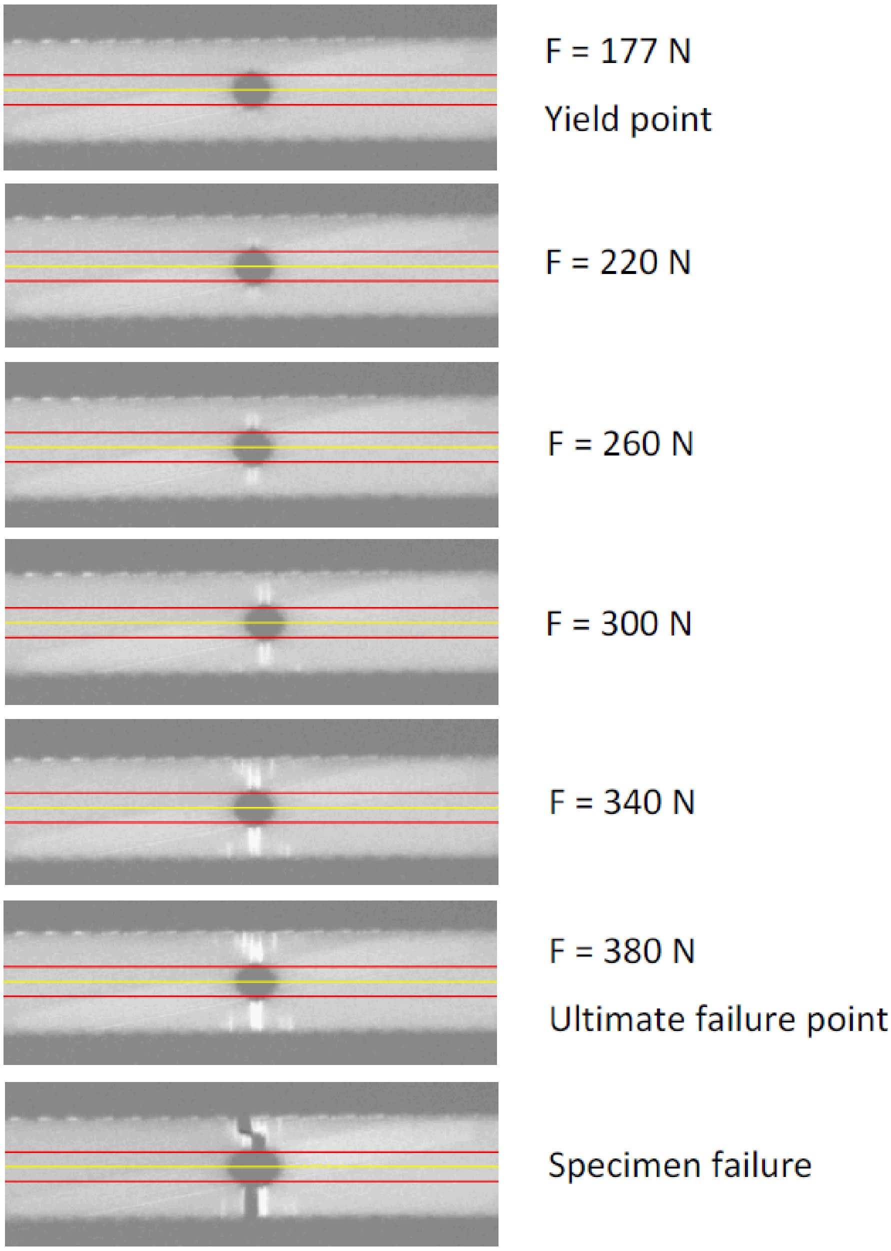

Figure 5.10: Progressive yielding around the specimen hole

Chapter 6

Conclusions

Mechanical in-plane properties of 3D printed thermoplastic material has been investigated and characterized. Two types of material and three different mesostructures have been considered. The results show that raster orientation significantly influences specimens mechanical properties, especially yield strength (considered as the maximum admissible stress state before yielding). Highest stiffness and strength values has been found for 0° specimens, i.e., when the filament extrusion direction is aligned with the loading direction. Conflicting values for configuration 4 elastic modulus, where tensile modulus at 90° is greater than tensile modulus at 0°, have been obtained, probably due to the different material composition. Classical Lamination Theory and Tsai-Hill Failure Theory were found to be capable of predicting in-plane stiffness and strength of 3D printed materials reasonably well. Comparison results show that mechanical properties also depends from the extruded filament's cross section area. Stiffness generally increases when raising cross section area. Fiber strength increases for lower cross sections, meaning that more, smaller, fibers exhibit higher overall strength than less, bigger fibers. Conversely, fiber to fiber strength increases when raising filament cross-section.

It has been shown that the mechanical properties can be used to print an optimized structural part, adjusting fiber orientation, layer thickness and specimen width. The sample "risk zones" have been identified in the finite element simulation and confirmed through the tensile tests: the yielding starts near the hole and propagates perpendicularly to the loading direction till the specimen edges. This phenomenon is explained by the stress gradient at the hole. The analyzed specimen's yielding point is 177 N and it has been shown that FE analysis is consistent with experimental data. From 177 N to 380 N, the regions around the specimen gradually begin to deform plastically, till its failure: therefore, at the moment it is not possible to describe the specimen's mechanical behavior when the applied load goes beyond the yielding value of 177 N.

The results of this work can be used in future research, as a guideline for mechanical characterization of other materials, where elastic and strength behavior are considered functions of fiber orientation and cross sectional area. The obtained mechanical properties can be used to design a functional, optimized 3D printed component. This work is a first step in the research of new technologies and methods to investigate, characterize and design 3D printed parts with optimized properties.

Further improvements can be made. The mechanical behavior of the material has been described only in its linear elasticity region: other, more complex, constitutive models which include plastic deformation, must be used, to find the ultimate failure load. The geometry of the specimen may be complicated, adding holes and optimizing its shape. In actual implants, few holes are used for removing mass and lighten the structure; the majority of holes are used as fasteners, in which screws are inserted. In this case a contact analysis may be required. The experimental procedure could be made easier and quicker, with the development of an application which modifies the single layers properties, given the desired input parameters.

Bibliography

[1] Aggarangsi, P. and J. L. Beuth (2006). Localized preheating approaches for reducing residual stress in additive manufacturing. In *Proc. SFF Symp., Austin*, pp. 709–720.

[2] Ahn, S.-H., M. Montero, D. Odell, S. Roundy, and P. K. Wright (2002). Anisotropic material properties of fused deposition modeling abs. *Rapid Prototyping Journal 8*(4), 248–257.

[3] Akay, M. and S. Ozden (1995). The influence of residual stresses on the mechanical and thermal properties of injection moulded abs copolymer. *Journal of materials science 30*(13), 3358–3368.

[4] (AMO), D. A. M. O. (2012, August). Additive manufacturing: Pursuing the promise.

[5] ASTM, E. (2004). 111-04, standard test method for young's modulus, tangent modulus, and chord modulus. *Annual Book of ASTM Standards 3*.

[6] Astolfi, A. (2005). Optimization, an introduction. *Estados Unidos, Octubre del*.

[7] Azzi, V. and S. Tsai (1965). Anisotropic strength of composites. *Experimental mechanics 5*(9), 283–288.

[8] Baldinger, M. and A. Duchi (2013). Price benchmark of laser sintering service providers. In *High Value Manufacturing: Advanced Research in Virtual and Rapid Prototyping: Proceedings of the 6th International Conference on Advanced Research in Virtual and Rapid Prototyping, Leiria, Portugal, 1-5 October, 2013*, pp. 37. CRC Press.

[9] Banks, J. (2013). Adding value in additive manufacturing: researchers in the united kingdom and europe look to 3d printing for customization. *IEEE pulse 4*(6), 22.

[10] Bartlett, S. (2013). Printing organs on demand. *The Lancet Respiratory Medicine 1*(9), 684.

[11] Bertoldi, M., M. Yardimci, C. Pistor, S. Guceri, and G. Sala (1998). Mechanical characterization of parts processed via fused deposition. In *Proceedings of the 1998 solid freeform fabrication symposium*, pp. 557–565.

[12] Bourell, D. L., M. C. Leu, and D. W. Rosen (2009). Roadmap for additive manufacturing: identifying the future of freeform processing. *The University of Texas at Austin, Austin, TX*.

[13] Boyd, S. P. and L. Vandenberghe (2004). Convex optimization (pdf). *Np: Cambridge UP*.

[14] Bullinger, H.-J. (2009). *Technology guide: Principles-applications-trends*. Springer Berlin Heidelberg.

[15] Caulfield, B., P. McHugh, and S. Lohfeld (2007). Dependence of mechanical properties of polyamide components on build parameters in the sls process. *Journal of Materials Processing Technology 182*(1), 477–488.

[16] Cevolini, F. (2006). Rapid manufacturing with carbon reinforced plastics: applications for motor sport, aerospace and automotive small lot production parts. In *Proceedings of the 2nd RM Technical Forum, Girona Spain.*

[17] Christiyan, K. J., U. Chandrasekhar, and K. Venkateswarlu (2016). A study on the influence of process parameters on the mechanical properties of 3d printed abs composite. In *IOP Conference Series: Materials Science and Engineering*, Volume 114, pp. 012109. IOP Publishing.

[18] Chua, C. K., K. F. Leong, and C. S. Lim (2003). Rapid prototyping data formats. *Rapid prototyping: Principle and Application*, 237–294.

[19] Cui, X., T. Boland, D. D D'Lima, and M. K Lotz (2012). Thermal inkjet printing in tissue engineering and regenerative medicine. *Recent patents on drug delivery & formulation 6*(2), 149–155.

[20] Deb, K., A. Pratap, S. Agarwal, and T. Meyarivan (2002). A fast and elitist multiobjective genetic algorithm: Nsga-ii. *IEEE transactions on evolutionary computation 6*(2), 182–197.

[21] Economist, T. (2011, 10 February). The printed world: Three-dimensional printing from digital designs will transform manufacturing and allow more people to start making things.

[22] Economist, T. (2013, 07 September). 3d printing 3d printing scales up.

[23] Es-Said, O., J. Foyos, R. Noorani, M. Mendelson, R. Marloth, and B. Pregger (2000). Effect of layer orientation on mechanical properties of rapid prototyped samples. *Materials and Manufacturing Processes 15*(1), 107–122.

[24] Frigge, M., D. C. Hoaglin, and B. Iglewicz (1989). Some implementations of the boxplot. *The American Statistician 43*(1), 50–54.

[25] Gausemeier, I. J. (2011). Thinking ahead the future of additive manufacturing–. *Analysis of Promising Industries, Heinz Nixdorf Institute, University of Paderborn Product Engineering, Paderborn*, 14.

[26] Gebhardt, A. (2012). *Understanding additive manufacturing: rapid prototyping-rapid tooling-rapid manufacturing.* Carl Hanser Verlag GmbH Co KG.

[27] Giffi, C., B. Gangula, and P. Illinda (2014). 3d opportunity for the automotive industry: Additive manufacturing hits the road.

[28] Gross, B. C., J. L. Erkal, S. Y. Lockwood, C. Chen, and D. M. Spence (2014). Evaluation of 3d printing and its potential impact on biotechnology and the chemical sciences. *Analytical chemistry 86*(7), 3240–3253.

[29] Guo, N. and M. C. Leu (2013). Additive manufacturing: technology, applications and research needs. *Frontiers of Mechanical Engineering 8*(3), 215–243.

[30] Hill, R. (1998). *The mathematical theory of plasticity*, Volume 11. Oxford university press.

[31] Huang, R., M. Riddle, D. Graziano, J. Warren, S. Das, S. Nimbalkar, J. Cresko, and E. Masanet (2015). Energy and emissions saving potential of additive manufacturing: the case of lightweight aircraft components. *Journal of Cleaner Production*.

[32] Huang, S. H., P. Liu, A. Mokasdar, and L. Hou (2013). Additive manufacturing and its societal impact: a literature review. *The International Journal of Advanced Manufacturing Technology 67*(5-8), 1191–1203.

[33] Hull, C. (1986, 11 March). Apparatus for production of three-dimensional objects by stereolithography. US Patent 4,575,330.

[34] Jones, R. M. (1975). *Mechanics of composite materials*, Volume 193. Scripta Book Company Washington, DC.

[35] Kaw, A. K. (2005). *Mechanics of composite materials@articletsai1968fundamental, title=Fundamental aspects of fiber reinforced plastic composites, author=Tsai, SW, journal=Ann Arbor, MI: University Michigen Press, year=1968* . CRC press.

[36] Khaled, S. A., J. C. Burley, M. R. Alexander, and C. J. Roberts (2014). Desktop 3d printing of controlled release pharmaceutical bilayer tablets. *International journal of pharmaceutics 461* (1), 105–111.

[37] Klahn, C., B. Leutenecker, and M. Meboldt (2015). Design strategies for the process of additive manufacturing. *Procedia CIRP 36*, 230–235.

[38] Klein, G. T., Y. Lu, and M. Y. Wang (2013). 3d printing and neurosurgery—ready for prime time? *World neurosurgery 80* (3), 233–235.

[39] Kulkarni, P. and D. Dutta (1999). Deposition strategies and resulting part stiffnesses in fused deposition modeling. *Journal of manufacturing science and engineering 121* (1), 93–103.

[40] Lee, B., J. Abdullah, and Z. Khan (2005). Optimization of rapid prototyping parameters for production of flexible abs object. *Journal of Materials Processing Technology 169* (1), 54–61.

[41] Lee, C., S. Kim, H. Kim, and S. Ahn (2007). Measurement of anisotropic compressive strength of rapid prototyping parts. *Journal of materials processing technology 187*, 627–630.

[42] Li, L., Q. Sun, C. Bellehumeur, and P. Gu (2002). Composite modeling and analysis for fabrication of fdm prototypes with locally controlled properties. *journal of Manufacturing Processes 4* (2), 129–141.

[43] Liou, F. W. (2007). *Rapid prototyping and engineering applications: a toolbox for prototype development.* CRC Press.

[44] Mallick, P. K. (2007). *Fiber-reinforced composites: materials, manufacturing, and design.* CRC press.

[45] Mertz, L. (2013a). Dream it, design it, print it in 3-d: what can 3-d printing do for you? *IEEE pulse 4* (6), 15–21.

[46] Mertz, L. (2013b). New world of 3-d printing offers" completely new ways of thinking": q&a with author, engineer, and 3-d printing expert hod lipson. *IEEE pulse 4* (6), 12–14.

[47] Mohamed, O. A., S. H. Masood, and J. L. Bhowmik (2015). Optimization of fused deposition modeling process parameters: a review of current research and future prospects. *Advances in Manufacturing 3* (1), 42–53.

[48] Mohr, S. and O. Khan (2015). 3d printing and its disruptive impacts on supply chains of the future. *Technology Innovation Management Review 5* (11), 20.

[49] Myers, R. H., D. C. Montgomery, and C. M. Anderson-Cook (2016). *Response surface methodology: process and product optimization using designed experiments.* John Wiley & Sons.

[50] Ozbolat, I. T. and Y. Yu (2013). Bioprinting toward organ fabrication: challenges and future trends. *IEEE Transactions on Biomedical Engineering 60*(3), 691–699.

[51] Paris, F., J. Cañas, J. Marín, A. Barroso, and E. Correa (2006). Introducción al análisis y diseño con materiales compuestos. *Universidad de Sevilla*.

[52] Rodríguez, J. F., J. P. Thomas, and J. E. Renaud (2001). Mechanical behavior of acrylonitrile butadiene styrene (abs) fused deposition materials. experimental investigation. *Rapid Prototyping Journal 7*(3), 148–158.

[53] Rodríguez, J. F., J. P. Thomas, and J. E. Renaud (2003a). Design of fused-deposition abs components for stiffness and strength. *Journal of Mechanical Design 125*(3), 545–551.

[54] Rodríguez, J. F., J. P. Thomas, and J. E. Renaud (2003b). Mechanical behavior of acrylonitrile butadiene styrene fused deposition materials modeling. *Rapid Prototyping Journal 9*(4), 219–230.

[55] Schubert, C., M. C. van Langeveld, and L. A. Donoso (2013). Innovations in 3d printing: a 3d overview from optics to organs. *British Journal of Ophthalmology*, bjophthalmol–2013.

[56] Sherman, L. M. (2004). 3d printers lead growth of rapid prototyping. *Plastics technology 50*(8), 43–46.

[57] Song, T.-H., J. Jang, Y.-J. Choi, J.-H. Shim, and D.-W. Cho (2015). 3d-printed drug/cell carrier enabling effective release of cyclosporin a for xenogeneic cell-based therapy. *Cell transplantation 24*(12), 2513–2525.

[58] Sood, A. K., R. Ohdar, and S. Mahapatra (2010). Parametric appraisal of mechanical property of fused deposition modelling processed parts. *Materials & Design 31*(1), 287–295.

[59] Sood, A. K., R. K. Ohdar, and S. S. Mahapatra (2012). Experimental investigation and empirical modelling of fdm process for compressive strength improvement. *Journal of Advanced Research 3*(1), 81–90.

[60] Srinivasan, V. and J. Bassan (2012). 3d printing and the future of manufacturing. In *CSC Leading Edge Forum*.

[61] Standard, A. (2000). D3039/d3039m-00. *Standard test method for tensile properties of polymer matrix composite materials*.

[62] Standard, A. (2010). D638: Standard test method for tensile properties of plastics. *West Conshohocken (PA): ASTM International*.

[63] Standard, A. (2012). F2792. 2012. standard terminology for additive manufacturing technologies. *ASTM F2792-10e1*.

[64] Tsai, S. (1968). Fundamental aspects of fiber reinforced plastic composites. *Ann Arbor, MI: University Michigen Press*.

[65] Tsai, S. W. and E. M. Wu (1971). A general theory of strength for anisotropic materials. *Journal of composite materials 5*(1), 58–80.

[66] Ursan, I., L. Chiu, and A. Pierce (2013). Three-dimensional drug printing: a structured review. *Journal of the American Pharmacists Association: JAPhA 53*(2).

[67] Wohlers, T. (2010). Wohlers report 2010: Additive manufacturing state of the industry annual worldwide progress report, wohlers associates. *Inc., Colorado, USA*.

[68] Wohlers, T. (2013). Wohlers report 2013: Additive manufacturing and 3d printing state of the industry–annual worldwide progress report, wohlers associates. *Inc., Fort Collins*.

[69] Wohlers, T., W. Associates, and T. Caffrey (2014). *Wohlers Report 2014: 3D Printing and Additive Manufacturing State of the Industry Annual Worldwide Progress Report*. Wohlers Associates.

[70] Wohlers, T. T. (2006). *Wohlers Report 2006: Rapid Prototyping & Manufacturing State of the Industry: Annual Worldwide Progress Report*. Wohlers Associates.

[71] Zein, I., D. W. Hutmacher, K. C. Tan, and S. H. Teoh (2002). Fused deposition modeling of novel scaffold architectures for tissue engineering applications. *Biomaterials 23*(4), 1169–1185.

[72] Zuccarello, B. (2008). Progettazione meccanica con materiali non convenzionali. *Modalità di rottura e criteri di resistenza (Cap 6). Publications*.

Online sources

[73] http://www.matse.psu.edu.

[74] http://bioprintingworld.com.

[75] http://www-2.unipv.it/compmech.

[76] http://3dprint.nih.gov.

[77] https://3dprint.com.

[78] https://www.chemx.com.

[79] https://www.studyblue.com.

[80] https://www.additively.com.

[81] http://3dprinting.com.

[82] http://elco.crsndoo.com.

[83] http://www.mdpi.com.

[84] http://manual.slic3r.org.

[85] https://en.wikipedia.org.

[86] http://www.elettroaffari.it.

[87] http://www.eng.nus.edu.sg.

[88] http://www.3dprinter.my.

[89] http://www.3ders.org.

[90] http://www.shapeways.com.

[91] http://newatlas.com.

[92] http://www.popularmechanics.com.

[93] https://all3dp.com.

[94] http://www.efunda.com.

[95] http://www.unime.it.

[96] http://www.forum.cabledatasheet.com.

[97] https://www.3dcontentcentral.com.

[98] http://electrochemical.asmedigitalcollection.asme.org.

Ringraziamenti

È difficile riassumere in poche righe la gratitudine e l'affetto che provo per tutte le persone che nel corso della mia vita hanno contribuito alla mia crescita e al mio costante miglioramento. Perchè questo traguardo è il frutto di tanti sacrifici e tanto impegno. Ho l'immensa fortuna di avere una famiglia e degli amici che mi hanno sempre sostenuto nei miei momenti difficili, che hanno sempre creduto nelle mie capacità, ben più di quanto ne credessi io stesso, e che ogni tanto mi hanno giustamente rimproverato, quando me lo meritavo.

Un grazie infinito alla mia famiglia, a mia mamma Pierangela, a mio papà Pierluigi e ai miei fratelli Paolo e Alessio, per la pazienza che hanno avuto durante i miei momenti di difficoltà, per avermi sempre sostenuto e avere sempre creduto in me. Ovviamente un grandissimo ringraziamento va alle mie nonne, per l'affetto e la stima che quotidianamente manifestano nei miei confronti. Un pensiero va anche ai miei nonni Paolo e Lino, che purtroppo non ci sono più, ma vivono ancora nel mio cuore. Un grande ringraziamento a tutti i parenti, per aver sempre avuto fiducia in me.

E che dire dei miei amici? Sinceramente, senza di voi, senza il vostro sostegno, non sarei qui a festeggiare. Grazie di tutto, veramente. Daniela, Eddy, Edriano, ci conosciamo da oltre 20 anni, e voi non avete mai fatto mancare la fiducia nei miei confronti, spronandomi, incitandomi a fare sempre meglio, offrendomi la vostra stima incondizionata. Non riuscirò mai a ringraziarvi abbastanza, questo traguardo è anche merito vostro. Francesco e Alì, quante ne abbiamo passate insieme, nei tetri meandri della Nave? Tante, ma mai troppe! Quante ore passate a studiare, a preparare esami difficili, apparentemente impossibili. E tra una pausa e l'altra, scherzi, battute e risate... Non potevo trovare compagni di università migliori di voi! Un grande ringraziamento a tutte le persone che hanno creduto in me e mi hanno incitato, non dimenticherò il vostro sostegno.

Un sentito ringraziamento va al mio relatore, il Prof. Ferdinando Auricchio, conosciuto al corso di biomeccanica e successivamente al corso di modelli costitutivi dei materiali. Grazie al suo impegno e alla sua passione durante le lezioni in aula ho potuto veramente apprezzare la sua materia. Non a caso ho scelto un ambito di tesi che verteva sui suoi argomenti.

Un grandissimo ringraziamento a Stefania e Valeria, del laboratorio 3D@UniPV, per avermi aiutato e sostenuto durante questi mesi, sin dai primi momenti. Grazie per avermi accolto nel migliore dei modi e per avermi sempre fatto sentire a mio agio. Al giorno d'oggi bisogna essere molto fortunati per trovare dei colleghi di lavoro che siano delle brave persone con cui scherzare e andare d'accordo. Beh, io lo sono stato. Ringrazio inoltre i miei compagni tesisti, Claudio, Alessandra, Franca, Erika, per la piacevole compagnia e i bei momenti durante questo periodo di tesi. Un ringraziamento speciale al collega Andrea Montanino, per i momenti di allegria che è sempre riuscito a portare in laboratorio, sollevando il morale della truppa. Grande Monti!!!

Un immenso ringraziamento lo dedico infine a Gianluca Alaimo, per l'infinita pazienza che ha mostrato nello spiegarmi tutti i concetti fondamentali allo svolgimento della mia tesi, ma soprattutto per avermi insegnato la giusta *forma mentis* e il senso critico necessari per affrontare le varie situazioni che si manifestano, in ambito didattico come nella vita.